Forward and Inverse Problems in Fluid-Structure Interaction. Application to Hemodynamics

Cristobal Bertoglio

Problèmes Directs et Inverses en Interaction Fluide-Structure. Application à l'hémodynamique.

THÈSE DE DOCTORAT

Présentée par

Cristóbal Andrés Bertoglio Beltrán

pour obtenir le grade de

DOCTEUR DE
L' UNIVERSITÉ PIERRE ET MARIE CURIE - Paris VI

Spécialité : Mathématiques Appliquées

Soutenue publiquement le 23 novembre 2012 devant le jury composé de:

Yvon Maday	Président
Jean-Frédéric Gerbeau	Directeur de thèse
Miguel Ángel Fernández	Directeur de thèse
Emmanuel Maitre	Rapporteur
Alessandro Veneziani	Rapporteur
Dominique Chapelle	Examinateur
Stéphane Avril	Examinateur
Franck Nicoud	Examinateur

Après avis favorables des rapporteurs: Emmanuel Maitre et Alessandro Veneziani

Thèse préparée au sein de l'équipe-projet REO
Laboratoire Jacques-Louis Lions
Université Pierre et Marie Curie - Paris 6
et **Centre de Recherche INRIA Paris-Rocquencourt**
Domaine de Voluceau, BP 105
78153 Le Chesnay CEDEX

The research leading to these results has received funding from the European Community's Seventh Framework Programme (FP7/2007-2013) under grant agreement 224495 (euHeart project).

Remerciements

Caminante, son tus huellas el camino, y nada más;
caminante, no hay camino, se hace camino al andar.
Al andar se hace camino, y al volver la vista atrás
se ve la senda que nunca se ha de volver a pisar.
Caminante, no hay camino, sino estelas en la mar.
Antonio Machado, "Cantares", 1912.

En premier lieu je tiens à remercier très chaleureusement mes directeurs de thèse, Jean-Frédéric Gerbeau et Miguel Fernández, pour m'avoir accueilli dans le monde passionnant du tandem mathématiques-biomédicine, où j'avais décidé de tenter ma chance vers la fin de mes études de génie civile. Je tiens à saluer leur encadrement scientifique et professionnel exceptionnel, leur disposition constante à clarifier et discuter des diverses aspects techniques et leur encouragement à participer à la recherche des points développés au sein du l'équipe REO. Je vous remercie également pour votre honnêteté et pour m'avoir permis d'apprendre de mes propres erreurs. Merci également de fond du cœur pour votre soutien humain, sans lequel ce projet de thèse ne serait jamais arrivé à bon port.

Ce travail de recherche n'aurait pas non plus été possible sans les efforts et l'excellence scientifique de mes collaborateurs à l'INRIA et ailleurs. Tout d'abord merci à Dominique Chapelle et Philippe Moireau, du projet MACS, pour leur apport crucial au développement et à la mise en œuvre des méthodes d'assimilation de données présentées dans la deuxième partie de ce manuscrit. Bien sûr, les résultats sur les problèmes physiques et les données réelles ont été produits grâce au travail d'acquisition et de traitement des données au Royaume-Uni, dans le cadre du projet européen qui m'a financé. I would like to thank sincerely Nick Gaddum, for the aortic phantom data, and Isra Valverde, for the patients aortic data at King's College in London, as well as David Barber, Cristina Staicu and Rod Hose for the segmentations and processing of this data. Anche ringrazio Alfonso "Franco" Caiazzo, non solo per la collaborazione nel accoppiamento 0D-3D, ma anche per tua amicizia e il supporto a Parigi e Berlino!

Je remercie très sincèrement aussi les rapporteurs Emmanuel Maitre et Alessandro Veneziani pour la lecture détaillée de ce manuscrit et leurs remarques critiques et pertinentes. J'adresse également mes plus vifs remerciements à Yvon Maday, Dominique Chapelle, Stéphane Avril et Franck Nicoud pour avoir accepté d'enrichir mon jury.

Tout ce travail n'aurait été pas si fructueux sans l'interaction avec mes collègues du bâtiment 16 à Rocquencourt. Tout d'abord Matteo pour toutes les discussions sur l'interaction fluide-structure "physiologique" ;-) et pour tous les moments que nous avons eu la chance de partager, à Paris, Cemracs et ailleurs! Grazie mille Franco! Je ne peux bien sûr pas pas oublier Joaquín, qui avec son passage en France m'a amené un morceau de mon cher pays et qui à été toujours disponible, quel que

soit le sujet sur lequel portait la discussion ... Aussi Radek pour sa disposition à m'enseigner les aspects médicaux, entre autres, mais surtout pour m'avoir rapproché de la passionnante "culture tchèque" :-) Děkuju moc Radku! (a ano, alkohol z rukou lékaře je lék!) Je remercie également Romain pour toutes les discussions qui ont inspiré le chapitre sur le couplage 0D-3D. Grazie Cesare anche a te per il tuo sopporto napoletano!

Je ne peux évidemment pas oublier les personnes de l'INRIA avec lesquelles je n'ai peut-être eu que peu d'interactions au niveau scientifique mais qui ont toujours été là pour me soutenir quand j'ai en eu besoin et avec lesquelles j'ai aussi partagé beaucoup de beaux moments, que je garderai dans mon cœur (et dans mon foie!) pendant longtemps. Merci à Alexandre, Anabelle, Anne-Claire, Asven, Ayman, Chadha, Damiano, Danielle, Elisa, Emanuele, Filippo, Frédérique, Gregorio, Ibrahim, Ignacio, Jeremie, Julien, Justine, Keijo, Luna, Marc, Maya, Nejib, Nick, Nicolae, Saverio, Stéphane, Thomas, et William. Merci également aux chercheurs plus "seniors" (mais toujours "juniors" dans l'âme!) pour avoir toujours pris le temps de clarifier mes doutes: Celine, Dirk, Irene, Laurent, Marc et Marina. Et bien sûr, à Maryse pour son aide précieuse !

Je dois remercier aussi ceux qui ont guidé mes premiers pas dans le monde de la recherche. Mon directeur de mastère au Chili, José Luis Almazán, avec qui j'espère que Bacchus écoutera nos prières :-). Aussi Boris Khoromskij, qui m'a accueilli dans son équipe à Leipzig et m'a appris de nombreux aspects du calcul scientifique. Je ne peux pas oublier Sergio Gutierrez, qui m'a fortement recommendé de faire ma thèse à l'INRIA.

Je souhaite exprimer ma gratitude aussi à ceux qui m'ont fortement marqué, il y a presque 10 ans, dans les couloirs de l'hôpital de Valdivia, et qui m'ont aidé a regarder de plus près le monde de la santé: para Benítez, Pájaro y Martínez (q.e.p.d.) y los demás va también dedicada esta tésis.

Ces trois années n'auraient jamais été les mêmes sans les personnes qui ont enrichi mon expérience hors de Rocquencourt. Tout d'abord mes "cousins", Jorge et Eduardo, pour avoir été toujours là et pour avoir partagé d'innombrables moments dont je me souviendrai toujours, surtout toutes les soirées mythiques dans le "Triangle des Bermudes" à Saint-Germain de Près.

D'autres ont été une partie importante de ma vie à Paris et je ne peux les laisser de côté dans ces remerciements, car eux il m'ont aidé à me sentir un peu comme chez moi. Merci à Marie, pour son accueil chaleureux, à Magali, qui a toujours voulu m'écouter et me prodiguer des conseils, et aussi partager bon nombre de moments culinaires. Merci à vous, Anna, Joanna et Maks, pour m'avoir toujours donné le sentiment d'avoir une famille loin de ma terre natale. Et à Mathilde aussi, que je suis heureux d'avoir pu revoir à Paris! Aussi à Carina pour son amitié désintéressée et son soutien et à Pancho et Gloria pour tous les beaux moments.

En me remémorant cette période, je me souviendrai non seulement de mes travaux de recherche mais aussi de toutes les personnes que je viens de mentionner et qui me sont si chères. Enfin, cet expérience a signifié aussi d'être loin de ma famille, que je n'ai jamais oubliée et à qui cette thèse est dédiée. Comme mon

compatriote, Pablo Neruda, l'a écrit en ces vers: *De alguna manera o de otra, yo viajo con nuestro territorio y siguen viviendo conmigo, allá lejos, las esencias longitudinales de mi patria" ....* sí, mi patria y mi gente, a pesar de esta distancia que duele, pero que como todo dolor a la vez me dió la fuerza para seguir adelante y dar lo mejor de mí. A mis padres, los cuales abandoné de adolescente para seguir mis sueños y sin su apoyo nunca hubiera logrado llegar al final de este camino. A mis abuelos, algunos de los cuales apenas conocí pero de los que sin duda heredé buena parte de mi carácter y mis raíces de las cuales me enorgullezco. A mi hermana, que me ha apoyado en todos los momentos importantes. Al igual que mis tíos y primos, que siempre me han hecho sentir querido. Herzlichen Dank auch an meine Bundesbrüder, die mir immer das Gefühl gegeben haben trotz der Ferne treu an meiner Seite zu bleiben.

Y por supuesto a Nicolás, que apareciste en mi vida cuando menos me lo esperaba, pero quizás cuando más lo necesitaba. Me diste fuerzas desde el principio para aguantar y llegar a la meta. Espero que no guardes rencor por no haber estado siempre a tu lado y puedas entender lo que viví.

A mé Barunce, za její obrovskou podporu a bezbřehou věrnost v každé chvíli od našeho setkání... Za tento drahocenný dar děkuji Tobě, Paříži. Doufám, že ho budu ochraňovat po dlouhou, předlouhou dobu...

Problèmes Directs et Inverses en Interaction Fluide-Structure. Application à l'hémodynamique

Resumé: Dans cette thèse nous traitons de la simulation d'interaction fluide-structure (FSI) dans les problèmes en hémodynamique, en mettant l'accent sur l'assimilation de données et sur la simulation dans les conditions physiologiques.

La première partie présente et analyse un schéma de couplage semi-implicite des équations de Navier-Stokes (NSE) et d'un modèle de conditions aux limites réduit, lorsque les NSE sont résolues avec une méthode de projection. Cela permet de simuler des problèmes de mécanique de fluides et de FSI de façon plus robuste, c'est à dire en évitant les possibles instabilités associées à des cas-tests réalistes.

La deuxième partie est consacrée à l'assimilation des données avec des méthodes séquentielles en FSI. Nous présentons d'abord une étude sur l'application d'un filtre de Kalman réduit pour l'estimation efficace des paramètres physiques d'intérêt, comme la distribution de la rigidité de la paroi de l'artère et la résistance proximale dans le fluide, à partir des mesures de deplacement à l'interface fluide-structure. Ensuite, nous analysons certains observateurs de Luenberger utilisés pour la mécanique des solides en FSI, dans le but de construire des estimateurs d'état efficaces pour des problèmes FSI de grande taille.

Dans la troisième et dernière partie, nous appliquons les méthodologies mentionnées ci-dessus aux problèmes physiques réels. Tout d'abord, la rigidité de la paroi est estimée (pour des modèles solides linéaires et non linéaires) à partir de données provenant d'un tube de silicone simulant une aorte. Pour finir, nous analysons une aorte réelle avec une coarctation réparée, nous testons les techniques d'estimation avec des données synthétiques et nous montrons quelques résultats obtenues à partir de données issues du patient.

Mots-clés: interaction fluide-structure, méthodes de projection, imagérie médicale, assimilation des données, filtre de Kalman, observateurs de Luenberger, coarctation de l'aorte.

Forward and Inverse Problems in Fluid-Structure Interaction. Application to Hemodynamics

Abstract: In this thesis we deal with the simulation of fluid-structure interaction (FSI) problems in hemodynamics, with the emphasis in data assimilation and simulation in physiological regimes.

The first part presents and analyzes a semi-implicit coupling scheme between the three-dimensional Navier-Stokes equations (NSE) and lumped parameter models, when the NSE are solved in a projection framework. This allows to simulate fluid and FSI problems more robustly, i.e., avoiding instabilities that may occur when dealing with realistic test-cases.

The second part of the work is devoted to the study of sequential data assimilation techniques in FSI. We first present a study about the application of a reduced-order Unscented Kalman Filter for the effective estimation of relevant physical parameters, like the stiffness distribution of the vessel wall and the proximal resistance in the fluid, from displacement measurements at the fluid-structure interface. Next, we analyze some Luenberger observers from solid mechanics in FSI, with the aim to construct tractable state estimators for large-scale FSI problems.

In the third and final part, we apply some of the aforementioned methodologies to real physical problems. First, we perform the estimation of the wall stiffness (for linear and non-linear solid models) from data coming from MR-images of a silicone rubber aortic phantom. To finish, we deal with the forward analysis of a real aorta with repaired coarctation and we test the estimation techniques with synthetic data and show some results with the patient's data.

Keywords: fluid-structure interaction, projection method, medical imaging, data assimilation, Kalman filtering, Luenberger observers, aortic coarctation.

Contents

Introduction

Die Arznei macht kranke,
die Mathematik traurige
und die Theologie sündhafte Leute.
Martin Luther.

Chapter 1

Introduction

In this chapter, we first provide a basis about the physiology, structure and mechanical properties of the elastic arteries, as well as some of the currently used methods for the quantification of the arterial wall stiffness. As a clinical relevant application, we refer to the pathology called *coarctation of the aorta*. Then, we summarize the rest of the thesis by reporting the main results of each chapter.

Contents

1.1 Estimation of the arterial stiffness

This section presents some basic material with the aim of discussing possible applications of the results of this thesis: the estimation of the mechanical properties of the aortic wall from three-dimensional and dynamic clinical data (e.g., medical images) using fluid-structure interaction models. We emphasize that the spirit is to give a general overview without entering into too technical details.

We start with an overview of the circulatory system, describing its anatomy and function, in particular detailing the cardiac cycle. Then we present the structure and properties of arteries, followed by a summary of the methodologies used in the clinical practice for estimating arterial stiffness.

Note that Sections 1.1 and 1.2 are mainly based on [Kla11, SS11, Pro09, Val12, Vir08, Hum02] and references therein, if no other bibliography is explicitly indicated.

1.1.1 The circulatory system and the cardiac cycle

The circulatory system consists of the organs responsible for the transportation of blood throughout the body. It is mainly composed of the heart (divided in four chambers, left and right atria and ventricles), arteries, capillaries, and veins (see Figure 1.1). It transports oxygenated blood from the lungs to the heart through the pulmonary veins and from the heart to the rest of the body through the systemic arteries. In the organs, the blood passes from the arteries to the capillaries, releases oxygen and nutrients to the cells, collects carbon dioxide and waste substances and then it continues flowing through the veins back to the heart.

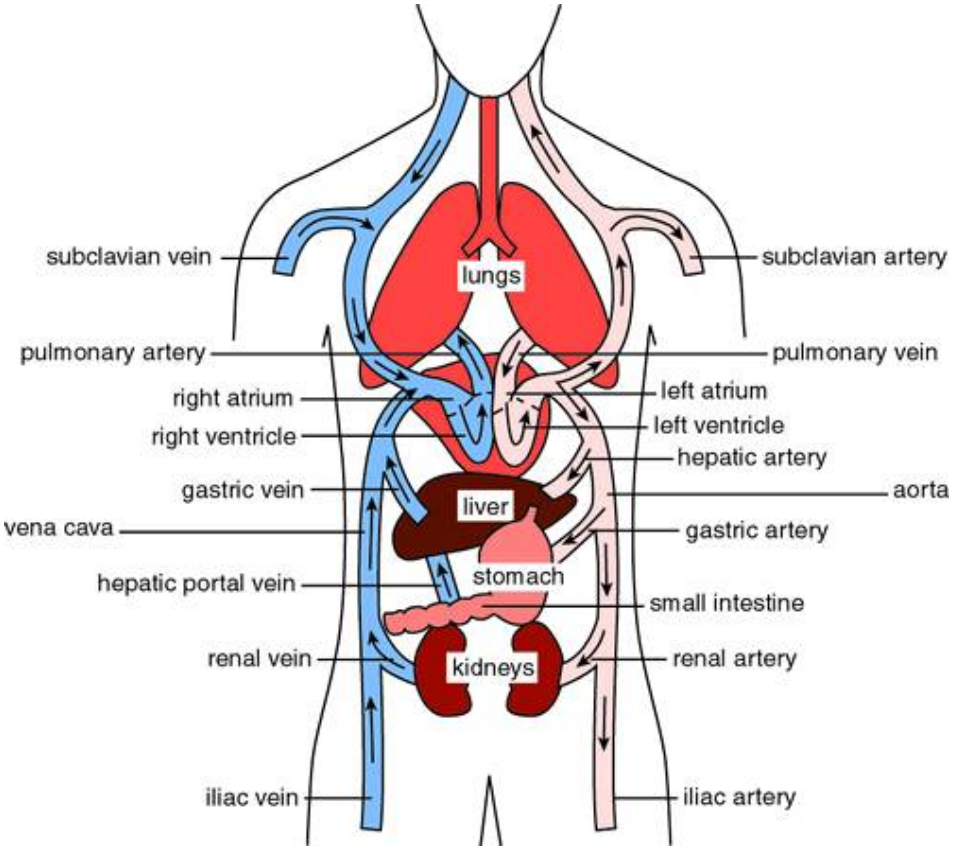

Figure 1.1: A schematic view of the circulatory system, representing the major vessels of the systemic and pulmonary circulation loops and the main organs (from [Tal11]).

The blood circulation. The circulation is divided in two parts forming a closed loop. The *systemic circulation* originates from the left chamber of the heart (see Figure 1.2), from where the blood flows through the aortic valve into the aorta. Directly behind the aortic valve two small arteries (called *coronary arteries*, not in the figure) branch off for the supply of blood to the heart. The aorta itself, see

Figure 1.3, initially follows an upward path (ascending aorta) and then forms a curve (aortic arch) before proceeding downwards (descending aorta) parallel to the spine.

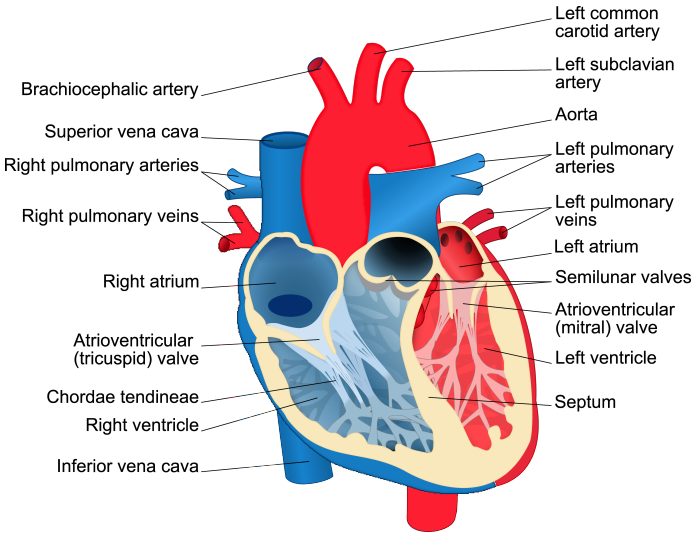

Figure 1.2: The heart and the sourrounding blood vessels (from [Wik11]).

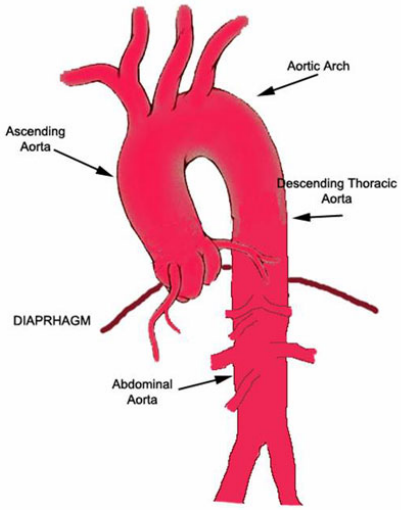

Figure 1.3: Scheme of the aorta (from *my.clevelandclinic.org*).

The *pulmonary circulation* begins in the right ventricle and ends in the left atrium. The right ventricle ejects the blood low in oxygen through the pulmonary trunk, which divides into the two pulmonary arteries (one for each lung). In the lungs, the vessels continue to branch out until capillaries. At this level, the blood releases carbon dioxide (expelled then during the exhalation), and oxygen (from

the inhaled air) is absorbed back to the blood. After this exchange of gases, the oxygenated blood returns to the heart via four large pulmonary veins into the left atrium.

Electrophysiology of the heart. The circulation of the blood is driven by the pump function of the heart, which is controlled by electrical commands initiating in the right atrium. Due to the conductive properties of the cardiac tissue, an electrical wave is propagated through the atrioventricular node to the ventricles. The passage of the wave activates the contraction of the myocardium (cardiac muscle), whereas after the wave pass through the tissue relaxes. The combination of contractions and relaxations in the different heart regions, together with the valves dynamics, induces pressure gradients through the different heart chambers. This mechanism rules the flow of the blood from and into the circulatory system.

The electrical charge of the cells is determined by the transfer of ions (sodium (Na^+), potassium (K^+) and calcium (Ca^{2+})). Without electrical stimuli, the cells are called to be *polarized*, namely the transmembrane potential[1] is negative due to the poor concentration of sodium and calcium ions in the cell. When the electrical stimuli arrives to the cell, the ion channels in the membrane open so that the transfer of sodium inwards the cell occurs. This is called *depolarization*, where the transmembrane potential becomes positive, leading to the contraction of the cardiac cells. After this, several exchanges of ions across the cell membrane occur in order to return to the electrical equilibrium (polarized) state.

The electrical activity of the heart is clinically quantified using the electrocardiogram (ECG), which consists in measuring the electrical potential on the body surface, and where the different phases of the wave propagation can be identified (cf. Figure 1.5).

The cardiac cycle. The cycle of activity of the heart is generally divided into two phases: the *diastole*, when the heart ventricles are relaxed (polarized) and the heart is being filled with blood; and the *systole*, when the ventricles contract (depolarized) and pump blood to the arteries. However, to analyze the phases in more detail, the cardiac cycle is usually divided into seven phases (see Figures 1.4 and 1.5):

(1) *Atrial contraction.* It follows by the atrial depolarization at the end of the diastole. The pressure within the atrial chambers increases, which forces the blood to flow across the open atrioventricular valves into the ventricles.

(2) *Isovolumetric contraction.* After atrial contraction is complete, the depolarization wave advances to the ventricles, which contract rapidly increasing the intraventricular pressure. This induces a pressure gradient reversal across the atrioventricular valves, leading to their closing. Then, the ventricular pressure continues rising due to the contraction without changing of the intraventricular volume, and also the atrial pressure begins to fall.

[1]Transmembrane potential is the difference in electrical potential between the interior and exterior of a biological cell.

(3) *Rapid ejection.* When the intraventricular pressures exceed the pressures within the aorta and pulmonary artery, aortic and pulmonic valves open and blood is ejected into these arteries. Maximal outflow velocity and maximal aortic and pulmonary artery pressures are achieved in this phase. Meanwhile, blood continues to flow into the atria from their respective venous inflow tracts and the atrial pressures begin to rise.

(4) *Slow ejection.* In this phase, ventricular repolarization, leads to a decline in ventricular active tension and therefore the rate of blood ejection into the ventricles falls. Ventricular pressure falls slightly below the aortic pressure; however, outward flow still occurs due to kinetic (or inertial) energy of the blood. Left and right atrial pressures gradually rise due to continued venous return from the lungs and from the systemic circulation, respectively.

(5) *Isovolumetric relaxation.* When the intraventricular pressures fall sufficiently due to the repolarization, the aortic and pulmonic valves abruptly close. Hence, ventricular volume remains constant while atrial pressures rise since they continue being filled.

(6) *Rapid filling.* As the ventricles continue to relax, the intraventricular pressures will fall below their respective atrial pressures. When this occurs, the atrioventricular valves rapidly open and ventricular filling begins. Despite the inflow of blood from the atria, intraventricular pressure continues to shortly fall because the ventricles are still undergoing relaxation. Once the ventricles are completely relaxed, their pressures will slowly rise as they are still being filled.

(7) *Slow filling.* As the ventricles continue being filled with blood and expand, they become less compliant[2] and the intraventricular pressures rise. This also reduces the pressure gradient across the atrioventricular valves so that the rate of filling falls. Aortic pressure and pulmonary arterial pressures keep falling during this period. After this phase the cardiac cycle restarts with the atrial contraction.

1.1.2 Structure and mechanical properties of arteries

Arteries are organs whose function is the transportation of the blood through the body. Particularly, arteries near to the heart allow to moderate the fluctuations in the cardiac outflow, serving as an elastic fluid reservoir. During the first half of systole, they distend elastically due to the increase of the aortic pressure. From end of systole to end of diastole, when the internal efforts of the distended arterial wall exceed the intraluminal pressure, the artery "press back" the blood discharging it towards the periphery. This helps to maintain a relatively constant pressure in the distal arteries despite the pulsating nature of the blood flow produced by the heart as it can be seen in Figure 1.5. The amount of blood that can be stored and the

[2]The stiffening of soft tissues with increasing loading occurs since the different structural components are gradually activated. We will see this in the case of the arteries in next section.

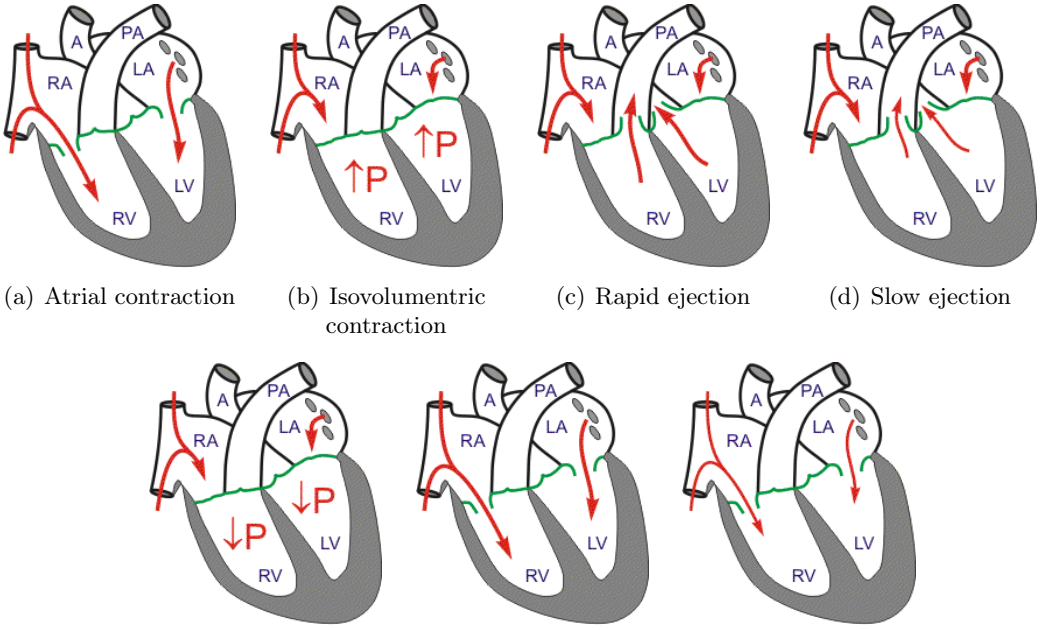

(a) Atrial contraction (b) Isovolumentric contraction (c) Rapid ejection (d) Slow ejection

(e) Isovolumetric relaxation (f) Rapid filling (g) Slow filling

Figure 1.4: The seven phases of cardiac cycle (from [Kla11]).

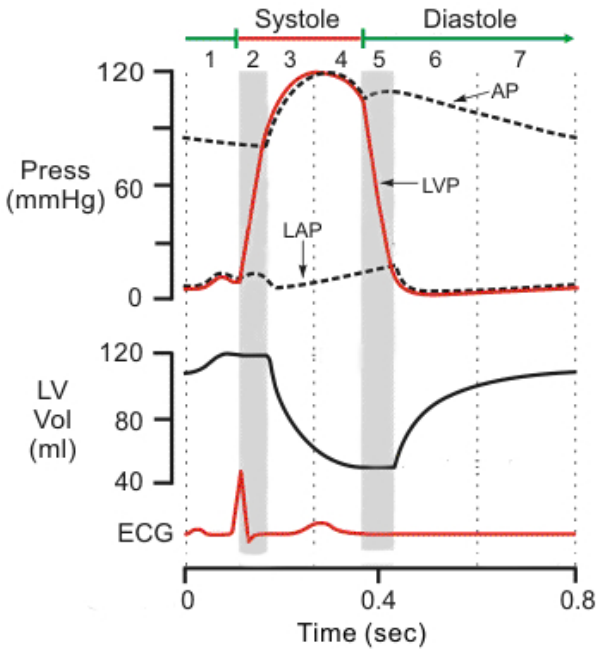

Figure 1.5: The cardiac cycle in terms of the physiological variables (adapted from [Kla11]). LAP, LVP and AP refer to the left atrium's, left ventricular's and arterial's pressure, respectively.

associated pressure, as well as the rate of release during diastole, it is determined by the total peripheral resistance[3] and by the elasticity of the arteries. Moreover, as it will be seen next, the mechanical properties of arteries also have a direct impact on the loading of the heart, i.e., on the forces that resist to the contraction, what can lead to severe cardiovascular pathologies.

Composition and structure. Arteries are mainly composed of three types of tissue: collagen, elastin and smooth muscle. Collagen and elastin are fibrous structural proteins that constitute the base of all connective tissues[4], where collagen is stiffer than elastin. Smooth muscle is one of the three types of muscle tissue in the body (smooth, cardiac and skeletal), and it is characterized by the absence of a definite striped pattern or *striations*, which are seen in the other two types. It generally forms the supporting tissue of blood vessels and internal organs such as the stomach, intestine and bladder. Similarly to the cardiac tissue, it is able to perform involuntary contractions, what is necessary for the physiological function of the organs where it is present.

The composition and mechanical properties of arteries vary throughout the arterial tree, depending on the different functions that each artery has to accomplish, but they can be classified into two main types: *elastic* and *muscular*. The elastic arteries are closer to the heart (e.g. the aorta and direct out-branching arteries like carotid and iliac), they have larger diameter and are more compliant since they contain higher proportions of elastin with respect to collagen. As mentioned above, their function is mainly to stabilize the pressure fluctuations and to store blood during systole. Muscular arteries are closer to capillaries and are smaller and less compliant (proportion of elastin decreases with respect to collagen and smooth muscle) with the main role of distributing the blood. Even they exhibit qualitatively a similar histological arrangement (see for instance [Hum02]), in the sequel we will focus on elastic arteries[5].

Despite of the heterogenous distribution of the arterial components throughout the body, in general three main layers or *tunicas* can be distinguished in the arterial wall structure: the intima, media and adventitia (see Figures 1.6 and 1.7).

The *intima* is the innermost layer of the artery, consisting of a single sheet of endothelial cells (in contact with the blood and usually alongated in the direction of the flow), plus a thin layer of connective tissue (collagen and elastin), called internal elastic laminae. The endothelial cells detect physical and chemical changes of the environment and can release vasodilators, which act on smooth muscle cells for adjusting the mechanical properties to acute stimuli, for example alterations in the blood pressure. In young healthy individuals, the contribution of the intima to

[3] Total peripheral resistance corresponds to the ratio between the pressure gradient across the systemic circulation and the cardiac output. It is mainly determined by the geometry of the arterial network [NOH05].

[4] Tissues composed of fibers forming a support structure for larger tissues and organs.

[5] The reason is that the emphasis of the numerical experiments in this thesis is the aorta, and the ultimate goal of this work is the estimation of its mechanical properties.

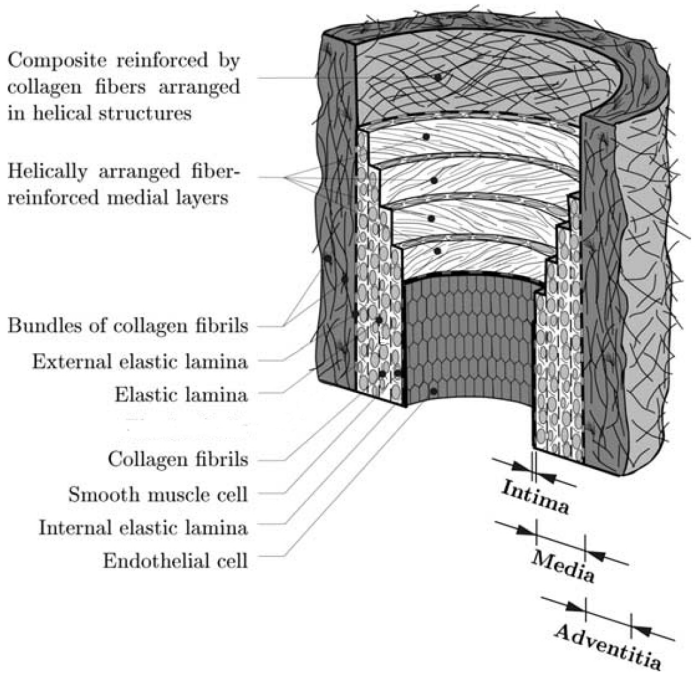

Figure 1.6: Schematic view of the tree tunics (adapted from [HGO00]).

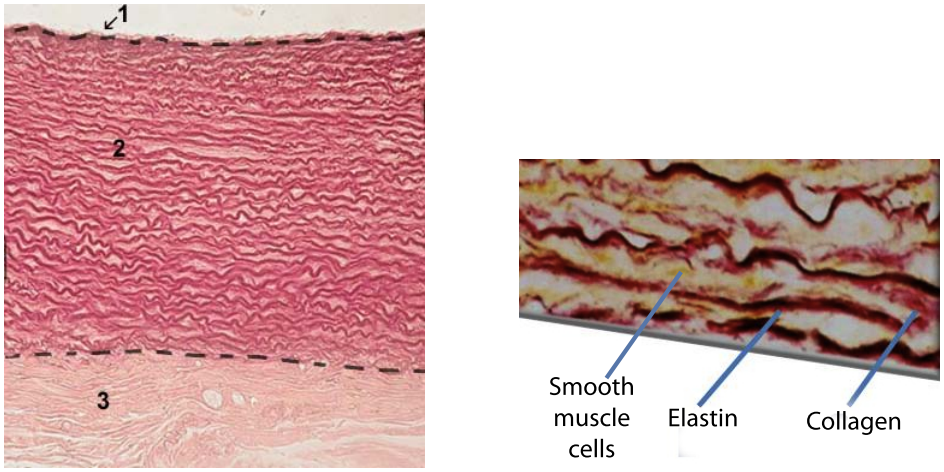

Figure 1.7: Histological cut of an aorta. Left: the three tunics, 1 intima, 2 media and 3 adventitia (from *http://histol.narod.ru*). Right: tunica media (from *http://www.ceessentials.net*).

the mechanical properties of the artery is insignificant. However, it is the location where atherosclerosis[6] develops.

The media is the middle layer of the artery and consists of a complex three-dimensional network of smooth muscle cells, elastin and collagen fibers (see Figure 1.7-right). It is the layer which gives the main mechanical properties to a healthy arterial wall. The media is separated into a varying number of concentrically fiber-reinforced layers. These layers are defined by wave-shaped elastin fibers similar to the internal elastic laminae. Between the elastin fibers, collagen fibers (with variable orientation) surround the smooth muscle cells. This structured arrangement gives the media high strength, flexibility and the resistance to loads in both the longitudinal and circumferential directions.

The adventitia mainly consists of connective tissue fibers (again, collagen and elastin). Collagen fibers contribute significantly to the stability and strength of the arterial wall, preventing it from acute over-distension. Moreover, it is common to find peripheral vessels[7] and nerves (for the innervation of the smooth muscles cells in the outer media). In many vessels, the adventitia blends with the connective tissue surrounding the vessel. Therefore, the definition of its outer limit is somewhat arbitrary.

Mechanical behavior. Due to their structure and composition, arteries have a nonlinear constitutive behavior (see Figure 1.8). The pressure exerted on the arterial wall is transferred from intima to adventitia, where the stresses are gradually passed from elastin to collagen increasing the stiffness. Moreover, they present hysteresis dissipating energy during the loading-unloading process.

Arteries also show an anisotropic mechanical behavior since collagen and elastin fibers are oriented in certain directions. In fact, collagen is the main constituent that gives the anisotropy to the artery, because its chains are more oriented than the elastin. In particular, the arterial wall is stiffer in the circumferential than in the axial direction.

The arterial pressure oscillates in a range of approximately 80-120 mmHg (see Figure 1.5), hence the arterial wall is permanently under the action of external forces. Moreover, it is widely accepted that residual stresses are presented in arteries (i.e., stresses at zero external load) resulting from their permanent grow and remodeling. These residual stresses are mainly resisted by the elastin fibers, which are responsible for the mechanical properties at low loads, as said above.

It is also important to mention that in addition to cells and connective tissue, the arterial wall contains an important amount of water (mainly extracellular) of

[6] Atherosclerosis is the most common arterial disease. It mainly consists of the deposition of fat, calcium and collagen in the intima. It dramatically affects the morphology of the lumen (augmenting resistance to flow) and the mechanical behavior of the arterial wall (increasing stiffness).

[7] The walls of large arteries are so thick that oxygen and nutrients from the lumen cannot perfuse the peripheral parts. Larger vessels have therefore attached smaller blood vessels which supply the adventitia and, in the largest vessels, the outer part of the media. They are called *vasa vasorum*, from latin "vessels of the vessels".

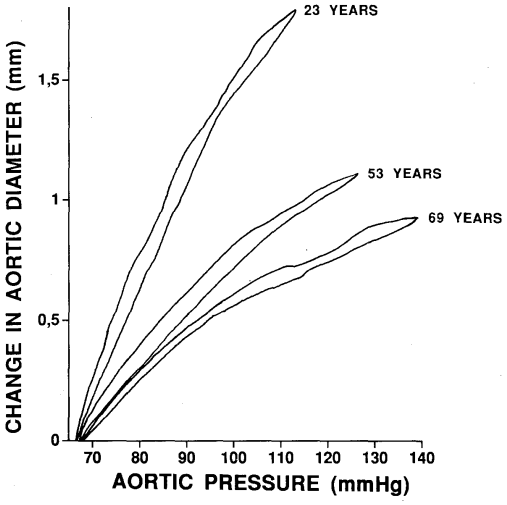

Figure 1.8: Sample curves for pressure-diameter relationship in three human aortas and variation with age (from [SLVH94]).

about 70% of the total mass. Hence, it is fairly reasonable to consider it as a nearly incompressible solid.

As other soft tissues, arteries are also capable to perform involuntary contractions, mainly due to the transmembrane calcium flux in the smooth muscle cells due to acute alterations of the environment. However, it occurs much more slowly than in striated muscle (e.g. myocardium), and taking in order for few seconds to achieve its maximum level. They can however maintain maximum contraction for much longer periods.

Constitutive modeling. The aforementioned mechanisms allow to control the propagation of the pressure wave and a more rapid recover to the original position after the fluid passes through. However, as we will see next, the clinically used indexes for representing the arterial stiffnesses are based on linear constitutive assumptions, namely,

$$\boldsymbol{\sigma}_{\mathrm{s}} = \mathbf{H}\boldsymbol{\varepsilon}_{\mathrm{s}}$$

with $\mathbf{H}$ the elasticity tensor depending typically on the Young's modulus E (stress-strain ratio in the case of uniaxial load) and the Poisson modulus ν (ratio between strains in parallel and perpendicular to an applied load). For modeling purposes, these approaches for quantifying the arterial stiffness can give a preliminary quantitative assessment of the arterial properties for setting up more complex mathematical constitutive models.

In biomechanics, the so called *hyperelastic* models are widely accepted to be an appropriate choice for representing the mechanical behavior of soft tissues. We briefly introduce them as follows.

Assume that a body undergoes a deformation field $x = \varphi(\hat{x})$, with $\hat{x}$ and x the spatial coordinates of the same material point at the reference and deformed configurations, respectively. Let us denote $\mathbf{F} = \nabla_{\hat{x}}\varphi$ the gradient of the deformation field. The hyperelastic materials are based on a representation of the stress-strain behavior in terms of the derivative of a strain-energy function W as [LT94, FFP79]

$$\boldsymbol{\sigma}_{\mathrm{s}} = \frac{\partial W}{\partial \mathbf{F}}.$$

This function W describes the density of elastic strain energy stored during the deformation of the body of interest. When the material is isotropic, this function has to be independent of any local rotation of the reference system, hence it can be written only in terms of the eigenvalues of the *right Cauchy-Green* tensor $\mathbf{C} = \mathbf{F}^T\mathbf{F}$, λ_i^2, $i = 1, \ldots, 3$, namely

$$W = W(I_1, I_2, I_3)\ , I_1 = \lambda_1^2 + \lambda_2^2 + \lambda_3^2\ ,\ I_2 = \lambda_1^2\lambda_2^2 + \lambda_2^2\lambda_3^2 + \lambda_3^2\lambda_1^2\ , I_3 = \lambda_1^2\lambda_2^2\lambda_3^2$$

with I_1, I_2, I_3, called the *invariants* of $\mathbf{C}$.

Some of the simplest hyperelastic material models are the compressible Neo-Hookean and Mooney-Rivlin models

$$W_{\mathrm{nH}} = c_1(\bar{I}_1 - 3) + \kappa(\bar{I}_3 - 1)\ ,\ W_{\mathrm{MR}} = W_{\mathrm{nH}} + c_2(\bar{I}_2 - 3) \tag{1.1}$$

respectively, with c_1, c_2, κ the material-dependent constitutive parameters and $\bar{I}_1 = I_3^{-2/3}I_1$, $\bar{I}_2 = I_3^{-4/3}I_2$. For representing the behavior of rubbers usually the Mooney-Rivlin model is the most popular choice. For the arterial wall, one popular choice is for instance the Holzapfel-Gasser-Odgen model [HGO00]

$$W_{\mathrm{HGO}} = c_1(\bar{I}_1 - 3) + \sum_{j=1}^{\ell} \frac{k_j}{2\,a}\{\exp(a(\bar{I}_{4,j} - 1)^2) - 1\}. \tag{1.2}$$

The first term (neo-Hookean model) represents the non-collagenous matrix material. The second term models the strong stiffening effect of the collagen fibers, where j denotes the layer-specific index with ℓ the number of tissue layers. In the invariant $\bar{I}_{4,j}$ is included the information about the angle of the collagen fibers at each layer j, and k_j, $j = 1, \ldots, \ell$ and a are material dependent (and layer specific) parameters. We refer to [HO10] for an extensive review of different constitutive modeling options.

1.1.3 Methods for estimating the arterial's mechanical properties

Arterial mechanical properties are well accepted as one of the most important determinants of hypertension in aging societies, hence contributing to stroke and myocardial infarction [LCVB+06]. Thus, their quantification is of increasing clinical interest for the assesment of cardiovascular risk.

Methods for the estimation of the arterial mechanical properties can be classified into: *direct*, where the mechanical parameter values are obtained directly from the

measurements, and *indirect*, where surrogates of these values are estimated. Methods can also be separated into: *local*, when all measurements come from one section of the artery, and *regional* when the estimated value corresponds to measures obtained in distal points of the arterial network. An additional classification can be assessed in terms of the character to the measurements as: *invasive*, where some dispositive has to be introduced into the arterial lumen in order to determine some of the quantities needed for the estimation (e.g. pressure catheterization), and *non-invasive*, where all measurements are obtained outside from the body (e.g., medical imaging and blood pulse).

As next we will overview some of the currently used methods for estimating the mechanical properties of the arterial wall.

Pulse Wave Velocity (PWV). PWV corresponds to the traveling speed of the pulse wave through a segment of the arterial tree, i.e.,

$$\mathrm{PWV} = \frac{\Delta L}{\Delta t}, \tag{1.3}$$

with ΔL the distance travelled by a pressure wave through an elastic vessel and Δt its transit time. Typical values of PWV in elastic arteries vary between 5 and 15 m/s and they increase with age and with mean blood pressure [The10]. This quantity can be related to the stiffness of the elastic vessel, for example through the well-known Moens-Korteweg equation

$$\mathrm{PWV} = \sqrt{\frac{Eh}{2\,(1-\nu^2)\,r\,\rho_{\mathrm{f}}}}, \tag{1.4}$$

with E the Young's modulus at the configuration with radius r, ρ_{f} the fluid mass density, ν the Poisson's ratio of the solid and h the thickness of the vessel wall. This expression can be computed by obtaining the wave speed resulting of the Navier-Stokes equations coupled to a generalized string model for the vessel wall on an infinite cylindrical domain, with the assumption of small deformations [FQV09].

PWV measurements is the gold-standard in clinical practice for the assessment of arterial stiffness since it is simple examination and reproducible among patients. It is also considered in clinics as an independent predictor of cardiovascular morbidity [CLRAM11].

Most of PWV clinical investigations are performed non-invasively by collocating pressure-sensitive transducers on the skin, typically at the carotid and femoral arteries. Also ultrasound (US) or magnetic resonance imaging (MRI) can be used in order to measure the flow pulse[8]. MRI has the advantage that the distance traveled by the wave can be assessed more accurately, especially in tortuous geometries (common in old subjects). Usually, the foot of the pulse wave is used to determine the transit time as explained in Figure 1.9.

[8]Pressure and flow pulse travel at the same velocity if the assumptions of the simplified fluid-solid model presented above hold, see [FQV09]

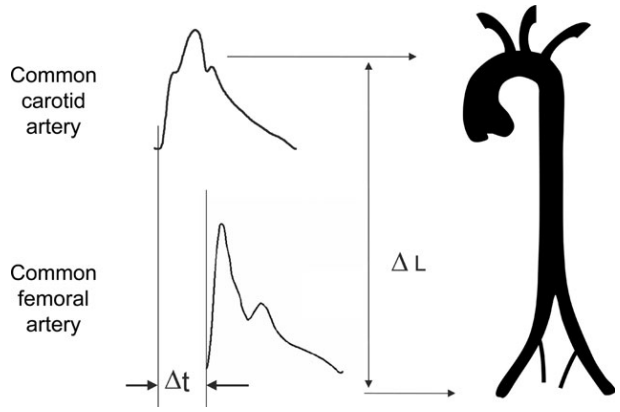

Figure 1.9: Illustration of the locations for measuring the pressure pulse for the determination of the PWV and the quantities used for its computation in Equation 1.3 (from [LCVB+06]).

Arterial compliance and distensibility. Arterial compliance C and distensibility D are direct and local measures of the arterial stiffness in a vessel by quantifying the change in volume ΔV due to a change in pressure ΔP as

$$C = \frac{\Delta V}{\Delta P} \ , \ D = \frac{C}{V} \ . \tag{1.5}$$

A first simple and non-invasive approximation of these quantities in the aorta can be obtained by: approximating ΔP through the pressure pulse (i.e., the difference between peak systolic and diastolic pressures) in the carotid artery, and simultaneously obtaining the change of cross sectional area of the artery at the same location by means of ultrasound or magnetic resonance imaging, see Figure 1.10. This approach lies on the assumption that the carotid artery has a similar composition as the aorta and it is more accessible for the measurement of diameter and pressure. For a more accurate determination of the arterial compliance, invasive and local pressure measurements (catheterization) are sometimes used, together with medical imaging for assessing the diameter change.

Compliance and distensibility measurements are not yet a validated or routinely used clinical index, but it is currently being matter of extensive research, see for example [LCVB+06]. Hence, for the moment in clinical practice invasive measurements for the assesment of the arterial compliance are obtained when there are other indications for the catheterization (stent placement, pressure gradient measure across the aorta, etc).

Vascular elastography. Elastography is a noninvasive technique for estimating the mechanical properties of tissues by propagating and imaging mechanical waves [Doy12]. The basic idea is to excite the tissue with harmonic pulses in order to get

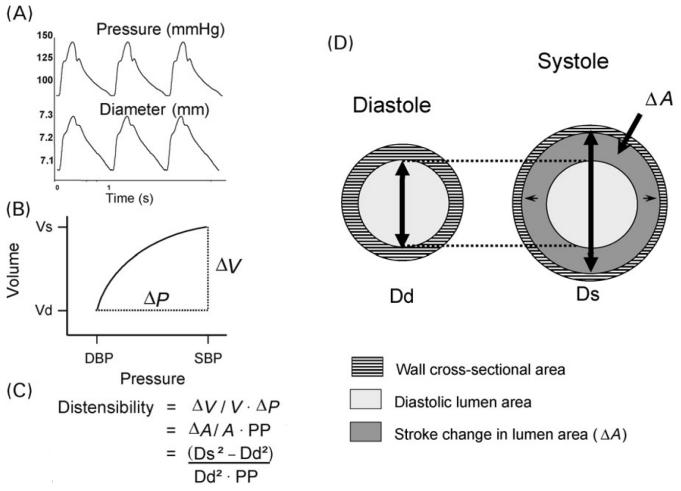

Figure 1.10: Scheme illustrating the local measurement of distensibility (from [LCVB+06]). (A) Simultaneous recording of pressure and diameter. (B) Pressure-diameter curve. (C) Calculation of distensibility. (D) Representation of the stroke change (ΔA) in lumen cross-sectional area.

an image of the strain field. Relating loads and measurements through, e.g., the Helmholtz equation in two or three dimensions can lead to estimates of some of the mechanical properties. It has been applied to quantitatively assess the viscoelastic properties of many human tissues in vivo, including breast, brain, muscle and liver [MGE10].

Ultrasound (US) based elastography has been used in arteries mainly with the aim of detecting artherosclerotic plaques, see for instance [dKHvdS11]. Moreover, in [BBC+07, BBC+10] the authors perform stiffness and viscosity estimation also using US-data but applying an inverse approach by means of reduced mathematical models.

However, US is limited to arteries close to the body surface (like the carotid). For the aorta, Magnetic Resonance Elastography (MRE) has been studied as an alternative to vascular US, where the imaged wavelength can be related to the Young's modulus [WRL+06, XCY+12], see examples in Figure 1.11. However, the estimation of the stiffness is based on the Moens-Korteweg equation (1.4), hence it is generally limited to long elastic cylindrical vessels and small displacements, and the loading induced by the mechanical waves is not necessary physiological.

Estimation of constitutive parameters. The direct estimation of constitutive parameters in human's arteries is a matter of great interest in the biomechanics community. Studies usually assume a long cylindrical geometry (for both models and experiments) and they fit hyperelastic materials parameters (typically models similar to (1.2)) to the data at the same locations of the measurements.

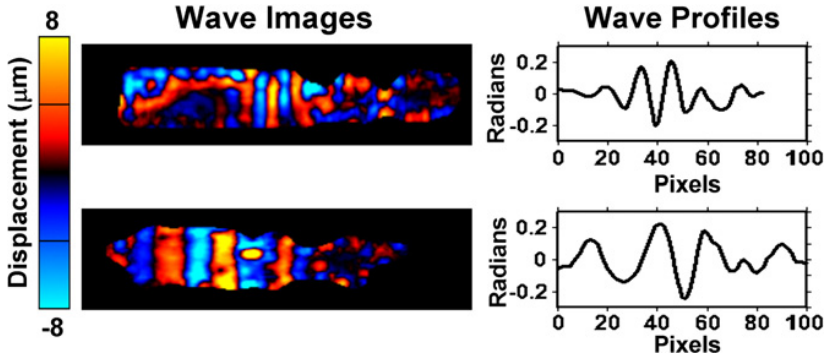

Figure 1.11: MRE for two arterial segments of porcine aortas tested *ex vivo* (from [XCY+12]). The image at the top corresponds effectively to a stiffer aorta, as was verified in independent mechanical tests.

Most of the studies have been carried out *ex vivo*, namely through data obtained from experiments with pieces of tissue extracted from the body and tested in a laboratory. The testing protocols *ex vivo* can be roughly classified into three categories:

- *Uniaxial tests*: where strain-stress relations are obtained by loading in one direction. This is however not enough to characterize the anisotropic behavior of the tissue, and hence additional histological information is needed, see for instance [Hol06].

- *Biaxial tests*: where tissue is loaded in two perpendicular directions, which usually allows a reasonable characterization of the model parameters for a given data set, see for instance [FVH11, SZP+11]. An example for data and model with fitted parameters is shown in Figure 1.12.

- *Inflation-extension tests*: where typically direct measurements of the pressure and diameter of the vessel are obtained, see for example [SH12, LBMV09, HZCM07, BALS12, ABD10] and references therein.

However, as discussed in [HO09], these protocols are not able to characterize the mechanical response of anisotropic materials, and more loading conditions like torsion or shear stress measurements are needed.

Studies *in vivo* usually are based on pressure-diameter data, typically obtained by catheterization and ultrasound imaging, similar to what is done in the inflation tests *ex vivo*. Examples of these studies can be found in [ZDRVB10, MBL+08, ASK+11, Sta09] and references therein.

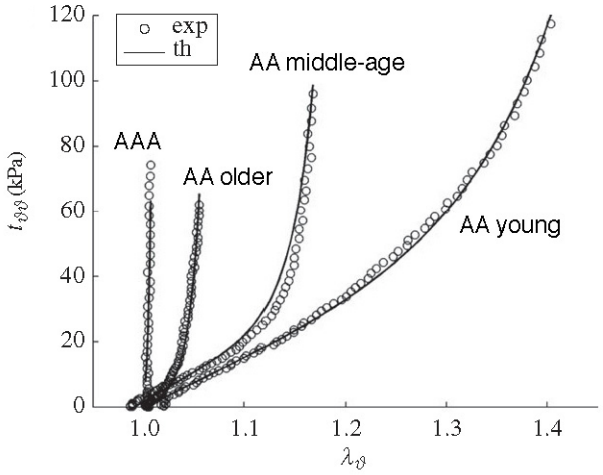

Figure 1.12: Example of data ("exp") and model result with fitted constitutive parameters ("th") for a biaxial tests of human abdominal aortas (AA) (adapted from from [FVH11]-Figure 4). The curves are expressed in terms of the circumferential strain λ_θ and stress $t_{\theta\theta}$. AA of four groups of subjects were studied: three healthy of different ages (less than 30, between 30-60 and more than 60 years old) and one with AA aneurism (AAA).

1.2 Coarctation of the aorta

In this section we overview some aspects about the congenital defect known as *coarctation of the aorta*, and we discuss how the estimation of these properties can help in determining the severity of the disease.

1.2.1 Description of the pathology

Coarctation of the aorta is a pathology with an occurrence around 5-8% of all congenital heart diseases. It corresponds to a narrowing of the descending aorta distal to the origin of the left subclavian artery (see Figure 1.13).

Pathogenesis. There is no clear evidence about which are the precise factors that cause the aortic coarctation. However, it is generally accepted that it is related with abnormalities in the arterial growing process and hemodynamics in the branch point of the ductus arteriosus with the aorta during fetal development. However, the precise etiology remains unknown. It seems to be multifactorial, with important genetic influence as shown in the association with Turner's, Noonan's and 22q11 deletion syndromes [VDK+05, PMLL09].

The theory that may have better perspectives to be proved through computational modeling tools correspond to the one postulated by Hutchins in [Hut71]. It suggests that the coarctation of the aorta is a consequence of the unbalanced blood

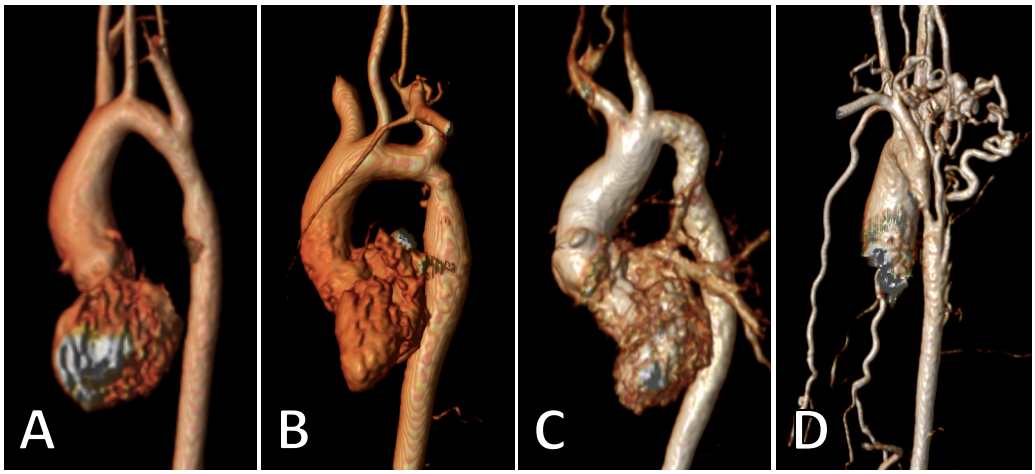

Figure 1.13: Examples of aortic coarctations. A. Mild narrowing, B. Moderate narrowing, C. Tortuous aortic arch, D. Severe narrowing and collateral circulation (from [Val12]).

flow patterns during the fetal life. In a healthy fetus the blood flow coming from the ascending aorta exceeds the flow coming from the ductus arteriosus[9], as illustrated in Figure 1.14. In the pathological case, the hypothesis postulates that a part of the blood from the ductus flowing upwards into the left subclavian artery. This would produce an abnormal stress patern on the aortic wall that would promote the genesis of the narrowing.

Pathophysiology. Due to the narrowing of the artery, coarctation of the aorta induces higher pressures in the upper body and left ventricle. Typically this abnormal hypertensive state stimulates the development of myocardial hypertrophy[10], in order to normalize wall stresses and maintain the cardiac output. If the hypertension is not treated, it can lead to congestive heart failure (CHF)[11].

When the disease is diagnosed during childhood or youth, patients do not usually develop CHF due to the presence of collateral arteries before the coarctation which help the blood to bypass the obstruction (Figure 1.13-D). Nevertheless, in all cases low pressures distal to the narrowing affect the perfusion[12] of lower extremities.

[9]The ductus arteriosus is a blood vessel present during fetal life that connects the pulmonary artery to the descending aorta. Its function corresponds to allow blood to bypass the lungs (not in function) from the right ventricle to the rest of the circulation, which is itself connected to the circulatory system of the mother. In a normal case it closes after birth.

[10]Increase of diameter of the myocites (cardiac cells), and therefore a thickening of the cardiac muscle.

[11]CHF is any inability of the heart to supply a sufficient amount of blood to the body.

[12]Delivery of arterial blood to the tissues.

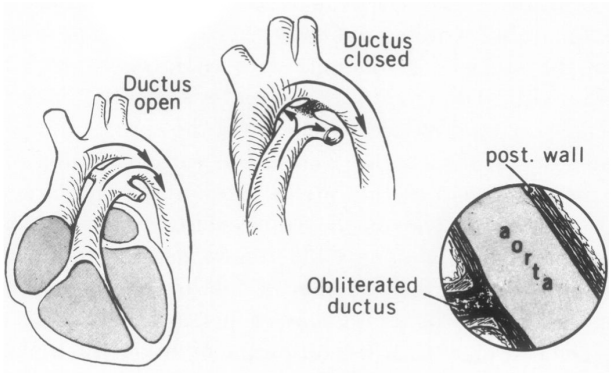

(a) Normal aorta

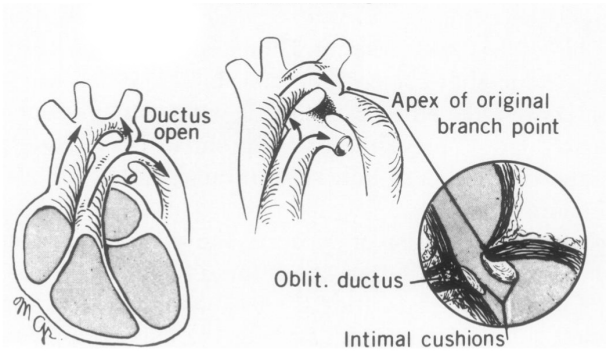

(b) Aorta with coarctation

Figure 1.14: Anatomical and hemodynamical configurations following Hutchins' theory (from [Hut71]).

Diagnosis. The severity of the coarctation is usually assessed by imaging studies and cardiac catheterization.

Chest radiography is useful for a preliminary assessment of signs of CHF like cardiac hypertrophy and pulmonary edema[13]. Echocardiography can give an insight into the geometry of the aorta around the coarctation region, for evaluation of the flow pattern around obstruction, as well as for estimation of the pressure gradient across the narrowing by solving the Bernoulli equation[14]. Magnetic resonance imaging (MRI) can provide excellent views of the entire aorta, for both geometry and flow, specially useful to quantify the collateral circulation. Computer Tomography (CT) is an alternative in the presence of metal stents after coarctation repair, which may result in artifacts in the MR-images. However, the radiation charge has to be carefully analyzed due to future radiation-based studies during the follow-up, hence preference to MRI should be given.

Imaging studies are sometimes not sufficient for a correct diagnosis and an assessment of the pressure gradient across the obstruction is required. A peak-to-peak systolic gradient[15] larger than 20 mmHg is generally considered indicative of significant obstruction. Nevertheless, the magnitude of the gradient is not the only factor indicating the severity of the pathology. Others factors like the development of collateral vessels and the stiffening of the arterial wall play a role. **Hence, in the case of severe coarctations the estimation of the aortic compliance distribution is important for a more precise evaluation of the severity and the possible treatments**.

However, due to the catheterization procedure the gradient is measured under general anesthesia. This is in fact not the normal patient's status and in the presence of hypertension the response to exercise can induce additional complications. Approximately 30% of the patients who underwent surgical repair who are normotensive at rest show an hypertensive response to exercise [Val12]. However, the clinical significance of exercise-induced hypertension is still unclear and remains a controversial matter. Moreover, evaluating the pressure gradient during exercise is even more challenging than during rest conditions, as it requires patient's cooperation and the motion may affect the accuracy of the measurements. Thus, in some centers catheter investigations during pharmacological stress[16] are performed in order to evaluate the hemodynamics in excercise-like conditions.

Treatment. Even though there are many associated defects to the aortic coarctation (aortic valve stenosis, hypertension, cardiac hypertrophy, etc), it is widely

[13] Accumulation of fluid in the air spaces in the lungs, and it is related to CHF when the heart cannot adequately remove the blood from the pulmonary circulation.

[14] $\Delta P = 4(V_{pre}^2 - V_{post}^2)$ assuming measured both pre- and postcoarctation velocities V_{pre} and V_{post}, respectively. It assumes a stationary, irrotational fluid and no energy loss, which is far from reality in the complex hemodynamics induced by the coarctation.

[15] Difference between the peak systolic pressure proximal and distal to the coarctation. It is usually measured by catheterization.

[16] Administration of drugs (e.g. isopraline) for augmenting the cardiac output and frequency for simulating the physiological effects to exercise.

accepted that aortic obstruction is usually the major contributing factor for the symptomatology. The American Heart Association [WWB+08] recommends intervention if peak-to-peak coarctation gradient $\geq$ 20 mmHg, or $\leq$ 20 mmHg if imaging evidence of anatomic significant coarctation with evidence of significant collateral flow (i.e, when collateral circulation is presented as in Figure 1.13-D).

There are several intervention alternatives for treating the coarctation (see Figure 1.15):

(1) *End-to-end anastomosis.* It consists in a procedure where both extremes proximal and distal to the coarctation are cut, the coarctated segment removed and the ends are sewn together.

(2) *Patch aortoplasty.* If the two ends of the aorta would be too far apart for performing an anastomosis, a prosthetic patch can be used. In this case, a longitudinal incision is made along the aorta from the origin of the left subclavian artery until the proximal descending aorta. Then, an elliptic patch of prosthetic material is sutured.

(3) *Balloon angioplasty.* It corresponds to a procedure where an inflation and deflation of a balloon catheter inside an artery is performed, stretching the intima and leaving a ragged interior surface. It is often considered an alternative when recoarctation occurs, and it is popular due to its minimally invasive character.

(4) *Stent placement.* Stents are tubes, usually made of a metal or plastic mesh-like material, that are placed in arteries when they become narrowed or blocked. In the context of aortic coarctation, this procedure is generally applied in case of recoarctation after surgery or balloon angioplasty, in case of unfavorable anatomy for balloon angioplasty (such as long-segment narrowing), or in case of high risk for surgical repair. It can also serves to the treatment of aneurysms present at the time of the intervention. However, some complications may appear including acute rupture or dissection of the aorta, stent fracture, incomplete stent expansion, stent migration, and thromboembolic events.

Follow up. Coarctation of the aorta is a lifelong disease, and many complications can appear during patient's life despite an apparent successful surgery. As with other forms of uncontrolled hypertension, patients may be at risk for premature atherosclerosis, ventricular disfunction, growing and rupture of cerebral aneurysm, and recoarctation. Thus, a proper follow up is vital for prematurely detecting complications of the disease.

1.2.2 Relevance of the arterial stiffness estimation

A number of mechanisms have been proposed to explain hypertension at rest and during and following exercise in individuals with apparently successful coarctation repair. The existence of abnormalities in vascular structure and function which

(a) End-to-end anastomosis

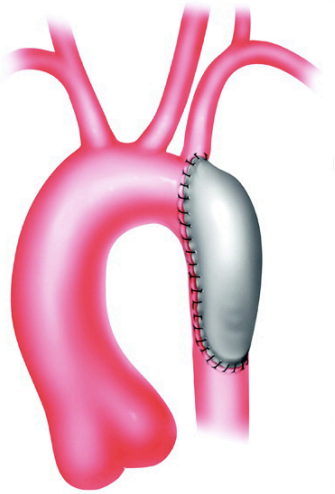

(b) Patch aortoplasty

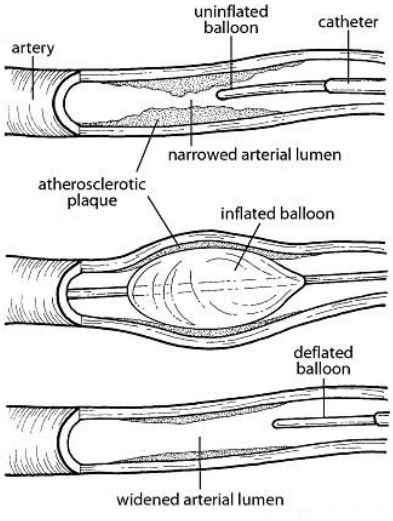

(c) Balloon angioplasty

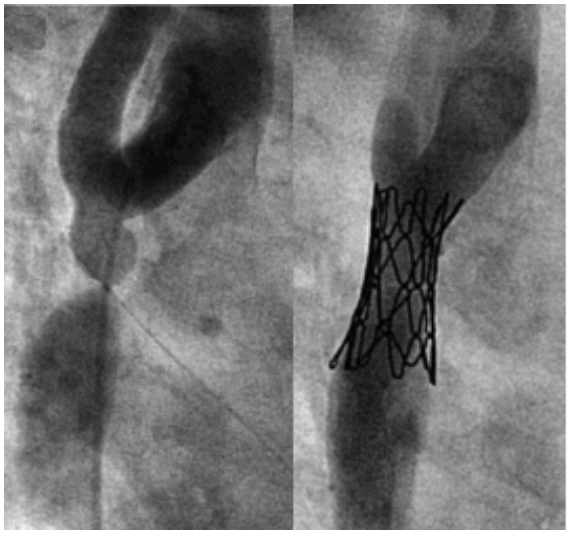

(d) Stent placement

Figure 1.15: Different types of interventions for the coarctation of the aorta ((a) and (b) from [GJDB08], (c) from [amh07] and (d) from [ESP+05]).

are not apparent from image analysis is the prevailing theory and has gained most research attention.

Several studies have evidenced increased aortic stiffness in individuals with repaired coarctation proximal to the site of the narrowing, without manifestation of recoarctation (see for example [Pro09] and references therein). In contrast, the descending aorta has been shown to have normal compliance (compared to healthy control individuals). This stiffening pattern is supported by histological evidence of increased percentage of collagen in the aortic wall and carotid arteries proximal but not distal to the coarctation. Moreover, the increased stiffness may remain until the adult life if repair is performed late (end of youth), and it can be present even in cases where no hypertension or other cardiovascular alterations appear. In addition, the amount of pre-surgical exposure to high pressures and flows proximal to narrowing may play a role in the elevated stiffness after repair.

Many of the measurements of the stiffness are obtained with quantities measured at different sites. For example, when the PWV (see Section 1.1.3) is measured in two points of the vessels far from each other, or when the pressure does not correspond to the same location of the deformation measurements in the case of the distensibility. Even though local measurements of stiffness using invasive pressure measurements are clinically feasible in some patients, these are usually restricted to few locations. Additionally, at the same time one would like to reduce the number and complexity of invasive data acquisitions.

Computational modeling has already shown a great potential to better understand the biomechanics involved in the coarctation of the aorta (see, e.g., [Pou07, LAVC+11, WSC+12]). However, assimilation of clinical data is a crucial step to increase the model reliability and hence to obtain several quantities of interest *in silico*. In particular, the usage of coupled fluid-structure models seems to be the most appropriate choice. Set-up appropriately, they can give a dynamic, three-dimensional distribution of quantities like blood pressure, stresses and mechanical properties in the aortic wall.

Despite the enormous progress achieved in the numerical resolution of coupled fluid-solid models in the last years, to the beginning of this thesis there was almost no work geared to their biophysical personalization using available clinical data. These data can be used for a more accurate estimation of models' outcome and the assessment of uncertain physical parameters, like the arterial stiffness distribution.

1.3 Thesis overview

In this thesis we deal with the simulation of fluid-structure systems arising in hemodynamics, with a special interest in data assimilation and simulations in physiological regimes. The document is divided in three main parts.

Part I (consisting only of a single chapter) presents the three-dimensional (3D) fluid-structure interaction equations, together with the lumped parameter models (0D) used as boundary conditions in the fluid. The main purpose is to formulate and

analyze a new numerical scheme for the 3D-0D coupling, when the 3D part is solved within a Chorin-Temam scheme. Both pure fluid and fluid-structure interaction cases are considered.

Part II is devoted to data assimilation techniques in fluid-structure interaction in hemodynamics based on sequential procedures. Chapter 3 deals with parameter estimation using a nonlinear Kalman filtering technique, whereas Chapter 4 focuses on the state estimation using Luenberger observers.

Finally, Part III is devoted to the application of the nonlinear Kalman filter using measured data from real physical problems. In Chapter 5 we perform the estimation of stiffness parameters of a silicone rubber vessel from MR-images, whereas in Chapter 6 we present the forward and inverse analysis (with synthetic and clinical data) in a real patient aorta.

1.3.1 Fluid-structure interaction in hemodynamics (Part I)

Mathematical model. We deal with the numerical resolution and the data assimilation of the mechanical interaction between an incompressible fluid and an elastic structure. The fluid is described by the Navier-Stokes equations (NSE), in a moving domain $\Omega^{\mathrm{f}} = \Omega^{\mathrm{f}}(t) \subset \mathbb{R}^d$, $d = 2, 3$, in an Arbitrary Lagrangian Eulerian (ALE) formulation, and the structure by the elastodynamic equations in $\Omega^{\mathrm{s}} = \Omega^{\mathrm{s}}(t) \subset \mathbb{R}^d$. The fluid-structure interface is denoted by $\Sigma = \partial\Omega^{\mathrm{s}} \cap \partial\Omega^{\mathrm{f}}$ and $\partial\Omega^{\mathrm{f}} = \Gamma^{\mathrm{in}} \cup \Gamma^{\mathrm{out}} \cup \Sigma$ are given partitions of the fluid and solid boundaries, respectively (see Figure 1.16).

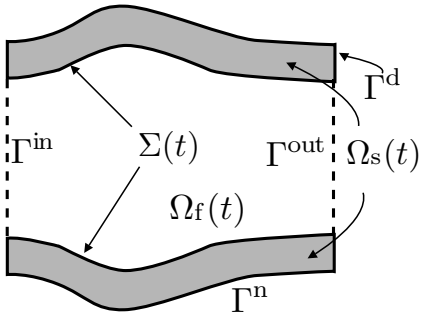

Figure 1.16: Domain of the fluid-structure coupled problem at time t.

The coupled FSI problem reads as follows: for $t > 0$, find the fluid velocity $\boldsymbol{u}_{\mathrm{f}}(t) : \Omega^{\mathrm{f}}(t) \to \mathbb{R}^d$, the fluid pressure $p(t) : \Omega^{\mathrm{f}}(t) \to \mathbb{R}$, the structure displacement $\boldsymbol{y}_{\mathrm{s}}(t) : \Omega^{\mathrm{s}}(t) \to \mathbb{R}^d$ and structure velocity $\boldsymbol{u}_{\mathrm{s}}(t) : \Omega^{\mathrm{s}}(t) \to \mathbb{R}^d$ such that

- Fluid equations:

$$\begin{cases} \rho_{\mathrm{f}} \dfrac{\partial \boldsymbol{u}_{\mathrm{f}}}{\partial t}\Big|_{\boldsymbol{\xi}} + \rho_{\mathrm{f}}(\boldsymbol{u}_{\mathrm{f}} - \boldsymbol{w}) \cdot \boldsymbol{\nabla} \boldsymbol{u}_{\mathrm{f}} - \boldsymbol{\nabla} \cdot \boldsymbol{\sigma}_{\mathrm{f}}(\boldsymbol{u}_{\mathrm{f}}, p) = \boldsymbol{0}, & \text{in} \quad \Omega^{\mathrm{f}}, \\ \boldsymbol{\nabla} \cdot \boldsymbol{u}_{\mathrm{f}} = 0, & \text{in} \quad \Omega^{\mathrm{f}}, \\ \boldsymbol{u}_{\mathrm{f}} = \boldsymbol{u}_{\mathrm{in}}, & \text{on} \quad \Gamma^{\mathrm{in}}, \\ \boldsymbol{\sigma}_{\mathrm{f}}(\boldsymbol{u}_{\mathrm{f}}, p) \cdot \boldsymbol{n}_{\mathrm{f}} = -P\, \boldsymbol{n}_{\mathrm{f}}, & \text{on} \quad \Gamma^{\mathrm{out}}. \end{cases} \tag{1.6a}$$

  with $\boldsymbol{\sigma}_{\mathrm{f}}(\boldsymbol{u}_{\mathrm{f}}, p) = -p\mathbb{1} + 2\mu_{\mathrm{f}}\, \boldsymbol{\varepsilon}(\boldsymbol{u}_{\mathrm{f}})$, where $\boldsymbol{\varepsilon}(\boldsymbol{u}_{\mathrm{f}})$ denotes the deformation rate tensor, μ_{f} the dynamic viscosity, and $\frac{\partial}{\partial t}\big|_{\boldsymbol{\xi}}$ the ALE derivative (see e.g. [FG09]). In the hemodynamics problems considered in this work, the outlet pressure P is obtained by solving the differential-algebraic equation

$$\begin{cases} P = \pi + R_p Q, \\ C_d \dfrac{d\pi}{dt} + \dfrac{\pi}{R_d} = \displaystyle\int_{\Gamma^{\mathrm{out}}} \boldsymbol{u}_{\mathrm{f}} \cdot \boldsymbol{n}_{\mathrm{f}}\, d\Gamma \end{cases} \tag{1.6b}$$

  Here, the distal resistance R_d, the proximal resistance R_p and the capacitance C_d are assumed to be given. This "zero-dimensional" equation is known as the three-element Windkessel model (see for example [FQV09]). It represents the resistance to the flow (R_p and R_d) and the compliance (C) of the vessels beyond the three-dimensional vasculature considered in the simulation.

- Structure equations:

$$\begin{cases} \partial_t \boldsymbol{y}_{\mathrm{s}} = \boldsymbol{u}_{\mathrm{s}}, & \text{in} \quad \Omega^{\mathrm{s}}, \\ \rho_{\mathrm{s}} \partial_t \boldsymbol{u}_{\mathrm{s}} - \eta_{\mathrm{s}} \boldsymbol{\nabla} \cdot \boldsymbol{\sigma}_{\mathrm{s}}(\boldsymbol{u}_{\mathrm{s}}, \theta_{\mathrm{s}}) - \boldsymbol{\nabla} \cdot \boldsymbol{\sigma}_{\mathrm{s}}(\boldsymbol{y}_{\mathrm{s}}, \theta_{\mathrm{s}}) = \boldsymbol{0}, & \text{in} \quad \Omega^{\mathrm{s}}, \\ \boldsymbol{y}_{\mathrm{s}} = \boldsymbol{y}_{\mathrm{in}}, & \text{on} \quad \Gamma^{\mathrm{d}}, \\ \eta_{\mathrm{s}} \boldsymbol{\sigma}_{\mathrm{s}}(\boldsymbol{u}_{\mathrm{s}}, \theta_{\mathrm{s}}) \boldsymbol{n}_{\mathrm{s}} + \boldsymbol{\sigma}_{\mathrm{s}}(\boldsymbol{y}_{\mathrm{s}}, \theta_{\mathrm{s}}) \boldsymbol{n}_{\mathrm{s}} = -c_\Gamma \boldsymbol{u}_{\mathrm{s}} - k_\Gamma \boldsymbol{y}_{\mathrm{s}}, & \text{on} \quad \Gamma^{\mathrm{n}}, \end{cases} \tag{1.6c}$$

  with $\boldsymbol{\sigma}_s(\boldsymbol{y}_{\mathrm{s}}, \theta_{\mathrm{s}})$ the stress tensor of the solid, which will be considered linear or nonlinear along this thesis. The vector $\theta_{\mathrm{s}} \in \mathbb{R}^{p_s}$ notes the set of solid constitutive parameters. The parameters c_Γ and k_Γ model in a simply way the external tissue effect on the vessel of interest, see for example [MXA+11].

- Coupling conditions:

$$\begin{cases} \boldsymbol{y}_{\mathrm{f}} = \mathrm{Ext}^{\mathrm{f}}_{\Sigma_0}\big(\boldsymbol{y}_{\mathrm{s}|\Sigma_0}\big), \quad \boldsymbol{w} = \partial_t \boldsymbol{y}_{\mathrm{f}}, \quad \Omega^{\mathrm{f}}(t) = \big(I_{\Omega^{\mathrm{f}}_0} + \boldsymbol{y}_{\mathrm{f}}(t)\big)(\Omega^{\mathrm{f}}_0), \\ \boldsymbol{u}_{\mathrm{f}} = \boldsymbol{u}_{\mathrm{s}}, \quad \text{on} \quad \Sigma, \\ \eta_{\mathrm{s}} \boldsymbol{\sigma}_{\mathrm{s}}(\boldsymbol{u}_{\mathrm{s}}) \cdot \boldsymbol{n}_{\mathrm{s}} + \boldsymbol{\sigma}_{\mathrm{s}}(\boldsymbol{y}_{\mathrm{s}}) \cdot \boldsymbol{n}_{\mathrm{s}} + \boldsymbol{\sigma}_{\mathrm{f}}(\boldsymbol{u}_{\mathrm{f}}, p) \cdot \boldsymbol{n}_{\mathrm{f}} = \boldsymbol{0}, \quad \text{on} \quad \Sigma\ , \end{cases} \tag{1.6d}$$

  with $\mathrm{Ext}^{\mathrm{f}}_{\Sigma_0}$ an extension operator from Σ_0 to Ω^{f}_0.

This problem is completed with appropriate initial conditions: velocity $\boldsymbol{u}_{\mathrm{f}}(0)$, domain displacement $\boldsymbol{y}_{\mathrm{f}}(0)$ and Windkessel's pressure $\pi(0)$ for the fluid, initial velocity

$\boldsymbol{u}_s(0)$ and displacement $\boldsymbol{y}_s(0)$ for the solid.

Coupling schemes between the 0D models and the 3D-NSE in projection formulation (Chapter 2). Independent of the numerical method used to solve the NSE, there are basically two approaches to include the 0D models as boundary conditions. The simplest way is, for example, to compute the pressures of the 0D part *explicitly*, namely using the flow of the 3D velocity field from the previous time step. However, it is well known that this approach can lead to numerical instabilities when backflow occurs, forcing to use smaller simulation time steps.

One possibility to overcome this is to solve the 3D and 0D monolithically. This implies either to sub-iterate between both models or to include both equations systems (after space-time discretization) in the same system. The first alternative can lead to a prohibitive number of sub-iterations to reach convergence when the algorithm is not appropriately chosen (see for example [MBDQ11]). The second leads to nonlocal relations between the degrees-of-freedom which could be difficult to implement due to the restrictions in the matrix structure in some codes (see, e.g., [MVCFM12]).

All previous studies are based in a monolithic velocity-pressure resolution of the NSE, i.e., where the flux at the 3D-0D interface can be directly computed from the 3D velocity field. In contrast, in this work we analyze the 0D-3D coupling when of a Chorin-Temam projection method is used to solve the incompressible NSE [Cho68, Tem69]. This approach consists in splitting the time iteration in two substeps. First, an advection-diffusion problem is solved to compute an approximation of the velocity field, which is not divergence-free. Then, a suitable pressure field is recovered by projecting the previously computed velocity onto a divergence-free space, and the divergence-free (also called *end-of-step*) velocity field can be obtained *a posteriori*. Doing so, the computational gain is obvious with respect to a monolithic velocity-pressure method. The fractional step nature of this scheme can also be exploited in the FSI framework [FGG07].

In the context of the projection method, we call the type of 3D-0D coupling *explicit*, when the Dirichlet boundary condition for the pressure projection step is obtained independent of the unknown pressure field. First, for the pure NSE (i.e., Equations (1.6) with $\boldsymbol{y}_s = \boldsymbol{u}_s = \boldsymbol{0}$), we present in particular the case when this value is obtained by solving the 0D model using the flux of the previously computed viscous velocity. We show here that dealing with single outlet geometries, this does not compromise stablity of the NSE since the energy computation of the 3D part does not include the imposed pressure. However, in the case of multiple outlets (as in patient-specific geometries), the stability condition of the 3D part depends on the imposed pressures at the outlets and hence the explicit coupling can become unstable.

Therefore, we introduce and analyze a *semi-implicitly* coupled pressure-flux formulation, which yields unconditional stability in the energy norm (up to the convection) based on the relation between pressure gradient, the viscous and the end-of-

step velocity. From the algorithmic point of view, it involves one additional pressure degree-of-freedom (*dof*) per outlet (with respect to the explicit approach), resulting in a nonlocal coupling for the outlet *dofs* only in the additional equations.

Furthermore, we study the extension of the formulation to fluid-structure interaction problems. Here we show that the explicit formulation introduces an artificial energy to the system even in the single-outlet geometries, whereas the implicit scheme remains stable as before.

The theoretical results will be confirmed on two numerical examples. For the pure NSE we use a patient specific aortic geometry obtained by magnetic resonance imaging. The second example corresponds to an idealized aortic aneurism geometry with realistic imposed velocity profile and outlet Windkessel parameters.

1.3.2 Data assimilation in fluid-structure interaction (Part II)

Basic data assimilation concepts. A physical system like blood flowing in a compliant artery can be observed through various measurement modalities: artery wall movements obtained from three-dimensional or multi-slice dynamic medical imaging – computed tomography (CT), magnetic resonance imaging (MRI) or ultrasound (US) – cross section blood flow rates by Phase Contrast MRI or US, pressure in few points provided by a catheter, *etc.* These measurements are usually limited to a few locations in space, and typically come from different cardiac cycles (in this case they are resynchronized with the electrocardiogram). They are of course subject to noise and their postprocessing can introduce some further inaccuracies. Moreover, only a limited number of physical quantities can be simultaneously obtained. An example of current data acquisition possibilities is shown in Figure 1.17.

The physical system of interest, in this case a blood vessel, can also be represented by mathematical models like Equations (1.6). In that case, many quantities – displacement, velocity, pressure, stress – are available in "all" locations and at "any" time instant. But of course, the model itself contains approximations – due for example to the modeling choices and the numerical solution – and relies on parameters that are not perfectly known. Typically in FSI applications in hemodynamics, these sets of parameters, which we call $\theta \in \mathbb{R}^p$ in the sequel, involves the solid constitutive parameters θ_{s}, boundary conditions for solid (e.g., c_Γ and k_Γ) and the fluid outflow parameters R_p, R_d and C. Moreover, in cardiovascular mechanics, the initial condition cannot usually be perfectly known.

The objective of data assimilation is to take advantage of both measurements and models. Measurements can be used to reduce the uncertainties of the model, and the model can be used to access some "hidden" physical quantities, for example the mechanical stress in the artery wall. Data assimilation can also be viewed as a way to reduce the measurements noise by means of a model that takes into account the underlying physical principles.

Assume that Equations (1.6) are already discretized in space, and we denote the collection of space-discrete fields $(\boldsymbol{y}_{\mathrm{s}}, \boldsymbol{u}_{\mathrm{s}}, \boldsymbol{y}_{\mathrm{f}}, \boldsymbol{u}_{\mathrm{f}}, \pi)$ as *state* $X(t) \in \mathbb{R}^N$ satisfying the

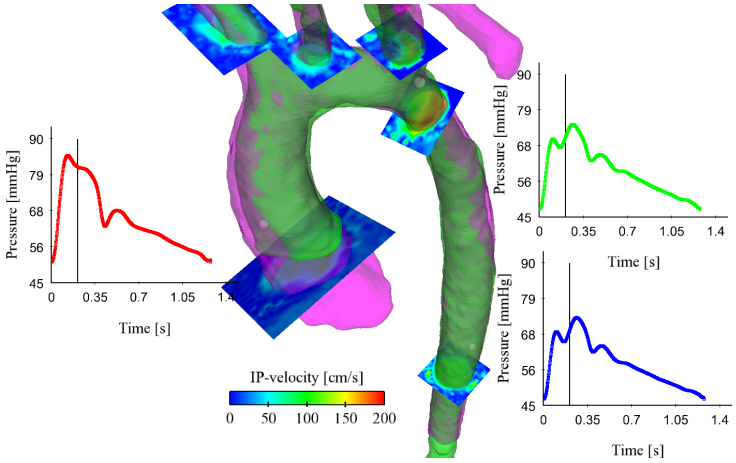

Figure 1.17: Measurements available for the study case 10 of the *euHeart* database. Static segmentation (pink geometry); dynamic segmentation (green geometry); invasive pressure measurements at three locations: ascending (red), descending (green) and abdominal (blue) aorta; and In-Plane velocity measurements. Courtesy of I. Valverde (King's College of London), D. Barber and C. Staicu (University of Sheffield).

dynamics

$$\dot{X} = A(X, \theta), \tag{1.7}$$

and a given initial condition X(0). Note that orders of magnitude of N and p are typically a few hundreds of thousands and a dozen respectively.

The measurements $Z(t)$ are defined by an observation operator $H(t)$ applied to the state $X(t)$ so that it holds

$$Z(t) = H(X) + \zeta^Z,$$

where ζ^Z represents the (additive) noise of the measurement device as well as the inaccuracy resulting from the discretizations. These measurements are assumed to be available at every simulation time step. When this is not the case, they are given by an interpolation in time.

Data assimilation techniques usually consists of minimizing a cost function like:

$$J(\hat{X}(0), \theta) = \int_0^T \|Z - H(\hat{X})\|^2_{W^{-1}} \, \mathrm{d}t + \|\theta - \hat{\theta}_0\|^2_{(P_0^\theta)^{-1}} + \|\hat{X}(0) - \hat{X}_0\|^2_{(P_0^X)^{-1}} \ ,$$

with $\hat{X}$ satisfying (1.7). In this expression, $\hat{X}_0$ and $\hat{\theta}_0$ are given *a priori* values for the initial condition and parameters, and $\|\cdot\|_{W^{-1}}$, $\|\cdot\|_{(P_0^X)^{-1}}$ and $\|\cdot\|_{(P_0^\theta)^{-1}}$ denote some norms used to measure the observations, the state and the parameters, respectively. These norms allow to give a different weight to the different terms and therefore account for the "confidence" in the different quantities. From a statistical

viewpoint, the "confidence" can be viewed as the inverse of covariance matrices (W, P_0^X and P_0^θ), which explains the notation.

Defining $\zeta^X = \hat{X}(0) - \hat{X}_0$, $\zeta^\theta = \theta - \hat{\theta}_0$, the optimization problem reads (keeping the same notation J for the cost function):

$$J(\zeta^X, \zeta^\theta) = \int_0^T \|Z - H(\hat{X})\|^2_{W^{-1}} \, \mathrm{d}t + \|\zeta^\theta\|^2_{(P_0^\theta)^{-1}} + \|\zeta^X\|^2_{(P_0^X)^{-1}}. \tag{1.8}$$

This minimization problem can be addressed by many techniques that are classically divided in two groups: the variational and the sequential approaches. The variational approach consists of minimizing this cost function by an optimization algorithm that is usually based on the computation of its gradient, obtained by solving an adjoint model (see e.g. [BK89, Cha09]). In this work we will focus on the sequential approaches, also known as *filtering*, which modify the forward dynamics with a correction term that takes into account the discrepancy between actual measurements and observations generated by the model:

$$\dot{\hat{X}} = A(\hat{X}, \theta) + K(Z - H(\hat{X})), \;\; \hat{X}(0) = \hat{X}_0, \tag{1.9}$$

where $\hat{X}$ is called *estimator* of X, and the quantity $Z - H(\hat{X})$ is known as the *innovation*, the operator K depends on the method. Note that Equation (1.9) considers only an uncertainty in the initial condition. In the case where θ has also to be included in the estimation procedure, the filtered dynamics can be written in a similar way by defining an *extended* estimator $\hat{X}_e = (\hat{X}, \hat{\theta})$ and its corresponding dynamics by

$$\dot{\hat{X}}_e = A_e(\hat{X}_e) + K_e(Z - H(\hat{X})), \;\; \hat{X}_e(0) = (\hat{X}_0, \hat{\theta}_0). \tag{1.10}$$

Note that the innovation still includes the original state only since dynamical measurements of the parameters are typically not available. Moreover, even if the parameter θ do not evolves in time, the estimated value $\hat{\theta}$ does.

Nonlinear Kalman filtering in FSI (Chapter 3). The most famous sequential approach is the Kalman filter [KB61]. On a given time interval $[0, T]$, and if all the operators are linear, the variational method (namely the minimization of functional (1.8)) and the Kalman filter algorithm turn out to give the same estimation at $t = T$. Concerning the computational complexity, whereas the variational method has to solve several forward and adjoint problems on the whole interval $[0, T]$, the estimation in the sequential algorithm is computed by solving only once the filtered dynamics (1.9). However, the optimal operator K is determined by operations (multiplications, inversions, *etc.*) involving full matrices of the size of the state and the observations, which makes Kalman-based filters prohibitive for discrete problems derived from partial differential equations (PDEs).

For these reasons, data assimilation of distributed mechanical systems are usually based on variational methods. Particularly in FSI for hemodynamics, this approach

has been investigated for simplified models in [Lag99, MCDG05, Sta09], and for three-dimensional problems in [DMP+11, PVV11] by modifying the minimization problem in order to avoid the resolution of the adjoint equations.

In Chapter 3 we deal with the application to FSI problems of the reduced order Unscented Kalman Filter presented in [MC11b], intending to optimize the model parameters for reducing error between model and measurements for all times in a least squares sense, as for instance in Equation (1.8). It is based on the assumption of low rank of the matrices involved in the Kalman filtering procedure, leading to a factorized and therefore tractable form of the Kalman gain K_e. Its main features are that it does not require any adjoint or tangent problems and it can easily be run in parallel, which is of great interest in fluid-structure problems where the forward simulation is already a challenge in itself. We illustrate this technique through the estimation of the Young's modulus of the arterial wall and the proximal Windkessel resistance R_p in a three-dimensional idealized abdominal aortic aneurysm. The measurements are assumed to be the nodal wall displacements. We also study the effect of a reasonable error in the initial condition, and propose a simple way to improve the estimation by including the Windkessel pressure π in the uncertainty space.

Luenberger observers in FSI (Chapter 4). In the case that one has to deal with uncertainties also in $\hat{X}(0)$, data assimilation methods suffer from the "curse of dimensionality" as explained by Bellman in [Bel57], which makes them intractable for systems coming from discretized partial differential equations. However, in [Lue71] Luenberger introduced a new class of estimators, called *observers*, for which he relaxed the optimality condition for computing the gain matrix K in the estimator dynamics (1.9). There, he only bases the filter design on the requirement that the error system $\tilde{X} = X - \hat{X}$ be asymptotically stable.

Thus, in Chapter 4 we study analytically and numerically the performance of the observers presented in [MCLT08, MCLT09] based on displacement and velocity measurements in the solid in the FSI framework. We first show that the straightforward usage of the these estimators in FSI lead to a considerably better performance of the displacement with respect to the velocity feedback, while in pure solid mechanics usually the opposite occurs. After a more detailed theoretical analysis, we conclude that the velocity feedback does not take into account (by construction) the added mass effect. Hence, we propose a way to improve its performance by including the added mass operator in the norm W^{-1}. We also point out that only measurements in the solid are not enough to stabilize the error of the whole fluid-structure system. Hence, the design of a feedback using measurements in the fluid is needed and we propose some fluid observers in Chapter 7.

1.3.3 Applications with real data (Part III)

In the third and final part, we apply the reduced-order Unscented Kalman Filter with data measured from real physical systems using FSI models.

Stiffness estimation of a silicon aortic phantom (Chapter 5). We perform the estimation of the stiffness parameters from data coming from MR-images of a silicone rubber aortic phantom.

We first briefly describe the experimental setup, basically consisting of MR-compatible emulator of the cardiovascular system with a flow pump, a valve, a silicon rubber tube, a compliance chamber and a venous return. The tube is imaged when the pump is enforcing flow through the system. The MR-images are then segmented obtaining a sequence of surfaces. The first one is used to build the geometry (meshes) of the FSI model. Moreover, the measured pressures are used as boundary conditions in the fluid.

All estimation results are reasonable in the sense that: (a) the estimation algorithm always reduces the discrepancy between model and segmented surfaces (for both linear and nonlinear solid models), (b) for pressure ranges where the linear model is more adequate, the estimated Young's modulus matches with the one obtained from nondestructive mechanical tests, and (c) for large pressure ranges, the estimated constitutive parameter of the linear model seems not to converge, whereas for the nonlinear solid does.

Towards biophysical personalization of a FSI aortic model (Chapter 6). Finally, we present the FSI analysis of a whole aorta with mild coarctation based on clinical data.

After a presentation about the relevant aspects of the available clinical data, we proceed with a detailed description of the FSI-model's setup. A special attention is dedicated to the definition of the solid boundary conditions, which are crucial to obtain proper simulation results. In particular, the extraction of the aortic motion close to the heart is detailed for the boundary conditions for the solid and fluid domains. Differently to [MXA+11], where the coronary arteries are tracked from the images, we were not able to identify some material points from the segmentation. Hence, the motion was extracted from the segmented surfaces by matching the model's nodes to the segmented surfaces at the solid's inlet. Moreover, the displacement field obtained at the intersection of the fluid and solid inlets were lifted to the interior of the fluid's inlet so that it deforms independently of the solid wall's dynamics. This makes the FSI simulation, in particular the ALE step, more robust for a larger range of physical parameters.

Next, we show that, without any additional effort, the nonlinear Kalman filter presented works also in this realistic physics using noisy synthetic measurements. In particular, we exemplify how the time and spatial resampling impacts the estimation results for the space distribution of the non-linear constitutive parameters.

Finally, we present some results for the same FSI-model and estimation setting using the segmented surfaces. Even though we are aware about the model limitations (which we describe in detail throughout the chapter), the estimation algorithm is able to reduce the discrepancy between model and measurements. At the same time, as for the phantom, the interpretation of the estimation results allow unmasking the

model's weaknesses and confirming its strengths.

1.4 Thesis context

1.4.1 The euHeart project

EuHeart (www.euheart.eu) is a european research initiative involving 17 industrial, clinical and academic partners, with the goal of developing computational tools and use patient-specific data for the personalized diagnosis and treatment of cardiovascular diseases. Examples of the pathologies studied are heart failure, heart rhythm disorders, coronary artery disease, and aortic disease. Key aspects of the euHeart project are the validation and the implementation of the tools in a clinical context.

The INRIA's REO team was part of the Workpage 9 (together with the University of Sheffield, King's College of London, HemoLab and the German Cancer Research Center), which was geared to the analysis of aortic and valve disease. The main focus of this thesis was the development of numerical algorithms for the data assimilation in the aorta. Other people in REO team were involve in the simulation of aortic valves.

Various meetings took place with several partners in order to, firstly, define the concrete clinical questions, and secondly, to setup the different technical developments and to exchange the clinical data. In particular, as shown in Chapters 5 and 6, this fruitful collaboration allowed to validate and apply the algorithms presented throughout the manuscript.

1.4.2 Software

As indicated at the beginning of each Chapter, the different parts of this work were the result of an active collaboration. In particular, the following solvers were used:

- The Navier-Stokes solver *Mistral*, developed by the REO team in C++.
- The structural mechanics solver *Heartlab*, incuding the state estimation components, developed by the MACS team at INRIA in *Matlab* (The MathWorks, Natick, MA, USA).
- The coupling between the both fluid and structural codes to perform FSI was done using the PVM-based package *masterFSI* developed by the REO team in C++.
- The parameter estimation algorithm, namely the Reduced Order Uscented Kalman Filter, is a joint effort between the MACS and REO teams implemented in the C++ and PVM-based code *masterSEIK*.
- Segmentation of the medical images was done using the software *Shirt*, developed by the Medical Physics Group at the University of Sheffield.

- Mesh processing and edition was done using the software *3-matic* (Materialise, Leuven, Belgium), *Gmsh* [GR09] and self-implemented *Matlab* routines.
- Postprocessing was donde using Ensight (CEI Software) and Cardioviz (developed by the ASCLEPIOS team at INRIA).

Pursuing a close collaboration between the MACS and REO teams, the contribution of this work has been mainly in developing new capabilities within these codes (mainly the new algorithm presented in Chapter 2) and coupling them in order to allow for data assimilation in realistic fluid-structure interaction problems.

Part I

Fluid-structure interaction in hemodynamics

Im Reich der Natur waltet Bewegung und Tat,
im Reiche der Freiheit Anlage und Willen.
Johann W. von Goethe, “Zur Naturwissenschaft", 1823.

Chapter 2

Coupling schemes of lumped parameter models and Navier-Stokes equations in projection formulation

In three-dimensional (3D) blood flow simulations, lumped parameter models (0D) are often used to model the neglected parts of the downstream circulatory system. We analyze two 3D-0D coupling approaches in which a fractional-step projection scheme is used in the fluid. Our analysis shows that explicit approaches might yield numerical instabilities, particularly in the case of realistic geometries with multiple outlets. We introduce and analyze an implicitly 3D-0D coupled formulation with enhanced stability properties and which requires a negligible additional computational cost. Furthermore, we also address the extension of these methods to fluid-structure interaction problems. The theoretical stability results are confirmed by meaningful numerical experiments in patient specific geometries coming from medical imaging.

The results presented in this chapter lead to the manuscript:
C. Bertoglio, A. Caiazzo, M.A. Fernández. **Fractional-step schemes for the coupling of distributed and lumped models in hemodynamics**. Submitted to SIAM Journal of Scientific Computing, 2012.

Contents

2.1 Problem setting

2.1.1 Model problem

In this section, we present the continuos equations for representing the three-dimensional (3D) fluid model, as well as the lumped parameter models (0D) used as boundary conditions for the 3D problem.

2.1.1.1 3D fluid equations

We consider a domain $\Omega^{\mathrm{f}} \subset \mathbb{R}^d$ $(d = 2, 3)$ with the following partition of its boundary

$$\partial\Omega^{\mathrm{f}} \stackrel{\mathrm{def}}{=} \Gamma^{\mathrm{in}} \cup \Sigma \cup \Gamma^{\mathrm{out}}.$$

In the context of blood flow simulations, Ω^{f} will represent the lumen of the vessel (see Figure 2.1), with Γ^{in}, Σ and Γ^{out} denoting, respectively, the inlet, vessel wall and outlet boundaries. The outlet boundary Γ^{out} is assumed to be made of $n_{0\mathrm{D}}$ components

$$\Gamma^{\mathrm{out}} = \bigcup_{l=1}^{n_{0\mathrm{D}}} \Gamma_l,$$

such that $\overline{\Gamma}_i \cap \overline{\Gamma}_j = \emptyset$ for $i, j = 1, \ldots, n_{0\mathrm{D}}$ with $i \neq j$ (see, e.g., Figure 2.1).

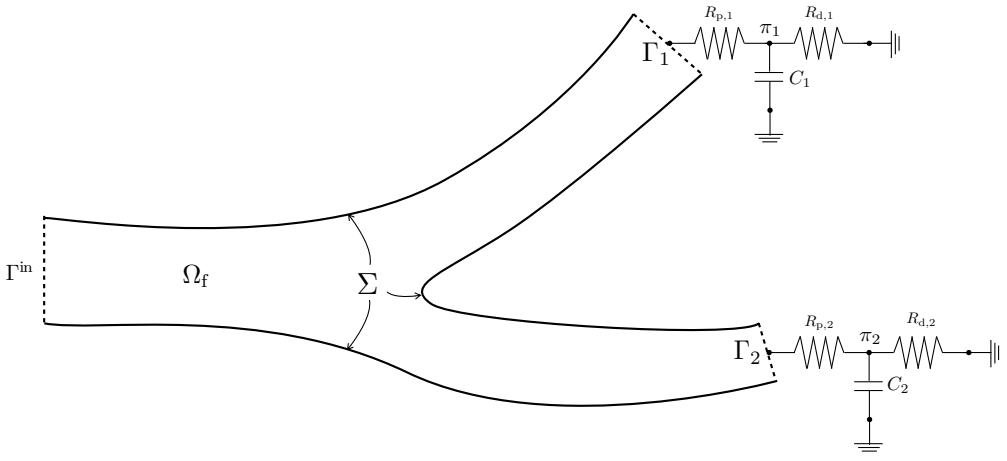

Figure 2.1: Fluid domain Ω^{f} with two outlet boundaries $\Gamma^{\mathrm{out}} = \Gamma_1 \cup \Gamma_2$, $(n_{0\mathrm{D}} = 2)$.

We now consider the incompressible Navier-Stokes Equations (NSE) for the ve-

locity $\boldsymbol{u}_\mathrm{f} : \Omega^\mathrm{f} \times \mathbb{R}^+ \to \mathbb{R}^d$ and the pressure $p : \Omega^\mathrm{f} \times \mathbb{R}^+ \to \mathbb{R}$:

$$\begin{cases} \rho_\mathrm{f} \dfrac{\partial \boldsymbol{u}_\mathrm{f}}{\partial t} + \rho_\mathrm{f} \boldsymbol{u}_\mathrm{f} \cdot \boldsymbol{\nabla} \boldsymbol{u}_\mathrm{f} - \boldsymbol{\nabla} \cdot \boldsymbol{\sigma}_\mathrm{f}(\boldsymbol{u}_\mathrm{f}, p) = \boldsymbol{0} & \text{in} \quad \Omega^\mathrm{f}, \\ \boldsymbol{\nabla} \cdot \boldsymbol{u}_\mathrm{f} = 0 & \text{in} \quad \Omega^\mathrm{f}, \\ \boldsymbol{u}_\mathrm{f} = \boldsymbol{u}_\mathrm{in} & \text{on} \quad \Gamma^\mathrm{in}, \\ \boldsymbol{u}_\mathrm{f} = \boldsymbol{0} & \text{on} \quad \Sigma, \end{cases} \tag{2.1}$$

where ρ_f stands for the density of the fluid and the fluid Cauchy-stress tensor is given by

$$\boldsymbol{\sigma}_\mathrm{f}(\boldsymbol{u}_\mathrm{f}, p) \overset{\text{def}}{=} -p\boldsymbol{I} + 2\mu\boldsymbol{\varepsilon}(\boldsymbol{u}_\mathrm{f}), \quad \boldsymbol{\varepsilon}(\boldsymbol{u}_\mathrm{f}) \overset{\text{def}}{=} \frac{1}{2}\left(\boldsymbol{\nabla}\boldsymbol{u}_\mathrm{f} + \boldsymbol{\nabla}\boldsymbol{u}_\mathrm{f}^\mathrm{T}\right),$$

μ being the dynamic viscosity of the fluid and $\boldsymbol{u}_\mathrm{in}$ being a given inlet velocity field.

2.1.1.2 0D Windkessel model

For computing boundary conditions we will consider *three elements Windkessel* model (see, e.g., [FQV09, Chapter 10]) where the pressure $P_l : \mathbb{R}^+ \to \mathbb{R}$ and the flux $Q_l : \mathbb{R}^+ \to \mathbb{R}$ on the outlet Γ_l are related through the following algebraic-differential equations:

$$\begin{cases} C_{d,l} \dfrac{\mathrm{d}\pi_l}{\mathrm{d}t} + \dfrac{\pi_l}{R_{\mathrm{d},l}} = Q_l, \\ P_l = R_{\mathrm{p},l} Q_l + \pi_l, \end{cases} \tag{2.2}$$

for $l = 1, \ldots, n_{0\mathrm{D}}$. Here, $R_{\mathrm{p},l}$ and $R_{\mathrm{d},l}$ model the proximal and distal vasculature, respectively, and the capacity $C_{d,l}$, take into account the deformability of the downstream vessels. The values P_l and π_l are also called *proximal* and *distal* pressures, respectively.

2.1.1.3 3D-0D coupling conditions

The 3D-0D coupling between (2.1) and (2.2) is defined through the following relations on each Γ_l

$$\begin{cases} Q_l = \displaystyle\int_{\Gamma_l} \boldsymbol{u}_\mathrm{f} \cdot \boldsymbol{n}_\mathrm{f}, \\ \boldsymbol{\sigma}_\mathrm{f}(\boldsymbol{u}_\mathrm{f}, p)\boldsymbol{n}_\mathrm{f} = -P_l \boldsymbol{n}_\mathrm{f} \quad \text{on} \quad \Gamma_l, \end{cases} \tag{2.3}$$

for $l = 1, \ldots, n_{0\mathrm{D}}$ and where $\boldsymbol{n}_\mathrm{f}$ denotes the exterior unit-vector normal of Ω^f.

Energy balance. Let the quantity

$$E(t) \overset{\text{def}}{=} \frac{\rho_\mathrm{f}}{2} \|\boldsymbol{u}_\mathrm{f}\|^2_{0,\Omega^\mathrm{f}} + \sum_{l=1}^{n_{0\mathrm{D}}} \frac{C_{d,l}}{2} \pi_l^2$$

denote the total (kinetic + potential) energy of the 3D-0D coupled system given by (2.1)-(2.3), while

$$D(t) \stackrel{\text{def}}{=} 2\mu \int_0^t \|\boldsymbol{\varepsilon}(\boldsymbol{u}_{\mathrm{f}}(s))\|^2_{0,\Omega^{\mathrm{f}}} \mathrm{d}s + \sum_{l=1}^{n_{0\mathrm{D}}} \int_0^t \left(\frac{\pi_l^2(s)}{R_{\mathrm{d},l}} + R_{\mathrm{p},l} Q_l^2(s) \right) \mathrm{d}s > 0 \tag{2.4}$$

represents the dissipative effects. Assuming that $\boldsymbol{u}_{\mathrm{in}} = \boldsymbol{0}$ (free system) and using a standard energy argument, we get the following identity

$$E(t) + D(t) + \int_0^t \left(\int_{\Gamma^{\mathrm{out}}} \frac{\rho_{\mathrm{f}}}{2} |\boldsymbol{u}_{\mathrm{f}}(s)|^2 \boldsymbol{u}_{\mathrm{f}}(s) \cdot \boldsymbol{n}_{\mathrm{f}} \right) \mathrm{d}s = E(0). \tag{2.5}$$

Remark 1
Since the last term of the right-hand side can be positive, this expression does not guarantee a correct energy balance across the 3D-0D interface Γ^{out}. This issue is well known in fluid mechanics, the interested reader is referred to [BGH+09] for a stabilization technique, and to [FMN07] for different 3D-1D coupling conditions.

2.1.2 Time semi-discretization

We are interested in the numerical approximation of the coupled Equations (2.1)-(2.3), when the incompressible NSE is solved with a projection method. In practice, different approximations of the Windkessel fluxes Q_l can be chosen, what will be focus of Section 2.2. In this section, we summarize the projection formulation for the NSE, and the time discretization of the Windkessel's model.

2.1.2.1 Fractional-step fluid time-marching

In what follows, the parameter τ denotes the time-step size, we set $t_n \stackrel{\text{def}}{=} n\tau$ for $n \in \mathbb{N}$ and $\partial_\tau x^n \stackrel{\text{def}}{=} (x^n - x^{n-1})/\tau$ stands for the first-order backward difference. Several variants of the original Chorin-Temam projection scheme [Cho68, Tem69] have been proposed in the literature (see, e.g., [GMS06] for a recent review). The methods presented and analyzed in section 2.2 below do not *a priori* depend on the specific formulation considered for the projection scheme. To fix the ideas and without generality loss, we consider the non-incremental pressure-correction version (see, e.g., [GMS06, Section 4]). Hence, we set $\widetilde{\boldsymbol{u}}_{\mathrm{f}}^0 = \boldsymbol{u}_{\mathrm{f}}^0 = \boldsymbol{u}_{\mathrm{f}}(0)$ and, for $n \geq 1$, we compute $(\boldsymbol{u}_{\mathrm{f}}^n, p^n, \widetilde{\boldsymbol{u}}_{\mathrm{f}}^n)$ by solving:

1. Viscous step:

$$\begin{cases} \rho_{\mathrm{f}} \dfrac{\widetilde{\boldsymbol{u}}_{\mathrm{f}}^n - \boldsymbol{u}_{\mathrm{f}}^{n-1}}{\tau} + \rho_{\mathrm{f}} \widetilde{\boldsymbol{u}}_{\mathrm{f}}^{n-1} \cdot \boldsymbol{\nabla} \widetilde{\boldsymbol{u}}_{\mathrm{f}}^n - 2\mu \boldsymbol{\nabla} \cdot \boldsymbol{\varepsilon}(\widetilde{\boldsymbol{u}}_{\mathrm{f}}^n) = \boldsymbol{0} & \text{in} \quad \Omega^{\mathrm{f}}, \\ \widetilde{\boldsymbol{u}}_{\mathrm{f}}^n = \boldsymbol{u}_{\mathrm{in}}(t_n) & \text{on} \quad \Gamma^{\mathrm{in}}, \\ \widetilde{\boldsymbol{u}}_{\mathrm{f}}^n = \boldsymbol{0} & \text{on} \quad \Sigma. \end{cases} \tag{2.6}$$

2. Projection step:

$$\begin{cases} \rho_{\mathrm{f}} \dfrac{\boldsymbol{u}_{\mathrm{f}}^n - \widetilde{\boldsymbol{u}}_{\mathrm{f}}^n}{\tau} + \boldsymbol{\nabla} p^n = \boldsymbol{0} & \text{in} \quad \Omega^{\mathrm{f}}, \\ \boldsymbol{\nabla} \cdot \boldsymbol{u}_{\mathrm{f}}^n = 0 & \text{in} \quad \Omega^{\mathrm{f}}, \\ \boldsymbol{u}_{\mathrm{f}}^n \cdot \boldsymbol{n}_{\mathrm{f}} = \boldsymbol{u}_{\mathrm{in}}(t_n) \cdot \boldsymbol{n}_{\mathrm{f}} & \text{on} \quad \Gamma^{\mathrm{in}}, \\ \boldsymbol{u}_{\mathrm{f}}^n = \boldsymbol{0} & \text{on} \quad \Sigma. \end{cases} \tag{2.7}$$

For the sake of computational efficiency, the projection step (2.7) is usually reformulated by as the pressure-Poisson problem

$$\begin{cases} -\dfrac{\tau}{\rho_{\mathrm{f}}} \Delta p^n = -\boldsymbol{\nabla} \cdot \widetilde{\boldsymbol{u}}_{\mathrm{f}}^n & \text{in} \quad \Omega^{\mathrm{f}}, \\ \dfrac{\tau}{\rho_{\mathrm{f}}} \dfrac{\partial p^n}{\partial \boldsymbol{n}_{\mathrm{f}}} = 0 & \text{on} \quad \Gamma^{\mathrm{in}} \cup \Sigma. \end{cases} \tag{2.8}$$

which requires further regularity on the pressure ($H^1(\Omega^{\mathrm{f}})$ instead of $L^2(\Omega^{\mathrm{f}})$ in practice). Then, the divergence free velocity $\boldsymbol{u}_{\mathrm{f}}^n$ is eliminated in (2.6) using the following relation (from $(2.7)_1$)

$$\boldsymbol{u}_{\mathrm{f}}^n = \widetilde{\boldsymbol{u}}_{\mathrm{f}}^n - \frac{\tau}{\rho_{\mathrm{f}}} \boldsymbol{\nabla} p^n. \tag{2.9}$$

2.1.2.2 Backward-Euler Windkessel time-marching

Without loss of generality, we consider a backward Euler time-discretization of (2.2), which yields

$$\begin{cases} C_{d,l} \partial_\tau \pi_l^n + \dfrac{\pi_l^n}{R_{\mathrm{d},l}} = Q_l^n, \\ P_l^n = R_{\mathrm{p},l} Q_l^n + \pi_l^n \end{cases} \tag{2.10}$$

or, equivalently,

$$\begin{cases} \pi_l^n = \alpha_l \pi_l^{n-1} + \beta_l Q_l^n, \\ P_l^n = \gamma_l Q_l^n + \alpha_l \pi_l^{n-1}, \end{cases} \tag{2.11}$$

with the notation

$$\alpha_l \overset{\text{def}}{=} \frac{R_{\mathrm{d},l} C_{d,l}}{R_{\mathrm{d},l}\, C_{d,l} + \tau}, \quad \beta_l \overset{\text{def}}{=} R_{\mathrm{d},l}(1 - \alpha_l), \quad \gamma_l \overset{\text{def}}{=} R_{\mathrm{p},l} + \beta_l. \tag{2.12}$$

2.1.3 Spatial discretization

In what follows, we will consider the usual Sobolev space $H^1(\Omega)$, for a given domain $\Omega \subset \mathbb{R}^d$. Then, for $X \subset \partial\Omega$ (with $\mathrm{meas}(X) > 0$), we define $H^1_X(\Omega)$ the subspace of $H^1(\Omega)$ with vanishing trace on X. The scalar product in $L^2(\Omega)$ is denoted by $(\cdot,\cdot)_\Omega$ and its associated norm by $\|\cdot\|_{0,\Omega}$.

We consider a family of triangulations $\{\mathcal{T}_{\mathrm{f},h}\}_{0<h\leq 1}$ of the domain Ω^{f} satisfying the usual requirements of finite element approximations (see, e.g., [EG04]). The subscript $h \in (0,1]$ refers to the level of refinement of the triangulations. In order to ease the presentation, we assume that the family of triangulations is quasi-uniform.

For the discretization in space of (2.1), we consider continuous Lagrange finite element approximations $\boldsymbol{V}_h$ and N_h of $[H^1(\Omega^{\mathrm{f}})]^3$ and $H^1(\Omega^{\mathrm{f}})$, respectively. Other choices of approximation spaces are possible for the projection method (see [GQ98] for a discussion). For a given $X \subset \partial\Omega^{\mathrm{f}}$ (with $\mathrm{meas}(X) > 0$), we set

$$\boldsymbol{V}_{X,h} \stackrel{\mathrm{def}}{=} \boldsymbol{V}_h \cap [H^1_X(\Omega^{\mathrm{f}})]^d, \quad \boldsymbol{N}_{X,h} \stackrel{\mathrm{def}}{=} \boldsymbol{N}_h \cap H^1_X(\Omega^{\mathrm{f}}).$$

2.2 Fractional-step time-marching and 3D-0D coupling schemes

In this section, we describe two coupling schemes (explicit and semi-implicit) resulting from appropriate time discretizations of the coupling conditions (2.3).

2.2.1 Explicit 3D-0D coupling scheme

In this case the 3D-0D coupling conditions (2.3) are time discretized as follows

$$\begin{cases} Q_l^n = \displaystyle\int_{\Gamma_l} \widetilde{\boldsymbol{u}}_{\mathrm{f}}^n \cdot \boldsymbol{n}_{\mathrm{f}}, \\ p^n = P_l^n \quad \text{on} \quad \Gamma_l, \\ 2\mu\boldsymbol{\varepsilon}(\widetilde{\boldsymbol{u}}_{\mathrm{f}}^n)\boldsymbol{n}_{\mathrm{f}} = \boldsymbol{0} \quad \text{on} \quad \Gamma_l, \end{cases} \tag{2.13}$$

for $l = 1, \ldots, n_{0\mathrm{D}}$. Note that the continuity of fluxes $(2.3)_1$ is treated explicitly by using the flux of the latest computed viscous velocity. For the relation $(2.3)_2$ we consider a Dirichlet boundary condition for the pressure, while the viscous part of the fluid stresses is set to zero. This is a usual procedure to decouple the projection and viscous steps in the framework of projection schemes with natural boundary conditions (see, e.g., [GMS06]).

The resulting fully discrete time-marching procedure is reported in Algorithm 1. In the viscous-step (2.14) we have considered the standard Temam's consistent term, $\frac{\rho_{\mathrm{f}}}{2}((\boldsymbol{\nabla}\cdot\widetilde{\boldsymbol{u}}^{n-1})\widetilde{\boldsymbol{u}}^n, \boldsymbol{v})_{\Omega^{\mathrm{f}}}$, which stabilizes the semi-implicit treatment of the convective term. The 3D-0D explicit coupling given by (2.13) allows a fully uncoupled computation of the Windkesel state, fluid pressure and velocity. This is particularly appealing from the implementation and computational efficiency point of view. Nevertheless, as suggested in Section 2.2.1.1 below (and then confirmed by numerical experiments in Section 2.4), Algorithm 1 may suffer from stability issues.

Algorithm 1 Explicit 3D-0D coupling scheme

Let $\boldsymbol{u}_{\mathrm{f}}^0 \stackrel{\mathrm{def}}{=} \boldsymbol{u}_{\mathrm{f}}(0)$, $\widetilde{\boldsymbol{u}}_{\mathrm{f}}^0 \in \boldsymbol{V}_h$ and $\pi_1^0, \ldots, \pi_{n_{0\mathrm{D}}}^0 \in \mathbb{R}$ be given initial data. For $n \geq 1$ perform:

1. Viscous step: Find $\widetilde{\boldsymbol{u}}_{\mathrm{f}}^n \in \boldsymbol{V}_{\Sigma,h}$ such that

$$\begin{cases} \widetilde{\boldsymbol{u}}_{\mathrm{f}}^n|_{\Gamma^{\mathrm{in}}} = \boldsymbol{u}_{\mathrm{in}}(t_n), \\ \dfrac{\rho_{\mathrm{f}}}{\tau}\left(\widetilde{\boldsymbol{u}}_{\mathrm{f}}^n, \boldsymbol{v}\right)_{\Omega^{\mathrm{f}}} + \rho_{\mathrm{f}}(\widetilde{\boldsymbol{u}}_{\mathrm{f}}^{n-1} \cdot \boldsymbol{\nabla}\widetilde{\boldsymbol{u}}_{\mathrm{f}}^n, \boldsymbol{v})_{\Omega^{\mathrm{f}}} + \dfrac{\rho_{\mathrm{f}}}{2}((\boldsymbol{\nabla} \cdot \widetilde{\boldsymbol{u}}_{\mathrm{f}}^{n-1})\widetilde{\boldsymbol{u}}_{\mathrm{f}}^n, \boldsymbol{v})_{\Omega^{\mathrm{f}}} \\ \quad + 2\mu\left(\boldsymbol{\varepsilon}(\widetilde{\boldsymbol{u}}_{\mathrm{f}}^n), \boldsymbol{\varepsilon}(\boldsymbol{v})\right)_{\Omega^{\mathrm{f}}} = \dfrac{\rho_{\mathrm{f}}}{\tau}\left(\boldsymbol{u}_{\mathrm{f}}^n, \boldsymbol{v}\right)_{\Omega^{\mathrm{f}}} \end{cases} \tag{2.14}$$

   for all $\boldsymbol{v} \in \boldsymbol{V}_{\Sigma\cup\Gamma^{\mathrm{in}},h}$. Thereafter set $\widetilde{Q}_l^n \stackrel{\mathrm{def}}{=} \int_{\Gamma_l} \widetilde{\boldsymbol{u}}_{\mathrm{f}}^n \cdot \boldsymbol{n}_{\mathrm{f}}$.

2. Windkessel step: For $l = 1, \ldots, n_{0\mathrm{D}}$, compute $(Q_l^n, \pi_l^n, P_l^n) \in \mathbb{R}^3$ from

$$\begin{cases} Q_l^n = \widetilde{Q}_l^n, \\ C_{d,l}\partial_\tau \pi_l^n + \dfrac{\pi_l^n}{R_{\mathrm{d},l}} = Q_l^n, \\ P_l^n = R_{\mathrm{p},l} Q_l^n + \pi_l^n. \end{cases} \tag{2.15}$$

3. Projection step: Find $p^n \in N_h$ such that

$$\begin{cases} p^n|_{\Gamma_l} = P_l^n, \quad l = 1, \ldots, n_{0\mathrm{D}}, \\ \dfrac{\tau}{\rho_{\mathrm{f}}}\left(\boldsymbol{\nabla} p^n, \boldsymbol{\nabla} q\right)_{\Omega^{\mathrm{f}}} = -\left(\boldsymbol{\nabla} \cdot \widetilde{\boldsymbol{u}}_{\mathrm{f}}^n, q\right)_{\Omega^{\mathrm{f}}} \end{cases} \tag{2.16}$$

   for all $q \in N_{\Gamma^{\mathrm{out}},h}$. Thereafter set $\boldsymbol{u}_{\mathrm{f}}^n \stackrel{\mathrm{def}}{=} \widetilde{\boldsymbol{u}}_{\mathrm{f}}^n + \frac{\tau}{\rho_{\mathrm{f}}}\boldsymbol{\nabla} p^n \in [L^2(\Omega^{\mathrm{f}})]^d$.

2.2.1.1 Stability analysis

Let the quantities

$$E^n \stackrel{\mathrm{def}}{=} \frac{\rho_{\mathrm{f}}}{2}\|\widetilde{\boldsymbol{u}}_{\mathrm{f}}^n\|_{0,\Omega^{\mathrm{f}}}^2 + \sum_{l=1}^{n_{0\mathrm{D}}} \frac{C_{d,l}}{2}|\pi_l^n|^2,$$

$$D^n \stackrel{\mathrm{def}}{=} 2\mu \sum_{m=1}^{n} \tau\|\boldsymbol{\varepsilon}(\widetilde{\boldsymbol{u}}_{\mathrm{f}}^m)\|_{0,\Omega^{\mathrm{f}}}^2 + \sum_{m=1}^{n-1}\sum_{l=1}^{n_{0\mathrm{D}}} \tau\left(\frac{|\pi_l^m|^2}{R_{\mathrm{d},l}} + R_{\mathrm{p},l}|Q_l^m|^2\right),$$

for $n \geq 1$, denote the energy and physical dissipation of the discrete system. Let us also set

$$E^0 \stackrel{\mathrm{def}}{=} \frac{\rho_{\mathrm{f}}}{2}\|\boldsymbol{u}_{\mathrm{f}}^0\|_{0,\Omega^{\mathrm{f}}}^2 + \sum_{l=1}^{n_{0\mathrm{D}}} \frac{C_{d,l}}{2}|\pi_0^n|^2,$$

We then have the following energy based result.

Proposition 1
Let $\left\{(\widetilde{\boldsymbol{u}}_{\mathrm{f}}^n, p^n)\right\}_{n\geq 1}$ *and* $\left\{(Q_l^n, \pi_l^n, P_l^n)_{1\leq l\leq n_{0\mathrm{D}}}\right\}_{n\geq 1}$ *be the approximated solution given by Algorithm 1 and assume that* $\boldsymbol{u}_{\mathrm{in}} = \boldsymbol{0}$ *(free system). The following inequality holds for* $n \geq 1$

$$E^n + D^n + \sum_{m=1}^{n} \frac{\rho_{\mathrm{f}}}{2}\tau(\widetilde{\boldsymbol{u}}_{\mathrm{f}}^{m-1}\cdot\boldsymbol{n}_{\mathrm{f}}, |\widetilde{\boldsymbol{u}}_{\mathrm{f}}^m|^2)_{\Gamma^{\mathrm{out}}} \leq E^0 - \sum_{m=1}^{n-1}\frac{\tau^2}{2\rho_{\mathrm{f}}}\|\boldsymbol{\nabla} p^m\|_{0,\Omega^{\mathrm{f}}}^2 + \sum_{m=1}^{n-1}\tau\left(\boldsymbol{\nabla}\cdot\widetilde{\boldsymbol{u}}_{\mathrm{f}}^m, \phi^m\right)_{\Omega^{\mathrm{f}}} + \sum_{m=1}^{n-1}\frac{\tau^2}{\rho_{\mathrm{f}}}\left(\boldsymbol{\nabla} p^m, \boldsymbol{\nabla}\phi^m\right)_{\Omega^{\mathrm{f}}}, \quad (2.17)$$

where $\phi^n \in N_h$ *is an arbitrary discrete lifting of the (unknown) proximal pressures, namely,*

$$\phi^n = P_l^n \quad on \quad \Gamma_l\ ,\ l = 1, \ldots, n_{0\mathrm{D}}. \quad (2.18)$$

Proof. We first test (2.14) with $\boldsymbol{v} = \widetilde{\boldsymbol{u}}_{\mathrm{f}}^n$ and integrate by parts the convective term. This yields the identity

$$\frac{\rho_{\mathrm{f}}}{2}\partial_\tau\|\widetilde{\boldsymbol{u}}_{\mathrm{f}}^n\|_{0,\Omega^{\mathrm{f}}}^2 + \frac{\rho_{\mathrm{f}}}{2\tau}\left\|\widetilde{\boldsymbol{u}}_{\mathrm{f}}^n - \widetilde{\boldsymbol{u}}_{\mathrm{f}}^{n-1}\right\|_{0,\Omega^{\mathrm{f}}}^2 + 2\mu\|\boldsymbol{\varepsilon}(\widetilde{\boldsymbol{u}}_{\mathrm{f}}^n)\|_{0,\Omega^{\mathrm{f}}}^2 + \left(\boldsymbol{\nabla} p^{n-1}, \widetilde{\boldsymbol{u}}_{\mathrm{f}}^n\right)_{\Omega^{\mathrm{f}}} + \frac{\rho_{\mathrm{f}}}{2}(\widetilde{\boldsymbol{u}}_{\mathrm{f}}^{n-1}\cdot\boldsymbol{n}_{\mathrm{f}}, |\widetilde{\boldsymbol{u}}_{\mathrm{f}}^n|^2)_{\Gamma^{\mathrm{out}}} = 0 \quad (2.19)$$

for $n \geq 2$, and for $n = 1$ we get

$$\frac{\rho_{\mathrm{f}}}{2\tau}\left(\left\|\widetilde{\boldsymbol{u}}_{\mathrm{f}}^1\right\|_{0,\Omega^{\mathrm{f}}}^2 - \left\|\boldsymbol{u}_{\mathrm{f}}^0\right\|_{0,\Omega^{\mathrm{f}}}^2\right) + \frac{\rho_{\mathrm{f}}}{2\tau}\left\|\widetilde{\boldsymbol{u}}_{\mathrm{f}}^1 - \boldsymbol{u}_{\mathrm{f}}^0\right\|_{0,\Omega^{\mathrm{f}}}^2 + 2\mu\left\|\boldsymbol{\varepsilon}(\widetilde{\boldsymbol{u}}_{\mathrm{f}}^1)\right\|_{0,\Omega^{\mathrm{f}}}^2 + \frac{\rho_{\mathrm{f}}}{2}(\widetilde{\boldsymbol{u}}_{\mathrm{f}}^0\cdot\boldsymbol{n}_{\mathrm{f}}, |\widetilde{\boldsymbol{u}}_{\mathrm{f}}^1|^2)_{\Gamma^{\mathrm{out}}} = 0. \quad (2.20)$$

Moreover, integration by parts in (2.16) at time step $n-1$ gives

$$\left(\boldsymbol{\nabla} p^{n-1}, \boldsymbol{\nabla} q\right)_{\Omega^{\mathrm{f}}} = \frac{\rho_{\mathrm{f}}}{\tau}\left(\widetilde{\boldsymbol{u}}_{\mathrm{f}}^{n-1}, \boldsymbol{\nabla} q\right)_{\Omega^{\mathrm{f}}} - \frac{\rho_{\mathrm{f}}}{\tau}\int_{\partial\Omega^{\mathrm{f}}}\widetilde{\boldsymbol{u}}_{\mathrm{f}}^{n-1}\cdot\boldsymbol{n}_{\mathrm{f}} q = \frac{\rho_{\mathrm{f}}}{\tau}\left(\widetilde{\boldsymbol{u}}_{\mathrm{f}}^{n-1}, \boldsymbol{\nabla} q\right)_{\Omega^{\mathrm{f}}},$$

since $q \in N_{\Gamma^{\mathrm{out}},h}$ and $\widetilde{\boldsymbol{u}}_{\mathrm{f}}^{n-1} \in \boldsymbol{V}_{\Gamma^{\mathrm{in}}\cup\Sigma,h}$, for $n \geq 2$. Then, testing the last equation with $q = \frac{\tau}{\rho_{\mathrm{f}}}\left(p^{n-1} - \phi^{n-1}\right) \in N_{\Gamma^{\mathrm{out}},h}$ we get

$$\frac{\tau}{\rho_{\mathrm{f}}}\left\|\boldsymbol{\nabla} p^{n-1}\right\|_{0,\Omega^{\mathrm{f}}}^2 - \left(\widetilde{\boldsymbol{u}}_{\mathrm{f}}^{n-1}, \boldsymbol{\nabla} p^{n-1}\right)_{\Omega^{\mathrm{f}}} + \left(\widetilde{\boldsymbol{u}}_{\mathrm{f}}^{n-1} - \frac{\tau}{\rho_{\mathrm{f}}}\boldsymbol{\nabla} p^{n-1}, \boldsymbol{\nabla}\phi^{n-1}\right)_{\Omega^{\mathrm{f}}} = 0.$$

Equivalently, we have

$$\frac{\tau}{\rho_{\mathrm{f}}}\left\|\boldsymbol{\nabla} p^{n-1}\right\|_{0,\Omega^{\mathrm{f}}}^2 - \left(\widetilde{\boldsymbol{u}}_{\mathrm{f}}^n, \boldsymbol{\nabla} p^{n-1}\right)_{\Omega^{\mathrm{f}}} + \left(\widetilde{\boldsymbol{u}}_{\mathrm{f}}^n - \widetilde{\boldsymbol{u}}_{\mathrm{f}}^{n-1}, \boldsymbol{\nabla} p^{n-1}\right)_{\Omega^{\mathrm{f}}} = -\left(\widetilde{\boldsymbol{u}}_{\mathrm{f}}^{n-1} - \frac{\tau}{\rho_{\mathrm{f}}}\boldsymbol{\nabla} p^{n-1}, \boldsymbol{\nabla}\phi^{n-1}\right)_{\Omega^{\mathrm{f}}}.$$

By using the Cauchy-Schwarz inequality and an arithmetic-geometric inequality, we

get

$$\frac{\tau}{2\rho_{\mathrm{f}}}\left\|\boldsymbol{\nabla} p^{n-1}\right\|_{0,\Omega^{\mathrm{f}}}^2-\frac{\rho_{\mathrm{f}}}{2\tau}\left\|\widetilde{\boldsymbol{u}}_{\mathrm{f}}^n-\widetilde{\boldsymbol{u}}_{\mathrm{f}}^{n-1}\right\|_{0,\Omega^{\mathrm{f}}}^2-\left(\widetilde{\boldsymbol{u}}_{\mathrm{f}}^n,\boldsymbol{\nabla} p^{n-1}\right)_{\Omega^{\mathrm{f}}} \\ \leq-\left(\widetilde{\boldsymbol{u}}_{\mathrm{f}}^{n-1}-\frac{\tau}{\rho_{\mathrm{f}}}\boldsymbol{\nabla} p^{n-1},\boldsymbol{\nabla}\phi^{n-1}\right)_{\Omega^{\mathrm{f}}}. \quad (2.21)$$

On the other hand, integrating by parts the first term in the right-hand side of (2.21) and using (2.15) and (2.18), we infer that

$$\frac{\tau}{2\rho_{\mathrm{f}}}\left\|\boldsymbol{\nabla} p^{n-1}\right\|_{0,\Omega^{\mathrm{f}}}^2-\frac{\rho_{\mathrm{f}}}{2\tau}\left\|\widetilde{\boldsymbol{u}}_{\mathrm{f}}^n-\widetilde{\boldsymbol{u}}_{\mathrm{f}}^{n-1}\right\|_{0,\Omega^{\mathrm{f}}}^2-\left(\widetilde{\boldsymbol{u}}_{\mathrm{f}}^n,\boldsymbol{\nabla} p^{n-1}\right)_{\Omega^{\mathrm{f}}} \\ \leq-\sum_{l=1}^{n_{0\mathrm{D}}}Q_l^{n-1}P_l^{n-1}+\left(\boldsymbol{\nabla}\cdot\widetilde{\boldsymbol{u}}_{\mathrm{f}}^{n-1},\phi^{n-1}\right)_{\Omega^{\mathrm{f}}}+\frac{\tau}{\rho_{\mathrm{f}}}\left(\boldsymbol{\nabla} p^{n-1},\boldsymbol{\nabla}\phi^{n-1}\right)_{\Omega^{\mathrm{f}}} \quad (2.22)$$

for $n\geq 2$. As a result, the summation of (2.19) and (2.22) gives

$$\frac{\rho_{\mathrm{f}}}{2}\partial_\tau\|\widetilde{\boldsymbol{u}}_{\mathrm{f}}^n\|_{0,\Omega^{\mathrm{f}}}^2+2\mu\|\boldsymbol{\varepsilon}(\widetilde{\boldsymbol{u}}_{\mathrm{f}}^n)\|_{0,\Omega^{\mathrm{f}}}^2+\frac{\rho_{\mathrm{f}}}{2}(\widetilde{\boldsymbol{u}}_{\mathrm{f}}^{n-1}\cdot\boldsymbol{n}_{\mathrm{f}},|\widetilde{\boldsymbol{u}}_{\mathrm{f}}^n|^2)_{\Gamma^{\mathrm{out}}} \\ \leq-\frac{\tau}{2\rho_{\mathrm{f}}}\left\|\boldsymbol{\nabla} p^{n-1}\right\|_{0,\Omega^{\mathrm{f}}}^2+\left(\boldsymbol{\nabla}\cdot\widetilde{\boldsymbol{u}}_{\mathrm{f}}^{n-1},\phi^n-1\right)_{\Omega^{\mathrm{f}}}+\frac{\tau}{\rho_{\mathrm{f}}}\left(\boldsymbol{\nabla} p^{n-1},\boldsymbol{\nabla}\phi^{n-1}\right)_{\Omega^{\mathrm{f}}}-\sum_{l=1}^{n_{0\mathrm{D}}}Q_l^{n-1}P_l^{n-1} \quad (2.23)$$

for $n\geq 2$. At last, we multiply $(2.15)_2$ at $n-1$ by π_l^{n-1} to obtain

$$\frac{C_{d,l}}{2}\partial_\tau|\pi_l^n|^2+\frac{C_{d,l}}{2}|\pi_l^n-\pi_l^{n-1}|^2+\frac{1}{R_{\mathrm{d},l}}|\pi_l^n|^2=Q_l^n\pi_l^n, \quad (2.24)$$

which combined with $(2.15)_3$ yields

$$\frac{C_{\mathrm{d},l}}{2}\partial_\tau|\pi_l^{n-1}|^2+\frac{1}{R_{\mathrm{d},l}}|\pi_l^{n-1}|^2+R_{\mathrm{p},l}|Q_l^{n-1}|^2\leq Q_l^{n-1}P_l^{n-1}. \quad (2.25)$$

We now proceed by inserting (2.25) into (2.23), multiplying by τ and summing over $m=2,...,n$. This yields the following estimate

$$E^n+D^n+\sum_{m=2}^{n}\frac{\rho_{\mathrm{f}}}{2}\tau(\widetilde{\boldsymbol{u}}_{\mathrm{f}}^{m-1}\cdot\boldsymbol{n}_{\mathrm{f}},|\widetilde{\boldsymbol{u}}_{\mathrm{f}}^m|^2)_{\Gamma^{\mathrm{out}}}\leq E^1-\sum_{m=1}^{n-1}\frac{\tau^2}{2\rho_{\mathrm{f}}}\|\boldsymbol{\nabla} p^m\|_{0,\Omega^{\mathrm{f}}}^2 \\ +\sum_{m=1}^{n-1}\tau\left(\boldsymbol{\nabla}\cdot\widetilde{\boldsymbol{u}}_{\mathrm{f}}^m,\phi^m\right)_{\Omega^{\mathrm{f}}}+\sum_{m=1}^{n-1}\frac{\tau^2}{\rho_{\mathrm{f}}}\left(\boldsymbol{\nabla} p^m,\boldsymbol{\nabla}\phi^m\right)_{\Omega^{\mathrm{f}}}$$

for $n\geq 2$. The estimate (2.17) is then recovered by simply adding to this inequality the expression (2.20) multiplied by τ, which completes the proof. ∎

The left-hand side of estimate (2.17) corresponds to the discrete counterpart of

(2.5). Nevertheless, the artificial power introduced by the last two terms of (2.17),

$$\sum_{m=1}^{n-1} \tau \left(\boldsymbol{\nabla} \cdot \widetilde{\boldsymbol{u}}_{\mathrm{f}}^{m}, \phi^{m}\right)_{\Omega^{\mathrm{f}}} + \sum_{m=1}^{n-1} \frac{\tau^{2}}{\rho_{\mathrm{f}}} \left(\boldsymbol{\nabla} p^{m}, \boldsymbol{\nabla} \phi^{m}\right)_{\Omega^{\mathrm{f}}}, \tag{2.26}$$

cannot be controlled, so that this estimate does not guarantee the energy stability of the approximations provided by Algorithm 1. Two remarks are now in order.

Remark 2
It is worth mentioning that the term (2.26) corresponds to the residual of the projection step (2.16) (note that $\phi^n \notin N_{\Gamma^{\mathrm{out}},h}$). In fact, for the space continuous counterpart of (2.16) we have

$$\begin{aligned}\left(\boldsymbol{\nabla} \cdot \widetilde{\boldsymbol{u}}_{\mathrm{f}}^{n}, \phi^{n}\right)_{\Omega^{\mathrm{f}}} + \frac{\tau}{\rho_{\mathrm{f}}} \left(\boldsymbol{\nabla} p^{n}, \boldsymbol{\nabla} \phi^{n}\right)_{\Omega^{\mathrm{f}}} &= \frac{\tau}{\rho_{\mathrm{f}}} \int_{\Gamma^{\mathrm{out}}} \frac{\partial p^{n}}{\partial \boldsymbol{n}_{\mathrm{f}}} \phi^{n} \\ &= -\sum_{l=1}^{n_{0\mathrm{D}}} \left(\int_{\Gamma_l} \boldsymbol{u}_{\mathrm{f}}^{n} \cdot \boldsymbol{n}_{\mathrm{f}} - \int_{\Gamma_l} \widetilde{\boldsymbol{u}}_{\mathrm{f}}^{n} \cdot \boldsymbol{n}_{\mathrm{f}} \right) P_{l}^{n}.\end{aligned}$$

Hence, the uncontrolled artificial power involved in the energy estimate (2.17) is due to the time-lag in the flux ($\int_{\Gamma_l} \widetilde{\boldsymbol{u}}_{\mathrm{f}}^{n} \cdot \boldsymbol{n}_{\mathrm{f}}$ instead of $\int_{\Gamma_l} \boldsymbol{u}_{\mathrm{f}}^{n} \cdot \boldsymbol{n}_{\mathrm{f}}$) introduced by the explicit treatment of the continuity of fluxes $(2.13)_1$ on the 3D-0D interfaces Γ_l.

Remark 3
In the case of a single outlet (i.e., $n_{0\mathrm{D}} = 1$), we can take $\phi^n = P^n$ in Ω^{f}, so that the right hand-side of (2.21) vanishes. From the proof of Proposition 1 we then recover the following energy estimate for the fluid

$$\begin{aligned}\frac{\rho_{\mathrm{f}}}{2} \|\widetilde{\boldsymbol{u}}_{\mathrm{f}}^{n}\|_{0,\Omega^{\mathrm{f}}}^{2} + 2\mu \sum_{m=1}^{n} \tau \|\boldsymbol{\varepsilon}(\widetilde{\boldsymbol{u}}_{\mathrm{f}}^{m})\|_{0,\Omega^{\mathrm{f}}}^{2} + \sum_{m=1}^{n} \frac{\rho_{\mathrm{f}}}{2} \tau (\widetilde{\boldsymbol{u}}_{\mathrm{f}}^{m-1} \cdot \boldsymbol{n}_{\mathrm{f}}, |\widetilde{\boldsymbol{u}}_{\mathrm{f}}^{m}|^{2})_{\Gamma^{\mathrm{out}}} \\ \leq \frac{\rho_{\mathrm{f}}}{2} \|\boldsymbol{u}_{\mathrm{f}}^{0}\|_{0,\Omega^{\mathrm{f}}}^{2} - \sum_{m=1}^{n-1} \frac{\tau^{2}}{2\rho_{\mathrm{f}}} \|\boldsymbol{\nabla} p^{m}\|_{0,\Omega^{\mathrm{f}}}^{2}.\end{aligned}$$

As a result, the energy stability of the fluid does not depend on the imposed outlet pressure.

2.2.2 Semi-implicit 3D-0D coupling scheme

In this case the 3D-0D coupling conditions (2.3) are time-discretized as follows

$$\begin{cases} Q_{l}^{n} = \displaystyle\int_{\Gamma_l} \boldsymbol{u}_{\mathrm{f}}^{n} \cdot \boldsymbol{n}_{\mathrm{f}}, \\ p^{n} = P_{l}^{n} \quad \text{on} \quad \Gamma_l, \\ 2\mu \boldsymbol{\varepsilon}(\widetilde{\boldsymbol{u}}_{\mathrm{f}}^{n}) \boldsymbol{n}_{\mathrm{f}} = \boldsymbol{0} \quad \text{on} \quad \Gamma_l, \end{cases} \tag{2.27}$$

for $l = 1, \ldots, n_{0\mathrm{D}}$. Note that, in comparison with (2.13), the above coupling scheme treats implicitly the continuity of fluxes on the outlet boundaries. This feature en-

hances stability, as we will show in Section 2.2.2.1. However, from the computational point of view, the relations $(2.27)_{1,2}$ and (2.10) apparently couple the evaluation of (2.8) and (2.9). Fortunately, this difficulty can be circumvented via an appropriate reformulation of the pressure $(2.27)_2$ boundary condition for the projection step (2.8). Indeed, by inserting (2.9) into $(2.27)_1$, we get

$$Q_l^n = \widetilde{Q}_l^n - \frac{\tau}{\rho_{\mathrm{f}}} \int_{\Gamma_l} \frac{\partial p^n}{\partial \boldsymbol{n}_{\mathrm{f}}}, \tag{2.28}$$

which with (2.11) and $(2.27)_2$ yields the following (implicit) boundary condition for the outlet pressures:

$$p^n|_{\Gamma_l} = \gamma_l \widetilde{Q}_l^n - \frac{\gamma_l \tau}{\rho_{\mathrm{f}}} \int_{\Gamma_l} \frac{\partial p^n}{\partial \boldsymbol{n}_{\mathrm{f}}} + \alpha_l \pi_l^{n-1} \tag{2.29}$$

for $l = 1, \ldots, n_{0\mathrm{D}}$. Note that this expression still enforces p^n to be constant on each Γ_l.

Multiplying $(2.8)_1$ by $q \in N_h$, integrating by parts, using $(2.8)_1$ and the fact that $q|_{\Gamma_l}$ is constant, we get

$$\frac{\tau}{\rho_{\mathrm{f}}} (\boldsymbol{\nabla} p^n, \boldsymbol{\nabla} q)_{\Omega^{\mathrm{f}}} - \frac{\tau}{\rho_{\mathrm{f}}} \sum_{l=1}^{n_{0\mathrm{D}}} \left(\int_{\Gamma_l} \frac{\partial p^n}{\partial \boldsymbol{n}_{\mathrm{f}}} \right) q|_{\Gamma_l} = -(\boldsymbol{\nabla} \cdot \widetilde{\boldsymbol{u}}_{\mathrm{f}}^n, q)_{\Omega^{\mathrm{f}}}$$

for all $q \in N_h$. We can eliminate the normal derivative of the pressure using (2.29), which yields the following modified variational formulation for the projection step: Find $p^n \in N_h$ such that

$$\frac{\tau}{\rho_{\mathrm{f}}} (\boldsymbol{\nabla} p^n, \boldsymbol{\nabla} q)_{\Omega^{\mathrm{f}}} + \sum_{l=1}^{n_{0\mathrm{D}}} \frac{(p^n|_{\Gamma_l})(q|_{\Gamma_l})}{\gamma_l} = \sum_{l=1}^{n_{0\mathrm{D}}} \left(\widetilde{Q}_l^n + \frac{\alpha_l \pi_l^{n-1}}{\gamma_l} \right) q|_{\Gamma_l} - (\boldsymbol{\nabla} \cdot \widetilde{\boldsymbol{u}}_{\mathrm{f}}^n, q)_{\Omega^{\mathrm{f}}} \tag{2.30}$$

for all $q \in N_h$. We can then set $P_l^n = p^n|_{\Gamma_l}$ and retreive (Q_l^n, π_l^n) from (2.11), for $l = 1, \ldots n_{0\mathrm{D}}$.

Remark 4

The well-posedness of the pressure-Poisson problem (2.30) follows from a generalized Poincaré's inequality, which guarantees the coercivity of the left-hand side of (2.30) in N_h.

Remark 5

Testing (2.30) with $q = 1$, and since $P_l^n = p^n|_{\Gamma_l}$, we have

$$\sum_{l=1}^{n_{0\mathrm{D}}} \frac{P_l^n - \alpha_l \pi_l^{n-1}}{\gamma_l} = \sum_{l=1}^{n_{0\mathrm{D}}} \widetilde{Q}_l^n + \int_{\Omega^{\mathrm{f}}} \boldsymbol{\nabla} \cdot \widetilde{\boldsymbol{u}}_{\mathrm{f}}^n.$$

Hence, integrating by parts in the last term, using $(2.11)_2$ and owing to $(2.6)_{2,3}$ we

get the following mass conservation for the Windkessel fluxes:

$$\sum_{l=1}^{n_{0D}} Q_l^n = -\int_{\Gamma^{in}} \boldsymbol{u}_{in}(t_n).$$

The complete time-marching procedures is reported in Algorithm 2.

Algorithm 2 3D-0D semi-implicit coupling scheme

Let $\boldsymbol{u}_f^0 = \boldsymbol{u}_f(0)$, $\widetilde{\boldsymbol{u}}_f^0 \in \boldsymbol{V}_h$, and $\pi_1^0, \dots, \pi_{n_{0D}}^0 \in \mathbb{R}$ be given initial data. For $n \geq 1$ perform:

1. Viscous step: Find $\widetilde{\boldsymbol{u}}_f^n \in \boldsymbol{V}_{\Sigma,h}$ such that

$$\begin{cases} \widetilde{\boldsymbol{u}}_f^n|_{\Gamma^{in}} = \boldsymbol{u}_{in}(t_n), \\ \dfrac{\rho_f}{\tau}\left(\widetilde{\boldsymbol{u}}_f^n, \boldsymbol{v}\right)_{\Omega^f} + \rho_f(\widetilde{\boldsymbol{u}}_f^{n-1} \cdot \boldsymbol{\nabla}\widetilde{\boldsymbol{u}}_f^n, \boldsymbol{v})_{\Omega^f} + 2\mu\left(\boldsymbol{\varepsilon}(\widetilde{\boldsymbol{u}}_f^n), \boldsymbol{\varepsilon}(\boldsymbol{v})\right)_{\Omega^f} \\ \quad + \dfrac{\rho_f}{2}((\boldsymbol{\nabla}\cdot\widetilde{\boldsymbol{u}}_f^{n-1})\widetilde{\boldsymbol{u}}_f^n, \boldsymbol{v})_{\Omega^f} = \dfrac{\rho_f}{\tau}\left(\boldsymbol{u}_f^{n-1}, \boldsymbol{v}\right)_{\Omega^f} \end{cases} \tag{2.31}$$

   for all $\boldsymbol{v} \in \boldsymbol{V}_{\Sigma\cup\Gamma^{in},h}$. Thereafter set $\widetilde{Q}_l^n \overset{\text{def}}{=} \int_{\Gamma_l} \widetilde{\boldsymbol{u}}_f^n \cdot \boldsymbol{n}_f$.

2. Projection-Windkessel step: Find $p^n \in N_h$ and such that

$$\frac{\tau}{\rho_f}(\boldsymbol{\nabla}p^n, \boldsymbol{\nabla}q)_{\Omega^f} + \sum_{l=1}^{n_{0D}} \frac{(p^n|_{\Gamma_l})(q|_{\Gamma_l})}{\gamma_l} = \sum_{l=1}^{n_{0D}} \left(\widetilde{Q}_l^n + \frac{\alpha_l \pi_l^{n-1}}{\gamma_l}\right) q|_{\Gamma_l} - (\boldsymbol{\nabla}\cdot\widetilde{\boldsymbol{u}}_f^n, q)_{\Omega^f} \tag{2.32}$$

   for all $q \in N_h$. Thereafter, set $P_l^n = p^n|_{\Gamma_l}$ and compute $(Q_l^n, \pi_l^n) \in \mathbb{R}^2$ from the relations

$$Q_l^n = \frac{P_l^n - \alpha_l \pi_l^{n-1}}{\gamma_l}, \quad \pi_l^n = \alpha_l \pi_l^{n-1} + \beta_l Q_l^n, \quad l = 1, \dots n_{0D} \tag{2.33}$$

   and set $\boldsymbol{u}_f^n \overset{\text{def}}{=} \widetilde{\boldsymbol{u}}_f^n - \frac{\tau}{\rho_f}\boldsymbol{\nabla}p^n \in [L^2(\Omega^f)]^d$.

2.2.2.1 Stability analysis

The focus of this section is to present the stability result of the formulation (2.31)-(2.33) summarized in the following proposition.

Proposition 2
Let $\left\{(\widetilde{\boldsymbol{u}}_f^n, p^n)\right\}_{n\geq 1}$ *and* $\left\{(Q_l^n, \pi_l^n, P_l^n)_{1\leq l\leq n_{0D}}\right\}_{n\geq 1}$ *be the approximated solution given by Algorithm 2 and assume that* $\boldsymbol{u}_{in} = \boldsymbol{0}$ *(free system). The following energy inequality holds*

$$E^n + D^n + \sum_{m=1}^{n} \frac{\rho_f}{2}(\widetilde{\boldsymbol{u}}_f^{m-1} \cdot \boldsymbol{n}_f, |\widetilde{\boldsymbol{u}}_f^m|^2)_{\Gamma^{out}} \leq E^0 - \sum_{m=1}^{n-1} \frac{\tau^2}{2\rho_f}\|\boldsymbol{\nabla}p^m\|_{0,\Omega^f}^2. \tag{2.34}$$

Proof. We proceed as in the proof of Proposition 1. Testing the viscous step (2.31) with $\boldsymbol{v} = \widetilde{\boldsymbol{u}}_{\mathrm{f}}^{n}$ yields

$$\frac{\rho_{\mathrm{f}}}{2}\partial_\tau\|\widetilde{\boldsymbol{u}}_{\mathrm{f}}^{n}\|_{0,\Omega^{\mathrm{f}}}^2+\frac{\rho_{\mathrm{f}}}{2\tau}\big\|\widetilde{\boldsymbol{u}}_{\mathrm{f}}^{n}-\widetilde{\boldsymbol{u}}_{\mathrm{f}}^{n-1}\big\|_{0,\Omega^{\mathrm{f}}}^2+2\mu\|\boldsymbol{\varepsilon}(\widetilde{\boldsymbol{u}}_{\mathrm{f}}^{n})\|_{0,\Omega^{\mathrm{f}}}^2 \\ +\big(\boldsymbol{\nabla}p^{n-1},\widetilde{\boldsymbol{u}}_{\mathrm{f}}^{n}\big)_{\Omega^{\mathrm{f}}}+\frac{\rho_{\mathrm{f}}}{2}(\widetilde{\boldsymbol{u}}_{\mathrm{f}}^{n-1}\cdot\boldsymbol{n}_{\mathrm{f}},|\widetilde{\boldsymbol{u}}_{\mathrm{f}}^{n}|^2)_{\Gamma^{\mathrm{out}}}=0 \quad (2.35)$$

for $n\geq 2$ and, for $n=1$, we get

$$\frac{\rho_{\mathrm{f}}}{2\tau}\big(\big\|\widetilde{\boldsymbol{u}}_{\mathrm{f}}^{1}\big\|_{0,\Omega^{\mathrm{f}}}^2-\big\|\boldsymbol{u}_{\mathrm{f}}^{0}\big\|_{0,\Omega^{\mathrm{f}}}^2\big)+\frac{\rho_{\mathrm{f}}}{2\tau}\big\|\widetilde{\boldsymbol{u}}_{\mathrm{f}}^{1}-\boldsymbol{u}_{\mathrm{f}}^{0}\big\|_{0,\Omega^{\mathrm{f}}}^2+2\mu\big\|\boldsymbol{\varepsilon}(\widetilde{\boldsymbol{u}}_{\mathrm{f}}^{1})\big\|_{0,\Omega^{\mathrm{f}}}^2+\frac{\rho_{\mathrm{f}}}{2}(\widetilde{\boldsymbol{u}}_{\mathrm{f}}^{0}\cdot\boldsymbol{n}_{\mathrm{f}},|\widetilde{\boldsymbol{u}}_{\mathrm{f}}^{1}|^2)_{\Gamma^{\mathrm{out}}}=0. \quad (2.36)$$

Thereafter, taking (2.32) at time step $n-1$, testing with $q=\frac{\tau}{\rho_{\mathrm{f}}}p^{n-1}$ and integrating by parts in its right-hand side it yields

$$\frac{\tau}{\rho_{\mathrm{f}}}\big\|\boldsymbol{\nabla}p^{n-1}\big\|_{0,\Omega^{\mathrm{f}}}^2+\sum_{l=1}^{n_{0\mathrm{D}}}\frac{P_l^{n-1}-\alpha_l\pi_l^{n-2}}{\gamma_l}P_l^{n-1}=\big(\widetilde{\boldsymbol{u}}_{\mathrm{f}}^{n-1},\boldsymbol{\nabla}p^{n-1}\big)_{\Omega^{\mathrm{f}}}.$$

for $n\geq 2$. Hence, the addition and subtraction of suitable terms and the application of the Cauchy-Schwarz and arithmetic-geometric inequalities yields

$$\frac{\tau}{2\rho_{\mathrm{f}}}\big\|\boldsymbol{\nabla}p^{n-1}\big\|_{0,\Omega^{\mathrm{f}}}^2-\frac{\rho_{\mathrm{f}}}{2\tau}\big\|\widetilde{\boldsymbol{u}}_{\mathrm{f}}^{n}-\widetilde{\boldsymbol{u}}_{\mathrm{f}}^{n-1}\big\|_{0,\Omega^{\mathrm{f}}}^2-\big(\widetilde{\boldsymbol{u}}_{\mathrm{f}}^{n},\boldsymbol{\nabla}p^{n-1}\big)_{\Omega^{\mathrm{f}}}+\sum_{l=1}^{n_{0\mathrm{D}}}\frac{P_l^{n-1}-\alpha_l\pi_l^{n-2}}{\gamma_l}P_l^{n-1}\leq 0. \quad (2.37)$$

As a result, the summation of (2.35) and (2.37) gives

$$\frac{\rho_{\mathrm{f}}}{2}\partial_\tau\|\widetilde{\boldsymbol{u}}_{\mathrm{f}}^{n}\|_{0,\Omega^{\mathrm{f}}}^2+2\mu\|\boldsymbol{\varepsilon}(\widetilde{\boldsymbol{u}}_{\mathrm{f}}^{n})\|_{0,\Omega^{\mathrm{f}}}^2+\frac{\rho_{\mathrm{f}}}{2}(\widetilde{\boldsymbol{u}}_{\mathrm{f}}^{n-1}\cdot\boldsymbol{n}_{\mathrm{f}},|\widetilde{\boldsymbol{u}}_{\mathrm{f}}^{n}|^2)_{\Gamma^{\mathrm{out}}} \\ +\sum_{l=1}^{n_{0\mathrm{D}}}\frac{P_l^{n-1}-\alpha_l\pi_l^{n-2}}{\gamma_l}P_l^{n-1}\leq-\frac{\tau}{2\rho_{\mathrm{f}}}\big\|\boldsymbol{\nabla}p^{n-1}\big\|_{0,\Omega^{\mathrm{f}}}^2 \quad (2.38)$$

for $n\geq 2$. At last, from (2.33) and its equivalence to (2.11), we have

$$\begin{aligned}\frac{P_l^{n}-\alpha_l\pi_l^{n-1}}{\gamma_l}P_l^{n}&=Q_l^{n}P_l^{n}=R_{\mathrm{p},l}|Q_l^{n}|^2+Q_l^{n}\pi_l^{n}\\&\geq\frac{C_{d,l}}{2}\partial_\tau|\pi_l^{n}|^2+\frac{1}{R_{\mathrm{d},l}}|\pi_l^{n}|^2+R_{\mathrm{p},l}|Q_l^{n}|^2\end{aligned} \quad (2.39)$$

for $n\geq 1$. Hence, by inserting the last inequality of (2.39) into (2.38), multiplying by τ and summing over $m=2,...,n$ we get the estimate

$$E^n+D^n+\sum_{m=2}^{n}\frac{\rho_{\mathrm{f}}}{2}(\widetilde{\boldsymbol{u}}_{\mathrm{f}}^{m-1}\cdot\boldsymbol{n}_{\mathrm{f}},|\widetilde{\boldsymbol{u}}_{\mathrm{f}}^{m}|^2)_{\Gamma^{\mathrm{out}}}\leq E^1-\sum_{m=1}^{n-1}\frac{\tau^2}{2\rho_{\mathrm{f}}}\|\boldsymbol{\nabla}p^{m}\|_{0,\Omega^{\mathrm{f}}}^2.$$

for $n \geq 2$. We recover the estimate (2.34) by simply adding to this inequality the expression (2.36) multiplied by τ, which completes the proof. ∎

The estimate (2.34) corresponds to the discrete counterpart of (2.5). Note that the right-hand side of (2.34) is a pure numerical dissipation term (the natural pressure stabilization of the projection scheme). Therefore, the 3D-0D coupling reported in Algorithm 2 does not introduce any uncontrolled artificial power and, hence, a guaranty of numerical stability. This feature will be illustrated in Section 2.4 via numerical experiments.

2.2.2.2 Implementation issues

In this section we discuss some issues concerning the computer implementation of the pressure problem (Equation (2.32)) in a finite element framework. For the sake of simplicity, and without loss of generality, we discuss the case of a single outlet.

We define the arrays $P, V \in \mathbb{R}^N$ corresponding to the degrees of freedom (*dofs*) of the pressure $p^n \in Q_h$ and of a general test function $q \in Q_h$, respectively. The bilinear form $(\boldsymbol{\nabla} p^n, \boldsymbol{\nabla} q)_{\Omega^{\mathrm{f}}}$, without imposing Dirichlet boundary conditions for p^n, can be written in matrix form as

$$(\boldsymbol{\nabla} p^n, \boldsymbol{\nabla} q)_{\Omega^{\mathrm{f}}} = V^T A\, P = \begin{bmatrix} V_I^T & V_O^T \end{bmatrix} \begin{bmatrix} A_{II} & A_{IO} \\ A_{OI} & A_{OO} \end{bmatrix} \begin{bmatrix} P_I \\ P_O \end{bmatrix},$$

where the subindexes O and I indicate the elements of the array corresponding to the *dofs* on Γ^{out} and $\bar{\Omega} \backslash \Gamma^{\mathrm{out}}$, respectively. Then, the pressure projection step with explicit Dirichlet boundary conditions can be formulated as

$$A_{II} P_I = \tilde{F}_I - A_{IO} \mathbb{1}_O\, p^n_{|\Gamma^{\mathrm{out}}} \tag{2.40}$$

where the right hand side is defined as

$$\begin{bmatrix} V_I^T & V_O^T \end{bmatrix} \begin{bmatrix} \tilde{F}_I \\ \tilde{F}_O \end{bmatrix} = \frac{\rho_{\mathrm{f}}}{\tau} \left(\boldsymbol{\nabla} \cdot \widetilde{\boldsymbol{u}}^n_{\mathrm{f}}, q \right)_{\Omega^{\mathrm{f}}},$$

and $\mathbb{1}_O \in \mathbb{R}^{N_O}$ denotes a vector of ones, N_O being the number of pressure *dofs* on Γ^{out}. This system is usually solved by means of a preconditioned conjugate gradient methods (PCG), with the preconditioning operator $\hat{A}_{II}^{-1}$ chosen, for example, as an incomplete Cholesky factorization.

With the notations introduced above, the matrix formulation for the semi-implicit formulation (2.32) is straightforward. Since

$$V_O = \mathbb{1}_O q_{|\Gamma^{\mathrm{out}}}, \quad P_O = \mathbb{1}_O p^n_{|\Gamma^{\mathrm{out}}},$$

we obtain

$$\begin{bmatrix} A_{II} & \mathbf{a} \\ \mathbf{a}^T & b \end{bmatrix} \begin{bmatrix} P_I \\ p^n_{|\Gamma^{\text{out}}} \end{bmatrix} = \begin{bmatrix} \tilde{F}_I \\ \mathbb{1}_O^T \tilde{F}_I + \dfrac{\rho_{\text{f}}}{\tau}\left(\widetilde{Q}^n + \dfrac{\alpha \pi^{n-1}}{\gamma}\right) \end{bmatrix} \tag{2.41}$$

with

$$\mathbf{a} = A_{IO}\mathbb{1}_O,\ b = \mathbb{1}_O^T A_{OO}\mathbb{1}_O + \frac{\rho_{\text{f}}}{\tau\,\gamma}.$$

It is worth noticing that the resulting matrix in (2.41) does not have a sparse structure of a finite element matrix. In our numerical experiments, we used a preconditioner defined as

$$\begin{bmatrix} \hat{A}_{II}^{-1} & 0 \\ 0 & b^{-1} \end{bmatrix},$$

which yielded practically the same number of PCG-iterations to solve problem (2.41) with respect to the explicit case (2.40).

In the general case of a domain Ω^{f} with multiple outlets, the aforementioned considerations can be extended by considering one additional equation for each outlet.

Concerning the computational cost, in our numerical simulations we did observe any relevant difference between the implicit and the explicit coupling.

2.2.2.3 Extension to higher order time-splitting schemes

Although widely used in practice, the original Chorin-Temam projection scheme might suffer of a limited accuracy in time and of spurious boundary layers, due to the unphysical homogenous Neumann boundary condition $(2.8)_3$. Among the several variants available (see *e.g.* [GMS06] for an overview), in this section we describe a possible extension of the implicit 3D-0D coupling (Algorithm 2) in the context of an incremental pressure projection scheme with a second order time discretization.

Following [GMS06], we decompose now the time iteration in a BDF2 time discretization for the viscous step:

$$\begin{cases} \rho_{\text{f}} \dfrac{\left(3\widetilde{\boldsymbol{u}}^n_{\text{f}} - 4\boldsymbol{u}^{n-1}_{\text{f}} + \boldsymbol{u}^{n-2}_{\text{f}}\right)}{2\tau} + \rho_{\text{f}}\widetilde{\boldsymbol{u}}^{n-1}_{\text{f}} \cdot \boldsymbol{\nabla}\widetilde{\boldsymbol{u}}^n_{\text{f}} - 2\mu\boldsymbol{\nabla}\cdot\boldsymbol{\varepsilon}(\widetilde{\boldsymbol{u}}^n_{\text{f}}) + \nabla p^{n-1} = \mathbf{0} & \text{in} \quad \Omega^{\text{f}}, \\ \widetilde{\boldsymbol{u}}^n_{\text{f}} = \boldsymbol{u}_{\text{in}}(t_n) & \text{on} \quad \Gamma^{\text{in}}, \\ \widetilde{\boldsymbol{u}}^n_{\text{f}} = \mathbf{0} & \text{on} \quad \Sigma, \\ 2\mu\boldsymbol{\varepsilon}(\widetilde{\boldsymbol{u}}^n_{\text{f}})\boldsymbol{n}_{\text{f}} = \mathbf{0} & \text{on} \quad \Gamma^{\text{out}}, \end{cases}$$

a projection step for the increment of pressure

$$\begin{cases} -\dfrac{\tau}{\rho_{\text{f}}}\Delta\delta p^n = -\dfrac{3}{2}\boldsymbol{\nabla}\cdot\widetilde{\boldsymbol{u}}^n_{\text{f}} & \text{in} \quad \Omega^{\text{f}}, \\ \dfrac{\tau}{\rho_{\text{f}}}\dfrac{\partial\delta p^n}{\partial\boldsymbol{n}_{\text{f}}} = 0 & \text{on} \quad \Gamma^{\text{in}} \cup \Sigma, \\ \delta p^n = P^n_l - P^{n-1}_l & \text{on} \quad \Gamma_l, \quad l = 1, \dots, n_{0\text{D}} \end{cases}$$

completed by the end-of-step updates:

$$p^n = p^{n-1} + \delta p^n, \quad \boldsymbol{u}_{\mathrm{f}}^n = \widetilde{\boldsymbol{u}}_{\mathrm{f}}^n - \frac{2\tau}{3\rho_{\mathrm{f}}}\boldsymbol{\nabla}\delta p^n.$$

In order to have a second-order time-discretization for the whole 3D-0D problem, we also discretize the 0D model with a BDF2 scheme, namely

$$\pi_l^n = \widehat{\alpha}_l \pi_l^{n-1} - \widehat{\psi}_l \pi_l^{n-2} + \widehat{\beta}_l Q_l^n, \quad P_l^n = \widehat{\gamma}_l Q_l^n + \widehat{\alpha}_l \pi_l^{n-1} - \widehat{\psi}_l \pi_l^{n-2}, \tag{2.42}$$

with

$$\widehat{\alpha}_l \overset{\text{def}}{=} \frac{2R_{\mathrm{d},l}C_{\mathrm{d},l}}{(3/2)R_{\mathrm{d},l}C_{\mathrm{d},l} + \tau}, \quad \widehat{\psi}_l \overset{\text{def}}{=} \frac{\widehat{\alpha}_l}{4} \quad , \quad \widehat{\beta}_l \overset{\text{def}}{=} \frac{R_{\mathrm{d},l}\tau}{(3/2)R_{\mathrm{d},l}C_{\mathrm{d},l} + \tau}, \quad \widehat{\gamma}_l \overset{\text{def}}{=} R_{\mathrm{p},l} + \widehat{\beta}_l.$$

Hence, using Equation $(2.42)_2$ to define the implicit coupling with the projection step, we obtain the following time-stepping method:

1. Viscous step: Find $\widetilde{\boldsymbol{u}}_{\mathrm{f}}^n \in \boldsymbol{V}_{\Sigma,h}$ such that

$$\begin{cases} \boldsymbol{u}_{\mathrm{f}}^n|_{\Gamma^{\mathrm{in}}} = \boldsymbol{u}_{\mathrm{in}}(t_n), \\ \dfrac{\rho_{\mathrm{f}}}{2\tau}\left(3\widetilde{\boldsymbol{u}}_{\mathrm{f}}n, \boldsymbol{v}\right)_{\Omega^{\mathrm{f}}} + \rho_{\mathrm{f}}(\widetilde{\boldsymbol{u}}_{\mathrm{f}}^{n-1} \cdot \boldsymbol{\nabla}\widetilde{\boldsymbol{u}}_{\mathrm{f}}^n, \boldsymbol{v})_{\Omega^{\mathrm{f}}} + 2\mu\left(\boldsymbol{\varepsilon}(\widetilde{\boldsymbol{u}}_{\mathrm{f}}^n), \boldsymbol{\varepsilon}(\boldsymbol{v})\right)_{\Omega^{\mathrm{f}}} \\ \quad + \dfrac{\rho_{\mathrm{f}}}{2}((\boldsymbol{\nabla}\cdot\widetilde{\boldsymbol{u}}_{\mathrm{f}}^{n-1})\widetilde{\boldsymbol{u}}_{\mathrm{f}}^n, \boldsymbol{v})_{\Omega^{\mathrm{f}}} = -\left(\boldsymbol{\nabla}p^n, \boldsymbol{v}\right) + \dfrac{\rho_{\mathrm{f}}}{2\tau}\left(4\boldsymbol{u}_{\mathrm{f}}^{n-1} - \boldsymbol{u}_{\mathrm{f}}^{n-2}, \boldsymbol{v}\right)_{\Omega^{\mathrm{f}}} \end{cases}$$

   for all $\boldsymbol{v} \in \boldsymbol{V}_{\Sigma\cup\Gamma^{\mathrm{in}},h}$. Thereafter set $\widetilde{Q}_l^n \overset{\text{def}}{=} \int_{\Gamma_l} \widetilde{\boldsymbol{u}}_{\mathrm{f}}^n \cdot \boldsymbol{n}_{\mathrm{f}}$.

2. Increment-Windkessel step: Find $\delta p^n \in R_h$ and such that

$$\frac{\tau}{\rho_{\mathrm{f}}}\left(\boldsymbol{\nabla}\delta p^n, \boldsymbol{\nabla}q\right)_{\Omega^{\mathrm{f}}} + \sum_{l=1}^{n_{0\mathrm{D}}} \frac{(\delta p^n|_{\Gamma_l})(q|_{\Gamma_l})}{\widehat{\gamma}_l} = \sum_{l=1}^{n_{0\mathrm{D}}} \left(\widetilde{Q}_l^n + \frac{\widehat{\alpha}_l\pi_l^{n-1} - \widehat{\psi}_l\pi_l^{n-2} - P_l^{n-1}}{\widehat{\gamma}_l}\right) q|_{\Gamma_l} - (\boldsymbol{\nabla}\cdot\widetilde{\boldsymbol{u}}_{\mathrm{f}}^n, q)_{\Omega^{\mathrm{f}}}$$

   for all $q \in R_h$.

3. End-of-step: Set $p^n \overset{\text{def}}{=} p^{n-1} + \delta p^n$, $\boldsymbol{u}_{\mathrm{f}}^n \overset{\text{def}}{=} \widetilde{\boldsymbol{u}}_{\mathrm{f}}^n - \dfrac{2\tau}{3\rho_{\mathrm{f}}}\boldsymbol{\nabla}\delta p^n \in [L^2(\Omega^{\mathrm{f}})]^d$, $P_l^n = p^n|_{\Gamma_l}$ and compute $(Q_l^n, \pi_l^n) \in \mathbb{R}^2$ from the relations (2.42).

Remark 6

It is well known that the stability of pressure-incremental projection scheme is only assured if the finite element spaces for velocity and pressure satisfy an *inf-sup* condition (see [GMS06] for an extended discussion).

2.2.2.4 Extension to more complex lumped parameter models

The algorithm and analysis presented above can be straightforwardly extended to more complex networks of lumped parameter models, namely a network of resistances, capacitances, and inductances. This can be for example obtained by connecting many Windkessel elements to eachother, when several components of the cardiovascular system are included in the model, see e.g. [SLH11, KS06, MVCFM12] and references therein.

Let us consider the following general lumped parameter model

$$\begin{cases} C\dfrac{\mathrm{d}P}{\mathrm{d}t} + RP = Q + H\Psi \\ L\dfrac{\mathrm{d}\Psi}{\mathrm{d}t} = -H^{\intercal}P \end{cases} \tag{2.43}$$

with

$$P^{\intercal} = \begin{bmatrix} P_1 & \dots & P_{n_{0\mathrm{D}}} & \pi_1 & \dots & \pi_{n_\pi} \end{bmatrix}$$

the collection of outlet P_l, $l = 1, \dots, n_{0\mathrm{D}}$ and distal pressures π_j, $j = 1, \dots, n_\pi$, and Ψ are the fluxes through the inductances, both representing the dynamical state of the lumped parameter model. Moreover, we assume that $Q(t) \in \mathbb{R}^{n_p}$ has the form

$$Q^{\intercal} = \begin{bmatrix} Q_1 & \dots & Q_{n_{0\mathrm{D}}} & 0 \dots 0 \end{bmatrix} .$$

with Q_l the input flux at the outlet Γ_l.

In Equation (2.43) $C \geq 0$, $R, L > 0$ denote the symmetric capacitances, resistances and inductances matrices. This ensures the correct energy balance of the system in the 3D-0D time-space continuos formulation, namely

$$\frac{\mathrm{d}}{\mathrm{d}t}\left(\frac{1}{2}P^{\intercal}CP + \frac{1}{2}\Psi^{\intercal}L\Psi\right) = -P^{\intercal}RP + P^{\intercal}Q \ .$$

since that the last term of the right-hand-side cancels out when coupling Equations (2.43) with the Navier-Stokes Equations.

As an example, the three-element Windkessel presented above – with an additional inductance L_p paralell to R_p – can be rewritten in this format obtaining the following expressions for the system matrices

$$C = \begin{bmatrix} 0 & 0 \\ 0 & C_d \end{bmatrix}, R = \begin{bmatrix} 1/R_p & -1/R_p \\ -1/R_p & 1/R_p + 1/R_d \end{bmatrix}, H = \begin{bmatrix} -1 \\ 1 \end{bmatrix}, L = L_p \ .$$

More complex models can be represented in this format analagously.

Discretizing (2.43) in time (e.g. using a backward Euler scheme), we obtain

$$P^n = AP^{n-1} + BQ^n + B\,H\Psi^{n-1} \,, \tag{2.44}$$

with

$$\begin{aligned} B &= (C/\tau + R)^{-1}\,, \\ A &= B\,(C/\tau + \tau H L^{-1} H^{\intercal})\,. \end{aligned} \tag{2.45}$$

As done in Equations (2.28)-(2.29) for the three-element Windkessel, in order to obtain an analogous of the implicit coupling scheme (Algorithm 2), we need explicit expressions for Q_l^n, $l = 1, \ldots, n_{0\mathrm{D}}$. These can be computed algebraically from Equation (2.44) by first isolating the degrees-of-freedom at the outlet by

$$\bar{\bar{B}} \begin{bmatrix} Q_1^n \\ \vdots \\ Q_{n_{0\mathrm{D}}}^n \end{bmatrix} = \begin{bmatrix} P_1^n \\ \vdots \\ P_{n_{0\mathrm{D}}}^n \end{bmatrix} - \bar{A} P^{n-1} - \bar{B}\, H \Psi^{n-1}$$

with $\bar{()}$ denoting the first $n_{0\mathrm{D}}$ rows and $\bar{\bar{()}}$ the first $n_{0\mathrm{D}}$ rows and columns, respectively. Hence, we obtain the following expression

$$\begin{bmatrix} Q_1^n \\ \vdots \\ Q_{n_{0\mathrm{D}}}^n \end{bmatrix} = G \begin{bmatrix} P_1^n \\ \vdots \\ P_{n_{0\mathrm{D}}}^n \end{bmatrix} - G \bar{A} P^{n-1} - G\, \bar{B}\, H \Psi^{n-1}$$

with $G = (\bar{\bar{B}})^{-1}$. Finally, combining the latter with (2.28), obtaining at each time step the following formulation of the pressure projection-windkessel step (compare with (2.32)): Find $p^n \in R_h$ such that

$$\frac{\tau}{\rho_{\mathrm{f}}} (\boldsymbol{\nabla} p^n, \boldsymbol{\nabla} q)_{\Omega^{\mathrm{f}}} + \sum_{k,l=1}^{n_{0\mathrm{D}}} g_{k,l} (p^n|_{\Gamma_k})(q|_{\Gamma_l}) = \sum_{l=1}^{n_{0\mathrm{D}}} (\widetilde{Q}_l^n + b_l^{n-1} q|_{\Gamma_l})(q|_{\Gamma_l}) - (\boldsymbol{\nabla} \cdot \widetilde{\boldsymbol{u}}^n, q)_{\Omega^{\mathrm{f}}} \tag{2.46}$$

for all $q \in R_h$ and with

$$g_{k,l} = [G]_{k,l},\ b_l^n = [G \bar{A} P^n + G\, \bar{B}\, H \Psi^n]_l\,. \tag{2.47}$$

Note that, in this general formulation, the pressure at the outlets can be coupled through the lumped parameter model since generally $g_{k,l} \neq 0$ for $k \neq l$.

Remark 7

Using the same arguments as in Section 2.2.2.1, the unconditional stability results of Theorem 2 can be extended to a fractional step scheme with the generalized pressure projection formulation (2.46).

2.3 Incompressible fluid-structure interaction

Fractional-step time-marching schemes have been a valuable tool for the design of efficient solution methods for incompressible fluid-structure interaction (FSI) problems, yielding the so-called projection semi-implicit coupling scheme

[FGG06, FGG07] (see also the subsequent works [ACF09, BQQ08, QQ07]). This coupling approach is based on the following three basic ideas:

- treat explicitly the geometrical non-linearities and the viscous-structure coupling, which reduces computational complexity;
- treat implicitly the presssure-structure coupling, which avoids numerical instability;
- perform this explicit-implicit splitting through a projection scheme in the fluid.

So far, the stability of this method has been analyzed within a simplified framework which enforces null pressure on the outlet boundaries (see [ACF09, FGG07]). In this section the analysis is extended to the case of a lumped parameter modeling of the outlet boundaries, with a pressure-Poisson formulation of the projection step based on the methods of Section 2.2.

2.3.1 Model problem

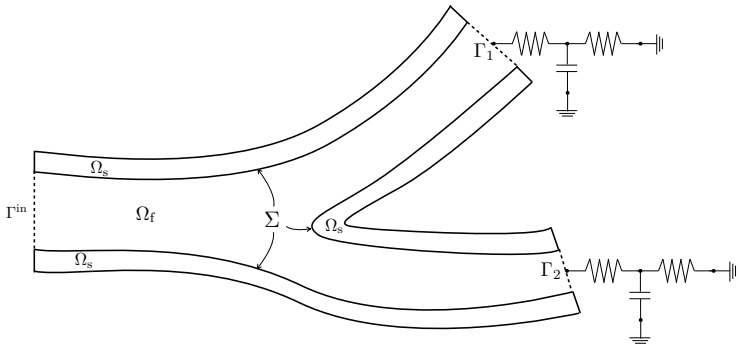

Figure 2.2: Example of geometric configurations with $\overline{\Omega^s} \neq \Sigma$.

For the sake of the analysis (see [FGG07]), we consider as model problem a coupled linear system in which the fluid is described by the Stokes equations, in the fixed domain Ω^f, and the structure either by the classical linear elastodynamics equations or by equations based on linear thin-solid models (e.g., plate, shell, etc.). The reference domain of the solid is denoted by Ω^s. It will be either a domain or a $(d-1)-$manifold of $\mathbb{R}^d$ (in this later case the elastic domain is identified to its mid-surface). We denote by $\Sigma \overset{\text{def}}{=} \partial\Omega^s \cap \partial\Omega^f$ the fluid-structure interface. In the case the structure is described by thin-solid model we have $\overline{\Omega^s} = \Sigma$ (see Figure 2.2). The resulting coupled system, describing the fluid velocity $\boldsymbol{u}_f : \Omega^f \times \mathbb{R}^+ \to \mathbb{R}^d$, fluid

pressure $p : \Omega^{\mathrm{f}} \times \mathbb{R}^+ \to \mathbb{R}$ and solid displacement $\boldsymbol{y}_{\mathrm{s}} : \Omega^{\mathrm{s}} \times \mathbb{R}^+ \to \mathbb{R}^d$, is given by

$$\begin{cases} \rho_{\mathrm{f}} \partial_t \boldsymbol{u}_{\mathrm{f}} - \boldsymbol{\nabla} \cdot \boldsymbol{\sigma}_{\mathrm{f}}(\boldsymbol{u}_{\mathrm{f}}, p) = \boldsymbol{0} & \text{in} \quad \Omega^{\mathrm{f}}, \\ \boldsymbol{\nabla} \cdot \boldsymbol{u}_{\mathrm{f}} = 0 & \text{in} \quad \Omega^{\mathrm{f}}, \\ \boldsymbol{u}_{\mathrm{f}} = \boldsymbol{u}_{\mathrm{in}} & \text{on} \quad \Gamma^{\mathrm{in}}, \\ \boldsymbol{u}_{\mathrm{f}} = \boldsymbol{u}_{\mathrm{s}} & \text{in} \quad \Sigma, \end{cases} \tag{2.48}$$

$$\begin{cases} \rho_{\mathrm{s}} \left(\partial_t \boldsymbol{u}_{\mathrm{s}}, \boldsymbol{v}_{\mathrm{s}}\right)_{\Omega^{\mathrm{s}}} + a_{\mathrm{s}}(\boldsymbol{y}_{\mathrm{s}}, \boldsymbol{v}_{\mathrm{s}}) = -\left(\boldsymbol{\sigma}_{\mathrm{f}}(\boldsymbol{u}_{\mathrm{f}}, p)\boldsymbol{n}_{\mathrm{f}}, \boldsymbol{v}_{\mathrm{s}}\right)_{\Sigma} \quad \forall \boldsymbol{v}_s \in \boldsymbol{W}, \\ \boldsymbol{u}_{\mathrm{s}} = \partial_t \boldsymbol{y}_{\mathrm{s}} \quad \text{in} \quad \Omega^{\mathrm{s}}, \end{cases} \tag{2.49}$$

completed with the lumped-parameter modeling (2.2)-(2.3) on the outlet boundary Γ^{out} (see Figure 2.2). Here, ρ_{s} denotes the solid density, the abstract bilinear form $a_{\mathrm{s}} : \boldsymbol{W} \times \boldsymbol{W} \to \mathbb{R}$ describes the elastic behavior of the structure and $\boldsymbol{W}$ stands for its space of admissible displacements. Note that Equation (2.49) represents also the variational formulation of the structure subproblem. Though simplified, problem (2.48)-(2.49) features some of the main numerical issues that appear in complex nonlinear fluid-structure interaction problems involving an incompressible fluid (see, e.g., [Fer11]).

Energy balance. Let the quantity

$$E(t) \overset{\text{def}}{=} \frac{\rho_{\mathrm{f}}}{2} \|\boldsymbol{u}_{\mathrm{f}}\|^2_{0,\Omega^{\mathrm{f}}} + \frac{\rho_{\mathrm{s}}}{2} \|\boldsymbol{u}_{\mathrm{s}}\|^2_{0,\Omega^{\mathrm{s}}} + \frac{1}{2} \|\boldsymbol{y}_{\mathrm{s}}\|^2_{\mathrm{s}} + \sum_{l=1}^{n_{0\mathrm{D}}} \frac{C_{d,l}}{2} \pi_l^2$$

denote the total (kinetic + potential) energy of the FSI-0D coupled system given by (2.48)-(2.49) and (2.2)-(2.3). Here, $\|\cdot\|_{\mathrm{s}}$ stands for the elastic energy norm of the solid, defined as $\|\boldsymbol{y}_{\mathrm{s}}\|^2_{\mathrm{s}} \overset{\text{def}}{=} a_{\mathrm{s}}(\boldsymbol{y}_{\mathrm{s}}, \boldsymbol{y}_{\mathrm{s}})$. Assuming that $\boldsymbol{u}_{\mathrm{in}} = \boldsymbol{0}$ (free system) and using a standard energy argument, we get the following identity

$$E(t) + D(t) = E(0), \tag{2.50}$$

with the dissipative term $D(t) > 0$ given as in (2.4).

Note that in this model problem we do not consider the convective term in the fluid, hence we have to solve the fluid in a fixed domain in order to get the right energy balance across the fluid-structure interface Σ.

2.3.1.1 Spatial discretization

Let $\{\mathcal{T}_{\mathrm{s},h}\}_{0<h\leq 1}$ be a quasi-uniform family of triangulations of the domain Ω^{s}. In order to ease the presentation, we assume that the fluid and solid triangulations $\mathcal{T}_{\mathrm{f},h}$ and $\mathcal{T}_{\mathrm{s},h}$ match at the interface Σ. For the discretization in space of the solid problem (2.49), we consider continuous Lagrange finite element approximations, $\boldsymbol{W}_h$ of $\boldsymbol{W}$, which match the fluid velocity discretizations at the interface. Hence,

$$\{\boldsymbol{v}|_{\Sigma} \mid \boldsymbol{v} \in \boldsymbol{V}_h\} = \{\boldsymbol{v}_{\mathrm{s}}|_{\Sigma} \mid \boldsymbol{v}_{\mathrm{s}} \in \boldsymbol{W}_h\}.$$

At last, we introduce the standard fluid-sided discrete lifting operator $\boldsymbol{\mathcal{L}}_h : \boldsymbol{W}_h \to \boldsymbol{V}_h$, such that, the nodal values of $\boldsymbol{\mathcal{L}}_h \boldsymbol{v}_\mathrm{s}$ vanish out of Σ and $(\boldsymbol{\mathcal{L}}_h \boldsymbol{v}_\mathrm{s})|_\Sigma = \boldsymbol{v}_\mathrm{s}|_\Sigma$, for all $\boldsymbol{v}_\mathrm{s} \in \boldsymbol{W}_h$. In what follows we shall make use of the following continuity estimates (from [FGG07, Lemma 1]) for the discrete lifting operator $\boldsymbol{\mathcal{L}}_h$:

$$\|\boldsymbol{\mathcal{L}}_h \boldsymbol{v}_\mathrm{s}\|_{0,\Omega^\mathrm{f}} \leq C_\mathrm{L} h^{\frac{1-\alpha}{2}} \|\boldsymbol{v}_\mathrm{s}\|_{0,\Omega^\mathrm{s}}, \quad \|\boldsymbol{\nabla} \boldsymbol{\mathcal{L}}_h \boldsymbol{v}_\mathrm{s}\|_{0,\Omega^\mathrm{f}} \leq C_\mathrm{L} h^{-\frac{1+\alpha}{2}} \|\boldsymbol{v}_\mathrm{s}\|_{0,\Omega^\mathrm{s}} \tag{2.51}$$

for all $\boldsymbol{v}_\mathrm{s} \in \boldsymbol{W}_h$ and with the notation

$$\alpha \overset{\text{def}}{=} \begin{cases} 0 & \text{if} \quad \overline{\Omega^\mathrm{s}} = \Sigma, \\ 1 & \text{if} \quad \overline{\Omega^\mathrm{s}} \neq \Sigma. \end{cases} \tag{2.52}$$

2.3.1.2 Fully semi-implicit FSI-0D scheme

In this case we consider numerical approximations of the coupled problem FSI-0D system (2.48)-(2.49) and (2.2)-(2.3) by combining the projection semi-implicit coupling scheme reported in [FGG07] with the 3D-0D semi-implicit coupling of Section 2.2.2. The resulting fully discrete time-marching procedure is reported in Algorithm 3. In the solid subproblem (2.56), the fluid residual terms are given by

$$\begin{aligned} \langle \mathcal{R}_\mu(\widetilde{\boldsymbol{u}}_\mathrm{f}^n), \boldsymbol{v} \rangle &\overset{\text{def}}{=} \frac{\rho_\mathrm{f}}{\tau} \left(\widetilde{\boldsymbol{u}}_\mathrm{f}^n, \boldsymbol{v}\right)_{\Omega^\mathrm{f}} + 2\mu \left(\boldsymbol{\varepsilon}(\widetilde{\boldsymbol{u}}_\mathrm{f}^n), \boldsymbol{\varepsilon}(\boldsymbol{v})\right)_{\Omega^\mathrm{f}} - \frac{\rho_\mathrm{f}}{\tau} \left(\boldsymbol{u}_\mathrm{f}^{n-1}, \boldsymbol{v}\right)_{\Omega^\mathrm{f}}, \\ \langle \mathcal{R}_p(p^n, \boldsymbol{u}_\mathrm{f}^n), \boldsymbol{v} \rangle &\overset{\text{def}}{=} \frac{\rho_\mathrm{f}}{\tau} \left(\boldsymbol{u}_\mathrm{f}^n, \boldsymbol{v}\right)_{\Omega^\mathrm{f}} - \frac{\rho_\mathrm{f}}{\tau} \left(\widetilde{\boldsymbol{u}}_\mathrm{f}^n, \boldsymbol{v}\right)_{\Omega^\mathrm{f}} - \left(p^n, \boldsymbol{\nabla} \cdot \boldsymbol{v}\right)_{\Omega^\mathrm{f}}. \end{aligned}$$

Let the quantities

$$\begin{aligned} E^n &\overset{\text{def}}{=} \frac{\rho_\mathrm{f}}{2} \|\boldsymbol{u}_\mathrm{f}^n\|_{0,\Omega^\mathrm{f}}^2 + \frac{\rho_\mathrm{s}}{2} \|\boldsymbol{u}_\mathrm{s}^n\|_{0,\Omega^\mathrm{s}}^2 + \frac{1}{2} \|\boldsymbol{y}_\mathrm{s}^n\|_\mathrm{s}^2 + \sum_{l=1}^{n_{0\mathrm{D}}} \frac{C_{d,l}}{2} |\pi_l^n|^2, \\ D^n &\overset{\text{def}}{=} 2\mu \sum_{m=1}^{n} \tau \|\boldsymbol{\varepsilon}(\widetilde{\boldsymbol{u}}_\mathrm{f}^m)\|_{0,\Omega^\mathrm{f}}^2 + \sum_{m=1}^{n-1} \sum_{l=1}^{n_{0\mathrm{D}}} \tau \left(\frac{|\pi_l^m|^2}{R_{\mathrm{d},l}} + R_{\mathrm{p},l} |Q_l^m|^2 \right) \end{aligned}$$

for $n \geq 1$, denote the energy and physical dissipation of the discrete FSI-0D system, respectively.

We then have the following energy based result.

Proposition 3
Let $\left\{(\widetilde{\boldsymbol{u}}_\mathrm{f}^n, p^n, \boldsymbol{y}_\mathrm{s}^n, \boldsymbol{u}_\mathrm{s}^n)\right\}_{n\geq 1}$ *and* $\left\{(Q_l^n, \pi_l^n, P_l^n)_{1\leq l\leq n_{0\mathrm{D}}}\right\}_{n\geq 1}$ *be the approximated solution given by Algorithm 3, and assume that* $\boldsymbol{u}_\mathrm{in} = \boldsymbol{0}$ *(free system) and that the following condition holds*

$$\rho_\mathrm{s} \geq 3 C_\mathrm{L} \left(\rho_\mathrm{f} h^{1-\alpha} + \frac{\mu \tau}{h^{1+\alpha}} \right), \tag{2.58}$$

Algorithm 3 Fully semi-implicit FSI/3D-0D scheme

Let $\boldsymbol{u}_{\mathrm{f}}^0 = \boldsymbol{u}_{\mathrm{f}}(0)$, $\pi_1^0, \dots, \pi_{n_{0\mathrm{D}}}^0 \in \mathbb{R}$ and $\boldsymbol{y}_{\mathrm{s}}^0, \boldsymbol{u}_{\mathrm{s}}^0 \in \boldsymbol{W}_h$ be given initial data. For $n \geq 1$ perform:

1. Viscous step: Find $\widetilde{\boldsymbol{u}}_{\mathrm{f}}^n \in \boldsymbol{V}_h$ such that

$$\begin{cases} \widetilde{\boldsymbol{u}}_{\mathrm{f}}^n|_{\Sigma} = \boldsymbol{u}_{\mathrm{s}}^{n-1}|_{\Sigma}, \\ \widetilde{\boldsymbol{u}}_{\mathrm{f}}^n|_{\Gamma^{\mathrm{in}}} = \boldsymbol{u}_{\mathrm{in}}(t_n), \\ \dfrac{\rho_{\mathrm{f}}}{\tau}\left(\widetilde{\boldsymbol{u}}_{\mathrm{f}}^n, \boldsymbol{v}\right)_{\Omega^{\mathrm{f}}} + 2\mu\left(\boldsymbol{\varepsilon}(\widetilde{\boldsymbol{u}}_{\mathrm{f}}^n), \boldsymbol{\varepsilon}(\boldsymbol{v})\right)_{\Omega^{\mathrm{f}}} = \dfrac{\rho_{\mathrm{f}}}{\tau}\left(\boldsymbol{u}_{\mathrm{f}}^{n-1}, \boldsymbol{v}\right)_{\Omega^{\mathrm{f}}} \end{cases} \tag{2.53}$$

for all $\boldsymbol{v} \in \boldsymbol{V}_{\Sigma\cup\Gamma^{\mathrm{in}},h}$. Thereafter set $\widetilde{Q}_l^n \stackrel{\mathrm{def}}{=} \int_{\Gamma_l} \widetilde{\boldsymbol{u}}_{\mathrm{f}}^n \cdot \boldsymbol{n}_{\mathrm{f}}$.

2. Implicit step (projection-Windkessel-solid step): Find $(p^n, \boldsymbol{u}_{\mathrm{f}}^n, \boldsymbol{y}_{\mathrm{s}}^n) \in N_h \times \boldsymbol{V}_h \times \boldsymbol{W}_h$ with $\boldsymbol{u}_{\mathrm{s}}^n = \partial_\tau \boldsymbol{y}_{\mathrm{s}}^n$ and such that

$$\begin{cases} \dfrac{\tau}{\rho_{\mathrm{f}}}\left(\boldsymbol{\nabla} p^n, \boldsymbol{\nabla} q\right)_{\Omega^{\mathrm{f}}} + \displaystyle\sum_{l=1}^{n_{0\mathrm{D}}} \frac{(p^n|_{\Gamma_l})(q|_{\Gamma_l})}{\gamma_l} = \quad \sum_{l=1}^{n_{0\mathrm{D}}} \left(\widetilde{Q}_l^n + \frac{\alpha_l \pi_l^{n-1}}{\gamma_l}\right) q|_{\Gamma_l} \\ \quad - \left(\boldsymbol{\nabla}\cdot\widetilde{\boldsymbol{u}}_{\mathrm{f}}^n, q\right)_{\Omega^{\mathrm{f}}} - \left((\boldsymbol{u}_{\mathrm{s}}^n - \widetilde{\boldsymbol{u}}_{\mathrm{f}}^n)\cdot\boldsymbol{n}_{\mathrm{f}}, q\right)_{\Sigma}, \end{cases} \tag{2.54}$$

$$\begin{cases} \boldsymbol{u}_{\mathrm{f}}^n|_{\Gamma^{\mathrm{in}}} = \boldsymbol{u}_{\mathrm{in}}(t_n), \\ \boldsymbol{u}_{\mathrm{f}}^n|_{\Sigma} = \boldsymbol{u}_{\mathrm{s}}^n|_{\Sigma}, \\ \dfrac{\rho_{\mathrm{f}}}{\tau}\left(\boldsymbol{u}_{\mathrm{f}}^n, \boldsymbol{v}\right)_{\Omega^{\mathrm{f}}} = \dfrac{\rho_{\mathrm{f}}}{\tau}\left(\widetilde{\boldsymbol{u}}_{\mathrm{f}}^n, \boldsymbol{v}\right)_{\Omega^{\mathrm{f}}} - \left(\boldsymbol{\nabla} p^n, \boldsymbol{v}\right)_{\Omega^{\mathrm{f}}}, \end{cases} \tag{2.55}$$

$$\rho_{\mathrm{s}}\left(\partial_\tau \boldsymbol{u}_{\mathrm{s}}^n, \boldsymbol{v}_{\mathrm{s}}\right)_{\Omega^{\mathrm{s}}} + a_{\mathrm{s}}(\boldsymbol{y}_{\mathrm{s}}^n, \boldsymbol{v}_{\mathrm{s}}) = -\left\langle \mathcal{R}_\mu(\widetilde{\boldsymbol{u}}_{\mathrm{f}}^n), \mathcal{L}_h \boldsymbol{v}_{\mathrm{s}}\right\rangle - \left\langle \mathcal{R}_p(\boldsymbol{u}_{\mathrm{f}}^n, p^n), \mathcal{L}_h \boldsymbol{v}_{\mathrm{s}}\right\rangle \tag{2.56}$$

for all $(q, \boldsymbol{v}, \boldsymbol{v}_{\mathrm{s}}) \in N_h \times \boldsymbol{V}_{\Sigma\cup\Gamma^{\mathrm{out}},h} \times \boldsymbol{W}_h$.

Thereafter, set $P_l^n = p^n|_{\Gamma_l}$ and compute $(Q_l^n, \pi_l^n) \in \mathbb{R}^2$ from the relations

$$Q_l^n = \frac{P_l^n - \alpha_l \pi_l^{n-1}}{\gamma_l}, \quad \pi_l^n = \alpha_l \pi_l^{n-1} + \beta_l Q_l^n, \quad l = 1, \dots n_{0\mathrm{D}}. \tag{2.57}$$

with α given by (2.52). Then, following energy inequality holds

$$E^n + D^n \lesssim E^0 - \sum_{m=1}^{n-1} \frac{\tau^2}{\rho_{\mathrm{f}}} \left\| \Pi_h^{\perp}(\boldsymbol{\nabla} p^n) \right\|_{0,\Omega^{\mathrm{f}}}^2, \tag{2.59}$$

with $\Pi_h : \boldsymbol{L}^2(\Omega^{\mathrm{f}}) \to \boldsymbol{V}_{\Sigma\cup\Gamma^{\mathrm{in}},h}$ stands for the L^2-projection operator into $\boldsymbol{V}_{\Sigma\cup\Gamma^{\mathrm{in}},h}$, and $\Pi_h^{\perp} \stackrel{\mathrm{def}}{=} I - \Pi_h$ for the corresponding orthogonal projection.

Proof. First, testing the viscous step (2.53) with $\boldsymbol{v} = \widetilde{\boldsymbol{u}}_{\mathrm{f}}^n - \mathcal{L}_h \boldsymbol{u}_{\mathrm{s}}^{n-1}$ yields

$$\frac{\rho_{\mathrm{f}}}{2\tau}\left(\|\widetilde{\boldsymbol{u}}_{\mathrm{f}}^n\|_{0,\Omega^{\mathrm{f}}}^2 - \|\boldsymbol{u}_{\mathrm{f}}^{n-1}\|_{0,\Omega^{\mathrm{f}}}^2\right) + \frac{\rho_{\mathrm{f}}}{2\tau}\|\widetilde{\boldsymbol{u}}_{\mathrm{f}}^n - \boldsymbol{u}_{\mathrm{f}}^{n-1}\|_{0,\Omega^{\mathrm{f}}}^2 + 2\mu\|\boldsymbol{\varepsilon}(\widetilde{\boldsymbol{u}}_{\mathrm{f}}^n)\|_{0,\Omega^{\mathrm{f}}}^2 - \langle \mathcal{R}_\mu(\widetilde{\boldsymbol{u}}_{\mathrm{f}}^n), \mathcal{L}_h \boldsymbol{u}_{\mathrm{s}}^{n-1}\rangle = 0. \quad (2.60)$$

On the other hand, testing (2.55) with $\boldsymbol{v} = \boldsymbol{u}_{\mathrm{f}}^n - \mathcal{L}_h \boldsymbol{u}_{\mathrm{s}}^n$ yields

$$\frac{\rho_{\mathrm{f}}}{2\tau}\left(\|\boldsymbol{u}_{\mathrm{f}}^n\|_{0,\Omega^{\mathrm{f}}}^2 - \|\widetilde{\boldsymbol{u}}_{\mathrm{f}}^n\|_{0,\Omega^{\mathrm{f}}}^2\right) + \frac{\rho_{\mathrm{f}}}{2\tau}\|\boldsymbol{u}_{\mathrm{f}}^n - \widetilde{\boldsymbol{u}}_{\mathrm{f}}^n\|_{0,\Omega^{\mathrm{f}}}^2 + (\boldsymbol{\nabla} p^n, \boldsymbol{u}_{\mathrm{f}}^n)_{\Omega^{\mathrm{f}}} - (p^n, \boldsymbol{u}_{\mathrm{s}}^n \cdot \boldsymbol{n}_{\mathrm{f}})_\Sigma - \langle \mathcal{R}_p(p^n, \boldsymbol{u}_{\mathrm{f}}^n), \mathcal{L}_h \boldsymbol{u}_{\mathrm{s}}^n\rangle = 0 \quad (2.61)$$

and taking $\boldsymbol{v}_{\mathrm{s}} = \boldsymbol{u}_{\mathrm{s}}^n$ in (2.56) yields

$$\frac{\rho_{\mathrm{s}}}{2}\partial_\tau\|\boldsymbol{u}_{\mathrm{s}}^n\|_{0,\Omega^{\mathrm{s}}}^2 + \frac{\rho_{\mathrm{s}}}{2\tau}\|\boldsymbol{u}_{\mathrm{s}}^n - \boldsymbol{u}_{\mathrm{s}}^{n-1}\|_{0,\Omega^{\mathrm{s}}}^2 + \frac{1}{2}\partial_\tau\|\boldsymbol{y}_{\mathrm{s}}^n\|_{\mathrm{s}}^2 + \frac{1}{2\tau}\|\boldsymbol{y}_{\mathrm{s}}^n - \boldsymbol{y}_{\mathrm{s}}^{n-1}\|_{\mathrm{s}}^2 = -\langle \mathcal{R}_\mu(\widetilde{\boldsymbol{u}}_{\mathrm{f}}^n), \mathcal{L}_h \boldsymbol{u}_{\mathrm{s}}^n\rangle - \langle \mathcal{R}_p(p^n, \boldsymbol{u}_{\mathrm{f}}^n), \mathcal{L}_h \boldsymbol{u}_{\mathrm{s}}^n\rangle. \quad (2.62)$$

As a result, by adding the equalities (2.60)-(2.62) we get

$$\begin{aligned}&\frac{\rho_{\mathrm{f}}}{2}\partial_\tau\|\boldsymbol{u}_{\mathrm{f}}^n\|_{0,\Omega^{\mathrm{f}}}^2 + 2\mu\|\boldsymbol{\varepsilon}(\widetilde{\boldsymbol{u}}_{\mathrm{f}}^n)\|_{0,\Omega^{\mathrm{f}}}^2 + \frac{\rho_{\mathrm{s}}}{2}\partial_\tau\|\boldsymbol{u}_{\mathrm{s}}^n\|_{0,\Omega^{\mathrm{s}}}^2 + \frac{1}{2}\partial_\tau\|\boldsymbol{y}_{\mathrm{s}}^n\|_{\mathrm{s}}^2 \\ &+\frac{\rho_{\mathrm{s}}}{2\tau}\|\boldsymbol{u}_{\mathrm{s}}^n - \boldsymbol{u}_{\mathrm{s}}^{n-1}\|_{0,\Omega^{\mathrm{s}}}^2 + \underbrace{(\boldsymbol{\nabla} p^n, \boldsymbol{u}_{\mathrm{f}}^n)_{\Omega^{\mathrm{f}}} - (p^n, \boldsymbol{u}_{\mathrm{s}}^n \cdot \boldsymbol{n}_{\mathrm{f}})_\Sigma}_{T_1} - \underbrace{\langle \mathcal{R}_\mu(\widetilde{\boldsymbol{u}}_{\mathrm{f}}^n), \mathcal{L}(\boldsymbol{u}_{\mathrm{s}}^n - \boldsymbol{u}_{\mathrm{s}}^{n-1})\rangle}_{T_2} \leq 0.\end{aligned} \quad (2.63)$$

Following the argument used in [ACF09]-Appendix A, from (2.54) we infer that

$$\widetilde{\boldsymbol{u}}_{\mathrm{f}}^n = \boldsymbol{u}_{\mathrm{f}}^n + \Pi_h^\perp\left(\widetilde{\boldsymbol{u}}_{\mathrm{f}}^n - \mathcal{L}_h \boldsymbol{u}_{\mathrm{s}}^n\right) + \frac{\tau}{\rho_{\mathrm{f}}}\Pi_h\left(\boldsymbol{\nabla} p^n\right). \quad (2.64)$$

Thereafter, taking $q = p^n$ in (2.54), integrating by parts in its right-hand side, and since $P_l^n = p^n|_{\Gamma_l}$, we have

$$\frac{\tau}{\rho_{\mathrm{f}}}\|\boldsymbol{\nabla} p^n\|_{0,\Omega^{\mathrm{f}}}^2 + \sum_{l=1}^{n_{0\mathrm{D}}}\frac{P_l^n - \alpha_l \pi_l^{n-1}}{\gamma_l}P_l^n - (\widetilde{\boldsymbol{u}}_{\mathrm{f}}^n, \boldsymbol{\nabla} p^n)_{\Omega^{\mathrm{f}}} + (p^n, \boldsymbol{u}_{\mathrm{s}}^n \cdot \boldsymbol{n}_{\mathrm{f}})_\Sigma = 0.$$

Now, by inserting (2.64) into this expression and using (2.39), we get

$$\begin{aligned}T_1 =& \frac{\tau}{\rho_{\mathrm{f}}}\left\|\Pi_h^\perp(\boldsymbol{\nabla} p^n)\right\|_{0,\Omega^{\mathrm{f}}}^2 + \sum_{l=1}^{n_{0\mathrm{D}}}\frac{P_l^n - \alpha_l \pi_l^{n-1}}{\gamma_l}P_l^n - \left(\Pi_h^\perp\left(\widetilde{\boldsymbol{u}}_{\mathrm{f}}^n - \mathcal{L}_h \boldsymbol{u}_{\mathrm{s}}^n\right), \boldsymbol{\nabla} p^n\right)_{\Omega^{\mathrm{f}}} \\ \geq& \frac{\tau}{\rho_{\mathrm{f}}}\left\|\Pi_h^\perp(\boldsymbol{\nabla} p^n)\right\|_{0,\Omega^{\mathrm{f}}}^2 + \frac{C_{d,l}}{2}\partial_\tau|\pi_l^n|^2 + \frac{1}{R_{\mathrm{d},l}}|\pi_l^n|^2 + R_{\mathrm{p},l}|Q_l^n|^2 \\ &- \underbrace{\left(\Pi_h^\perp\left(\widetilde{\boldsymbol{u}}_{\mathrm{f}}^n - \mathcal{L}_h \boldsymbol{u}_{\mathrm{s}}^n\right), \boldsymbol{\nabla} p^n\right)_{\Omega^{\mathrm{f}}}}_{T_3}.\end{aligned}$$

Therefore, by applying this lower bound to (2.63) we get

$$\frac{\rho_{\mathrm{f}}}{2}\partial_\tau\|\boldsymbol{u}_{\mathrm{f}}^n\|_{0,\Omega^{\mathrm{f}}}^2+\frac{\rho_{\mathrm{f}}}{2\tau}\left\|\widetilde{\boldsymbol{u}}_{\mathrm{f}}^n-\boldsymbol{u}_{\mathrm{f}}^{n-1}\right\|_{0,\Omega^{\mathrm{f}}}^2+2\mu\|\boldsymbol{\varepsilon}(\widetilde{\boldsymbol{u}}_{\mathrm{f}}^n)\|_{0,\Omega^{\mathrm{f}}}^2+\frac{\rho_{\mathrm{s}}}{2}\partial_\tau\|\boldsymbol{u}_{\mathrm{s}}^n\|_{0,\Omega^{\mathrm{s}}}^2+\frac{1}{2}\partial_\tau\|\boldsymbol{y}_{\mathrm{s}}^n\|_{\mathrm{s}}^2$$
$$+\frac{\rho_{\mathrm{s}}}{2\tau}\left\|\boldsymbol{u}_{\mathrm{s}}^n-\boldsymbol{u}_{\mathrm{s}}^{n-1}\right\|_{0,\Omega^{\mathrm{s}}}^2+\frac{\tau}{\rho_{\mathrm{f}}}\left\|\Pi_h^{\perp}(\boldsymbol{\nabla}p^n)\right\|_{0,\Omega^{\mathrm{f}}}^2+\frac{C_{d,l}}{2}\partial_\tau|\pi_l^n|^2+\frac{1}{R_{\mathrm{d},l}}|\pi_l^n|^2+R_{\mathrm{p},l}|Q_l^n|^2$$
$$\leq T_2+T_3. \quad (2.65)$$

Term T_2 can be bounded as in [FGG07], using (2.51), which yields

$$\begin{aligned}T_2\leq&\frac{\rho_{\mathrm{f}}}{\tau}\|\widetilde{\boldsymbol{u}}_{\mathrm{f}}^n-\boldsymbol{u}_{\mathrm{f}}^{n-1}\|_{0,\Omega^{\mathrm{f}}}\|\mathcal{L}_h(\boldsymbol{u}_{\mathrm{s}}^n-\boldsymbol{u}_{\mathrm{s}}^{n-1})\|_{0,\Omega^{\mathrm{f}}}+2\mu\|\boldsymbol{\varepsilon}(\widetilde{\boldsymbol{u}}_{\mathrm{f}}^n)\|_{0,\Omega^{\mathrm{f}}}\|\boldsymbol{\varepsilon}(\mathcal{L}_h(\boldsymbol{u}_{\mathrm{s}}^n-\boldsymbol{u}_{\mathrm{s}}^{n-1}))\|_{0,\Omega^{\mathrm{f}}}\\
\leq&\varepsilon_1\frac{\rho_{\mathrm{f}}}{2\tau}\|\widetilde{\boldsymbol{u}}_{\mathrm{f}}^n-\boldsymbol{u}_{\mathrm{f}}^{n-1}\|_{0,\Omega^{\mathrm{f}}}^2+\varepsilon_2\mu\|\boldsymbol{\varepsilon}(\widetilde{\boldsymbol{u}}_{\mathrm{f}}^n)\|_{0,\Omega^{\mathrm{f}}}^2\\
&+C_{\mathrm{L}}\left(\frac{\rho_{\mathrm{f}}}{2\tau\varepsilon_1}h^{1-\alpha}+\frac{\mu}{\varepsilon_2}h^{-1-\alpha}\right)\|\boldsymbol{u}_{\mathrm{s}}^n-\boldsymbol{u}_{\mathrm{s}}^{n-1}\|_{0,\Omega^{\mathrm{s}}}^2.\end{aligned} \quad (2.66)$$

Term T_3 can be bounded following the argument used in [ACF09], which yields

$$\begin{aligned}T_3=&\left(\Pi_h^{\perp}\left(\mathcal{L}_h(\boldsymbol{u}_{\mathrm{s}}^{n-1}-\boldsymbol{u}_{\mathrm{s}}^n)\right),\Pi_h^{\perp}(\boldsymbol{\nabla}p^n)\right)_{\Omega^{\mathrm{f}}}\\
\leq&\varepsilon_3\frac{\tau}{2\rho_{\mathrm{f}}}\|\Pi_h^{\perp}(\boldsymbol{\nabla}p^n)\|_{0,\Omega^{\mathrm{f}}}^2+\frac{\rho_{\mathrm{f}}}{2\tau\varepsilon_3}C_{\mathrm{L}}h^{1-\alpha}\|\boldsymbol{u}_{\mathrm{s}}^n-\boldsymbol{u}_{\mathrm{s}}^{n-1}\|_{0,\Omega^{\mathrm{s}}}^2.\end{aligned} \quad (2.67)$$

Hence, by inserting (2.66)-(2.67) into (2.65) we get the energy estimate

$$\frac{\rho_{\mathrm{f}}}{2}\partial_\tau\|\boldsymbol{u}_{\mathrm{f}}^n\|_{0,\Omega^{\mathrm{f}}}^2+\frac{\rho_{\mathrm{f}}}{2\tau}(1-\varepsilon_1)\left\|\widetilde{\boldsymbol{u}}_{\mathrm{f}}^n-\boldsymbol{u}_{\mathrm{f}}^{n-1}\right\|_{0,\Omega^{\mathrm{f}}}^2+\mu(2-\varepsilon_2)\|\boldsymbol{\varepsilon}(\widetilde{\boldsymbol{u}}_{\mathrm{f}}^n)\|_{0,\Omega^{\mathrm{f}}}^2+\frac{\rho_{\mathrm{s}}}{2}\partial_\tau\|\boldsymbol{u}_{\mathrm{s}}^n\|_{0,\Omega^{\mathrm{s}}}^2$$
$$+\frac{1}{2}\partial_\tau\|\boldsymbol{y}_{\mathrm{s}}^n\|_{\mathrm{s}}^2+\left[\frac{\rho_{\mathrm{s}}}{2\tau}-C_{\mathrm{L}}\frac{\rho_{\mathrm{f}}}{2\tau}h^{1-\alpha}\left(\frac{1}{\varepsilon_1}+\frac{1}{\varepsilon_3}\right)-C_{\mathrm{L}}\frac{\mu}{\varepsilon_2}h^{-1-\alpha}\right]\left\|\boldsymbol{u}_{\mathrm{s}}^n-\boldsymbol{u}_{\mathrm{s}}^{n-1}\right\|_{0,\Omega^{\mathrm{s}}}^2$$
$$+\frac{\tau}{\rho_{\mathrm{f}}}\left(1-\frac{\varepsilon_3}{2}\right)\left\|\Pi_h^{\perp}(\boldsymbol{\nabla}p^n)\right\|_{0,\Omega^{\mathrm{f}}}^2+\sum_{l=1}^{n_{0\mathrm{D}}}\left(\frac{C_{d,l}}{2}\partial_\tau|\pi_l^n|^2+\frac{1}{R_{\mathrm{d},l}}|\pi_l^n|^2+R_{\mathrm{p},l}|Q_l^n|^2\right)\leq 0.$$

At last, the energy estimate (2.59) follows by taking in the latter $\varepsilon_1=\frac{1}{2}$, $\varepsilon_2=\varepsilon_3=1$, summing over n and using (2.58), which completes the proof. ∎

Proposition 3 guarantees the conditional stability of Algorithm 3. Note that the stability condition is similar to the one obtained in [FGG07] with a Darcy-like formulation of the projection step. The estimate (2.59) corresponds to the discrete counterpart of (2.50), the right-hand side of (2.59) is a dissipative numerical term related to the natural pressure stabilization of the projection scheme. Moreover, up to our experience in the field of computational hemodynamics, the simulations in physiological regimes with the semi-implicit FSI coupling [FGG07] do not suffer of stability problems, which suggests that condition (2.58) is generally fulfilled.

2.3.1.3 Semi-implicit FSI coupling scheme with explicit 3D-0D coupling scheme

We now consider numerical approximations of the coupled problem FSI-0D system (2.48)-(2.49) and (2.2)-(2.3) by combining the projection semi-implicit coupling scheme reported in [FGG07] with the 3D-0D explicit coupling of Section 2.2.1. The resulting fully discrete time-marching procedure is reported in Algorithm 4.

Algorithm 4 Semi-implicit FSI coupling scheme with explicit 3D-0D coupling

Let $\boldsymbol{u}_{\mathrm{f}}^0 = \boldsymbol{u}_{\mathrm{f}}(0)$, $\pi_1^0, \dots, \pi_{n_{0\mathrm{D}}}^0 \in \mathbb{R}$ and $\boldsymbol{y}_{\mathrm{s}}^0, \boldsymbol{u}_{\mathrm{s}}^0 \in \boldsymbol{W}_h$ be given initial data. For $n \geq 1$ perform:

1. Viscous step: Find $\widetilde{\boldsymbol{u}}_{\mathrm{f}}^n \in \boldsymbol{V}_h$ such that

$$\begin{cases} \widetilde{\boldsymbol{u}}_{\mathrm{f}}^n|_{\Sigma} = \boldsymbol{u}_{\mathrm{s}}^{n-1}|_{\Sigma}, \\ \widetilde{\boldsymbol{u}}_{\mathrm{f}}^n|_{\Gamma^{\mathrm{in}}} = \boldsymbol{u}_{\mathrm{in}}(t_n), \\ \dfrac{\rho_{\mathrm{f}}}{\tau}\left(\widetilde{\boldsymbol{u}}_{\mathrm{f}}^n, \boldsymbol{v}\right)_{\Omega^{\mathrm{f}}} + 2\mu\left(\boldsymbol{\varepsilon}(\widetilde{\boldsymbol{u}}_{\mathrm{f}}^n), \boldsymbol{\varepsilon}(\boldsymbol{v})\right)_{\Omega^{\mathrm{f}}} = \dfrac{\rho_{\mathrm{f}}}{\tau}\left(\boldsymbol{u}_{\mathrm{f}}^{n-1}, \boldsymbol{v}\right)_{\Omega^{\mathrm{f}}} \end{cases} \tag{2.68}$$

   for all $\boldsymbol{v} \in \boldsymbol{V}_{\Sigma\cup\Gamma^{\mathrm{in}},h}$. Thereafter set $\widetilde{Q}_l^n \overset{\mathrm{def}}{=} \int_{\Gamma_l} \widetilde{\boldsymbol{u}}_{\mathrm{f}}^n \cdot \boldsymbol{n}_{\mathrm{f}}$.

2. Windkessel step: For $l = 1, \dots, n_{0\mathrm{D}}$, compute $(Q_l^n, \pi_l^n, P_l^n) \in \mathbb{R}^3$ from

$$\begin{cases} Q_l^n = \widetilde{Q}_l^n, \\ C_{d,l}\partial_\tau \pi_l^n + \dfrac{\pi_l^n}{R_{\mathrm{d},l}} = Q_l^n, \\ P_l^n = R_{\mathrm{p},l} Q_l^n + \pi_l^n. \end{cases} \tag{2.69}$$

3. Implicit projection-solid step: Find $(p^n, \boldsymbol{u}_{\mathrm{f}}^n, \boldsymbol{y}_{\mathrm{s}}^n) \in N_h \times \boldsymbol{V}_h \times \boldsymbol{W}_h$ with $\boldsymbol{u}_{\mathrm{s}}^n = \partial_\tau \boldsymbol{y}_{\mathrm{s}}^n$ and such that

$$\begin{cases} p^n|_{\Gamma_l} = P_l^n, \quad l = 1, \dots, n_{0\mathrm{D}}, \\ \dfrac{\tau}{\rho_{\mathrm{f}}}\left(\boldsymbol{\nabla} p^n, \boldsymbol{\nabla} q\right)_{\Omega^{\mathrm{f}}} = -\left(\boldsymbol{\nabla}\cdot\widetilde{\boldsymbol{u}}_{\mathrm{f}}^n, q\right)_{\Omega^{\mathrm{f}}} - \left((\boldsymbol{u}_{\mathrm{s}}^n - \widetilde{\boldsymbol{u}}_{\mathrm{f}}^n)\cdot\boldsymbol{n}_{\mathrm{f}}, q\right)_{\Sigma} \end{cases} \tag{2.70}$$

$$\begin{cases} \boldsymbol{u}_{\mathrm{f}}^n|_{\Gamma^{\mathrm{in}}} = \boldsymbol{u}_{\mathrm{in}}(t_n), \\ \boldsymbol{u}_{\mathrm{f}}^n|_{\Sigma} = \boldsymbol{u}_{\mathrm{s}}^n|_{\Sigma}, \\ \dfrac{\rho_{\mathrm{f}}}{\tau}\left(\boldsymbol{u}_{\mathrm{f}}^n, \boldsymbol{v}\right)_{\Omega^{\mathrm{f}}} = \dfrac{\rho_{\mathrm{f}}}{\tau}\left(\widetilde{\boldsymbol{u}}_{\mathrm{f}}^n, \boldsymbol{v}\right)_{\Omega^{\mathrm{f}}} - \left(\boldsymbol{\nabla} p^n, \boldsymbol{v}\right)_{\Omega^{\mathrm{f}}}, \end{cases} \tag{2.71}$$

$$\rho_{\mathrm{s}}\left(\partial_\tau \boldsymbol{u}_{\mathrm{s}}^n, \boldsymbol{v}_{\mathrm{s}}\right)_{\Omega^{\mathrm{s}}} + a_{\mathrm{s}}(\boldsymbol{y}_{\mathrm{s}}^n, \boldsymbol{v}_{\mathrm{s}}) = -\left\langle \mathcal{R}_\mu(\widetilde{\boldsymbol{u}}_{\mathrm{f}}^n), \mathcal{L}_h \boldsymbol{v}_{\mathrm{s}}\right\rangle - \left\langle \mathcal{R}_p(\boldsymbol{u}_{\mathrm{f}}^n, p^n), \mathcal{L}_h \boldsymbol{v}_{\mathrm{s}}\right\rangle \tag{2.72}$$

   for all $(q, \boldsymbol{v}, \boldsymbol{v}_{\mathrm{s}}) \in N_{\Gamma^{\mathrm{out}},h} \times \boldsymbol{V}_{\Sigma\cup\Gamma^{\mathrm{in}},h} \times \boldsymbol{W}_h$.

The following proposition provides an energy estimate for the approximations provided by Algorithm 4.

Proposition 4
Let $\left\{(\widetilde{\boldsymbol{u}}_{\mathrm{f}}^n, p^n, \boldsymbol{y}_{\mathrm{s}}^n, \boldsymbol{u}_{\mathrm{s}}^n)\right\}_{n\geq 1}$ *and* $\left\{(Q_l^n, \pi_l^n, P_l^n)_{1\leq l\leq n_{0\mathrm{D}}}\right\}_{n\geq 1}$ *be the approximated solution given by Algorithm 4 and assume that* $\boldsymbol{u}_{\mathrm{in}} = \boldsymbol{0}$ *(free system). Then, under the condition (2.58), the following energy inequality holds*

$$E^n + D^n \lesssim E^0 - \sum_{m=1}^{n-1} \frac{\tau^2}{2\rho_{\mathrm{f}}} \left\| \Pi_h^{\perp}(\boldsymbol{\nabla} p^m) \right\|_{0,\Omega^{\mathrm{f}}}^2 + \sum_{m=1}^{n-1} \tau \left(\boldsymbol{\nabla}\cdot\widetilde{\boldsymbol{u}}_{\mathrm{f}}^m, \phi^m\right)_{\Omega^{\mathrm{f}}} + \sum_{m=1}^{n-1} \frac{\tau^2}{\rho_{\mathrm{f}}} \left(\boldsymbol{\nabla} p^m, \boldsymbol{\nabla}\phi^m\right)_{\Omega^{\mathrm{f}}} + \sum_{m=1}^{n-1} \tau \left(\boldsymbol{u}_{\mathrm{s}}^m \cdot \boldsymbol{n}_{\mathrm{f}}, \phi^m\right)_{\Sigma}. \quad (2.73)$$

Proof. The result follows by combining the arguments involved in the proofs of Propositions 1 and 3. Hence, only partial details are given. The main difference lies on the estimation of term T_1 in (2.63). Since $q \in N_{\Gamma^{\mathrm{out}},h}$, integration by parts in (2.70) gives

$$\left(\boldsymbol{\nabla} p^n, \boldsymbol{\nabla} q\right)_{\Omega^{\mathrm{f}}} = \frac{\rho_{\mathrm{f}}}{\tau}\left(\widetilde{\boldsymbol{u}}_{\mathrm{f}}^n, \boldsymbol{\nabla} q\right)_{\Omega^{\mathrm{f}}} - \left(\boldsymbol{u}_{\mathrm{s}}^n \cdot \boldsymbol{n}_{\mathrm{f}}, q\right)_{\Sigma},$$

so that by testing with $q = (p^n - \phi^n) \in N_{\Gamma^{\mathrm{out}},h}$ we get

$$\frac{\tau}{\rho_{\mathrm{f}}}\|\boldsymbol{\nabla} p^n\|_{0,\Omega^{\mathrm{f}}}^2 - \left(\widetilde{\boldsymbol{u}}_{\mathrm{f}}^n, \boldsymbol{\nabla} p^n\right)_{\Omega^{\mathrm{f}}} + \left(\boldsymbol{u}_{\mathrm{s}}^n \cdot \boldsymbol{n}_{\mathrm{f}}, p^n\right)_{\Sigma} + \left(\widetilde{\boldsymbol{u}}_{\mathrm{f}}^n - \frac{\tau}{\rho_{\mathrm{f}}}\boldsymbol{\nabla} p^n, \boldsymbol{\nabla}\phi^n\right)_{\Omega^{\mathrm{f}}} - \left(\boldsymbol{u}_{\mathrm{s}}^n \cdot \boldsymbol{n}_{\mathrm{f}}, \phi^n\right)_{\Sigma} = 0. \quad (2.74)$$

As in the proof of Proposition 3, from (2.71) we get (2.64). Hence, inserting this expression into (2.74) we get

$$\begin{aligned} -\left(\boldsymbol{\nabla} p^n, \boldsymbol{u}_{\mathrm{f}}^n\right)_{\Omega^{\mathrm{f}}} + \left(p^n, \boldsymbol{u}_{\mathrm{s}}^n \cdot \boldsymbol{n}_{\mathrm{f}}\right)_{\Sigma} + \frac{\tau}{\rho_{\mathrm{f}}}\left\|\Pi_h^{\perp}(\boldsymbol{\nabla} p^n)\right\|_{0,\Omega^{\mathrm{f}}}^2 - \left(\Pi_h^{\perp}\left(\widetilde{\boldsymbol{u}}_{\mathrm{f}}^n - \mathcal{L}_h \boldsymbol{u}_{\mathrm{s}}^n\right), \boldsymbol{\nabla} p^n\right)_{\Omega^{\mathrm{f}}} \\ = -\left(\widetilde{\boldsymbol{u}}_{\mathrm{f}}^n - \frac{\tau}{\rho_{\mathrm{f}}}\boldsymbol{\nabla} p^n, \boldsymbol{\nabla}\phi^n\right)_{\Omega^{\mathrm{f}}} + \left(\boldsymbol{u}_{\mathrm{s}}^n \cdot \boldsymbol{n}_{\mathrm{f}}, \phi^n\right)_{\Sigma} \\ - \sum_{l=1}^{n_{0\mathrm{D}}} Q_l^n P_l^n + \left(\boldsymbol{\nabla}\cdot\widetilde{\boldsymbol{u}}_{\mathrm{f}}^n, \phi^n\right)_{\Omega^{\mathrm{f}}} + \frac{\tau}{\rho_{\mathrm{f}}}\left(\boldsymbol{\nabla} p^n, \boldsymbol{\nabla}\phi^n\right)_{\Omega^{\mathrm{f}}} + \left(\boldsymbol{u}_{\mathrm{s}}^n \cdot \boldsymbol{n}_{\mathrm{f}}, \phi^n\right)_{\Sigma} \quad (2.75) \end{aligned}$$

and the estimate (2.73) follows using the same arguments than in the proof of Proposition 3. ∎

Remark 8
A comparison of the energy estimates (2.17) and (2.73) suggests that the fluid-solid interaction introduces and additional destabilizing effect in the explicit splitting of the 3D-0D coupling (2.13), due to the presence of the artificial interface term

$$\sum_{m=1}^{n-1} \tau \left(\boldsymbol{u}_{\mathrm{s}}^m \cdot \boldsymbol{n}_{\mathrm{f}}, \phi^m\right)_{\Sigma}.$$

In particular, it is worth noting that the observation made in Remark 3 for the

case of a single outlet is not valid in the FSI framework, since the above term does not vanish for $\phi^m = P^m$ in Ω^{f}. This point will be illustrated trough numerical experiments in Section 2.4

2.4 Numerical experiments

In this section we deal with two numerical examples. The first one corresponds to a patient-specific aorta, when considering only the Navier-Stokes equations. In the second example we will show the stability issues in the FSI case on a academic, but realistic, idealized Abdominal Aortic Aneurism (AAA).

2.4.1 A patient-specific aorta

Our first example (Navier-Stokes only) consists of a patient-specific aorta with repaired coarctation (Figure 2.3). The geometry comes from the **euHeart** database (www.euheart.eu). A segment growing registration algorithm [BOFH07, BSV+12] was used for the segmentation of the geometry from the medical image. The resulting surface was pre-processed with 3-matic (Materialise, Leuven, Belgium) and the final mesh was produced with Gmsh [GR09].

The inflow curve used as boundary condition (Figure 2.5, right, black line) was obtained from the same patient with Phase Contrast MRI. The initial constant pressure was set as 62650 bary, and the Windkessel parameters (see Table 2.1) where calibrated in order to have approximately the measured pressure at the coarctation and the measured flow at every outlet. The physical parameters of the fluid are $\mu = 0.035\,\mathrm{Po}$ and $\rho_{\mathrm{f}} = 1\,\mathrm{gr/cm^3}$. For the numerical simulation, we use $\mathbb{P}_1$ finite elements for both pressure and velocity fields (with a SUPG stabilization for the viscous step) and a time step $\tau = 10^{-3}\,\mathrm{s}$. A snapshot of the simulation results is shown in Figure 2.4).

The spurious oscillations in the approximation provided by the explicit 3D-0D coupling scheme are clearly visible, while the implicit formulation guarantees stability within the whole cardiac cycle. Hence, these results are in agreement with the stability estimates provided by Theorems 1 and 2. As further validation of the numerical scheme, Figure 2.7 shows the pressures and flows curves computed using a monolithic solver, implicitely coupled with the 0D-model, showing a satisfactory agreement of the results.

	Outlet 1	Outlet 2	Outlet 3	Outlet 4
R_p $(\mathrm{dyn}\cdot\mathrm{s}\cdot\mathrm{cm}^{-5})$	250	683	615	94
R_d $(\mathrm{dyn}\cdot\mathrm{s}\cdot\mathrm{cm}^{-5})$	10^4	$1.296\cdot 10^4$	$1.1664\cdot 10^4$	$0.1794\cdot 10^4$
C $(\mathrm{cm}^5\cdot\mathrm{dyn}^{-1})$	$4\cdot 10^{-4}$	$2\cdot 10^{-4}$	$2\cdot 10^{-4}$	$14\cdot 10^{-4}$

Table 2.1: Parameters for the Windkessel's model. The outlets are ordered in direction of the flow.

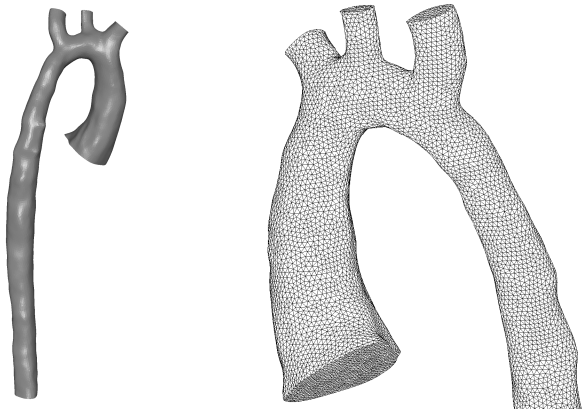

Figure 2.3: Patient-specific aorta. Left: geometry. Right: surface mesh.

2.4.2 FSI in an idealized AAA

We consider an idealized abdominal aortic aneurysm (AAA) shown in Figure 2.8, of length 22.95 cm, minimal diameter 1.7 cm (tubular part), maximal diameter 4.98 cm (aneurysm) and wall thickness 0.2 cm. The solid has Young's modulus $1\,MPa$, Poisson ratio is 0.46 and density $1.2\,g/cm^3$. The fluid viscosity is $\mu = 0.035\,Po$ and its density $1\,g/cm^3$.

The boundary conditions are set as follows. The inlet and the outlet parts of the solid are clamped. In the fluid, a parabolic velocity profile is enforced at the inlet, with a realistic inflow (peak velocity $\approx 96\,cm/s$). The Windkessel parameters are $R_p = 700\,\mathrm{dyn}\cdot\mathrm{s}\cdot\mathrm{cm}^{-5}$, $R_d = 5\cdot 10^3\,\mathrm{dyn}\cdot\mathrm{s}\cdot\mathrm{cm}^{-5}$ and $C = 2\cdot 10^{-4}\,\mathrm{cm}^5\cdot\mathrm{dyn}^{-1}$.

At $t = 0$, the pressure is constant and equal to 80 $mmHg$, whereas all the other state variables are zero. During the whole simulation, the stress received by the structure is corrected by the initial one. Doing so, the solid only responds to the difference with the diastolic phase. In this way, the load applied to the structure is kept reasonable small so that the linearity assumptions holds.

The results are summarized in Figure 2.9, showing the Windkessel pressures P for a time step of $\tau = 0.001\,s$. Note that the semi-implicit algorithm with explicit 0D-3D coupling (Algorithm 4) is unstable whereas the semi-implicit scheme (Algorithm 3) remains always stable. In fact, from the results one can infer that the interface term outlined in Remark 8, namely $(\boldsymbol{u}_\mathrm{s}^n, P^n\boldsymbol{n}_\mathrm{f})_\Sigma$, injects a positive artificial power into the system (an augmentation of the pressure $P^n > 0$ leads in this case to $\boldsymbol{u}_\mathrm{s}^n \cdot \boldsymbol{n}_\mathrm{f} > 0$).

2.5 Conclusions

In this Chapter we discussed in detail different formulations for the 3D-0D coupling of the Navier-Stokes Equations and Windkessel models, when the former are solved with a projection method. In particular, through an energy based stabil-

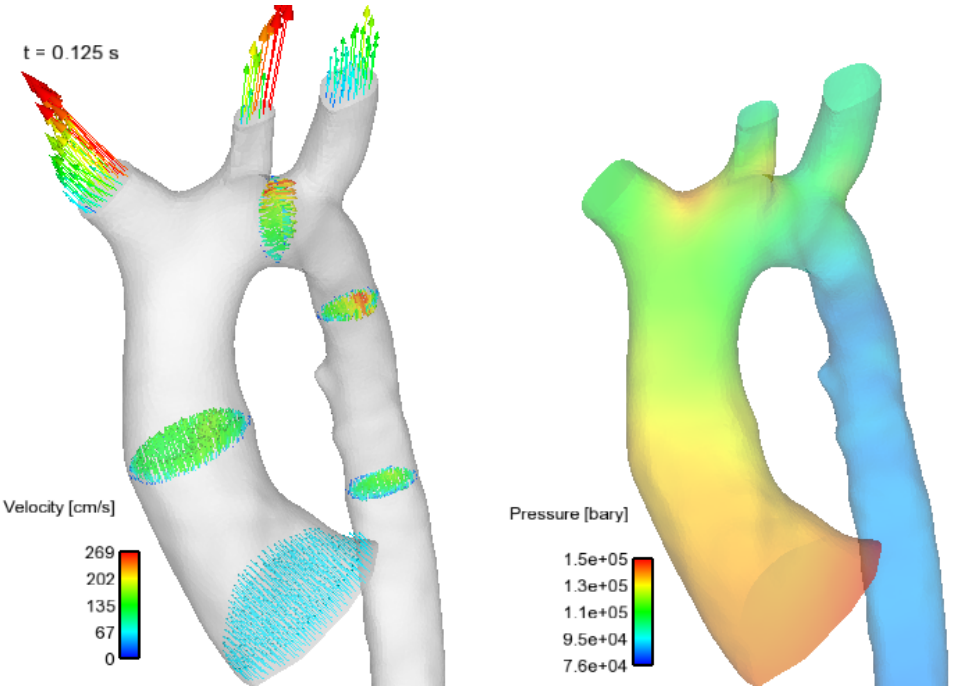

Figure 2.4: Simulation results for the aorta for peak systole. Left: velocity field for few cutting planes. Right: pressure distribution.

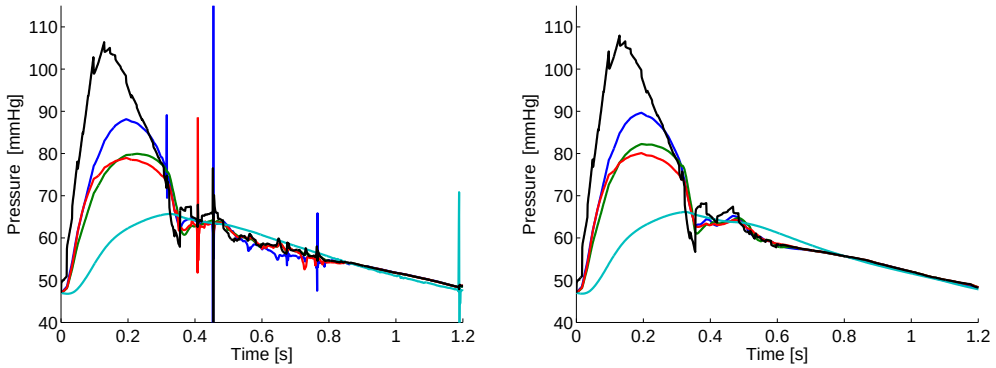

Figure 2.5: Mean pressures at inlet (black) and outlets 1 to 4 (blue, green, red, cyan). Explicit (left) and semi-implicit (right) schemes.

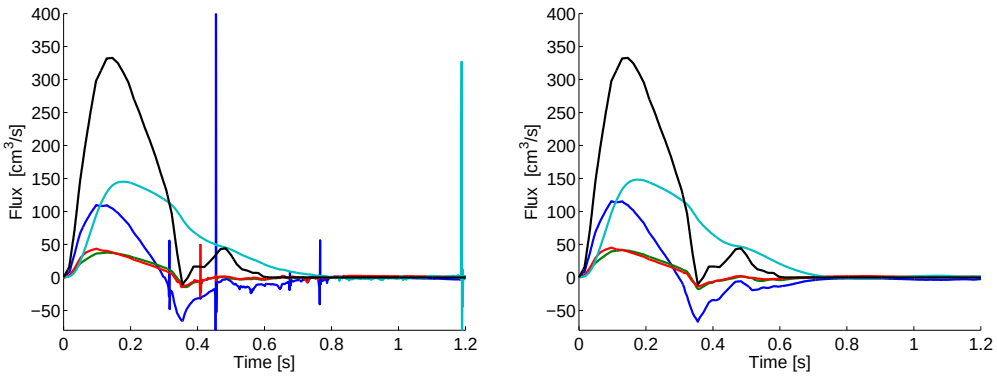

Figure 2.6: Fluxes for inlet (black) and outlets 1 to 4 (blue, green, red, cyan). Explicit (left) and semi-implicit (right) schemes.

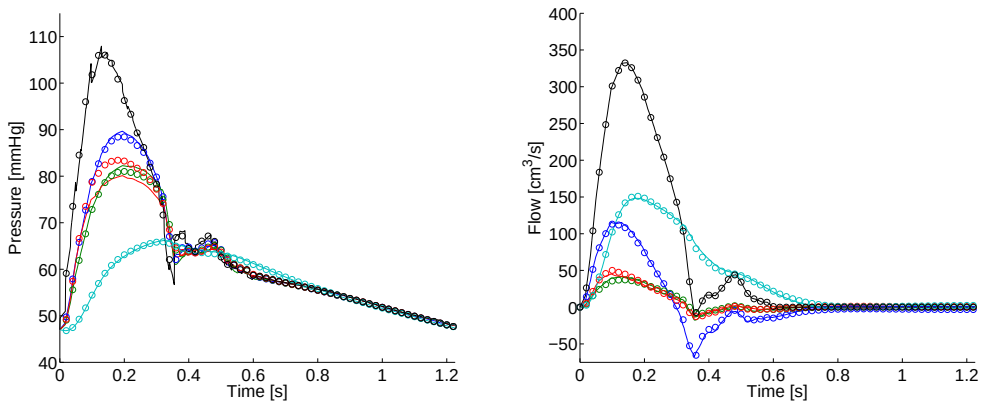

Figure 2.7: Pressures (left) and fluxes (right) for inlet (black) and outlets 1–4 (blue, green, red, cyan) obtained with a monolithic method (circles) and with the projection method (continuos) using an implicit 3D-0D coupling.

ity analysis we showed that the explicit coupling approaches are only conditionally stable in presence of multiple outlets. This results extends also to the case of fluid-structure interaction.

To fix these issues, we proposed a semi-implicit coupling scheme that, with a negligible additional computational cost (one additional degree of freedom for each outlet), yields unconditional stability. The theoretical findings have been confirmed through numerical experiments of practical interest, including fluid-structure interaction simulations.

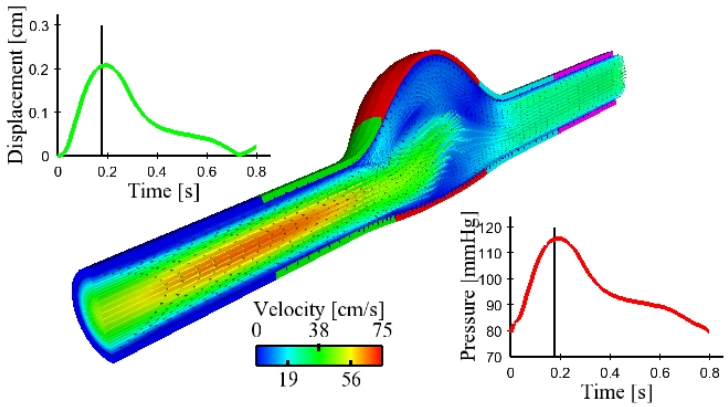

Figure 2.8: Snapshot of the velocity field inside the idealized AAA. The curves show outlet pressure and displacements of the aneurysm wall.

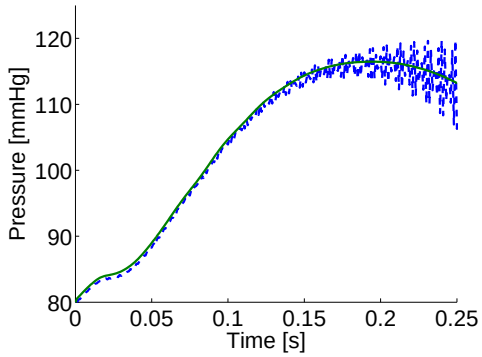

Figure 2.9: Windkessel pressure for the AAA: comparison between semi-implicit (solid line) and explicit (dashed line) fluid-Windkessel coupling.

Part II

Data assimilation in fluid-structure interaction

God, give us grace to accept with serenity the things that cannot be changed,
courage to change the things which should be changed
and the wisdom to distinguish the one from the other.
Reinhold Niebuhr.

Chapter 3

Nonlinear Kalman filtering in FSI

We present a robust and computationally efficient parameter estimation strategy for fluid-structure interaction problems. The method is based on a filtering algorithm, known as the reduced order Unscented Kalman Filter [MC11b]. It does not require any adjoint or tangent problems. In addition, it can easily be run in parallel, which is of great interest in fluid-structure problems where the computational cost of the forward simulation is already a challenge in itself. We illustrate our methodology with the estimation of the artery wall stiffness from the wall displacement measurements – as they could be extracted from medical imaging – in a three-dimensional idealized abdominal aortic aneurysm. We also show preliminary results about the estimation of the proximal Windkessel resistance, which is an important parameter for setting appropriate fluid boundary conditions.

The results presented in this chapter lead to the article:
C. Bertoglio, P. Moireau, J.-F. Gerbeau. **Sequential parameter estimation in fluid-structure problems. Application to hemodynamics**. Int. J. Num. Meth. Biomed. Engng., Volume 28, Issue 4, pages 434–455, 2012.

Contents

3.1 The linear Kalman Filter

In this section we derive the equations for the linear Kalman filter. We start with the (static) least-squares estimation of a vector based on partial measurements and an initial guess, and then we treat the estimation of the state of a discrete dynamical system where a set of measurements in time is available. We will deal with both deterministic (useful for the analogy with variational methods) and probabilistic approaches, which allows to extend these techniques to nonlinear problems.

3.1.1 Static linear case: least squares estimation

Let start with the task that, for a unknown vector $X \in \mathbb{R}^N$, we want to find an estimator $\hat{X}$ assuming that a "guess" $\hat{X}^-$ is available, for example provided by a model, associated with a confidence matrix $(P^-)^{-1}$. Assume also that partial observations Z of X are available, and we write their relation by $Z = HX + \zeta^Z$. Since ζ^Z is unknown, we also associate a confidence matrix W^{-1} with the observations.

A quantity accounting for $\hat{X}^-$ and Z, with their respective levels of confidence, can simply be obtained by minimizing the quadratic cost function:

$$J(\hat{X}) = \frac{1}{2}(\hat{X} - \hat{X}^-)^\intercal (P^-)^{-1}(\hat{X} - \hat{X}^-) + \frac{1}{2}(Z - H\hat{X})^\intercal W^{-1}(Z - H\hat{X}).$$

i.e., find $\hat{X}$ such that

$$\frac{dJ}{d\hat{X}} = -H^\intercal W^{-1} Z + H^\intercal W^{-1} H\hat{X} - (P^-)^{-1}\hat{X}^- + (P^-)^{-1}\hat{X} \equiv 0 \ . \tag{3.1}$$

Thus, the value $\hat{X}^+$ that forces (3.1) to be zero can be obtained as

$$\begin{aligned}
\left((P^-)^{-1} + H^\intercal W^{-1} H\right)\hat{X}^+ &= (P^-)^{-1}\hat{X}^- + H^\intercal W^{-1} Z \\
\left((P^-)^{-1} + H^\intercal W^{-1} H\right)\hat{X}^+ &= \left((P^-)^{-1} + H^\intercal W^{-1} H\right)\hat{X}^- + H^\intercal W^{-1}(Z - H\hat{X}^-) \\
\hat{X}^+ &= \hat{X}^- + K\left(Z - H\hat{X}^-\right) \ ,
\end{aligned} \tag{3.2}$$

where

$$K = P^+ H^\intercal W^{-1} \tag{3.3}$$

is the Kalman matrix and

$$P^+ = \left((P^-)^{-1} + H^\intercal W^{-1} H\right)^{-1} . \tag{3.4}$$

Applying the Woodbury's matrix inversion lemma to P^+, the Kalman matrix can

also be written as

$$\begin{aligned} K &= \left(P^- - P^- H^\intercal \left(W + HP^- H^\intercal\right)^{-1} HP^-\right) H^\intercal W^{-1} \\ &= P^- H^\intercal \left(W^{-1} - \left(W + HP^- H^\intercal\right)^{-1} HP^- H^\intercal W^{-1}\right) \\ &= P^- H^\intercal \left(W + HP^- H^\intercal\right)^{-1} \left(\left(W + HP^- H^\intercal\right) W^{-1} - HP^- H^\intercal W^{-1}\right) \\ &= P^{XZ} \left(P^Z\right)^{-1} \ , \end{aligned} \tag{3.5}$$

with

$$P^{XZ} = P^- H^\intercal \quad \text{and} \quad P^Z = W + HP^- H^\intercal \ . \tag{3.6}$$

3.1.2 Statistical approach to linear least squares

The result presented above can be also obtained with statistical arguments considering the unknown state X as a random variable. Assume that $\hat{X}^- = \mathbb{E}(X)$ and that the error on the guess has a covariance matrix $P^- = \mathbb{E}((X - \hat{X}^-)(X - \hat{X}^-)^\intercal)$ (which is the inverse of the above "confidence matrix"). We also consider ζ^Z as a random variable with zero-mean and covariance W.

Assume that $\hat{X}^+$ corresponds to a combination of $\hat{X}^-$ and Z in the form $\hat{X}^+ = L\hat{X}^- + KZ$, such that the error $\widetilde{X}^+ = X - \hat{X}^+$ can be written as

$$\widetilde{X}^+ = X - L\hat{X}^- - KZ = (I - KH)X - L\hat{X}^- - K\zeta^Z \ .$$

Hence, to have an unbiased estimator, i.e., $\mathbb{E}(\widetilde{X}^+) = 0$, we have to choose $L = I - KH$ since, by hypothesis, $\mathbb{E}(\zeta^Z) = 0$ and $\mathbb{E}(\hat{X}^-) = \mathbb{E}(X)$. Then, the a posteriori estimation can be expressed in the Kalman form $\hat{X}^+ = \hat{X}^- + K\left(Z - H\hat{X}^-\right)$ as in the deterministic case. Note that unbiased property of this estimator does not depend on the choice of the matrix K. In particular, we interested in a matrix K such that

$$K = \operatorname{argmin} \operatorname{tr}(P^+) = \operatorname{argmin} \operatorname{tr}(\mathbb{E}(\widetilde{X}^+(\widetilde{X}^+)^\intercal)) \ .$$

where P^+ corresponds to the *a posteriori* covariance of the estimator $\hat{X}^+$.

To obtain now the optimal K we proceed as follows. Defining $\widetilde{X}^- = X - \hat{X}^-$, we can rewrite the expression for $\widetilde{X}^+(\widetilde{X}^+)^\intercal$ as

$$\begin{aligned} \widetilde{X}^+(\widetilde{X}^+)^\intercal &= ((I - KH)\widetilde{X}^- - K\zeta^Z)(\dots)^\intercal \\ &= (I - KH)\widetilde{X}^-(\widetilde{X}^-)^\intercal(I - KH)^\intercal + K\zeta^Z(\zeta^Z)^\intercal K^\intercal \\ &\cdots - (I - KH)\widetilde{X}^-(\zeta^Z)^\intercal K^\intercal - K\zeta^Z(\widetilde{X}^-)^\intercal(I - KH)^\intercal \ . \end{aligned} \tag{3.7}$$

Then, taking the expected value of (3.7) we obtain

$$P^+ = \mathbb{E}(\widetilde{X}^+(\widetilde{X}^+)^\intercal) = (I - KH)P^-(I - KH)^\intercal + KWK^\intercal \tag{3.8}$$

since, by hypothesis, the cross terms are statistically independent. Hence, by using

the identity

$$\frac{\partial \mathrm{tr}(ABA^\intercal)}{\partial A} = 2AB \ , \tag{3.9}$$

the optimality criterion reads

$$\frac{\partial \mathrm{tr}(P^+)}{\partial K} = -(I - KH)P^- H^\intercal + KW \equiv 0 \ , \tag{3.10}$$

leading to the optimal Kalman matrix

$$K = P^- H^\intercal (HP^- H^\intercal + W)^{-1} \ , \tag{3.11}$$

what corresponds exactly to the same expression as in (3.5).

Moreover, we can verify that P^Z corresponds to the covariance of the innovation $\Gamma = Z - H\hat{X}^- = H\widetilde{X}^- + \zeta^Z$. It is clear that $\mathbb{E}(\Gamma) = 0$ and therefore

$$\begin{aligned} \mathrm{Cov}(\Gamma) &= \mathbb{E}\left((H\widetilde{X}^- + \zeta^Z)(H\widetilde{X}^- + \zeta^Z)^\intercal\right) \\ &= HP^- H^\intercal + W = P^Z \ , \end{aligned}$$

since, again, cross terms are statistically independent. Analogously, P^{XZ} can be obtained by

$$\begin{aligned} \mathrm{Cov}(\hat{X}^-, \Gamma) &= \mathbb{E}\left((\hat{X}^- - \mathbb{E}(\hat{X}^-))(H\widetilde{X}^- + \zeta^Z)^\intercal\right) \\ &= \mathbb{E}\left(\left(\hat{X}^- - \mathbb{E}(\hat{X}^-)\right)(\widetilde{X}^-)^\intercal H^\intercal\right) \\ &= \mathbb{E}\left((\widetilde{X}^-)(\widetilde{X}^-)^\intercal\right) H^\intercal = P^- H^\intercal = P^{XZ} \ . \end{aligned}$$

Note also that combining expressions (3.8) and (3.11) by

$$\begin{aligned} P^+ = (I - P^{XZ}\left(P^Z\right)^{-1} H)P^-(I - P^{XZ}\left(P^Z\right)^{-1} H)^\intercal \\ \cdots + P^{XZ}\left(P^Z\right)^{-1} W(P^{XZ}\left(P^Z\right)^{-1})^\intercal \end{aligned} \tag{3.12}$$

and multiplying out it we directly obtain (3.4).

In fact, the statistical interpretation of these matrices is the key in the extension of the Kalman filter to non-linear problems. We will come back to this issue in Section 3.2.1.

3.1.3 Dynamic linear case: the Kalman filter

Now assume that the state variable satisfies a linear dynamics, without any model uncertainties:

$$\dot{X} = AX + F,$$

and with an initial guess $X(0) = \hat{X}_0 + \zeta^X$ ($\hat{X}_0$ being given and ζ^X unknown). After time discretization, the dynamics reads:

$$X_n = A_n X_{n-1} + F_n. \tag{3.13}$$

Suppose that the following observations at each time step are available:

$$Z_n = H_n X_n + \zeta_n^Z, \tag{3.14}$$

where ζ_{n-1}^Z includes the measurement noise and the discretization error.

The *linear Kalman filter* [KB61] can simply be presented as follows. Assume that $\hat{X}_{n-1}^+$ is known with a covariance P_{n-1}^+. First, the model is used to compute a *prediction*:

$$\hat{X}_n^- = A_n \hat{X}_{n-1}^+ + F_n, \tag{3.15}$$

By linearity of A_n, the covariance $P_n^- = \mathbb{E}((X_n - \hat{X}_n^-)(X_n - \hat{X}_n^-)^\intercal)$ is given by

$$P_n^- = A_n P_{n-1}^+ A_n^\intercal. \tag{3.16}$$

Then, repeating *mutatis mutandis* the least squares argument of the case without dynamics, a *correction* taking into account the observation is given by:

$$\hat{X}_n^+ = \hat{X}_n^- + K_n(Z_n - H_n \hat{X}_n^-). \tag{3.17}$$

with

$$K_n = P_n^{XZ}(P_n^Z)^{-1} \tag{3.18}$$

where $P_n^{XZ} = P_n^- H_n^\intercal$ and $P_n^Z = W_n + H_n P_n^- H_n^\intercal$. As in the static case, the covariance associated with $\hat{X}_n^+$ is given by

$$P_n^+ = P_n^- - P_n^{XZ}\left(P_n^Z\right)^{-1}\left(P_n^{XZ}\right)^\intercal. \tag{3.19}$$

Thus, we can iterate and perform the prediction step at the new time step n.

Analogy with variational approach. It can be proved that these estimations of the state and covariances can also be obtained by minimizing the functional

$$J(\zeta^X) = \frac{1}{2}\|\zeta\|^2_{(P_0^-)^{-1}} + \frac{1}{2}\sum_{k=0}^{n}\|Z_k - HX_k\|^2_{W_k^{-1}} \tag{3.20}$$

under the constraint (3.13). In other words, the Kalman filter estimator $\hat{X}_n^+$ is equal to $X_n(\bar{\zeta}^X)$, where $\bar{\zeta}^X$ is the minimizer of the variational problem on $[0, t^n]$. For a detailed proof we refer, for example, to [Moi08].

3.2 The reduced-order Unscented Kalman filter

The aim of this section is to present a comprehensive derivation of the reduced-order Unscented Kalman Filter used later for the parameter estimation in our fluid-structure problems. As first, we present the *Extended Kalman Filter* (EKF), based on the linearization of the non-linear operators, where we sketch the approximation order of both estimated mean and covariances. This motivates the application of the so-called *unscented transforms* for improving the approximation order of the EKF (and also to avoid the computation of tangent operators), what is the base Unscented Kalman Filter (UKF) algorithm. We end the section with the derivation of the factorized form of the UKF which allows to treat problems where the uncertainties are concentrated on a reduced number of quantities, as estimating the physical parameters of a dynamical system when the initial condition is known.

3.2.1 Extensions to nonlinear cases

The Kalman filter presented above is only valid when the dynamics and the observation operator are linear. To address the fluid-structure problems considered in this work, it is necessary to extend the algorithm to nonlinear cases.

The most straightforward extension consists of applying steps (3.16), (3.18) and (3.19) with the tangent operators $A'_n \overset{\text{def}}{=} A'_n(\hat{X}^+_{n-1})$ and $H'_n \overset{\text{def}}{=} H'_n(\hat{X}^-_n)$, and steps (3.15) and (3.17) with the nonlinear operators $A_n(\cdot)$ and $H_n(\cdot)$:

$$\begin{cases} \hat{X}^-_n = A_n(\hat{X}^+_{n-1}) \\ P^-_n = A'_n P^+_{n-1} (A')^\intercal \\ P^{XZ}_n = P^-_n (H')^\intercal \ , \ P^Z_n = W_n + H' P^-_n (H'_n)^\intercal \\ \hat{X}^+_n = \hat{X}^-_n + K_n(Z_n - H_n(\hat{X}^-_n)) \ , \ K_n = P^{XZ}_n (P^Z_n)^{-1} \\ P^+_n = P^-_n - P^{XZ}_n \left(P^Z_n\right)^{-1} \left(P^{XZ}_n\right)^\intercal \end{cases} \tag{3.21}$$

But the resulting algorithm, called *Extended Kalman Filter* (EKF), has two drawbacks: the computation of the tangent operators and the precision of the estimated values.

To understand the latter issue, it is interesting to consider how the mean value of a random variable is transported by a nonlinear operator $\mathcal{A}$. Let X denote a random variable in $\mathbb{R}^N$, its mean value $\hat{X} = \mathbb{E}(X)$ and its covariance $\mathcal{P} = \mathbb{E}((X - \hat{X})(X - \hat{X})^\intercal)$. A Taylor expansion around $\hat{X}$ gives:

$$Y \overset{\text{def}}{=} \mathcal{A}(X) = \mathcal{A}(\hat{X}) + \mathcal{A}'(\hat{X}) \cdot (X - \hat{X}) + \frac{1}{2}(X - \hat{X})^\intercal \cdot \mathcal{A}''(\hat{X}) \cdot (X - \hat{X}) + \mathcal{O}(|X - \hat{X}|^3)$$

Hence, the propagated mean is given by

$$\mathbb{E}(Y) = \mathcal{A}(\hat{X}) + \frac{1}{2}\mathcal{A}''(\hat{X}) : \mathcal{P} + \mathcal{O}(\mathbb{E}(|X - \hat{X}|^3)) \ , \tag{3.22}$$

and the propagated covariance by

$$\mathbb{E}\left((Y-\mathbb{E}(Y))\,(Y-\mathbb{E}(Y)^{\mathsf{T}}\right) = \mathcal{A}'(\hat{X})\,\mathcal{P}\left(\mathcal{A}'(\hat{X})\right)^{\mathsf{T}} + \mathcal{O}(\mathbb{E}(|X-\hat{X}|^3)) \ . \tag{3.23}$$

We see in (3.22) that the simple propagation of the mean value by the nonlinear operator is only locally second order accurate (the term $\mathcal{A}''(\hat{X}) : \mathcal{P}$ being second order in $|X-\hat{X}|$). This will be improved with the technique presented in Section 3.2.2.

Another way to approximate means and covariances consists of choosing a set of vectors $X^{(i)}$, $1 \leq i \leq r$, called *particles*, which are propagated with the operator $\mathcal{A}(\cdot)$, i.e.,

$$Y^{(i)} = \mathcal{A}(X^{(i)}) \quad , \ 1 \leq i \leq r \ .$$

Then, the mean and covariances are obtained by computing the empirical statistics of the propagated particles $Y^{(i)}$. Of course, to be effective, the particles have to be carefully chosen. In this work, we use this type of mean and covariance approximations in the context of the *Unscented Kalman Filter* [JUDW95, JUDW00], which is based on deterministic particles. It will be briefly presented in the next section.

The UKF filter presents a lot of similarities with the *Ensemble Kalman Filter* [Eve09] which also uses a moderate number of particles – even if this number is often a larger than for UKF – to compute empirical statistics. Moreover nonlinear particle filters consider a random generation of the particles $X^{(i)}$ according to a given probability density function. These filters usually involve a very large number of particles, which yields a very large number of solutions of the forward problem. We refer for example to [Sim09].

3.2.2 Unscented transforms and application to Kalman filtering

The *Unscented Kalman Filter* (UKF) algorithm is based on the *unscented transformation*. Its principle is to approximate the nonlinear propagation of the mean and the covariance of a random vector *via* the propagation of well-chosen deterministic particles.

The basic idea can easily be explained in one dimension. Let X be a random variable in $\mathbb{R}$ (so $N=1$), let $\hat{X}$ denote its mean value $\mathbb{E}(X)$ and $\sigma = \sqrt{\mathrm{Var}(X)}$ its standard deviation. Two particles are defined: $\hat{X}^{(1)} = \hat{X} + \sigma$, $\hat{X}^{(2)} = \hat{X} - \sigma$. These particles are constructed by adding to the known state $\hat{X}$ two values σ and $-\sigma$ called *sigma-points*. The empirical mean value of the particles, namely $(\hat{X}^{(1)} + \hat{X}^{(2)})/2$, is by construction equals to the mean value $\hat{X}$. In order to evaluate the empirical mean value of the particles propagated by the nonlinear operator, let us consider the Taylor expansions:

$$\mathcal{A}(\hat{X}^{(1)}) = \mathcal{A}(\hat{X}) + \sigma\mathcal{A}'(\hat{X}) + \frac{\sigma^2}{2}\mathcal{A}''(\hat{X}) + \mathcal{O}(|\hat{X}^{(1)}-\hat{X}|^3) \ ,$$

$$\mathcal{A}(\hat{X}^{(2)}) = \mathcal{A}(\hat{X}) - \sigma\mathcal{A}'(\hat{X}) + \frac{\sigma^2}{2}\mathcal{A}''(\hat{X}) + \mathcal{O}(|X^{(2)}-\hat{X}|^3) \ .$$

The empirical mean is by construction

$$\hat{Y} \overset{\text{def}}{=} \frac{1}{2}\left(\mathcal{A}(X^{(1)}) + \mathcal{A}(X^{(2)})\right) = \mathcal{A}(\hat{X}) + \frac{\sigma^2}{2}\mathcal{A}''(\hat{X}) + \mathcal{O}(|\hat{X}^{(1)} - \hat{X}|^3) + \mathcal{O}(|\hat{X}^{(2)} - \hat{X}|^3). \tag{3.24}$$

Thus, we see that the empirical mean of the propagated particle is an approximation of $\mathbb{E}(\mathcal{A}(X))$ better than $\mathcal{A}(\hat{X})$ since it includes by construction the second order term $\sigma^2\mathcal{A}''(\hat{X})/2$ (see (3.22) with $\mathcal{P} = \sigma^2 I$). Note that the covariance are approximated with the same order of accuracy in the two methods.

This idea can be generalized in N-dimensions by defining appropriate sigma-points and their respective weights – see [MC11b] for a comprehensive review. The natural generalization of the one-dimensional standard deviation is the square root of the covariance matrix. Its computation, for example by a Cholesky factorization, is the most expensive part of the UKF algorithm, but usually negligible compared to the propagation step for the problems considered in this work.

The empirical mean and covariance are defined by:

$$\bar{X} \overset{\text{def}}{=} E_\alpha\left(X^{(*)}\right) \overset{\text{def}}{=} \sum_{1\le i\le r} \alpha_i X^{(i)}, \mathrm{Cov}_\alpha\left(X^{(*)}, Z^{(*)}\right) \overset{\text{def}}{=} \sum_{1\le i\le r} \alpha_i (X^{(i)} - \bar{X})(Z^{(i)} - \bar{Z})^\intercal, \tag{3.25}$$

where the weights $\alpha_i \in \mathbb{R}^+$ are given and depend on the choice of the sigma-points. In the present work, we use the ones proposed in [Jul03], only based on $r = N + 1$ particles (see later in Section 3.2.4).

It remains to explain how to use the unscented transformation in the filtering algorithm. The idea is to replace the formulae (3.6) used in the original Kalman algorithm by the evaluations of the empirical covariance and mean value of the particles. More precisely, P^{XZ} is replaced by $\mathrm{Cov}_\alpha(Y^{(*)}, Z^{(*)})$, with $Y^{(i)} = \mathcal{A}(X^{(i)})$ and $Z^{(i)} = H(Y^{(i)})$, and P^Z is replaced by $W + \mathrm{Cov}_\alpha(Z^{(*)}, Z^{(*)})$.

To summarize, here is the UKF algorithm. Assume that the sigma-points $I^{(i)}$, $1 \le i \le r$, are given, as well as $\hat{X}_0^+$ and P_0^+. For $n > 0$, we have a 3 steps recursive algorithm:

- **Sampling.** Generation of the particles:

$$\begin{cases} C_{n-1} = \sqrt{P_{n-1}^+} & \text{(Cholesky factorization)} \\ \hat{X}_{n-1}^{(i)+} = \hat{X}_{n-1}^+ + C_n^\intercal I^{(i)}, \quad 1 \le i \le r \end{cases} \tag{3.26}$$

- **Prediction.** Resolution of one time step of the model for each particle (can naturally be done in parallel) and computation of the empirical mean value and covariance:

$$\begin{cases} \hat{X}_n^{(i)-} = A_n(\hat{X}_{n-1}^{(i)+}) \quad , \ 1 \le i \le r \\ \hat{X}_n^- = E_\alpha(\hat{X}_n^{(*)-}) \\ P_n^- = \mathrm{Cov}_\alpha(\hat{X}_n^{(*)-}, \hat{X}_n^{(*)-}) \end{cases} \tag{3.27}$$

- **Correction.**

$$\begin{cases} Z_n^{(i)} = H(\hat{X}_n^{(i)-}) \quad , \ 1 \leq i \leq r \\ P_n^Z = \mathrm{Cov}_\alpha(Z_n^{(*)}, Z_n^{(*)}) + W_n \\ P_n^{XZ} = \mathrm{Cov}_\alpha(\hat{X}_n^{(*)-}, \hat{Z}_n^{(*)-}) \\ K_n = P_n^{XZ}(P_n^Z)^{-1} \\ \hat{X}_n^+ = \hat{X}_n^- + K_n(Z_n - E_\alpha(Z_n^{(*)})) \\ P_n^+ = P_n^- - P_n^{XZ}\left(P_n^Z\right)^{-1}\left(P_n^{XZ}\right)^\intercal \end{cases} \tag{3.28}$$

3.2.3 Factorized formulation of the UKF

In this section, we show how the construction of P_n^+, P_n^{XZ} and P_n^Z is modified when the covariance matrix P_n^- can be factorized in the form $LU^{-1}L^\intercal$, with $L \in \mathcal{M}_{N,p}$ and $U \in \mathcal{M}_{p,p}$. This will be useful to derive the reduced-order UKF algorithm in the next section.

We consider a family of sigma-points $I^{(i)} \in \mathbb{R}^p$, $i = 1 \dots r$. It is proved in [MC11b, Sect. 2.2.1] that the empirical covariance of the particles $X^{(i)}$ and $Z^{(i)}$ (see (3.25)) can be expressed as

$$\mathrm{Cov}_\alpha(X^{(*)}, Z^{(*)}) = [X^{(*)}]D_\alpha[I^{(*)}]^\intercal \left([I^{(*)}]D_\alpha[I^{(*)}]^\intercal\right)^{-1}[I^{(*)}]D_\alpha[Z^{(*)}]^\intercal \tag{3.29}$$

where $[X^{(*)}] \in \mathcal{M}_{N,r}$ is the matrix whose column i corresponds to the particle $X^{(i)}$, $1 \leq i \leq r$ (analogously for $[I^{(*)}]$ and $[Z^{(*)}]$), and where $D_\alpha \overset{\text{def}}{=} \mathrm{diag}\,[\alpha_i] \in \mathcal{M}_{r,r}$ is the diagonal matrix containing the weights of formulae (3.25).

The covariance matrix P_n^- is by definition $\mathrm{Cov}_\alpha(\hat{X}_n^{(*)-}, \hat{X}_n^{(*)-})$. Thus, defining

$$L_n^X \overset{\text{def}}{=} [\hat{X}_n^{(*)-}]D_\alpha[I^{(*)}]^\intercal \text{ and } \ P_\alpha \overset{\text{def}}{=} [I^{(*)}]D_\alpha[I^{(*)}]^\intercal \tag{3.30}$$

we can rewrite P_n^- according to (3.29) as

$$P_n^- = L_n^X P_\alpha^{-1}(L_n^X)^\intercal. \tag{3.31}$$

Similarly, applying again (3.29) to P_n^Z and P_n^{XZ} (see their definition in (3.28)):

$$P_n^Z = W_n + L_n^Z P_\alpha^{-1}(L_n^Z)^\intercal \ , \ P_n^{XZ} = L_n^X P_\alpha^{-1}(L_n^Z)^\intercal, \tag{3.32}$$

with

$$L_n^Z \overset{\text{def}}{=} [Z_n^{(*)}]D_\alpha[I^{(*)}]^\intercal. \tag{3.33}$$

Thus, the *a posteriori* covariance P_n^+ can be written as:

$$\begin{aligned} P_n^+ &= P_n^- - P_n^{XZ}\left(P_n^Z\right)^{-1}\left(P_n^{XZ}\right)^\intercal \\ &= L_n^X\left(P_\alpha^{-1} - P_\alpha^{-1}\left(L_n^Z\right)^\intercal\left(W_n + L_n^Z P_\alpha^{-1}\left(L_n^Z\right)^\intercal\right)^{-1} L_n^Z P_\alpha^{-1}\right)\left(L_n^X\right)^\intercal \\ &= L_n^X U_n^{-1}\left(L_n^X\right)^\intercal \ , \end{aligned} \tag{3.34}$$

where U_n is defined, applying the Woodbury inversion lemma, by

$$U_n \stackrel{\text{def}}{=} P_\alpha + \left(L_n^Z\right)^\intercal W_n^{-1} L_n^Z. \tag{3.35}$$

Next, applying again the Woodbury inversion lemma to P_n^Z, we obtain:

$$\left(P_n^Z\right)^{-1} = W_n^{-1} - W_n^{-1} L_n^Z U_n^{-1} \left(L_n^Z\right)^\intercal W_n^{-1} \ . \tag{3.36}$$

Thus, we deduce the factorized form of the Kalman-like matrix $K_n = P_n^{XZ}(P_n^Z)^{-1}$:

$$\begin{aligned} K_n &= \left(L_n^X P_\alpha^{-1} \left(L_n^Z\right)^\intercal\right) \left(W_n^{-1} - W_n^{-1} L_n^Z U_n^{-1} \left(L_n^Z\right)^\intercal W_n^{-1}\right) \\ &= L_n^X U_n^{-1} \left(L_n^Z\right)^\intercal W_n^{-1} \ . \end{aligned} \tag{3.37}$$

The key point here is to be able to perform operations with P_n^+ and K_n using only L_n^X, L_n^Z and P_α, and not directly P_n^-. This property proves to be extremely useful when the rank of P_n^- is much smaller than the size of X, as will be shown in the next section.

Remark 9
According to (3.3), $K = P^+ H^\intercal W^{-1}$. Thus, using the expression (3.34) of P^+, we obtain $K = L^X U^{-1} \left(L^X\right)^\intercal H^\intercal W^{-1}$. By comparison with (3.37), we see that L^Z formally corresponds to HL^X, the "observed state sensitivity". The Matrix $L^X(L^\theta)^{-1}$ corresponds to the sensitivity of the state X with respect to the parameters θ. The factorization formula (3.29) is instrumental in identifying these analogies. We refer to [MC11b] for more details.

3.2.4 Reduced-order UKF for parameter estimation

State and parameter estimation. In principle, the UKF algorithm can easily be generalized to those cases when the uncertainties also affect the parameters. To do so, we consider an *augmented state* $\mathcal{X} = (X, \theta)$ whose size is $N + p$. At $t = 0$, $\mathcal{X}(0) = \mathcal{X}_0 + \zeta^{\mathcal{X}} = (X_0, \theta_0) + (\zeta^X, \zeta^\theta)$. The extended dynamical system reads:

$$\mathcal{X}_n \stackrel{\text{def}}{=} (X_n, \theta_n) = \mathcal{A}_n(\mathcal{X}_{n-1}) \ , \tag{3.38}$$

with the initial condition $\mathcal{X}_0 = (X_0, \theta_0)$. When the parameters θ are constant in time, $\mathcal{A}_n$ is simply defined by $\mathcal{A}_n(\mathcal{X}_{n-1}) = (A_n(X_{n-1}, \theta_n), \theta_n)$. Then, even with a small number of parameters, classical Kalman-like filter cannot be applied to this augmented state because of the initial state size. However, if we assume that the uncertainties only affect the part θ of vector $\mathcal{X}$, we will show in the next paragraph how to use a reduced order filter formulation which limits the computation of the filter operator to a subspace of small dimension – here the parameter space – and therefore can be computed.

Reduced order UKF. We now have all the material to present the reduced-order UKF algorithm that is used in this paper to estimate some parameters of a fluid-structure interaction system.

As explained above, any Kalman-like algorithm can be used to estimate the state and the parameter by simply considering an augmented dynamical system in the variable $\mathcal{X} = (X, \theta)$. Nevertheless, as already mentioned, this approach is intractable with large system as those considered here. To circumvent this difficulty, the choice made in this study is to assume that the uncertainty is limited to the p parameters θ. Thus, the covariance matrix has a rank p and we can take advantage from the factorized formulation of Section 3.2.3.

Suppose that we do not have any uncertainties in the initial condition of the state, i.e., $\zeta^X = 0$. Then the initial covariance can be factorized:

$$P_0^+ = \begin{bmatrix} 0 & 0 \\ 0 & \mathrm{Cov}(\zeta^\theta) \end{bmatrix} = \begin{bmatrix} L_0^X \\ L_0^\theta \end{bmatrix} U_0^{-1} \begin{bmatrix} (L_0^X)^\intercal & (L_0^\theta)^\intercal \end{bmatrix} ,$$

where $U_0 \overset{\text{def}}{=} \left(\mathrm{Cov}(\zeta^\theta)\right)^{-1}$ is a (small) $p \times p$ matrix, $L_0^X \overset{\text{def}}{=} 0$, $L_0^\theta \overset{\text{def}}{=} \mathbb{1}$. Hence, and this is a key point, we only need $p+1$ sigma-points in $\mathbb{R}^p$ for the sampling step in the UKF algorithm:

$$\begin{cases} C_0 = \sqrt{U_0^{-1}} & \text{(Cholesky factorization)} \\ \hat{X}_0^{(i)+} = \hat{X}_0^+ + L_0^X C_0^\intercal I^{(i)} = \hat{X}_0^+, \quad 1 \le i \le p+1 \\ \hat{\theta}_0^{(i)+} = \hat{\theta}_0^+ + L_0^\theta C_0^\intercal I^{(i)}, \quad 1 \le i \le p+1 \ . \end{cases}$$

Reduced order estimation algorithm. Consider the simplex sigma-points $I^{(i)}, 1 \le i \le p+1$, their weights collected in the matrix $D_\alpha \overset{\text{def}}{=} \mathrm{diag}\,[\alpha_i] \in \mathcal{M}_{p+1,p+1}$. Then, for given values of $\hat{X}_0$, $\hat{\theta}_0$ and $\mathrm{Cov}(\zeta^\theta)$, perform

- **Initialization:** initialize the sensitivities as

$$L_0^\theta = \mathbb{1}, \quad L_0^X = 0, \quad U_0 = \mathrm{Cov}(\zeta_\theta)^{-1} \tag{3.39a}$$

- **Sampling:** generate the particles by

$$\begin{cases} C_{n-1} = \sqrt{U_{n-1}^{-1}} & \text{(Cholesky factorization)} \\ \hat{X}_{n-1}^{(i)+} = \hat{X}_{n-1}^+ + L_{n-1}^X C_{n-1}^\intercal I^{(i)}, \quad 1 \le i \le p+1 \\ \hat{\theta}_{n-1}^{(i)+} = \hat{\theta}_{n-1}^+ + L_{n-1}^\theta C_{n-1}^\intercal I^{(i)}, \quad 1 \le i \le p+1 \end{cases} \tag{3.39b}$$

- **Prediction:** propagate the particles with the dynamical system

$$\begin{cases} (\hat{X}_n^{(i)-}, \hat{\theta}_n^{(i)-}) = A_n(\hat{X}_{n-1}^{(i)+}, \hat{\theta}_{n-1}^{(i)+}) \\ \hat{X}_n^- = E_\alpha(\hat{X}_n^{(*)-}) \\ \hat{\theta}_n^- = E_\alpha(\hat{\theta}_n^{(*)-}) \end{cases} \tag{3.39c}$$

- **Correction:** use the innovation $\Gamma_n^{(i)} = Z_n - H(\hat{X}_n^{(i)-})$ $(1 \leq i \leq p+1)$ to correct the predicted state and parameters

$$\begin{cases} L_n^X = [\hat{X}_n^{(*)-}] D_\alpha [I^{(*)}]^\intercal \in \mathcal{M}_{N,p} \\ L_n^\theta = [\hat{\theta}_n^{(*)-}] D_\alpha [I^{(*)}]^\intercal \in \mathcal{M}_p \\ L_n^\Gamma = [\Gamma_n^{(*)}] D_\alpha [I^{(*)}]^\intercal \\ U_n = P_\alpha + (L_n^\Gamma)^\intercal W_n^{-1} L_n^\Gamma \in \mathcal{M}_p \\ \hat{X}_n^+ = \hat{X}_n^- - L_n^X U_n^{-1} \left(L_n^\Gamma\right)^\intercal W_n^{-1} E_\alpha(\Gamma_n^{(*)}) \\ \hat{\theta}_n^+ = \hat{\theta}_n^- - L_n^\theta U_n^{-1} \left(L_n^\Gamma\right)^\intercal W_n^{-1} E_\alpha(\Gamma_n^{(*)}) \end{cases} \tag{3.39d}$$

  and note that we use $L_n^\Gamma = -L_n^Z$ instead of L_n^Z as in the previous sections.

Choice of sigma points. In this work we used the so-called *simplex* sigma-points $I^{(i)}$, $r = p+1$, that correspond to vectors of zero mean and $\sqrt{p}$ covariance in $\mathbb{R}^p$. Together with the weights α_i, they are computed recursively as (see [PVG98, HPB02])

$$[I_1^*] = \left(-\frac{1}{\sqrt{2\alpha}} \ , \ \frac{1}{\sqrt{2\alpha}} \right) \ , \ \alpha = \frac{1}{p+1} = \alpha_i \ \forall i \ ,$$

and

$$[I_d^*] = \begin{bmatrix} & & & 0 \\ & [I_{d-1}^*] & & \vdots \\ & & & 0 \\ \dfrac{1}{\sqrt{\alpha d(d+1)}} & \cdots & \dfrac{1}{\sqrt{\alpha d(d+1)}} & \dfrac{-d}{\sqrt{\alpha d(d+1)}} \end{bmatrix} \ , \ 2 \leq d \leq p \ .$$

Remark 10

We have implicitly used some specific properties of the simplex sigma-points in the derivation of the algorithm as fully described in [MC11b]. For more general sigma-points, the algorithm is more intricate. We refer to [MC11b] and in particular its erratum [MC11a].

3.3 Reduced Order filtering for FSI problems

In this section, we deal with some specific issues of the application of the RO-UKF presented above for fluid-structure problems, with emphasis in hemodynamics. We present now some considerations when combining the nonlinear filtering when the dynamic operator A_n corresponds to the semi-implicit approach presented in Chapter 2, but now considering a non-linear fluid and a Newmark scheme for the structure. Note also the that pressure-solid coupling conditions are simplified with respect to Algorithm 3, which however has a negligible influence on the numerical results. The numerical scheme is detailed in Algorithm 5 with all notations following Chapter 2. In this thesis, a partitioned matrix free Newton method [GV03] is used to solve the interface equation resulting from the coupling between (3.42) and (3.43).

3.3.1 Algorithmic aspects of FSI filtering

Implementation. Beside its efficiency, a very appealing feature of the proposed approach is the simplicity of its implementation. In algorithm (3.39a)-(3.39d), steps (3.39a), (3.39b) and (3.39d) are totally independent of the forward problem and can be implemented in an external software. Since this part is generic, it is very simple to change the number and the kind of parameters that are used in the filter. Step (3.39c) corresponds to one time step of the dynamical system with a given initial condition. It therefore only requires to be able to "restart" the solvers from any state.

Particle initialization. Let us give some more details about the "restart" of the fluid-structure algorithm, since this is an important aspect of the estimation procedure. First, we define the discrete state of the FSI-system as $X_{n-1} \overset{\text{def}}{=} (\widetilde{\boldsymbol{u}}_{\mathrm{f}}^n, \boldsymbol{y}_{\mathrm{f}}^n, \pi_l^n, \ldots, \pi_{n_{0\mathrm{D}}}^n, \boldsymbol{y}_{\mathrm{s}}^n, \boldsymbol{u}_{\mathrm{s}}^n, \mathbf{a}_{\mathrm{s}}^n)$. However, after the ROUKF performs the correction of the state X_{n-1}, for the propagation of the particles X_{n-1} at the next time step we need the corrected pressure p^{n-1} for the viscous step in Algorithm 5, as well as the mid-step velocity $\boldsymbol{u}_{\mathrm{s}}^{n-3/2}$ for the Dirichlet conditions for the velocity. We propose then to perform the following computations prior to step 1 in Algorithm (5) in order to reconstruct these quantities from the particle X_{n-1}:

- In the solid recover $\boldsymbol{u}_{\mathrm{s}}^{n-3/2} = \boldsymbol{u}_{\mathrm{s}}^{n-1} - \frac{\tau}{2}\mathbf{a}_{\mathrm{s}}^{n-1}$.
- In the fluid:
  - Reconstruct $\Omega_{\mathrm{f}}^{n-1} = (\boldsymbol{I}_{\Omega_{\mathrm{f}}^0} + \boldsymbol{y}_{\mathrm{f}}^{n-1})(\Omega_{\mathrm{f}}^0)$.

Algorithm 5 Fully semi-implicit FSI/3D-0D scheme in ALE formulation.

Let $\widetilde{\boldsymbol{u}}_{\mathrm{f}}^0 = \boldsymbol{u}_{\mathrm{f}}^0$, $\pi_1^0, \dots, \pi_{n_{0\mathrm{D}}}^0 \in \mathbb{R}$ and $\boldsymbol{y}_{\mathrm{s}}^0, \boldsymbol{u}_{\mathrm{s}}^0 \in \boldsymbol{W}_h$ be given initial data. For $n \geq 1$ perform:

1. Update fluid domain (ALE step):

$$\begin{aligned} \boldsymbol{y}_{\mathrm{f}}^n &= \mathrm{Ext}(\boldsymbol{y}_{\mathrm{s}}^{n-1}|_{\Sigma_0}), \quad \Omega_{n-1}^{\mathrm{f}} = (\boldsymbol{I}_{\Omega_0^{\mathrm{f}}} + \boldsymbol{y}_{\mathrm{f}}^n)(\Omega_0^{\mathrm{f}}), \\ \boldsymbol{w}^n &= \partial_\tau \boldsymbol{y}_{\mathrm{f}}^n \quad \text{in} \quad \Omega_{n-1}^{\mathrm{f}} \,, \end{aligned} \tag{3.40}$$

2. Viscous step: Find $\widetilde{\boldsymbol{u}}_{\mathrm{f}}^n \in \boldsymbol{V}_h$ such that

$$\begin{cases} \widetilde{\boldsymbol{u}}_{\mathrm{f}}^n|_\Sigma = \boldsymbol{u}_{\mathrm{s}}^{n-3/2}|_\Sigma, \text{with } \boldsymbol{u}_{\mathrm{s}}^{-3/2} \stackrel{\mathrm{def}}{=} \boldsymbol{u}_{\mathrm{s}}^0, \\ \widetilde{\boldsymbol{u}}_{\mathrm{f}}^n|_{\Gamma^{\mathrm{in}}} = \boldsymbol{u}_{\mathrm{in}}(t_{n-1}), \\ \dfrac{\rho_{\mathrm{f}}}{\tau}\left(\widetilde{\boldsymbol{u}}_{\mathrm{f}}^n, \boldsymbol{v}\right)_{\Omega_{n-1}^{\mathrm{f}}} + \rho_{\mathrm{f}}((\widetilde{\boldsymbol{u}}_{\mathrm{f}}^{n-1} - \boldsymbol{w}^n)\cdot\boldsymbol{\nabla}\widetilde{\boldsymbol{u}}_{\mathrm{f}}^n, \boldsymbol{v})_{\Omega_{n-1}^{\mathrm{f}}} + 2\mu\left(\boldsymbol{\varepsilon}(\widetilde{\boldsymbol{u}}_{\mathrm{f}}^n), \boldsymbol{\varepsilon}(\boldsymbol{v})\right)_{\Omega_{n-1}^{\mathrm{f}}} \\ + \rho_{\mathrm{f}}((\boldsymbol{\nabla}\cdot(\dfrac{1}{2}\widetilde{\boldsymbol{u}}_{\mathrm{f}}^{n-1} - \boldsymbol{w}^n))\widetilde{\boldsymbol{u}}_{\mathrm{f}}^n, \boldsymbol{v})_{\Omega_{n-1}^{\mathrm{f}}} = \dfrac{\rho_{\mathrm{f}}}{\tau}\left(\widetilde{\boldsymbol{u}}_{\mathrm{f}}^{n-1}, \boldsymbol{v}\right)_{\Omega_{n-1}^{\mathrm{f}}} - \left(\boldsymbol{\nabla}p^{n-1}, \boldsymbol{v}\right)_{\Omega_{n-1}^{\mathrm{f}}} \end{cases} \tag{3.41}$$

for all $\boldsymbol{v} \in \boldsymbol{V}_{\Sigma\cup\Gamma^{\mathrm{in}},h}$. Thereafter set $\widetilde{Q}_l^n \stackrel{\mathrm{def}}{=} \int_{\Gamma_l} \widetilde{\boldsymbol{u}}_{\mathrm{f}}^n \cdot \boldsymbol{n}_{\mathrm{f}}$.

3. Implicit step (projection-Windkessel-solid step): Find $(p^n, \boldsymbol{y}_{\mathrm{s}}^n, \boldsymbol{u}_{\mathrm{s}}^n) \in N_h \times \boldsymbol{W}_h \times \boldsymbol{W}_h$ such that

$$\begin{cases} \dfrac{\tau}{\rho_{\mathrm{f}}}\left(\boldsymbol{\nabla}p^n, \boldsymbol{\nabla}q\right)_{\Omega_{n-1}^{\mathrm{f}}} + \displaystyle\sum_{l=1}^{n_{0\mathrm{D}}} \frac{(p^n|_{\Gamma_l})(q|_{\Gamma_l})}{\gamma_l} = \sum_{l=1}^{n_{0\mathrm{D}}}\left(\widetilde{Q}_l^n + \frac{\alpha_l \pi_l^{n-1}}{\gamma_l}\right) q|_{\Gamma_l} \\ - \left(\boldsymbol{\nabla}\cdot\widetilde{\boldsymbol{u}}_{\mathrm{f}}^n, q\right)_{\Omega_{n-1}^{\mathrm{f}}} - \left((\boldsymbol{u}_{\mathrm{s}}^{n-1/2} - \widetilde{\boldsymbol{u}}_{\mathrm{f}}^n)\cdot\boldsymbol{n}_{\mathrm{f}}, q\right)_{\Sigma_{n-1}}, \end{cases} \tag{3.42}$$

$$\begin{cases} \rho_{\mathrm{s}}\left(\partial_\tau \boldsymbol{u}_{\mathrm{s}}^n, \boldsymbol{v}_{\mathrm{s}}\right)_{\Omega_0^{\mathrm{s}}} + a_{\mathrm{s}}((\boldsymbol{y}_{\mathrm{s}}^{n-1/2}, \boldsymbol{v}_{\mathrm{s}}) = -\left\langle \mathcal{R}_\mu(\widetilde{\boldsymbol{u}}_{\mathrm{f}}^n), \mathcal{L}_h \boldsymbol{v}_{\mathrm{s}}\right\rangle + (p^n \boldsymbol{n}_{\mathrm{f}}, \boldsymbol{v}_{\mathrm{s}})_\Sigma \\ (\boldsymbol{y}_{\mathrm{s}}^n - \boldsymbol{y}_{\mathrm{s}}^{n-1})/\tau = (\boldsymbol{u}_{\mathrm{s}}^n + \boldsymbol{u}_{\mathrm{s}}^{n-1})/2 \stackrel{\mathrm{def}}{=} \boldsymbol{u}_{\mathrm{s}}^{n-1/2} \end{cases} \tag{3.43}$$

for all $(q, \boldsymbol{v}_{\mathrm{s}}) \in N_h \times \boldsymbol{W}_h$. Set then $\mathbf{a}_{\mathrm{s}}^n = (\boldsymbol{u}_{\mathrm{s}}^n - \boldsymbol{u}_{\mathrm{s}}^{n-1})/\tau$, $P_l^n = p^n|_{\Gamma_l}$ and compute $(Q_l^n, \pi_l^n) \in \mathbb{R}^2$ from the relations

$$Q_l^n = \frac{P_l^n - \alpha_l \pi_l^{n-1}}{\gamma_l}, \quad \pi_l^n = \alpha_l \pi_l^{n-1} + \beta_l Q_l^n, \quad l = 1, \dots n_{0\mathrm{D}}. \tag{3.44}$$

– Reconstruct the pressure: Find $p^{n-1} \in N_h$ such that

$$\begin{cases} \dfrac{\tau}{\rho_{\mathrm{f}}}\left(\boldsymbol{\nabla}p^{n-1}, \boldsymbol{\nabla}q\right)_{\Omega^{\mathrm{f}}} + \displaystyle\sum_{l=1}^{n_{0\mathrm{D}}} \frac{(p^{n-1}|_{\Gamma_l})(q|_{\Gamma_l})}{R_{p,l}} = \sum_{l=1}^{n_{0\mathrm{D}}}\left(\widetilde{Q}_l^{n-1} + \frac{\pi_l^{n-1}}{R_{p,l}}\right) q|_{\Gamma_l} \\ - \left(\boldsymbol{\nabla}\cdot\widetilde{\boldsymbol{u}}_{\mathrm{f}}^{n-1}, q\right)_{\Omega^{\mathrm{f}}} - \left((\boldsymbol{u}_{\mathrm{s}}^{n-3/2} - \widetilde{\boldsymbol{u}}_{\mathrm{f}}^{n-1})\cdot\boldsymbol{n}_{\mathrm{f}}, q\right)_{\Sigma}, \end{cases} \tag{3.45}$$

which derived from the equality coming from the Windkessel's model

$$Q_l^n = \frac{P_l^n - \alpha_l \pi_l^{n-1}}{\gamma_l} = \frac{P_l^n - \pi_l^n}{R_{p,l}}.$$

Note that π_l^{n-1} is known in this case, differently to (3.42).

Note also that actually, within the semi-implicit scheme, not the whole acceleration $\mathbf{a}_{\mathrm{s}}^{n-1}$ but only the values at Σ are needed for the pressure's restart for computing the proper Neumann boundary condition (3.45).

Total vs. incremental ALE. In many ALE solvers, the domain is updated in an incremental way, from Ω^{n-1} to Ω^n, i.e.,

$$\boldsymbol{w}^{n-1} = \mathrm{Ext}(\boldsymbol{u}_{\mathrm{s}}^{n-\frac{3}{2}}|_{\Sigma^n}), \quad \Omega_{\mathrm{f}}^n = \Omega_{\mathrm{f}}^{n-1} + \tau \boldsymbol{w}^{n-1}.$$

This approach is not suitable in the present framework since the fluid domains are not properly restarted in each particle. This is the reason why we update the domain from Ω_{f}^0 using the Lagrangian displacement $\boldsymbol{y}_{\mathrm{f}}^n$. For very large displacements, this may complicate the computation of the mesh deformation (using for example a nonlinear pseudo-elasticity problem). In the applications presented in this work, a simple linear harmonic extension proved to be sufficient.

Parameter range constraints. For physical reasons, the parameters are usually restricted to a subset of $\mathbb{R}^p$. For instance, Young's modulus, densities and viscosities have to be positive. This constraint can simply be enforced by reparametrizing the physical parameters in such a way that the estimation can indeed be done in the whole space $\mathbb{R}^p$. In this work, the physical parameters (e.g. the Young's modulus) are written as $a_0 \cdot 2^\theta$, with a_0 a reference value of the parameter of interest, and the estimation is performed on θ. Note that this reparametrization modifies the statistical meaning of the covariance. For example, when the covariance on θ is equal to identity, the Young's modulus 2^θ has the same probability to be twice or half as the initial value.

Choice of the covariance W_n. Due to the analogy with variational methods (i.e., comparing for instance (3.20) and (1.8)), we use $W_{n-1}^{-1} = \gamma M_{\Gamma_{\mathrm{m}}}$, with $M_{\Gamma_{\mathrm{m}}}$ the L^2 mass matrix of the observation region Γ_{m}, or its diagonal-lumped version. Hence, we propose to choose

$$\gamma = \beta\, w^{-1} \tag{3.46}$$

where β is a positive scalar value that has to be set and

$$w^{-1} = \frac{\tau_{obs}\, \sigma^{-2}}{T_{ref}\, H_{ref}}\ , \tag{3.47}$$

where T_{ref} is a fixed reference time, $H_{ref} \approx |\Gamma_{\mathrm{m}}|$, and τ_{obs} is the time sampling of the observations, and assuming that $\zeta^Z \sim \mathcal{N}(0, \sigma^2 I)$. These definitions are motivated by keeping dimensionless the user-defined gain β associated with the measures and the *a priori* knowledge of the parameters. Note that the measure term "tends" to the continuous space-time norm when spatial and temporal resolution get higher.

3.4 Numerical examples

In this section, we present a numerical example of the ROUKF applied to a three-dimensional realistic FSI problem. The idea is not only to show that the estimation procedure is capable to deal with this complex problems, but also to get an insight to how the estimation results look like and how they can be interpreted.

3.4.1 Estimation of the Young's modulus

Forward model setting. The example considered here corresponds exactly to the same of Section 2.4.2, i.e., an idealized Abdominal Aortic Aneurism (AAA). The parameters used for generating the synthetic measurements are the same as in Section 2.4.2.

Estimation setting. We apply the reduced order UKF to estimate the Young's moduli, $E_i = 2^{\hat{\theta}_i}\, MPa$, starting from $\hat{\theta}_i = 0$, $i = 1, \ldots, 5$. The measurements are the displacements on all nodes of the fluid-structure interface Σ_0. In other words, the observation operator H consists of a $m \times n_y$ matrix (whose entries are only 0 or 1), where n_y is the number of displacement degrees of freedom of the whole solid and m is the number of displacement degrees of freedom at the interface Σ_0.

This kind of Lagrangian measurements can be obtained from processed and registered tagged MRI and should be understood as a gold standard. However, for more conventional imaging techniques (Cine MRI or CT), an observation operator involving the distance between the contours surfaces extracted from the image and the computational mesh can be considered as a generalization. We refer to [MCLT09] for details about this observation operator and to [CML+11] for an application with real data in cardiac mechanics. We will however describe and apply this generalized observation operator to real world problems in Part III.

When the measurements are not available at a given simulation time step, we can still generate an interpolated observation which only perturb the estimation by a consistency term of the order of magnitude of the data sampling.

The initial parameter covariance is assumed to be

$$\mathrm{Cov}(\zeta_\theta) = \alpha \mathbb{1} \tag{3.48}$$

where α is a given positive parameter. The noised signal is given by

$$Z_n = H\, Y_s^n + \sigma \hat{\zeta}\ ,$$

where Y_s^n is a synthetic solid displacement, $\hat{\zeta} \sim \mathcal{N}(0, I)$, and $\sigma = 0.2\,mm$, i.e., 10% of the maximal displacement at the solid wall. The measurements covariance is computed as indicated in Section 3.3.1. The scalar gain w^{-1} is obtained by formulae (3.47) setting $T_{ref} = 0.8\,s$, $H_{ref} = 76\,cm^2 \approx |\Sigma_0|$. Moreover, we resample the noised measurements Z_n in time with $\tau_{obs} = 10\tau = 0.02s$, and we re-interpolate linearly so that the filter can be applied at every time step of the simulation. The perfect signals and the noise (without time resampling for the sake of clarity) are shown in Figure 3.1 for representative points of the five regions of the vessel. Note that the signal-to-noise ratio decreases when going from the center to the ends of the AAA.

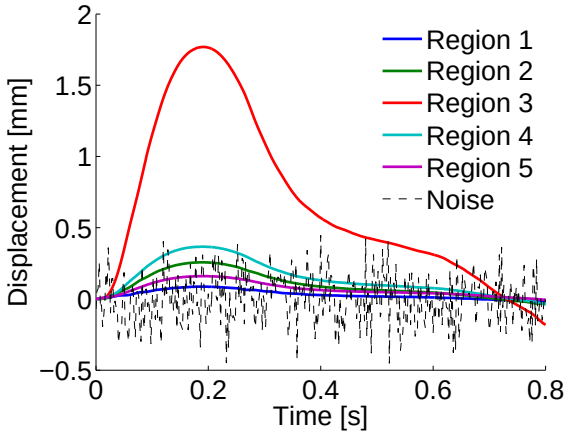

Region	SNR
1	0.43
2	1.25
3	8.8
4	1.8
5	0.75

Figure 3.1: Noise compared to the typical wall displacements in the five regions. Time responses (left), and signal-to-noise ratio (SNR: signal mean divided by standard deviation) (right).

First estimation results. In Figure 3.2, we present two estimation results for $E_i = 2^{\theta_i}$ obtained for two different covariances $\alpha = 4$ and $\alpha = 9$ for θ_i in (3.48). We remind that the higher α the lower the confidence in the initial values of the parameters. The constant β in (3.46) is for the moment fixed to 1, which corresponds to a rather low confidence in the measurements.

Several comments are in order. First, comparing the two graphs of Figure 3.2, we observe that the estimation algorithm has more freedom to adapt the parameters for large values of α. Second, the result is very good in region 3 but seems poor in the other regions. This is of course a consequence of the low SNR and the low value of β. Nevertheless, even in those cases, the algorithm is able to distinguished regions with high and low stiffness. This can be considered as a promising result for applications like detection of arteriosclerosis plaques from very noisy measurements.

Sensitivity with respect to β. The results presented in Figure 3.2 can be improved by increasing the value of β, which means increasing our confidence in the

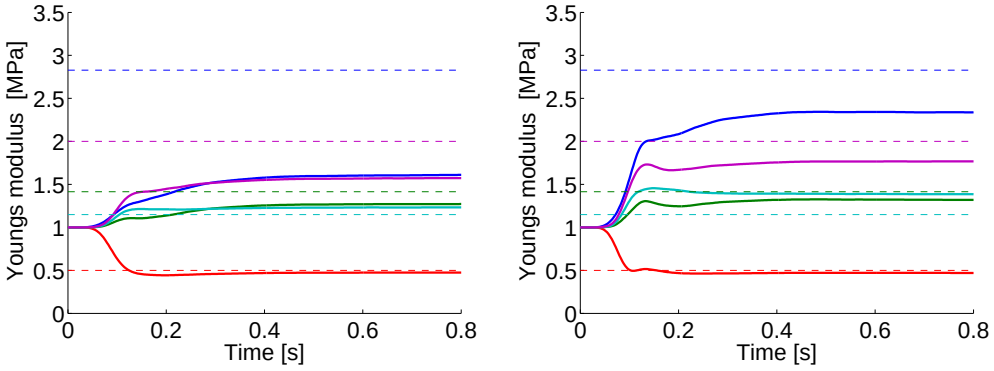

Figure 3.2: Results for the estimation of the Young's modulus with the reduced UKF algorithm for $\alpha = 4$ (left) and $\alpha = 9$ (right) for $\beta = 1$. The dashed lines correspond to the correct values. The color are the same as in Figure 3.1.

measurements. Figure 3.3 shows the behavior of the estimated parameter at the end of the cardiac cycle when β varies.

As expected, the sensitivity to β is higher for large *a priori* covariances $\mathrm{Cov}(\zeta^\theta) = \alpha\mathbb{1}$, and the estimated value is much more sensitive to α in region 1, which has the poorest SNR. But we also observe that for β reasonably large (about 10), the values of E are correctly estimated in all the other regions. Hence, at least for this example, we can conclude that, when the noise is not too high, the estimation does not strongly depend on the user-defined parameters α and β.

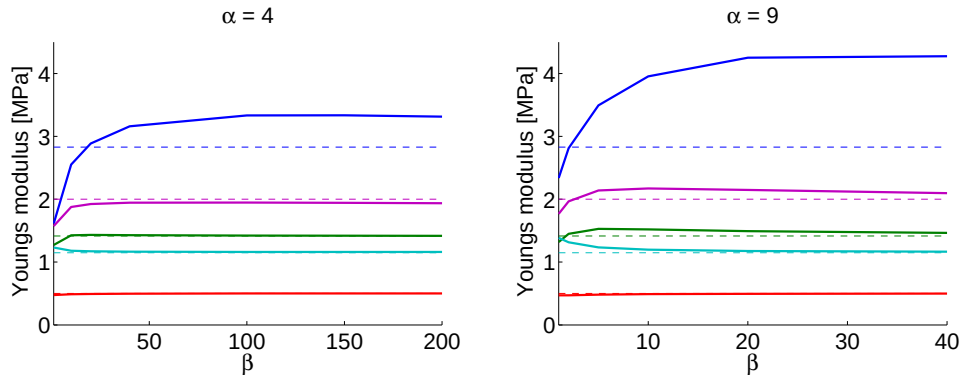

Figure 3.3: Results for the estimation of the Young's modulus (at $t = 0.8$) with the reduced UKF algorithm for $\alpha = 4, 9$, for each section and different values of β. The relation between color and region is the same as in Figure 3.1. The dashed lines represents the reference values.

Estimation of the covariance. The results presented so far correspond to the estimated mean value of the parameters. An important feature of Kalman filtering is to also provide the estimated covariances, which is a valuable information about the confidence we can have in the results.

In the reduced UKF framework, the *a posteriori* covariance of the parameters is given by

$$P_n^\theta = L_n^\theta U_n^{-1} \left(L_n^\theta\right)^\mathsf{T} .$$

Figure 3.4 shows the results for the parameters mean $\hat{\theta}_{n-1}$ and mean plus/minus the standard deviation $\hat{\theta}_{n-1} \pm \sqrt{\mathrm{diag}(P_n^\theta)}$. For the sake of clarity, the results are presented here in terms of θ instead of 2^θ, and only for the worst and best regions (1 and 3 respectively). We observe that the *a posteriori* variance is much higher in the region where the parameter is poorly estimated. We are therefore informed by the algorithm that the results are less reliable in that case, even when the correct value is unknown. This point is particularly important when dealing with real data.

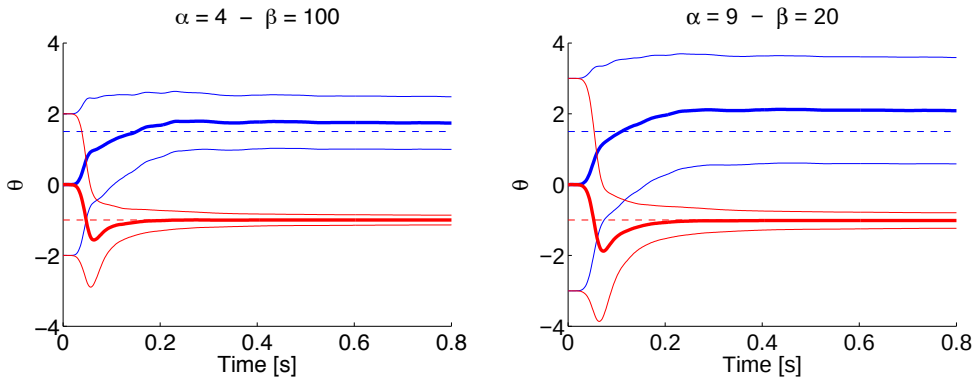

Figure 3.4: Results for $\hat{\theta}_{n-1}$ for Regions 1 (blue) and 3 (red) with $\alpha = 4$, $\beta = 100$ and $\alpha = 9$, $\beta = 20$ (β chosen in both cases to be in the flat region of Figure 3.3). The thick continuos lines represent the mean value, the thin continuous lines the mean plus/minus standard deviation, and the dashed lines the reference value as before.

3.4.2 Estimation of the Windkessel's proximal resistance

As indicated in Section 3.3.1, this estimation strategy does not involve many changes in the original software and can be implemented in a generic way outside the specific solvers. It is therefore quite simple to change or add parameters to estimate. In order to illustrate this versatility, we estimated the Windkessel's proximal resistance R_p from the same measurements as before, i.e. synthetic noisy wall displacements (see Figure 3.1). For this preliminary test, all the other parameters were supposed to be known (inclusive the stiffness distribution). As for the Young's modulus, we reparametrize R_p as $R_p = 500 \cdot 2^\theta$, and we perform the estimation on

θ. The result shown in Figure 3.5 was obtained with $\mathrm{Cov}(\zeta^\theta) = \alpha\mathbb{1}$, with $\alpha = 1$. The value of $\beta = 100$ was chosen so that the final estimation result is not sensitive to it anymore. Note that can almost perfectly recover the reference value of R_p.

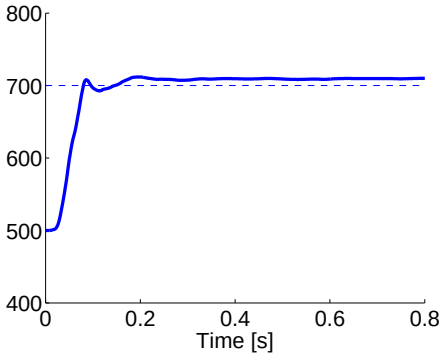

Figure 3.5: Results for the estimation of the proximal Windkessel resistance R_p with $\beta = 100$.

3.4.3 Error in the initial condition and filtering Windkessel's pressure

Up to now, it has been assumed that the initial state is perfectly known. This is of course not the case in practice, and we would like to illustrate in this section the impact of an error in the initial condition in the estimation results. We will also show that the results can be improved by considering the Windkessel's pressure as a part of the filtered variables in the reduced UKF algorithm (we remind that up to now the filtered variables were restricted to the parameters).

Estimation with inexact initial condition. To generate the inexact initial condition, the forward model is first run for one cardiac cycle with an homogeneous Young's modulus corresponding to $\theta_i = 0$. The initial condition $\hat{X}_0$ used for the estimation corresponds to the state obtained at the end of the cycle ($t = 0.8\,s$). Compared to the exact solution, the pressure difference is $2.4\,mmHg$ and the displacement difference is $0.16\,mm$ in the AAA center (see Figure 3.6). The velocity and displacement differences in the fluid and the solid are negligible.

Figure 3.7 (left) shows the parameter estimation results obtained with $\alpha = 4$, $\beta = 100$ (the value of β is chosen so that we are in the flat zone shown in Figure 3.3) . Comparing with Figure 3.2, we see how the perturbation of the initial state deteriorates the estimation results. The pressure is lower due to the error in the initial condition (Figure 3.8, right, dashed cyan curve), which affects the parameter estimation.

As already mentioned, a first solution to address this problem is to filter the state with a physical Luenberger feedback, like in [MCLT08] for elastodynamics and later

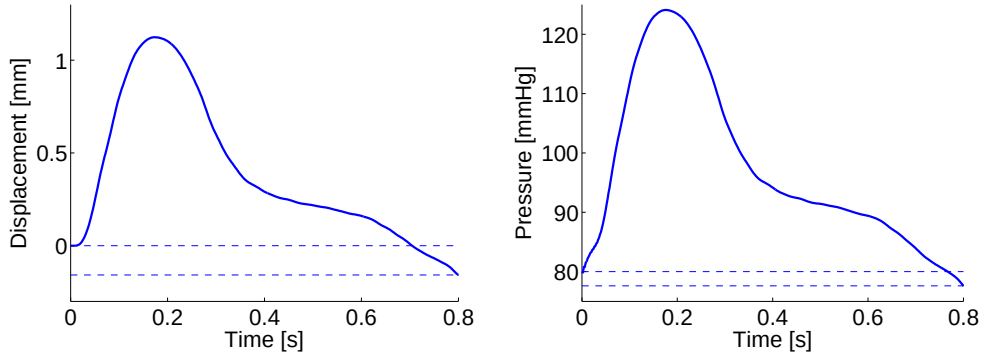

Figure 3.6: Response of the forward model with $\theta_i = 0$, $\forall\, i$, for displacements at the AAA center and proximal pressure $\bar{p}$ at Γ^{out}. The dashed lines show the gap between $t = 0\,s$ and $t = 0.8\,s$.

extended to FSI in Chapter 4. The complexity of Luenberger filters remains moderate when the system dimension increases since it is based on regular mechanical stabilization terms. In the next section we propose a simpler solution, less general, but apparently quite efficient for blood flow simulations.

Filtering the Windkessel's pressure. So far, the reduced order UKF algorithm has only been applied to the parameters. Now we propose to also apply it to the Windkessel's pressure π which is a state variable of the problem. Contrary to the other state variables – the fluid and solid velocities and displacements, which depend on the spatial discretization – π^n has by definition a limited size: just one real value in the experiment considered here, or a few real values in a case with several outlets. Therefore, it is straightforward to include it in the parameter space. From a practical viewpoint, this only consists of considering π^n as a (time dependent) parameter in the above algorithm. If an additional CPU is available for the new particle associated to this parameter, the total computational cost remains almost unaffected. From the physical point of view, the fluid pressure is mainly governed by the Windkessel's pressure. Hence, improving the knowledge of this quantity would have a global impact on the estimation of the whole FSI system. Figure 3.7 (right) shows the estimation results in the case with an initial condition error (see the previous paragraph). We observe that the result is significantly improved.

Figure 3.8 shows the displacements and the pressure for different cases: reference (the solution to recover), not filtered, estimated with a perfectly known initial condition, estimated with error in the initial condition with and without filtering the Windkessel's pressure. Note that in all the filtered cases, the displacements are properly recovered. But we observe a substantial improvement in the pressure estimation when the Windkessel's pressure is filtered. This good estimation of the general amount of stress in the system, combined with the displacement accuracy, implies that the Young's modulus estimation is better than in the situation when

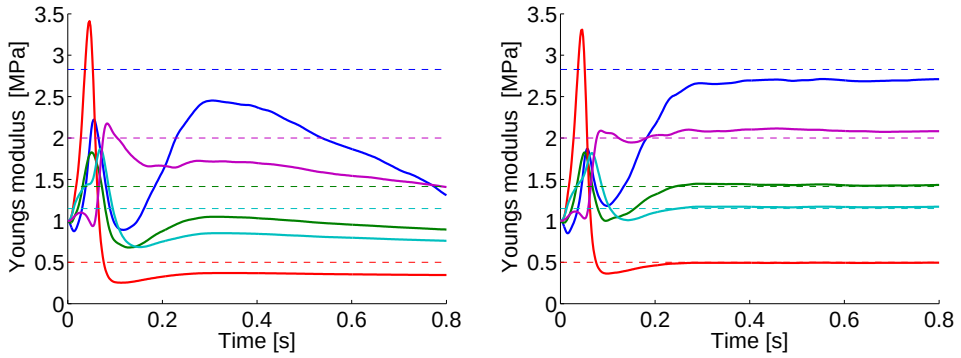

Figure 3.7: Parameter estimation in presence of an error in the initial condition with $\alpha = 4$, $\beta = 100$. Only 5 stiffness parameters included in the parameter space for the reduced UKF (left), and and effect of inclusion the Windkessel's pressure (right).

π^n is not filtered.

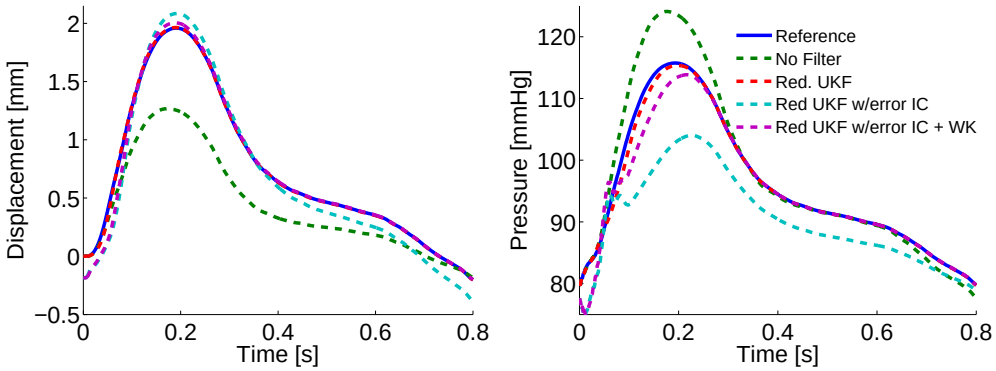

Figure 3.8: Results for the estimation of displacement at the AAA centre and Windkessel's pressure. All reduced UKF curves are obtained with $\alpha = 4$ and $\beta = 100$.

3.5 Conclusions

We have derived a procedure to estimate uncertain physical parameters in systems involving the mechanical interaction of a viscous incompressible fluid and an elastic structure. The method is based on the reduced-order Unscented Kalman Filter, introduced in [MC11b]. The algorithm does not need any tangent or adjoint problems and can easily be run in parallel, using as many processors as the number of parameters plus one. Doing so, the computational time needed to solve the inverse problem is of the same order as the time needed by a forward simulation using one processor.

Some numerical results have been presented for noised synthetic data corresponding to an idealized geometry of aneurysm. We have estimated the artery Young's modulus in 5 regions using measurements of the wall displacement. We have first considered a problem with a perfectly known initial condition, and we have investigated the sensitivity of the results to the noise and the *a priori* parameter covariance matrices. Then, we have perturbed the initial condition of the system in order to illustrate its impact on the parameter estimation. Finally, we have shown that considering the Windkessel's pressure as a parameter is a simple way to improve the estimation performance, without significantly increasing the computational cost, and without any additional measurements. To illustrate the versatility of the method, we have also presented a preliminary result about Windkessel resistance estimation.

Chapter 4

Luenberger observers in FSI

We analyze the performance of various Luenberger observers to estimate the state of a dynamical system involving a viscous incompressible fluid and an elastic structure. The measurements are assumed to be limited to displacements and velocities in the solid. We show that the behavior observed in fluid-structure interaction (FSI) and in solid mechanics may differ dramatically in some situations. We explain this observation, numerically and analytically, with various simplified models and we propose a new filter that accounts for the specificity of FSI.

The results presented in this chapter lead to the manuscript:
C. Bertoglio, D. Chapelle, M. Fernández, J.-F. Gerbeau and P. Moireau. **State observers of a vascular fluid-structure interaction model through measurements in the solid**. Submitted to Computer Methods in Applied Mechanics and Engineering, 2012.

Contents

4.1 Observers for the fluid-structure interaction problem

In this section we introduce the formulations for the fluid-structure observers when velocities or displacements are available in a subpart of the solid domain. In order to make this chapter as self-contained as possible, we recall the strong form of

the coupled fluid-structure equations. Then, we present different definitions of the discrepancy between observations and model for two types of solid measurements. Next, we present the respective observers, and we finalize with some numerical experiments in order to illustrate their performance.

4.1.1 Fluid-structure interaction equations

We consider the mechanical interaction between an incompressible fluid and an elastic structure. The fluid is described by the Navier-Stokes equations, in a moving domain $\Omega^{\mathrm{f}}(t) \subset \mathbb{R}^d$, $d = 2, 3$, in an Arbitrary Lagrangian Eulerian (ALE) formulation, and the structure by the linear elasticity equations in $\Omega_0^{\mathrm{s}} \subset \mathbb{R}^d$, with $\Omega_0^{\mathrm{s}} = \Omega^{\mathrm{s}}(0)$ and $\Omega^{\mathrm{s}} = \Omega^{\mathrm{s}}(t)$ the deformed solid domain at time t. The fluid-structure interface is denoted by $\Sigma = \partial\Omega^{\mathrm{s}} \cap \partial\Omega^{\mathrm{f}}$ and $\partial\Omega^{\mathrm{f}} = \Gamma^{\mathrm{in}} \cup \Gamma^{\mathrm{out}} \cup \Sigma$, $\partial\Omega_0^{\mathrm{s}} = \Gamma_0^{\mathrm{d}} \cup \Gamma_0^{\mathrm{n}} \cup \Sigma_0$, are given partitions of the fluid and solid boundaries, respectively (see Figure 4.1). The coupled FSI problem reads as follows:

For $t > 0$, find the fluid velocity $\boldsymbol{u}_{\mathrm{f}}(t) : \Omega_{\mathrm{f}}(t) \to \mathbb{R}^d$, the fluid pressure $p(t) : \Omega_{\mathrm{f}}(t) \to \mathbb{R}$, the structure displacement $\boldsymbol{y}_{\mathrm{s}}(t) : \Omega_0^{\mathrm{s}} \to \mathbb{R}^d$ and structure velocity $\boldsymbol{u}_{\mathrm{s}}(t) : \Omega_0^{\mathrm{s}} \to \mathbb{R}^d$ such that

- Fluid equations:

$$\begin{cases} \rho_{\mathrm{f}} \dfrac{\partial \boldsymbol{u}_{\mathrm{f}}}{\partial t}\Big|_{\boldsymbol{\xi}} + \rho_{\mathrm{f}}(\boldsymbol{u}_{\mathrm{f}} - \boldsymbol{w}) \cdot \boldsymbol{\nabla}\boldsymbol{u}_{\mathrm{f}} - \boldsymbol{\nabla} \cdot \boldsymbol{\sigma}_{\mathrm{f}}(\boldsymbol{u}_{\mathrm{f}}, p) = \boldsymbol{0}, & \text{in} \quad \Omega^{\mathrm{f}}(t), \\ \boldsymbol{\nabla} \cdot \boldsymbol{u}_{\mathrm{f}} = 0, & \text{in} \quad \Omega^{\mathrm{f}}(t), \\ \boldsymbol{u}_{\mathrm{f}} = \boldsymbol{u}_{\mathrm{in}}, & \text{on} \quad \Gamma^{\mathrm{in}}, \\ \boldsymbol{\sigma}_{\mathrm{f}}(\boldsymbol{u}_{\mathrm{f}}, p) \cdot \boldsymbol{n}_{\mathrm{f}} = -P\,\boldsymbol{n}_{\mathrm{f}}, & \text{on} \quad \Gamma^{\mathrm{out}}. \end{cases} \tag{4.1a}$$

  with $\boldsymbol{\sigma}_{\mathrm{f}}(\boldsymbol{u}_{\mathrm{f}}, p) = -p\mathbb{1} + 2\mu_{\mathrm{f}}\,\boldsymbol{\varepsilon}(\boldsymbol{u}_{\mathrm{f}})$, where $\boldsymbol{\varepsilon}(\boldsymbol{u}_{\mathrm{f}})$ denotes the deformation rate tensor, μ_{f} the dynamic viscosity, and $\frac{\partial}{\partial t}|_{\boldsymbol{\xi}}$ the ALE derivative (see e.g. [FG09]). In the hemodynamics problems considered in this work, the outlet pressure P is obtained by solving the differential-algebraic equation

$$\begin{cases} P = \pi + R_{\mathrm{p}} Q, \\ C\dfrac{d\pi}{dt} + \dfrac{\pi}{R_{\mathrm{d}}} = Q, \\ Q = \displaystyle\int_{\Gamma^{\mathrm{out}}} \boldsymbol{u}_{\mathrm{f}} \cdot \boldsymbol{n}_{\mathrm{f}}\, d\Gamma \end{cases} \tag{4.1b}$$

  Here, the distal resistance R_{d}, the proximal resistance R_p and the capacitance C are assumed to be given. This "zero-dimensional" equation is known as the three-element Windkessel model (see for example [FQV09]). It represents the flow resistance (R_{p} and R_{d}) and the compliance (C) of the vessels beyond the 3D portion considered in the simulation.

- Structure equations:

$$\begin{cases} \partial_t \boldsymbol{y}_\mathrm{s} = \boldsymbol{u}_\mathrm{s}, & \text{in} \quad \Omega_0^\mathrm{s}, \\ \rho_\mathrm{s}\partial_t \boldsymbol{u}_\mathrm{s} - \eta_\mathrm{s}\boldsymbol{\nabla}\cdot\boldsymbol{\sigma}_\mathrm{s}(\boldsymbol{u}_\mathrm{s}) - \boldsymbol{\nabla}\cdot\boldsymbol{\sigma}_\mathrm{s}(\boldsymbol{y}_\mathrm{s}) = \boldsymbol{0}, & \text{in} \quad \Omega_0^\mathrm{s}, \\ \boldsymbol{y}_\mathrm{s} = \boldsymbol{0}, & \text{on} \quad \Gamma_0^\mathrm{d}, \\ \eta_\mathrm{s}\boldsymbol{\sigma}_\mathrm{s}(\boldsymbol{u}_\mathrm{s})\cdot\boldsymbol{n}_\mathrm{s} + \boldsymbol{\sigma}_\mathrm{s}(\boldsymbol{y}_\mathrm{s})\cdot\boldsymbol{n}_\mathrm{s} = \boldsymbol{0}, & \text{on} \quad \Gamma_0^\mathrm{n}, \end{cases} \tag{4.1c}$$

  with $\boldsymbol{\sigma}_s(\boldsymbol{y}_\mathrm{s}) = \lambda_s \mathrm{Tr}(\boldsymbol{\varepsilon}(\boldsymbol{y}_\mathrm{s}))\mathbb{1} + 2\mu_s\boldsymbol{\varepsilon}(\boldsymbol{y}_\mathrm{s})$ where, λ_s and μ_s are the Lamé constants and η_s a viscous modulus.

- Coupling conditions:

$$\begin{cases} \boldsymbol{y}_\mathrm{f} = \mathrm{Ext}^\mathrm{f}_{\Sigma_0}\big(\boldsymbol{y}_{\mathrm{s}|\Sigma_0}\big), \quad \boldsymbol{w} = \partial_t \boldsymbol{y}_\mathrm{f}, \quad \Omega^\mathrm{f}(t) = \big(I_{\Omega_0^\mathrm{f}} + \boldsymbol{y}_\mathrm{f}(t)\big)(\Omega_0^\mathrm{f}), & \\ \boldsymbol{u}_\mathrm{f} = \boldsymbol{u}_\mathrm{s}, \quad \text{on} \quad \Sigma(t), & \\ \eta_\mathrm{s}\boldsymbol{\sigma}_\mathrm{s}(\boldsymbol{u}_\mathrm{s})\cdot\boldsymbol{n}_\mathrm{s} + \boldsymbol{\sigma}_\mathrm{s}(\boldsymbol{y}_\mathrm{s})\cdot\boldsymbol{n}_\mathrm{s} + J_\mathrm{f}\boldsymbol{\sigma}_\mathrm{f}(\boldsymbol{u}_\mathrm{f}, p)\cdot\boldsymbol{F}_\mathrm{f}^{-T}\cdot\boldsymbol{n}_\mathrm{f} = \boldsymbol{0}, \quad \text{on} \quad \Sigma_0\ , & \end{cases} \tag{4.1d}$$

  with $\mathrm{Ext}^\mathrm{f}_\Sigma$ an extension operator from Σ to Ω_f, $\boldsymbol{F}_\mathrm{f}$ the deformation gradient and $J_\mathrm{f} = \det\boldsymbol{F}_\mathrm{f}$.

Note that the continuity of the domain displacements could be limited to their normal components.

This problem is completed with appropriate initial conditions: velocity $\boldsymbol{u}_\mathrm{f}(0)$, domain displacement $\boldsymbol{y}_\mathrm{f}(0)$ and Windkessel's pressure $\pi(0)$ for the fluid, initial velocity $\boldsymbol{u}_\mathrm{s}(0)$ and displacement $\boldsymbol{y}_\mathrm{s}(0)$ for the solid.

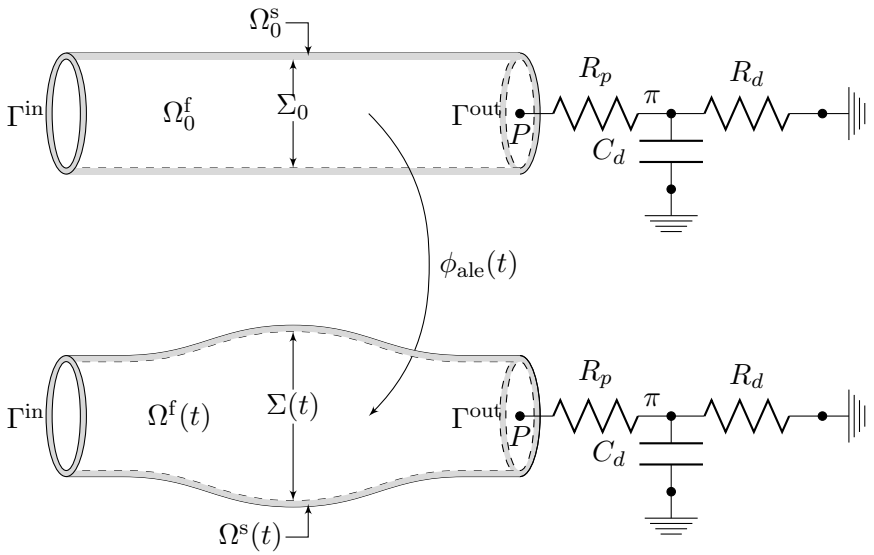

Figure 4.1: Reference (top) and current domain (bottom) in the ALE formulation

Energy balance - In what follows, the quantity

$$E(t) = \underbrace{\frac{\rho_{\mathrm{f}}}{2}\|\boldsymbol{u}_{\mathrm{f}}\|^2_{L^2(\Omega_{\mathrm{f}}(t))} + \frac{\rho_{\mathrm{s}}}{2}\|\boldsymbol{u}_{\mathrm{s}}\|^2_{L^2(\Omega^{\mathrm{s}}_0)}}_{\text{Kinetic energy}} + \underbrace{\frac{1}{2}\|\boldsymbol{y}_{\mathrm{s}}\|^2_{\mathcal{E}^s_l} + \frac{C}{2}\pi^2}_{\text{Potential energy}}$$

denotes the total mechanical energy of the fluid-structure system described by (4.1), with $\|\cdot\|_{\mathcal{E}^s_l}$ standing for the elastic energy-norm of the structure, that is,

$$\|\boldsymbol{d}_{\mathrm{s}}\|_{\mathcal{E}^s_l} = \sqrt{\langle \boldsymbol{d}_{\mathrm{s}}, \boldsymbol{d}_{\mathrm{s}}\rangle_{\mathcal{E}^s_l}}, \quad \langle \boldsymbol{d}_{\mathrm{s}}, \boldsymbol{v}_{\mathrm{s}}\rangle_{\mathcal{E}^s_l} = \int_{\Omega^{\mathrm{s}}_0} \boldsymbol{\sigma}_{\mathrm{s}}(\boldsymbol{d}_{\mathrm{s}}) : \boldsymbol{\varepsilon}_{\mathrm{s}}(\boldsymbol{v}_{\mathrm{s}})\, d\Omega$$

for all $\boldsymbol{d}_{\mathrm{s}}, \boldsymbol{v}_{\mathrm{s}} \in \mathcal{V}^d_s$.

The next result states the energy equation of the coupled system (4.1). As expected, dissipation only comes from the viscosity in the fluid, the solid and the resistive terms in the outlet boundary conditions. In particular, the power exchanged by the fluid and the structure exactly balances at the interface, as a direct consequence of the coupling conditions (4.1d).

Proposition 5
The following identity holds for $t > 0$:

$$\frac{\mathrm{d}}{\mathrm{d}t}E(t) = -D(t) - \int_{\Gamma^{\mathrm{in}}} \frac{\rho_{\mathrm{f}}}{2}\boldsymbol{u}_{\mathrm{in}} \cdot \boldsymbol{n}_{\mathrm{f}}|\boldsymbol{u}_{\mathrm{in}}|^2 - \int_{\Gamma^{\mathrm{out}}} \frac{\rho_{\mathrm{f}}}{2}\boldsymbol{u}_{\mathrm{f}} \cdot \boldsymbol{n}_{\mathrm{f}}|\boldsymbol{u}_{\mathrm{f}}|^2\, d\Gamma \tag{4.2}$$

with

$$D(t) = 2\mu\|\boldsymbol{\varepsilon}(\boldsymbol{u}_{\mathrm{f}})\|^2_{L^2(\Omega_{\mathrm{f}}(t))} + \eta_{\mathrm{s}}\|\boldsymbol{u}_{\mathrm{s}}\|^2_{\mathcal{E}^s_l} + \frac{\pi^2}{R_{\mathrm{d}}} + R_{\mathrm{p}}Q^2.$$

Proof. The identity (4.2) can be derived from a standard energy argument (see, e.g., [FG09]). We first multiply $(4.1a)_1$ by $\boldsymbol{u}_{\mathrm{f}}$, integrate over $\Omega_{\mathrm{f}}(t)$ and apply the Green formula to the divergence term. Similarly, we then multiply $(4.1c)_2$ by $\boldsymbol{u}_{\mathrm{s}}$, integrate over Ω^{s}_0 and apply the Green formula once more. By adding the resulting expressions and using (4.1d) and (4.1b) we get (4.2). ∎

Note that, as well known, the overall stability of the system is not ensured in the case of backflow on Γ^{out} is presented. For the numerical experiments consider in this work, this is in fact not an issue.

State-space form. Finally we introduce the standard state-space representation of System (4.1) classically used to present control and observation problems [Cor07, CZ95]. First we introduce the state of the system as the combination $x = (\boldsymbol{y}_{\mathrm{s}}, \boldsymbol{u}_{\mathrm{s}}, \boldsymbol{y}_{\mathrm{f}}, \boldsymbol{u}_{\mathrm{f}}, \pi)$. Then, we can formally define an evolution operator $\mathcal{A}$ –

nonlinear in our case – such that System (4.1) reads

$$\begin{cases} \dot{x} = \mathcal{A}(x) \\ x(0) = x_0 + \zeta \end{cases} \tag{4.3}$$

Note that in this formulation the distributed fluid pressure does not appear directly in (4.3) since it corresponds to a Lagrange multiplier of the fluid incompressibility constraint prescribed through the fluid space definition.

4.1.2 Observer based on solid measurements

We now present the fluid-structure observer based on displacement measurements in the solid. We begin by defining the types of discrepancy operators and detailing the filtering setting. Then we present the specific formulations for the velocities- and displacements-based observers.

4.1.2.1 Discrepancy measure minimization

Usually, computational models only use the data to define the initial state and the boundary conditions. By contrast, an *observer* is a system which can benefit from the whole set of data to improve the result of the model. For example, the data are used in [MCLT08] to reduce the error on the initial condition for an elasticity problem, and in [CCM] to reduce the discretization error for a wave-like equation.

In the cardiovascular context, the most common type of non-invasive measurements is provided by medical images which contain information about the solid kinematics. In [MCLT09], this type of measurements is used to define an observer for a solid problem. Here, we aim at extending this methodology to an FSI system. In this study, we limit ourselves to measurements of structure displacements or velocities. But the observers presented here can be extended to more realistic measurements, like for example the distance to segmented surfaces. This has been proposed in [MCLT09] for solid mechanics problems, applied in [CML+11] with MRI images, and in [MBX+12] with CT images for an FSI problem.

In the present work, we will consider measurements defined for example by

$$\boldsymbol{z}_d = \mathcal{H}_d \boldsymbol{y}_{\mathrm{s}}^{\mathrm{ref}}, \tag{4.4}$$

where $\mathcal{H}_d$ is the observation operator which e.g. selects the field $\boldsymbol{y}_{\mathrm{s}}$ in a subdomain $\omega \in \Omega_0^{\mathrm{s}}$ or the trace of the field at some interface, e.g. the fluid-structure interface Σ_0. In these cases, we have

$$\boldsymbol{z}_d = \boldsymbol{y}_{\mathrm{s}|\omega}^{\mathrm{ref}}, \tag{4.5a}$$

or

$$\boldsymbol{z}_d = \boldsymbol{y}_{\mathrm{s}|\Sigma_0}^{\mathrm{ref}}. \tag{4.5b}$$

Even if velocity measurements are rarely directly accessible, we will also consider

$$\boldsymbol{z}_v = \mathcal{H}_v \boldsymbol{u}_{\mathrm{s}}^{\mathrm{ref}} \tag{4.6}$$

because this kind of observation can be helpful to understand how to derive adequate observers.

When these two types of measurements are simultaneously available, the operators can be aggregated to obtain

$$z = \begin{pmatrix} \boldsymbol{z}_d \\ \boldsymbol{z}_v \end{pmatrix} = \begin{pmatrix} \mathcal{H}_d & 0 \\ 0 & \mathcal{H}_v \end{pmatrix} \begin{pmatrix} \boldsymbol{y}_{\mathrm{s}}^{\mathrm{ref}} \\ \boldsymbol{u}_{\mathrm{s}}^{\mathrm{ref}} \end{pmatrix}.$$

More generally for $x^{\mathrm{ref}} = (\boldsymbol{y}_{\mathrm{s}}^{\mathrm{ref}}, \boldsymbol{u}_{\mathrm{s}}^{\mathrm{ref}}, \boldsymbol{y}_{\mathrm{f}}^{\mathrm{ref}}, \boldsymbol{u}_{\mathrm{f}}^{\mathrm{ref}}, \pi^{\mathrm{ref}})$, we can define

$$z = \mathcal{H} x^{\mathrm{ref}} + \chi$$

with χ some additive measurement noise.

The principle of optimal filtering in data assimilation – with Kalman filtering [KB61] and various extensions thereof [Sim06] – is to minimize in time – up to additive regularization terms – a discrepancy measure comparing a given state $x = (\boldsymbol{y}_{\mathrm{s}}, \boldsymbol{u}_{\mathrm{s}}, \boldsymbol{y}_{\mathrm{f}}, \boldsymbol{u}_{\mathrm{f}}, \pi)$ with the measurements z. Considering again the example (4.5), the discrepancy measure can be

$$\mathrm{meas}_{L^2(\omega)}\{x, z\}(t) = \frac{1}{2} \int_{\omega} |\boldsymbol{z}_d - \boldsymbol{y}_{\mathrm{s}}|^2 \, d\Omega, \tag{4.7a}$$

or

$$\mathrm{meas}_{L^2(\Sigma_0)}\{x, z\}(t) = \frac{1}{2} \int_{\Sigma_0} |\boldsymbol{z}_d - \boldsymbol{y}_{\mathrm{s}}|^2 \, d\Gamma, \tag{4.7b}$$

when choosing an L^2-norm for comparing the two fields. Alternativaly, other norms can be chosen, for instance on the boundary we can consider an $H^{\frac{1}{2}}(\Sigma_0)$ type norm, while for a subdomain we can employ an $H^1(\omega)$-norm. Then, we use

$$\mathrm{meas}_{H^1(\omega)}\{x, z\}(t) = \frac{1}{2} \| \mathrm{Ext}_{\omega}^{s}(\boldsymbol{z} - \boldsymbol{y}_{\mathrm{s}|\omega}) \|^2_{H_1(\Omega_0^{\mathrm{s}})}, \tag{4.8a}$$

or

$$\mathrm{meas}_{H^{1/2}(\Sigma_0)}\{x, z\}(t) = \frac{1}{2} \| \mathrm{Ext}_{\Sigma_0}^{s}(\boldsymbol{z} - \boldsymbol{y}_{\mathrm{s}|\Sigma_0}) \|^2_{H_1(\Omega_0^{\mathrm{s}})}, \tag{4.8b}$$

where $\mathrm{Ext}_{\Sigma_0}^{s}$ and $\mathrm{Ext}_{\omega}^{s}$ are extension operators defined in the structure domain and based on the elasticity formulation. The advantage of the state space form is to summarize all these discrepancy measures in

$$\mathrm{meas}_{\mathcal{M}}\{x, z\}(t) = \frac{1}{2} \| z - \mathcal{H} x \|^2_{\mathcal{M}} \tag{4.9}$$

for a given norm $\mathcal{M}$. Therefore, optimal filters are built by considering the mini-

mization of a least square criterion

$$J(x(0),T) = \frac{1}{2}\|x(0)-x_0\|^2_{\mathcal{E}} + \frac{1}{2}\int_0^T \|z(s)-\mathcal{H}x(s)\|^2_{\mathcal{M}} ds,$$

for $x(\cdot)$ following the dynamics (4.3). The norm $\|\|_{\mathcal{E}}$ is typically an energy norm naturally associated with the system, and we minimize on the initial condition which entirely determines the rest of the trajectory.

Then the optimal observer – denoted by $\hat{x}$ since it follows its own evolution equation – is defined by

$$\begin{cases} \dot{\hat{x}} = \mathcal{A}(\hat{x}) + \mathcal{P}\mathcal{H}'(z-\mathcal{H}\hat{x}) \\ \hat{x}(0) = x_0 \end{cases} \tag{4.10}$$

where $\mathcal{H}'$ is the adjoint of the operator $\mathcal{H}$ with respect to the norm $\mathcal{M}$, and $\mathcal{P}$ an operator deriving from a Riccati equation in Kalman-like filtering or from a Hamilton-Jacobi-Bellman equation for nonlinear systems [Fle97]. In all cases, these filters suffer from the "curse of dimensionality" as explained by Bellman [Bel57], which makes them intractable with partial differential equations. In [Lue71], Luenberger introduced a new class of filter, named *observers*, for which he relaxed the optimality condition to only base the filter design requiring that the error $\tilde{x} = x^{\text{ref}} - \hat{x}$ to be asymptotically stable. To that purpose, a possible approach is to differentiate the discrepancy measure (4.9), namely

$$\nabla_x(\text{meas}_{\mathcal{M}}\{x,z\}(t)) = -\mathcal{H}'(z-\mathcal{H}x),$$

and use this gradient as the correction descent direction. Hence, a good observer candidate in state-space form is

$$\dot{\hat{x}} = \mathcal{A}(\hat{x}) + \gamma\mathcal{H}'(z-\mathcal{H}\hat{x}), \tag{4.11}$$

with γ a scalar characterizing the correction intensity. In the case of a linear dynamics operator $\mathcal{A}(\cdot) = \mathcal{A}_l \cdot$ we can derive the dynamics of the error $\tilde{x} = x^{\text{ref}} - \hat{x}$ between the real system x^{ref} and the observer $\hat{x}$ to ge the autonomous system

$$\dot{\tilde{x}} = (\mathcal{A}_l - \gamma\mathcal{H}'\mathcal{H})\tilde{x} - \gamma\mathcal{H}'\chi.$$

Hence, the principle of the observer is to ensure that the semi-group generated by $\mathcal{A}_l - \gamma\mathcal{H}'\mathcal{H}$ is asymptotically stable. We will analyze our strategy in this light in Section 4.2, by considering linear fluid models in our coupled fluid-structure problem.

Let us now specify in the next two paragraphs how the strong formulation for the classical FSI problem is modified when constructing an FSI observer in the case of velocities or displacement measurements.

4.1.2.2 Observer based on solid velocities measurements

We first consider the simplest observer based on solid velocities. Assuming that we measure the velocities on a subdomain ω or the boundary part Σ_0 , we have the following discrepancy measure

$$\text{meas}_{L^2(\omega)}\{x,z\}(t) = \frac{1}{2}\int_\omega |\boldsymbol{z}_v - \boldsymbol{u}_\text{s}|^2\, d\Omega, \tag{4.12a}$$

or

$$\text{meas}_{L^2(\Sigma_0)}\{x,z\}(t) = \frac{1}{2}\int_{\Sigma_0} |\boldsymbol{z}_v - \boldsymbol{u}_\text{s}|^2\, d\Gamma, \tag{4.12b}$$

and corresponding tangent operators

$$\forall \boldsymbol{v}_\text{s} \in \mathcal{V}_s^v, \quad \mathcal{P}_{L^2(\omega)}\{x,z\}(t)(\boldsymbol{v}_\text{s}) = \int_\omega (\boldsymbol{z}_v - \boldsymbol{u}_\text{s})\cdot \boldsymbol{v}_\text{s}\, d\Omega, \tag{4.13a}$$

or

$$\forall \boldsymbol{v}_\text{s} \in \mathcal{V}_s^v, \quad \mathcal{P}_{L^2(\Sigma_0)}\{x,z\}(t)(\boldsymbol{v}_\text{s}) = \int_{\Sigma_0} (\boldsymbol{z}_v - \boldsymbol{u}_\text{s})\cdot \boldsymbol{v}_\text{s}\, d\Gamma. \tag{4.13b}$$

In this case the control operator $\gamma\mathcal{H}'$ generates a force proportional to the discrepancy between the computed and measured velocities, so that the tangent expression (4.13a) or (4.13b) appears as an external virtual power in the principle of virtual power. The resulting filter is called *Direct Velocity Feedback* (DVF), widely used in structural control [Pre02], and already applied in [MCLT08] for state estimation of solid mechanics systems. The corresponding observer consists in modifying in System (4.1) the solid formulation (4.1c) into

$$\left\{\begin{aligned} \partial_t \hat{\boldsymbol{y}}_\text{s} &= \hat{\boldsymbol{u}}_\text{s}, && \text{in} \quad \Omega_0^\text{s},\\ \rho_\text{s}\partial_t \hat{\boldsymbol{u}}_\text{s} - \eta_\text{s}\boldsymbol{\nabla}\cdot\boldsymbol{\sigma}_\text{s}(\hat{\boldsymbol{u}}_\text{s}) - \boldsymbol{\nabla}\cdot\boldsymbol{\sigma}_\text{s}(\hat{\boldsymbol{y}}_\text{s}) &= \gamma_v \mathbb{1}_\omega(\boldsymbol{z}_v - \hat{\boldsymbol{u}}_\text{s}|_\omega), && \text{in} \quad \Omega_0^\text{s},\\ \hat{\boldsymbol{y}}_\text{s} &= \boldsymbol{0}, && \text{on} \quad \Gamma_0^\text{d},\\ \eta_\text{s}\boldsymbol{\sigma}_\text{s}(\hat{\boldsymbol{u}}_\text{s})\cdot\boldsymbol{n}_\text{s} + \boldsymbol{\sigma}_\text{s}(\hat{\boldsymbol{y}}_\text{s})\cdot\boldsymbol{n}_\text{s} &= \boldsymbol{0}, && \text{on} \quad \Gamma_0^\text{n}, \end{aligned}\right. \tag{4.14a}$$

with γ_v corresponding gain for the DVF. The case of velocities measured on a boundary is more intricate because the velocity is usually defined in $L^2(\Omega_0^\text{s})$ in System (4.1) and therefore does not *a priori* have a trace on the boundary. However, assuming this regularity present in the reference solution – justifying the fact that we can measure it – some hidden regularity can be justified for the observer as recalled in [CMLT09] and more precisely discussed in [LT03]. In the case of measurements on Σ_0, the observer consists now only in changing the coupling conditions (4.1d) of

System (4.1) into

$$\begin{cases} \hat{\boldsymbol{y}}_{\mathrm{f}} = \mathrm{Ext}^{\mathrm{f}}_{\Sigma_0}\big(\hat{\boldsymbol{y}}_{\mathrm{s}|\Sigma_0}\big), \quad \hat{\boldsymbol{w}} = \partial_t \hat{\boldsymbol{y}}_{\mathrm{f}}, \quad \Omega^{\mathrm{f}}(t) = \big(I_{\Omega^{\mathrm{f}}_0} + \hat{\boldsymbol{y}}_{\mathrm{f}}(t)\big)(\Omega^{\mathrm{f}}_0), \\ \qquad\qquad\qquad\qquad\qquad\qquad\qquad\qquad\qquad\qquad \hat{\boldsymbol{u}}_{\mathrm{f}} = \hat{\boldsymbol{u}}_{\mathrm{s}}, \quad \text{on} \quad \Sigma(t), \\ \eta_{\mathrm{s}}\boldsymbol{\sigma}_{\mathrm{s}}(\hat{\boldsymbol{u}}_{\mathrm{s}})\cdot\boldsymbol{n}_{\mathrm{s}} + \boldsymbol{\sigma}_{\mathrm{s}}(\hat{\boldsymbol{y}}_{\mathrm{s}})\cdot\boldsymbol{n}_{\mathrm{s}} + J_{\mathrm{f}}\boldsymbol{\sigma}_{\mathrm{f}}(\hat{\boldsymbol{u}}_{\mathrm{f}},\hat{p})\cdot\hat{\boldsymbol{F}}_{\mathrm{f}}^{-T}\cdot\boldsymbol{n}_{\mathrm{f}} = \gamma_v(\boldsymbol{z}_v - \hat{\boldsymbol{u}}_{\mathrm{s}}), \quad \text{on} \quad \Sigma_0\ , \end{cases} \tag{4.14b}$$

Energetic aspects for the observer. The dissipative character of the DVF filter can be highlighted by a simple energy argument, as in Proposition 5. Thus, for the coupled systems (4.1a), (4.14a), (4.1d), (4.1b) or (4.1a), (4.1c), (4.14b), (4.1b) the identity (4.2) becomes

$$\frac{\mathrm{d}}{\mathrm{d}t}\hat{E}(t) \leq -\hat{D}(t) - \frac{\gamma_v}{2}\|\hat{\boldsymbol{u}}_{\mathrm{s}}\|^2_{L^2(\omega)} + \frac{\gamma_v}{2}\|\boldsymbol{z}_v\|^2_{L^2(\omega)} - \int_{\Gamma^{\mathrm{in}}\cup\Gamma^{\mathrm{out}}} \frac{\rho_{\mathrm{f}}}{2}\hat{\boldsymbol{u}}_{\mathrm{f}}\cdot\boldsymbol{n}_{\mathrm{f}}|\hat{\boldsymbol{u}}_{\mathrm{f}}|^2\, d\Gamma,$$

with obvious notation

$$\begin{aligned} \hat{E}(t) =& \frac{\rho_{\mathrm{f}}}{2}\|\hat{\boldsymbol{u}}_{\mathrm{f}}\|^2_{L^2(\Omega_{\mathrm{f}}(t))} + \frac{\rho_{\mathrm{s}}}{2}\|\hat{\boldsymbol{u}}_{\mathrm{s}}\|^2_{L^2(\Omega^{\mathrm{s}}_0)} + \frac{1}{2}\|\hat{\boldsymbol{y}}_{\mathrm{s}}\|^2_{\mathcal{E}^s_l} + \frac{C}{2}\hat{\pi}^2, \\ \hat{D}(t) =& 2\mu\|\boldsymbol{\varepsilon}(\hat{\boldsymbol{u}}_{\mathrm{f}})\|^2_{L^2(\Omega_{\mathrm{f}}(t))} + \eta_{\mathrm{s}}\|\hat{\boldsymbol{u}}_{\mathrm{s}}\|^2_{\mathcal{E}^s_l} + \frac{\hat{\pi}^2}{R_{\mathrm{d}}} + R_{\mathrm{p}}\hat{Q}^2. \end{aligned}$$

4.1.2.3 Observer based on solid displacement measurements

In practice, displacement-like measurements are more common [MCLT09] and, taking into account the time sampling of the measurements in medical imaging, we cannot afford to time-differentiate them to generate velocity measurements without unduly amplifying the noise. Therefore, we directly apply an observer of the form (4.10) which uses the $H^{\frac{1}{2}}(\widehat{\Sigma})$ or $H^1(\omega)$ discrepancy measure as proposed in [MCLT09, CCdBM11] with the *Schur Displacement Feedback* (SDF) filter. Note that in this filter of the form (4.11) the control operator $\gamma\mathcal{H}'$ does not appear as a force applying on the mechanical system, but instead modifies the velocity to displacement time-derivative identity. In fact the discrepancy measure (4.8a) or (4.8b) has as corresponding tangent operator

$$\forall \boldsymbol{d}_{\mathrm{s}} \in \mathcal{V}^d_s, \quad \mathcal{P}_{H^1(\omega)}\{x,z\}(t)(\boldsymbol{d}_{\mathrm{s}}) = \big\langle \mathrm{Ext}^{\mathrm{s}}_{\omega}(\boldsymbol{z}_d - \hat{\boldsymbol{y}}_{\mathrm{s}}|_{\omega}), \mathrm{Ext}^{\mathrm{s}}_{\omega}(\boldsymbol{d}_{\mathrm{s}}|_{\omega})\big\rangle_{\mathcal{E}^s_l}, \tag{4.15a}$$

$$\forall \boldsymbol{d}_{\mathrm{s}} \in \mathcal{V}^d_s, \quad \mathcal{P}_{H^{\frac{1}{2}}(\Sigma_0)}\{x,z\}(t)(\boldsymbol{d}_{\mathrm{s}}) = \big\langle \mathrm{Ext}^{\mathrm{s}}_{\Sigma_0}(\boldsymbol{z}_d - \hat{\boldsymbol{y}}_{\mathrm{s}}|_{\omega}), \mathrm{Ext}^{\mathrm{s}}_{\Sigma_0}(\boldsymbol{d}_{\mathrm{s}}|_{\omega})\big\rangle_{\mathcal{E}^s_l}, \tag{4.15b}$$

that, for instance for (4.15b), can be shown to be equivalent to

$$\forall \boldsymbol{d}_{\mathrm{s}} \in \mathcal{V}^d_s, \quad \mathcal{P}_{H^{\frac{1}{2}}(\Sigma_0)}\{x,z\}(t)(\boldsymbol{d}_{\mathrm{s}}) = \big\langle \mathrm{Ext}^{\mathrm{s}}_{\Sigma_0}(\boldsymbol{z}_d - \hat{\boldsymbol{y}}_{\mathrm{s}}|_{\Sigma_0}), \boldsymbol{d}_{\mathrm{s}}\big\rangle_{\mathcal{E}^s_l}, \tag{4.16}$$

using the extension characterization

$$\forall \boldsymbol{d}_{\mathrm{s}} \text{ such that } \boldsymbol{d}_{\mathrm{s}}\big|_{\Sigma_0} = 0, \quad \big\langle \mathrm{Ext}^{\mathrm{s}}_{\Sigma_0}(\boldsymbol{z}_d - \hat{\boldsymbol{y}}_{\mathrm{s}}|_{\Sigma_0}), \boldsymbol{d}_{\mathrm{s}}\big\rangle_{\mathcal{E}^s_l} = 0.$$

Similarly for (4.15a), we also have

$$\forall \boldsymbol{d}_{\mathrm{s}} \in \mathcal{V}_s^d, \quad \mathcal{P}_{H^1(\omega)}\{x,z\}(t)(\boldsymbol{d}_{\mathrm{s}}) = \big\langle \mathrm{Ext}_\omega^{\mathrm{s}}(\boldsymbol{z}_d - \hat{\boldsymbol{y}}_{\mathrm{s}}|_\omega), \boldsymbol{d}_{\mathrm{s}} \big\rangle_{\mathcal{E}_l^s}. \tag{4.17}$$

The corresponding observer consists in modifying in System (4.1) the solid formulation (4.1c) into

$$\begin{cases} \partial_t \hat{\boldsymbol{y}}_{\mathrm{s}} = \hat{\boldsymbol{u}}_s + \gamma_d \mathrm{Ext}_*^{\mathrm{s}}(\boldsymbol{z}_d - \hat{\boldsymbol{y}}_{\mathrm{s}}|_*), & \text{in} \quad \Omega_0^{\mathrm{s}}, \\ \rho_{\mathrm{s}} \partial_t \hat{\boldsymbol{u}}_{\mathrm{s}} - \eta_{\mathrm{s}} \boldsymbol{\nabla} \cdot \boldsymbol{\sigma}_{\mathrm{s}}(\hat{\boldsymbol{u}}_{\mathrm{s}}) - \boldsymbol{\nabla} \cdot \boldsymbol{\sigma}_{\mathrm{s}}(\hat{\boldsymbol{y}}_{\mathrm{s}}) = \boldsymbol{0}, & \text{in} \quad \Omega_0^{\mathrm{s}}, \\ \hat{\boldsymbol{y}}_{\mathrm{s}} = \boldsymbol{0}, & \text{on} \quad \Gamma_0^{\mathrm{d}}, \\ \eta_{\mathrm{s}} \boldsymbol{\sigma}_{\mathrm{s}}(\hat{\boldsymbol{u}}_{\mathrm{s}}) \cdot \boldsymbol{n}_{\mathrm{s}} + \boldsymbol{\sigma}_{\mathrm{s}}(\hat{\boldsymbol{y}}_{\mathrm{s}}) \cdot \boldsymbol{n}_{\mathrm{s}} = \boldsymbol{0}, & \text{on} \quad \Gamma_0^{\mathrm{n}}, \end{cases} \tag{4.18}$$

with Ext_* corresponding to Ext_ω or Ext_{Σ_0} depending on the type of observations, and γ_d the corresponding gain for the SDF. Note that such a correction can be considered for the observer $\hat{x}$ only because it is a virtual numerical system.

Energetic aspects for the observer. The dissipative character of the SDF filter can be highlighted by an energy argument, as in Proposition 5. The key point here lies in the treatment of the term $\langle \hat{\boldsymbol{y}}_{\mathrm{s}}, \hat{\boldsymbol{u}}_{\mathrm{s}} \rangle_{\mathcal{E}_l^s}$ from $(4.18)_2$, which becomes non-standard due to the perturbed displacement-velocity relation $(4.18)_1$.

We proceed as in [MCLT09], by evaluating the $\langle \cdot, \cdot \rangle_{\mathcal{E}_l^s}$-inner-product of $(4.18)_1$ with $\boldsymbol{y}_{\mathrm{s}}$. This yields the identity

$$\langle \hat{\boldsymbol{u}}_{\mathrm{s}}, \hat{\boldsymbol{y}}_{\mathrm{s}} \rangle_{\mathcal{E}_l^s} = \langle \partial_t \hat{\boldsymbol{y}}_{\mathrm{s}}, \hat{\boldsymbol{y}}_{\mathrm{s}} \rangle_{\mathcal{E}_l^s} + \gamma_d \big\langle \mathrm{Ext}_*^{\mathrm{s}}(\hat{\boldsymbol{y}}_{\mathrm{s}} - \boldsymbol{z}_d), \hat{\boldsymbol{y}}_{\mathrm{s}} \big\rangle_{\mathcal{E}_l^s}.$$

Hence, from (4.16) and (4.17), we infer that

$$\begin{aligned} \langle \hat{\boldsymbol{u}}_{\mathrm{s}}, \hat{\boldsymbol{y}}_{\mathrm{s}} \rangle_{\mathcal{E}_l^s} &= \langle \partial_t \hat{\boldsymbol{y}}_{\mathrm{s}}, \hat{\boldsymbol{y}}_{\mathrm{s}} \rangle_{\mathcal{E}_l^s} + \gamma_d \big\langle \mathrm{Ext}_*^{\mathrm{s}}(\hat{\boldsymbol{y}}_{\mathrm{s}} - \boldsymbol{z}_d), \mathrm{Ext}_*^{\mathrm{s}}(\hat{\boldsymbol{y}}_{\mathrm{s}}) \big\rangle_{\mathcal{E}_l^s} \\ &\geq \frac{1}{2} \frac{\mathrm{d}}{\mathrm{d}t} \|\hat{\boldsymbol{y}}_{\mathrm{s}}\|_{\mathcal{E}_l^s}^2 + \frac{\gamma_d}{2} \|\mathrm{Ext}_*^{\mathrm{s}}(\hat{\boldsymbol{y}}_{\mathrm{s}})\|_{\mathcal{E}_l^s}^2 - \frac{\gamma_d}{2} \|\mathrm{Ext}_*^{\mathrm{s}}(\boldsymbol{z}_d)\|_{\mathcal{E}_l^s}^2. \end{aligned}$$

Therefore, for the coupled systems (4.1a), (4.1b), (4.18), (4.1d), the identity (4.2) becomes

$$\frac{\mathrm{d}}{\mathrm{d}t} \hat{E}(t) \leq -\hat{D}(t) - \frac{\gamma_d}{2} \|\mathrm{Ext}_*^{\mathrm{s}}(\hat{\boldsymbol{y}}_{\mathrm{s}})\|_{\mathcal{E}_l^s}^2 + \frac{\gamma_d}{2} \|\mathrm{Ext}_*^{\mathrm{s}}(\boldsymbol{z}_d)\|_{\mathcal{E}_l^s}^2 - \int_{\Gamma^{\mathrm{in}} \cup \Gamma^{\mathrm{out}}} \frac{\rho_{\mathrm{f}}}{2} \hat{\boldsymbol{u}}_{\mathrm{f}} \cdot \boldsymbol{n}_{\mathrm{f}} |\hat{\boldsymbol{u}}_{\mathrm{f}}|^2 \, d\Gamma. \tag{4.19}$$

It should be noted that thanks to the stability properties of the extension operator $\mathrm{Ext}_*^{\mathrm{s}}$, the term in the right-hand side of (4.19) can be controlled by $\frac{\gamma_d}{2} \|\boldsymbol{z}_d\|_{H^1(\omega)}^2$ or by $\frac{\gamma_d}{2} \|\boldsymbol{z}_d\|_{H^{\frac{1}{2}}(\Sigma_0)}^2$, depending on the choice of the tangent operator (4.15a) or (4.15b). At last, it is worth mentioning that such energy estimates are often a valuable tool for the well-posedness analysis of this type of coupled problems (see, e.g., [Mad09] for a recent review).

Remark 11 (Coupling relations at the interface)
The modification of the relationship between the velocity and the displacement in the solid has to be carefully considered for the interaction with the fluid. First, it is desirable to preserve the kinematic compatibility at the fluid-structure interface, so we move $\Omega^{\mathrm{f}}(t)$ with an extension of the Lagrangian displacements of the solid, and not from a displacement recomputed from the solid velocity. Secondly, to get a correct energy balance, the following term has to be added to the fluid equation on Σ:

$$\frac{\rho_{\mathrm{f}}}{2}(\hat{\boldsymbol{u}}_{\mathrm{f}} - \hat{\boldsymbol{w}}) \cdot \boldsymbol{n}_{\mathrm{f}} \hat{\boldsymbol{u}}_{\mathrm{f}}$$

which is nonzero when the SDF is active, since $\hat{\boldsymbol{u}}_{\mathrm{f}}$ is obtained from $\hat{\boldsymbol{u}}_s$ while $\hat{\boldsymbol{w}}$ is obtained from the derivative of $\hat{\boldsymbol{y}}_{\mathrm{s}}$. When the standard relationship between $\hat{\boldsymbol{u}}_s$ and $\hat{\boldsymbol{y}}_{\mathrm{s}}$ holds, this additional term vanishes. It can be therefore be viewed as "strongly consistent", in the sense that it vanishes as soon as the measurements match the result of the model.

4.1.3 First numerical experiments

In order to have a first insight into the behavior and efficiency in FSI of the DVF and SDF observers, we now present two fluid-structure numerical experiments. The first one is purely illustrative, and the second one is representative of blood flows in large arteries. In Section 4.2, the estimators will be analyzed in more detail to better understand the different results obtained in this section.

All the physical quantities will be given in cgs units. In both experiments, we consider a straight tube of length 10 with diameter 1.7 and thickness 0.2 (see Figure 4.5). The solid density is $\rho_{\mathrm{s}} = 1.2$, the Young modulus is $E = 3.\,10^5$, the Poisson ratio is $\nu = 0.46$, the viscoelastic coefficient is $\eta_{\mathrm{s}} = 10^{-3}$. Fluid viscosity and density are respectively $\mu = 0.035$, $\rho_{\mathrm{f}} = 1$.

For the discretization, we apply a staggered solution to compute the fluid-structure problem, allowing to keep structure and fluid solvers independent. For the structure, we choose a Newmark scheme, whereas for the fluid we employ a semi-implicit coupling algorithm based on a Chorin-Temam projection scheme [FGG06] and detailed in Algorithm 5, Chapter 3. The viscous effects and the geometrical and convective nonlinearities are treated explicitly, and the pressure step is coupled implicitly to the solid. For the space discretization, we use conforming finite element triangulations in the fluid and solid domains, with first-order piecewise polynomials for all fluid and solid variables.

4.1.3.1 Example 1 – Stabilization at rest configuration

In the first experiment, the tube wall is clamped at the inlet and the outlet, a zero velocity is enforced at the inlet of the fluid and a zero traction is enforced at the outlet. At $t = 0$, a displacement is imposed to the solid – taken from Example

2 at maximum deformation – hence

$$\boldsymbol{y}_{\mathrm{s}}(0) \neq 0 \ , \ \boldsymbol{u}_{\mathrm{s}}(0) = 0 \ , \ \boldsymbol{y}_{\mathrm{f}}\big|_{\Sigma_0}(0) = \boldsymbol{y}_{\mathrm{s}}\big|_{\Sigma_0}(0) \ , \ \boldsymbol{w}(0) = \boldsymbol{u}_{\mathrm{f}}(0) = 0.$$

Since no external forces are applied, the system goes naturally back to equilibrium (fluid and solid at rest) due to the physical dissipation. Figure 4.2 shows the deformed domain at $t = 0$ and the time response of the radial displacement at a point of the wall.

The purpose of this test is to compare the efficiency of the DVF and the SDF at accelerating this convergence to equilibrium. The measurements are therefore assumed to be zero for the velocity and displacement at the fluid-structure interface.

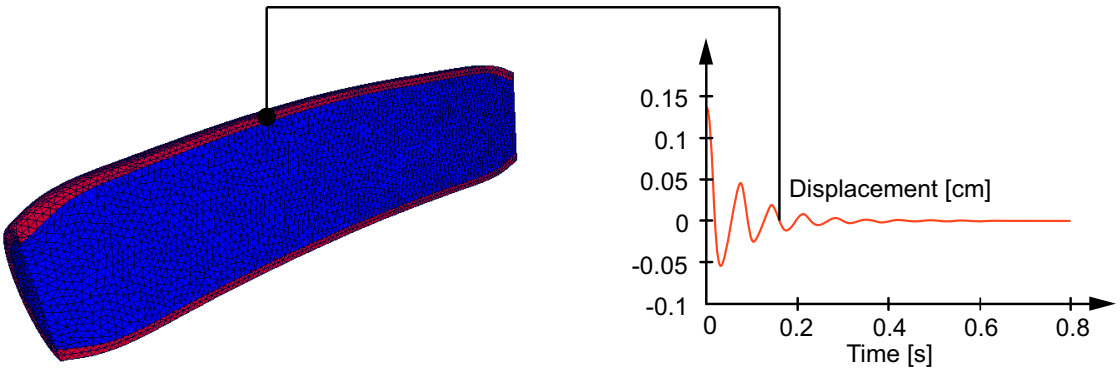

Figure 4.2: Initial deformed domain (left), displacements amplified 5 times, and time response of the displacement of one node of the wall (right).

The results are summarized in Figure 4.3 and in Figure 4.4 for the error $\tilde{x} = x^{\mathrm{ref}} - \hat{x}$ in the energy norm. To have a better insight into the effect of the feedbacks, we also plot separately the different components of the energy: elastic and kinematic in the solid and kinematic in the fluid.

Interestingly, it appears that the SDF works much better than the DVF, contrary to what is observed for pure solid experiments [MCLT09]. Indeed, even if the SDF has been designed to have performances similar to the DVF for pure solid cases (see [MCLT09] and Section 4.2.2), it does generally not outperform it. This fact is directly related to the interaction of the solid with the fluid. In Section 4.2, we will propose an explanation, and a way to significantly improve the performance of the DVF for FSI problems.

4.1.3.2 Example 2 – Cylinder with pulsatile flow

In the second experiment, a time varying parabolic velocity profile is prescribed at the inlet with a peak velocity of about 110, see Figure 4.5. At the outlet, the pressure P is assumed to be given by the Windkessel model in (4.1b) with $R_p = 400$, $R_d = 6.2 \cdot 10^3$ and $C = 2.72 \cdot 10^{-4}$.

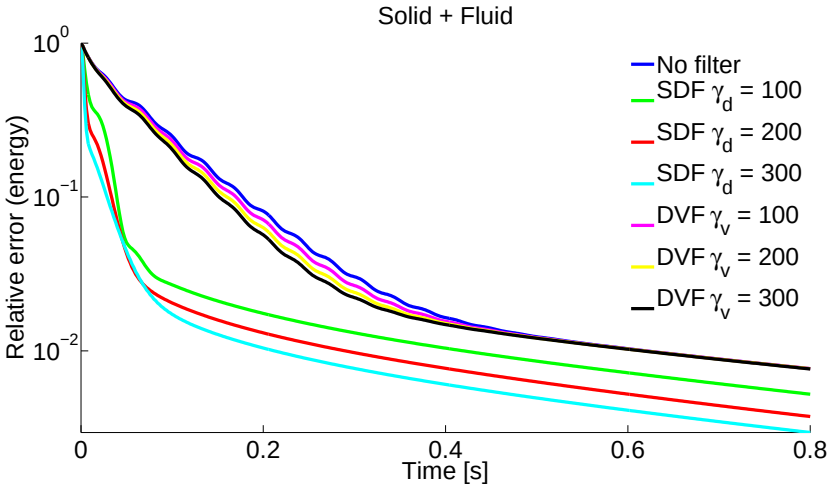

Figure 4.3: Decay of the total error in the energy norm for Example 1 (all curves are normalized with the initial energy).

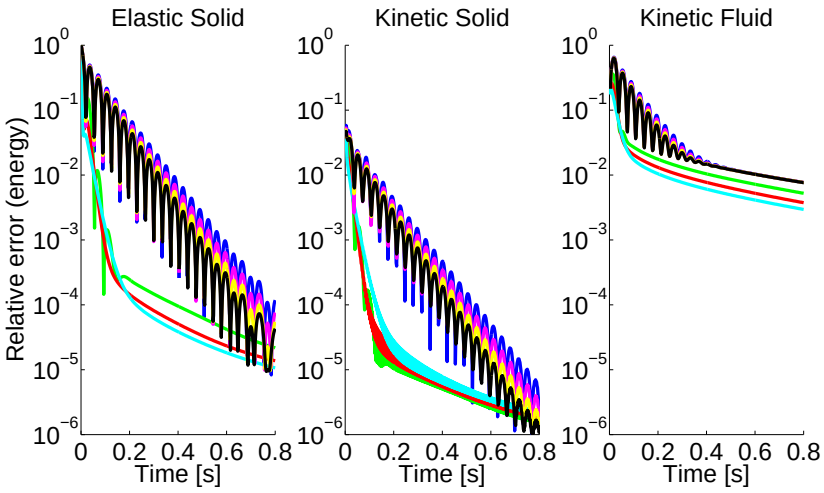

Figure 4.4: Decay of the error for solid and fluid in the energy norm for Example 1 (all curves are normalized with the initial energy). The colors correspond to the legend of Figure 4.3.

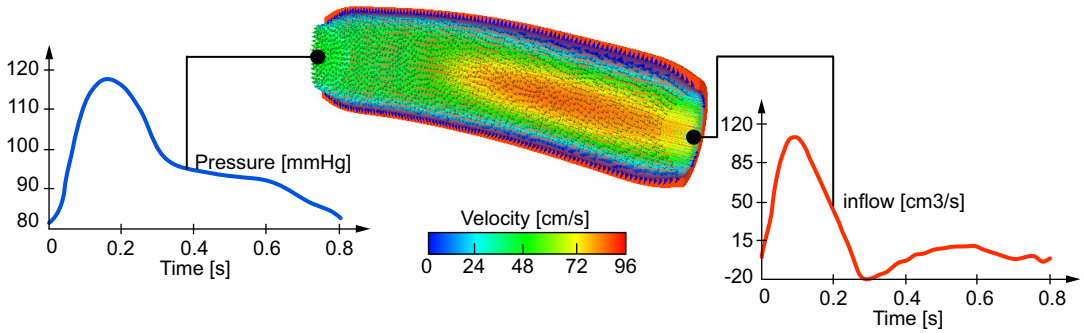

Figure 4.5: Geometry, inflow and velocity field of the straight vessel.

The reference simulation used to generate the synthetic measurements is set as follows. At $t = 0$, the pressure is constant and equal to $p(0) = 106664 \approx 80\ mmHg$, whereas all the other state variables are zero. During the whole simulation, the stress received by the structure is corrected by the initial one. Doing so, the solid only "feels" the difference with the initial phase. This is a simple way to account for the prestress in linear elastodynamics. We refer to [GFW10, MXA+11], and references therein, for a discussion about prestress computation in a more general framework.

To test the filters, we proceed as in the reference simulation until $t = 0.8$ except that a perturbation is introduced in the Windkessel pressure P at $t = 0$, i.e., $P(0) \approx 70\,mmHg$. Then a filter is applied for the second fluid-structure cycle ($0.8 \leq t \leq 1.6$). Doing so, the filter acts on a system for which all state variables are perturbed with respect to the reference simulation (see Figure 4.6).

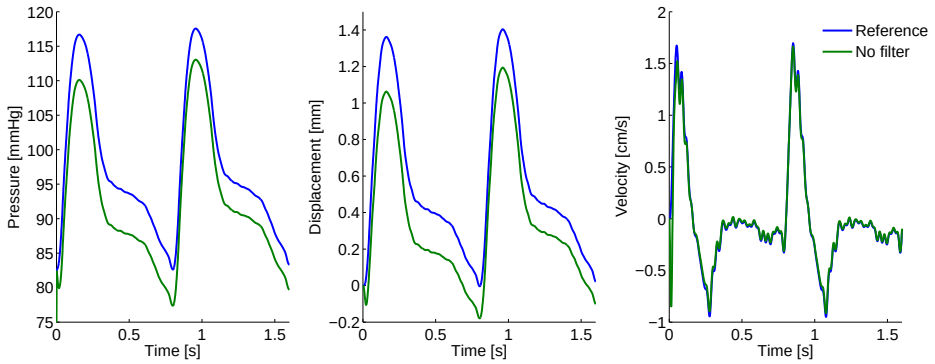

Figure 4.6: Construction of the error in the initial condition for Example 2. Value of the pressure, displacement, and velocity halfway through the vessel.

The efficiency of the Luenberger filters are compared using the energy norm of the error (including the Windkessel's energy). The results are reported in Figure 4.7 and Figure 4.8. As in the first experiment, the SDF outperforms the DVF. Note that for

the DVF and the non-filtered case, the decay rate is governed by the Windkessel time scale $R_dC \approx 1.7$. The negligible impact of the DVF on the Windkessel dynamics will be further illustrated in Section 4.2. With the SDF filter, at the very beginning the displacement correction increases the solid velocity error which propagates to the fluid velocity (see the solid and fluid kinetic energies at $t = 0.8$ in Figure 4.8). But after few milliseconds, this perturbation is quickly stabilized by the SDF filter. From about $t = 1.2\,s$, the global error is dominated by the fluid error which reaches a plateau, whereas the error in the solid and the Windkessel keeps decreasing. Again, we will propose an explanation of these observations in Section 4.2.

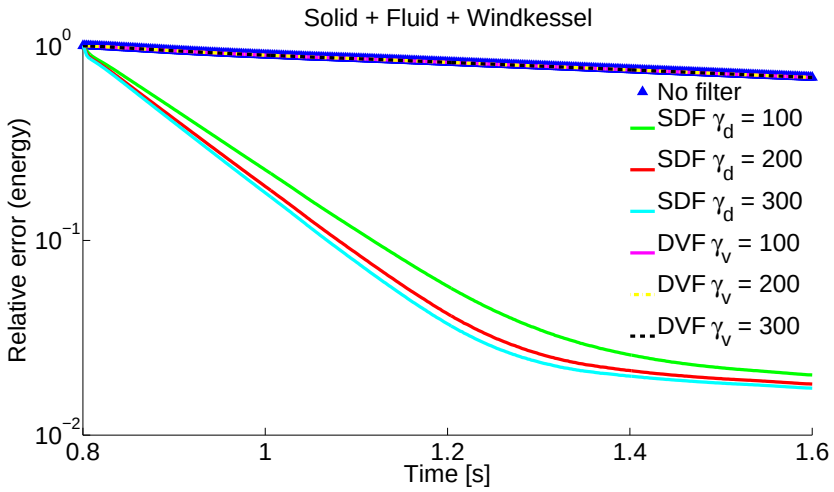

Figure 4.7: Decay of the total error in the energy norm for Example 2 (all curves are normalized with the initial energy).

Effect of noise. We now briefly comment on the effect of noise in the estimation results. Consider for example the SDF, with a Gaussian noise added to synthetic measurements. The amount of noise is chosen as a certain percentage of the maximum displacement of the reference simulation, denoted by χ in the figure legend. The results corresponding to two levels of noise are plotted in Figure 4.9, together with the quantity

$$\left\langle \mathrm{Ext}^{\mathrm{s}}_*(\chi), \mathrm{Ext}^{\mathrm{s}}_*(\chi) \right\rangle^{\frac{1}{2}}_{\mathcal{E}^s_l} \tag{4.20}$$

which represents the energy norm of the extension of the noise in the solid domain. Note that Gaussian noise is generated independently for each degree of freedom, which explains the dramatic amplification effect observed in the elastic energy norm. Nevertheless, in both cases the SDF is still capable of effectively reducing the error much below the noise level.

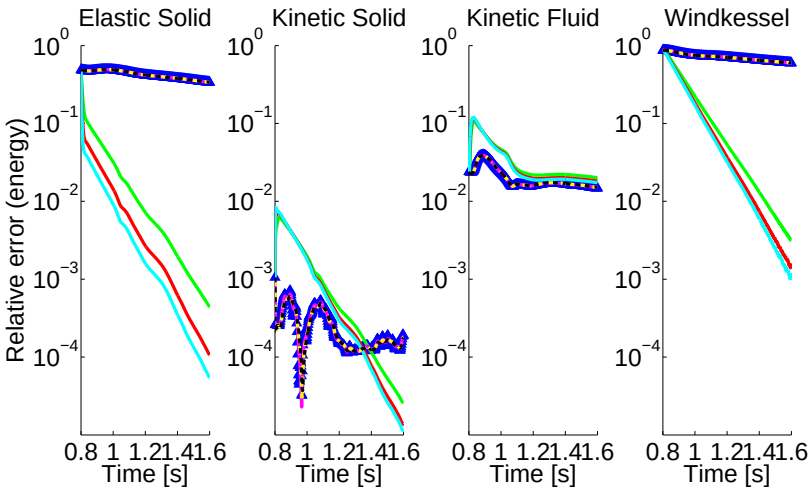

Figure 4.8: Decay of the error for solid and fluid in the energy norm for Example 2 (all curves are normalized with the initial energy). The colors correspond to the legend of Figure 4.7.

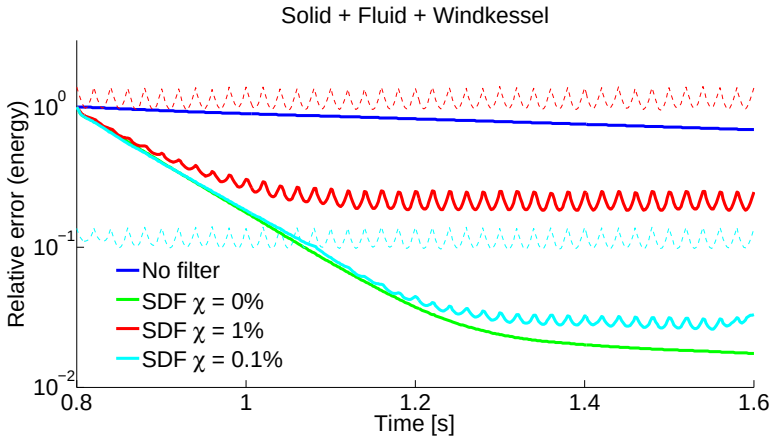

Figure 4.9: Effect of noise on the total error decay in Example 2 for the SDF with $\gamma_d = 300$. The dashed lines corresponds to formula (4.20).

4.2 Analysis of the estimators

4.2.1 General considerations

As said above, the purpose of the estimator (4.11) is to converge in time to the system (4.3), meaning that the error system denoted by

$$\tilde{x} = x^{\text{ref}} - \hat{x}$$

should stabilize to 0. For an FSI problem involving nonlinear formulations for the fluid and for the structure, the error system is a non-autonomous nonlinear system and the stabilization is therefore a largely open problem. As presented in [Cor07], a sufficient condition can be proven by studying the linearization of the error around 0, namely a linearization of the observer around the real trajectory. In the FSI case, this linearized formulation consists in assuming small displacements for the structure and fluid domains and neglecting the advection in the fluid. The problem of the stabilization to zero of FSI-systems has been addressed in various papers including models where a generic heat model is coupled to an elastic model [ZZ07]. The stabilization of the error has also been studied for particular configurations with very specific feedback terms in [Ray10].

Even for this linearized situation the complete analysis of the estimator remains largely open, both qualitatively – in terms of exponential stability – and even more quantitatively when trying to investigate the convergence time constant which purports to be much lower than the simulation time. For example the stabilization in the very recent result [GVD09] is assessed with a full dissipation on the solid, whereas here we only assume partial observations, hence partial stabilization. Therefore, we undertake a numerical study of the characteristics of our estimator to assess its performance. As is classically done – see e.g. [MCLT09] – we will compute the poles of the linearized error system. At least, this strategy will allow to distinguish good estimator candidates from dead end strategies.

We denote by capital letters the discretized state and operators of our FSI problem, and since we use standard Galerkin discretizations we still have access to the underlying variational formulation at the discrete level. We can then compute the poles of the eigenproblem

$$(A - KH)\,\widetilde{X} = \lambda \widetilde{X}, \tag{4.21}$$

associated with the dynamics of the error $\widetilde{X} = X - \widehat{X}$. The operator K discretizing $\gamma H'$ will be formalized in each case to adequately transcript the sense of the adjoint. The eigenvalue will help us quantify the decay rate – with slowest decay for highest real part. Hence, for reducing the error by a factor β in a time T_c, the feedback term should be designed so that

$$\max\{\Re(\lambda)\} \leq \frac{\ln \beta}{T_c}. \tag{4.22}$$

In cardiovascular problems and assuming, for example, that we have already around

10% of error in the initial condition, we could intend to reduce this error to around 1% (hence $\beta = 0.1$) in about $T_c \approx 0.1\,s$, considering a cardiac cycle of $1\,s$. This gives a requirement on $\max\{\Re(\lambda)\}$ of ≈ -25.

4.2.2 Pure elastodynamics

We start our investigation by recalling some results on a pure elastodynamics system. We consider a structure loaded with a given time-dependent pressures at its interface.

$$\begin{cases} \partial_t \boldsymbol{y}_\mathrm{s} = \boldsymbol{u}_\mathrm{s}, & \text{in} \quad \Omega_0^\mathrm{s}, \\ \rho_\mathrm{s}\partial_t \boldsymbol{u}_\mathrm{s} - \eta_\mathrm{s}\boldsymbol{\nabla}\cdot\boldsymbol{\sigma}_\mathrm{s}(\boldsymbol{u}_\mathrm{s}) - \boldsymbol{\nabla}\cdot\boldsymbol{\sigma}_\mathrm{s}(\boldsymbol{y}_\mathrm{s}) = \boldsymbol{0}, & \text{in} \quad \Omega_0^\mathrm{s}, \\ \boldsymbol{y}_\mathrm{s} = \boldsymbol{0}, & \text{on} \quad \Gamma_0^\mathrm{d}, \\ \eta_\mathrm{s}\boldsymbol{\sigma}_\mathrm{s}(\boldsymbol{u}_\mathrm{s})\cdot\boldsymbol{n}_\mathrm{s} + \boldsymbol{\sigma}_\mathrm{s}(\boldsymbol{y}_\mathrm{s})\cdot\boldsymbol{n}_\mathrm{s} = \boldsymbol{0}, & \text{on} \quad \Gamma_0^\mathrm{n}, \\ \eta_\mathrm{s}\boldsymbol{\sigma}_\mathrm{s}(\boldsymbol{u}_\mathrm{s})\cdot\boldsymbol{n}_\mathrm{s} + \boldsymbol{\sigma}_\mathrm{s}(\boldsymbol{y}_\mathrm{s})\cdot\boldsymbol{n}_\mathrm{s} = -p\,\boldsymbol{n}_\mathrm{s}, & \text{on} \quad \Sigma_0 \end{cases} \tag{4.23}$$

with the same notation as in Equation (4.1c). We define the finite element discretization of (4.23) on the finite dimensional subspace $\mathcal{V}_{s,h} \subset \mathcal{V}_s$ and obtain the finite dimensional dynamical system in state space form

$$\begin{bmatrix} K_\mathrm{s} & 0 \\ 0 & M_\mathrm{s} \end{bmatrix} \begin{bmatrix} \dot{Y}_\mathrm{s} \\ \dot{U}_\mathrm{s} \end{bmatrix} = \begin{bmatrix} 0 & K_\mathrm{s} \\ -K_\mathrm{s} & -C_\mathrm{s} \end{bmatrix} \begin{bmatrix} Y_\mathrm{s} \\ U_\mathrm{s} \end{bmatrix} + \begin{bmatrix} 0 \\ F \end{bmatrix}, \tag{4.24}$$

where the mass matrix M_s, stiffness matrix K_s and F are defined by

$$\begin{aligned} \forall \boldsymbol{u}_\mathrm{s}, \boldsymbol{v}_\mathrm{s} \in \mathcal{V}_{s,h}, \quad V_\mathrm{s}^\intercal M_\mathrm{s} U_\mathrm{s} &= \int_{\Omega_0^\mathrm{s}} \rho_\mathrm{s}\boldsymbol{u}_\mathrm{s}\cdot\boldsymbol{v}_\mathrm{s}\,d\Omega, \\ \forall \boldsymbol{y}_\mathrm{s}, \boldsymbol{v}_\mathrm{s} \in \mathcal{V}_{d,h}, \quad V_\mathrm{s}^\intercal K_\mathrm{s} Y_\mathrm{s} &= \int_{\Omega_0^\mathrm{s}} \boldsymbol{\sigma}_\mathrm{s}(\boldsymbol{y}_\mathrm{s}) : \boldsymbol{\varepsilon}(\boldsymbol{v}_\mathrm{s})\,d\Omega, \\ \forall \boldsymbol{v}_\mathrm{s} \in \mathcal{V}_{s,h}, \quad V_\mathrm{s}^\intercal F &= -\int_{\Sigma_0} p\,\boldsymbol{v}_\mathrm{s}\cdot\boldsymbol{n}_\mathrm{s}\,d\Gamma, \end{aligned}$$

and $C_\mathrm{s} = \eta_\mathrm{s} K_\mathrm{s}$. We used K_s in the identity written in the first line of System (4.24) in order to emphasize the norm associated with the displacement field.

4.2.2.1 Case of solid velocity measurements

For this model, assuming that some velocity measurements are available, we can define a DVF state estimator

$$\begin{cases} \partial_t \hat{\boldsymbol{y}}_\mathrm{s} = \hat{\boldsymbol{u}}_s & \text{in} \quad \Omega_0^\mathrm{s}, \\ \rho_\mathrm{s}\partial_t \hat{\boldsymbol{u}}_\mathrm{s} - \eta_\mathrm{s}\boldsymbol{\nabla}\cdot\boldsymbol{\sigma}_\mathrm{s}(\hat{\boldsymbol{u}}_\mathrm{s}) - \boldsymbol{\nabla}\cdot\boldsymbol{\sigma}_\mathrm{s}(\hat{\boldsymbol{y}}_\mathrm{s}) = \gamma_v \mathbb{1}_*(\boldsymbol{z}_v - \hat{\boldsymbol{u}}_\mathrm{s}|_*), & \text{in} \quad \Omega_0^\mathrm{s}, \\ \hat{\boldsymbol{y}}_\mathrm{s} = \boldsymbol{0}, & \text{on} \quad \Gamma_0^\mathrm{d}, \\ \eta_\mathrm{s}\boldsymbol{\sigma}_\mathrm{s}(\hat{\boldsymbol{u}}_\mathrm{s})\cdot\boldsymbol{n}_\mathrm{s} + \boldsymbol{\sigma}_\mathrm{s}(\hat{\boldsymbol{y}}_\mathrm{s})\cdot\boldsymbol{n}_\mathrm{s} = \boldsymbol{0}, & \text{on} \quad \Gamma_0^\mathrm{n}, \\ \eta_\mathrm{s}\boldsymbol{\sigma}_\mathrm{s}(\hat{\boldsymbol{u}}_\mathrm{s})\cdot\boldsymbol{n}_\mathrm{s} + \boldsymbol{\sigma}_\mathrm{s}(\hat{\boldsymbol{y}}_\mathrm{s})\cdot\boldsymbol{n}_\mathrm{s} = -p\,\boldsymbol{n}_\mathrm{s}, & \text{on} \quad \Sigma_0 \end{cases} \tag{4.25}$$

discretized into

$$\begin{bmatrix} K_\mathrm{s} & 0 \\ 0 & M_\mathrm{s} \end{bmatrix} \begin{bmatrix} \dot{\hat{Y}}_\mathrm{s} \\ \dot{\hat{U}}_\mathrm{s} \end{bmatrix} = \begin{bmatrix} 0 & K_\mathrm{s} \\ -K_\mathrm{s} & -C_\mathrm{s} - \gamma_v H_v^\intercal M_* H_v \end{bmatrix} \begin{bmatrix} \hat{Y}_\mathrm{s} \\ \hat{U}_\mathrm{s} \end{bmatrix} + \begin{bmatrix} 0 \\ F + \gamma H_v^\intercal M_* Z \end{bmatrix}, \quad (4.26)$$

where H_v is the discretization of the observation operator in $\mathcal{V}_{s,h}^v$ and M_* is the matrix associated with the L^2 norm on the measurement domain. For instance, considering measurements on the interface, we can decompose the vector of degrees of freedom U_s on the degrees of freedom of Σ_0 and the internal degrees of freedom. Then we have

$$\forall U_\mathrm{s}, \quad H_v U_\mathrm{s} = [\mathbb{1} \quad 0] \begin{bmatrix} U_{\mathrm{s},\Sigma_0} \\ U_{\mathrm{s,I}} \end{bmatrix} = U_{\mathrm{s},\Sigma_0}$$

and get

$$\forall \boldsymbol{u}_\mathrm{s}, \boldsymbol{v}_\mathrm{s} \in \mathcal{V}_{s,h}, \quad V_\mathrm{s}^\intercal H_v^\intercal M_{\Sigma_0} H_v U_\mathrm{s} = V_{\mathrm{s},\Sigma_0}^\intercal M_{\Sigma_0} U_{\mathrm{s},\Sigma_0} = \int_{\Sigma_0} \boldsymbol{u}_\mathrm{s} \cdot \boldsymbol{v}_\mathrm{s} \, d\Gamma.$$

Note that if the observations are undersampled, H_v can be seen as a projector $\Pi_{\mathcal{Z}}$ on the subspace where the observation are defined and

$$\forall \boldsymbol{u}_\mathrm{s}, \boldsymbol{v}_\mathrm{s} \in \mathcal{V}_{s,h}, \quad V_\mathrm{s}^\intercal H_v^\intercal M_{\Sigma_0} H_v U_\mathrm{s} = \int_{\Sigma_0} \Pi_{\mathcal{Z}}(\boldsymbol{u}_\mathrm{s}) \cdot \Pi_{\mathcal{Z}}(\boldsymbol{v}_\mathrm{s}) \, d\Gamma.$$

From (4.21), we deduce the associated eigenvalue problem:

$$\text{Find } (\Phi_d, \Phi_v, \lambda) \text{ such that } \begin{bmatrix} 0 & K_\mathrm{s} \\ -K_\mathrm{s} & -C_\mathrm{s} - \gamma_v H_v^\intercal M_* H_v \end{bmatrix} \begin{bmatrix} \Phi_d \\ \Phi_v \end{bmatrix} = \lambda \begin{bmatrix} K_\mathrm{s} & 0 \\ 0 & M_\mathrm{s} \end{bmatrix} \begin{bmatrix} \Phi_d \\ \Phi_v \end{bmatrix}. \quad (4.27)$$

Spectral sensitivity analysis. For the DVF, when eliminating Φ_v in (4.27), the computation of the poles can be performed by solving the following quadratic eigenvalue problem typical of the underlying second order PDE

$$\left(\lambda^2 M_\mathrm{s} + \lambda(C_\mathrm{s} + \gamma_v H_v^\intercal M_* H_v) + K_\mathrm{s}\right) \Phi_d = 0 \ , \quad (4.28)$$

The solution (λ, Φ_d) of (4.28) is a function of γ_v and we denote by (λ_0, Φ_0) the solutions for $\gamma_v = 0$. Recalling that $C_s = \eta_s K_s$, they verify

$$K_\mathrm{s}\Phi_0 = \omega_s^2 M_\mathrm{s}\Phi_0, \text{ and } \lambda_0^2 + \eta_s\omega_s^2\lambda_0 + \omega_s^2 = 0,$$

and we can normalize the modes such that $\Phi_0^\intercal M_s \Phi_0 = 1$.

Therefore, if we differentiate (4.28) with respect to γ_v and evaluate the resulting expression at $\gamma_v = 0$, we obtain

$$\left(2\lambda_0 \frac{\partial\lambda}{\partial\gamma_v}\Big|_{\gamma_v=0} M_\mathrm{s} + \lambda_0 H_v^\intercal M_* H_v + \frac{\partial\lambda}{\partial\gamma_v} C_s\right) \Phi_0 + \left(\lambda_0^2 M_\mathrm{s} + \lambda_0 C_s + K_\mathrm{s}\right) \frac{\partial\Phi}{\partial\gamma_v}\Big|_{\gamma_v=0} = 0. \quad (4.29)$$

Finally, left-multiplying by $\Phi_0^\intercal$ and using that, by definition $(\lambda_0^2 M_\mathrm{s} + \lambda_0 C_s + K_\mathrm{s})\Phi_0 = 0$, we obtain

$$\big(2 + \eta_s \frac{\omega_s^2}{\lambda_0}\big) \frac{\partial \lambda}{\partial \gamma_v}\Big|_{\gamma_v=0} = -\Phi_0^\intercal (H_v^\intercal M_* H_v)\Phi_0.$$

Then for an undamped initial structure the initial eigenvalues on the imaginary axis $\lambda_0^2 = -\omega_s^2$ are moved to the half plane of negative real parts by

$$\frac{\partial \lambda}{\partial \gamma_v}\Big|_{\gamma_v=0} = -\frac{\Phi_0^\intercal (H_v^\intercal M_* H_v)\Phi_0}{2} = -\frac{1}{2}\frac{\|H_v \Phi_0\|_{M_*}^2}{\|\Phi_0\|_{M_s}^2}.$$

Furthermore, when considering complete observations, we have $H_v = \mathbb{1}$ and we can rescale $M_* = M_\mathrm{s}$ such that

$$\frac{\partial \lambda}{\partial \gamma_v}\Big|_{\gamma_v=0} = -\frac{1}{2}. \tag{4.30}$$

4.2.2.2 Case of solid displacement measurements

Assuming now that we have at our disposal some displacement measurements, we define the SDF state estimator

$$\begin{cases} \partial_t \hat{\boldsymbol{y}}_\mathrm{s} = \hat{\boldsymbol{u}}_s + \gamma_d \mathrm{Ext}_*^s(\boldsymbol{z}_d - \hat{\boldsymbol{y}}_\mathrm{s}|_*), & \text{in} \quad \Omega_0^\mathrm{s}, \\ \rho_\mathrm{s} \partial_t \hat{\boldsymbol{u}}_\mathrm{s} - \eta_\mathrm{s} \boldsymbol{\nabla} \cdot \boldsymbol{\sigma}_\mathrm{s}(\hat{\boldsymbol{u}}_\mathrm{s}) - \boldsymbol{\nabla} \cdot \boldsymbol{\sigma}_\mathrm{s}(\hat{\boldsymbol{y}}_\mathrm{s}) = \boldsymbol{0}, & \text{in} \quad \Omega_0^\mathrm{s}, \\ \hat{\boldsymbol{y}}_\mathrm{s} = \boldsymbol{0}, & \text{on} \quad \Gamma^\mathrm{d}, \\ \eta_\mathrm{s} \boldsymbol{\sigma}_\mathrm{s}(\hat{\boldsymbol{u}}_\mathrm{s}) \cdot \boldsymbol{n}_\mathrm{s} + \boldsymbol{\sigma}_\mathrm{s}(\hat{\boldsymbol{y}}_\mathrm{s}) \cdot \boldsymbol{n}_\mathrm{s} = \boldsymbol{0}, & \text{on} \quad \Gamma_0^\mathrm{n}, \\ \eta_\mathrm{s} \boldsymbol{\sigma}_\mathrm{s}(\hat{\boldsymbol{u}}_\mathrm{s}) \cdot \boldsymbol{n}_\mathrm{s} + \boldsymbol{\sigma}_\mathrm{s}(\hat{\boldsymbol{y}}_\mathrm{s}) \cdot \boldsymbol{n}_\mathrm{s} = -p\, \boldsymbol{n}_\mathrm{s}, & \text{on} \quad \Sigma_0 \end{cases} \tag{4.31}$$

Following [MCLT09], we can compute the extension by a penalization method. We define the operator

$$L_{s,*}^\varepsilon : Z_d \to \arg\min_X \left\{ \frac{1}{2}\varepsilon X^\intercal K_s X + \frac{1}{2}\|Z_d - H_d X\|_{M_*} \right\}^2.$$

with ε a small parameter with respect to the inverse of the Young modulus of the structure, such that

$$\forall Z_d, \quad L_{s,*}^\varepsilon Z_d = (\varepsilon K_\mathrm{s} + H_d^\intercal M_* H_d)^{-1} H_d^\intercal M_* Z_d$$

is a discretization of $\mathrm{Ext}_*^\mathrm{s}(\boldsymbol{z}_d)$. Thus we have

$$\forall \boldsymbol{d}_\mathrm{s} \in \mathcal{V}_s, h \quad \big\langle \mathrm{Ext}_*^\mathrm{s}(\boldsymbol{z}_d - \hat{\boldsymbol{y}}_\mathrm{s}), \boldsymbol{d}_\mathrm{s} \big\rangle_{\mathcal{E}_l^s} = D_\mathrm{s}^\intercal K_\mathrm{s} (\varepsilon K_\mathrm{s} + H_d^\intercal M_* H_d)^{-1} H_d^\intercal M_* (Z_d - H_d Y_\mathrm{s}),$$

Therefore, the discretized system reads

$$\begin{bmatrix} (\varepsilon K_\mathrm{s} + H_d^\intercal M_* H_d) & 0 \\ 0 & M_\mathrm{s} \end{bmatrix} \begin{bmatrix} \dot{\hat{Y}}_\mathrm{s} \\ \dot{\hat{U}}_\mathrm{s} \end{bmatrix} = \begin{bmatrix} -\gamma_d H_d^\intercal M_* H_d & (\varepsilon K_\mathrm{s} + H_d^\intercal M_* H_d) \\ -K_\mathrm{s} & -C_\mathrm{s} \end{bmatrix} \begin{bmatrix} \hat{Y}_\mathrm{s} \\ \hat{U}_\mathrm{s} \end{bmatrix} + \begin{bmatrix} \gamma_d H_d^\intercal M_* Z \\ F \end{bmatrix}, \tag{4.32}$$

and the associated eigenvalue problem becomes

Find $(\Phi_d, \Phi_v, \lambda)$ such that

$$\begin{bmatrix} -\gamma_d H_d^\intercal M_* H_d & (\varepsilon K_\mathrm{s} + H_d^\intercal M_* H_d) \\ -K_\mathrm{s} & -C_\mathrm{s} \end{bmatrix} \begin{bmatrix} \Phi_d \\ \Phi_v \end{bmatrix} = \lambda \begin{bmatrix} (\varepsilon K_\mathrm{s} + H_d^\intercal M_* H_d) & 0 \\ 0 & M_\mathrm{s} \end{bmatrix} \begin{bmatrix} \Phi_d \\ \Phi_v \end{bmatrix} \tag{4.33}$$

Spectral sensitivity analysis. For the SDF, the eigenvalue problem can also be solved using a quadratic eigenvalue problem inferred from (4.33) which takes the form

$$\left(\lambda^2 M_\mathrm{s} + \lambda(C_\mathrm{s} + \gamma_d M_\mathrm{s} L_{s,*}^\varepsilon H_d) + K_\mathrm{s} + \gamma_d C_\mathrm{s} L_{s,*}^\varepsilon H_d\right) \Phi_d = 0, \tag{4.34}$$

and note that in presence of viscosity the SDF adds stiffness to the system. The solutions of (4.34) for $\gamma_d = 0$, are still given by (λ_0, Φ_0) the solutions of the DVF quadratic eigenvalue problem with $\gamma_v = 0$. In the case of $\eta_\mathrm{s} = 0$ we verify that

$$\frac{\partial \lambda}{\partial \gamma_d}\Big|_{\gamma_d=0} = -\frac{\Phi_0^\intercal M_\mathrm{s} L_{s,*}^\varepsilon H_d \Phi_0}{2}$$

Then by recalling that $K_\mathrm{s}\Phi_0 = \omega_s^2 M_\mathrm{s}\Phi_0$, we obtain

$$\Phi_0^\intercal M_\mathrm{s} L_{s,*}^\varepsilon H_d \Phi_0 = \frac{1}{\omega_s^2} \Phi_0^\intercal K_\mathrm{s} (\varepsilon K_\mathrm{s} + H_d^\intercal M_* H_d)^{-1} H_d^\intercal M_* H_d \Phi_0$$

in which $K_\mathrm{s}(\varepsilon K_\mathrm{s} + H_d^\intercal M_* H_d)^{-1} H_d^\intercal M_* H_d = K_\mathrm{s} L_{s,*}^\varepsilon H_d$ is symmetric positive as established in [MCLT09]. In fact, note that all D_s associated with $\boldsymbol{d}_\mathrm{s} \in \mathcal{V}_{s,h}$ can be trivially decomposed as

$$D_s = D_s^\sharp + L_{s,*}^\varepsilon H_d D_s \ , \ D_s^\sharp = D_s - L_{s,*}^\varepsilon H_d D_s$$

so that it holds $H_d(D_s^\sharp) = 0$. We have then the identity for all data vector Z_d

$$(D_s^\sharp)^\intercal (\varepsilon K_\mathrm{s} + H_d^\intercal M_* H_d) L_{s,*}^\varepsilon Z_d = (D_s^\sharp)^\intercal H_d^\intercal M_* Z_d = 0$$

which is the counterpart of the continuous identity (4.15a). From this follows that $(D_s^\sharp)^\intercal K_\mathrm{s} L_{s,*}^\varepsilon Z_d = 0$, and hence for all D_s it holds

$$D_s^\intercal K_\mathrm{s} L_{s,*}^\varepsilon H_d D_s = (L_{s,*}^\varepsilon H_d D_s)^\intercal K_\mathrm{s} L_{s,*}^\varepsilon H_d D_s$$

which allows to rewrite

$$\frac{\partial \lambda}{\partial \gamma_d}\Big|_{\gamma_d=0} = -\frac{\Phi_0^\intercal H_d^\intercal (L_{s,*}^\varepsilon)^\intercal K_\mathrm{s} L_{s,*}^\varepsilon H_d \Phi_0}{2\omega_s^2} = -\frac{1}{2}\frac{\|L_{s,*}^\varepsilon (H_d \Phi_0)\|_{K_s}^2}{\|\Phi_0\|_{K_s}^2}. \tag{4.35}$$

In the last expression we retrieve the norm of the lifting of the observed part of a vector as it appeared in the continuous energy balance (4.19). Hence, when considering

complete observations, we have for the SDF in elastodynamics

$$\frac{\partial \lambda}{\partial \gamma_d}\Big|_{\gamma_d=0} = -\frac{1}{2}, \tag{4.36}$$

as we had for the DVF.

4.2.2.3 Spectral numerical experiments

We now verify numerically the analytical observations of the previous paragraph by means of a spectral analysis. For the computations, we consider the geometry and parameters of Section 4.1.3. In Figure 4.10, we report the corresponding 10 poles of smallest modulus for different values of the gains γ_d and γ_v.

As expected from the sensitivity analysis of the previous paragraph, both filters have a similar behavior with respect to the gain when considering full observations. Moreover, we observe that the SDF adds some slight stiffness due to the presence of damping in the system, particularly for the highest frequency poles. For large values of the gains, the trajectory of the poles agree with the results presented in [MCLT08, MCLT09].

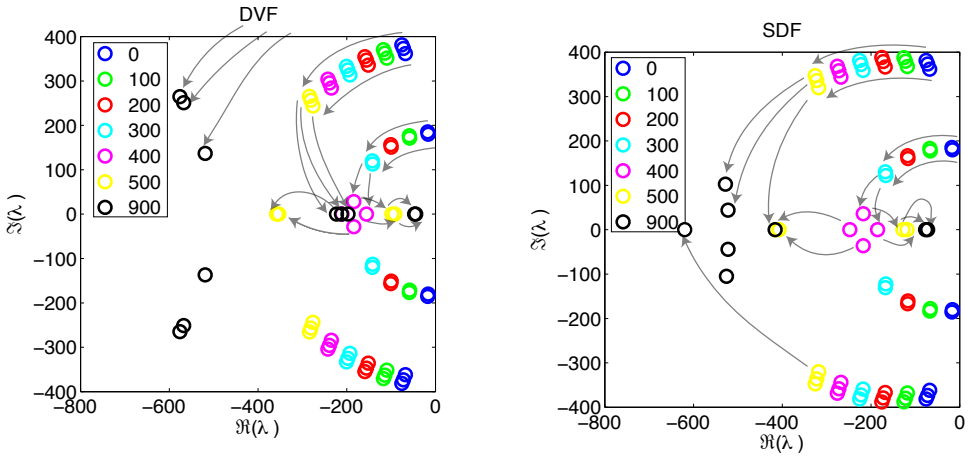

Figure 4.10: Poles of the DVF (left) and the SDF (right) estimators in elastodynamics with full observation and for different values of the gain. The grey arrows sketch the trajectory of the poles when increasing feedback gain.

4.2.3 Added mass effect for elastodynamics coupled with potential flow

We now investigate the impact of the fluid coupling on the filters performance, by first considering an inviscid incompressible fluid. Hence, the forcing pressure p

in Equation (4.23) is driven by the following elliptic problem

$$\begin{cases} -\Delta p = 0, & \text{in} \quad \Omega_0^{\mathrm{f}}, \\ \boldsymbol{\nabla} p \cdot \boldsymbol{n}_{\mathrm{f}} = 0, & \text{on} \quad \Gamma^{\mathrm{in}}, \\ p = 0, & \text{on} \quad \Gamma^{\mathrm{out}} \end{cases} \tag{4.37}$$

with $\Omega_0^{\mathrm{f}} = \Omega_{\mathrm{f}}(0)$ and the interface coupling conditions reduce to

$$\begin{cases} \boldsymbol{\nabla} p \cdot \boldsymbol{n}_{\mathrm{f}} = -\rho_{\mathrm{f}} \partial_t \boldsymbol{u}_{\mathrm{s}} \cdot \boldsymbol{n}_{\mathrm{f}}, & \text{on} \quad \Sigma, \\ \eta_{\mathrm{s}} \boldsymbol{\sigma}_{\mathrm{s}}(\boldsymbol{u}_{\mathrm{s}}) \cdot \boldsymbol{n}_{\mathrm{s}} + \boldsymbol{\sigma}_{\mathrm{s}}(\boldsymbol{y}_{\mathrm{s}}) \cdot \boldsymbol{n}_{\mathrm{s}} - p\, \boldsymbol{n}_{\mathrm{f}} = \boldsymbol{0}, & \text{on} \quad \Sigma_0. \end{cases} \tag{4.38}$$

Although simplified, it is well known that the coupled problem derived from (4.23)-(4.37)-(4.38) contains some of the main features involved in FSI in blood flows, particularly, the so-called added-mass effect (see e.g. [CGN05]).

After discretization in space, we get the following system of ordinary differential equations:

$$\begin{bmatrix} K_{\mathrm{s}} & 0 \\ 0 & M_{\mathrm{s}} + M_A \end{bmatrix} \begin{bmatrix} \dot{Y}_{\mathrm{s}} \\ \dot{U}_{\mathrm{s}} \end{bmatrix} = \begin{bmatrix} 0 & K_{\mathrm{s}} \\ -K_{\mathrm{s}} & -C_{\mathrm{s}} \end{bmatrix} \begin{bmatrix} Y_{\mathrm{s}} \\ U_{\mathrm{s}} \end{bmatrix}, \tag{4.39}$$

where M_A denotes the discrete version of the added-mass operator, given by

$$M_A = \rho_{\mathrm{f}} G K_p^{-1} G^{\intercal}.$$

Here, K_p and stand for the finite element matrices of the Laplacian and G is associated to the boundary term

$$\forall P \in \mathcal{V}_{p,h},\, U_s \in \mathcal{V}_{s,h}, \quad U_{\mathrm{s}}^{\intercal} G P = \int_{\Sigma_0} p\, \boldsymbol{u}_{\mathrm{s}} \cdot \boldsymbol{n}_{\mathrm{f}}\, d\Gamma. \tag{4.40}$$

Then, we can straightforwardly repeat the analysis performed in Section 4.2.2. Hence, the eigenproblems associated to the DVF and SDF estimators are obtained from (4.27) and (4.33) by simply replacing M_{s} by $M_{\mathrm{s}} + M_A$ in the right-hand side.

4.2.3.1 The added mass effect on stabilization efficiency

We now investigate the impact of the added-mass operator M_A on the effectiveness of the estimators, by analyzing the sensitivity of the eigenvalues of these systems with respect to the filter gains γ_d and γ_v. According to the previous paragraph, we can write the quadratic eigenvalue problems as

$$\left(\lambda^2 (M_{\mathrm{s}} + M_A) + \lambda (C_{\mathrm{s}} + \gamma_v H_v^{\intercal} M_* H_v) + K_{\mathrm{s}}\right) \Phi_d = 0 \tag{4.41}$$

for the DVF, and

$$\left(\lambda^2 (M_{\mathrm{s}} + M_A) + \lambda \big(C_{\mathrm{s}} + \gamma_d (M_{\mathrm{s}} + M_A) L_{s,*}^{\varepsilon} H_d\big) + K_{\mathrm{s}} + \gamma_d C_{\mathrm{s}} L_{s,*}^{\varepsilon} H_d\right) \Phi_d = 0\ , \tag{4.42}$$

for the SDF. Assuming again $C_\mathrm{s} = 0$ and introducing, this time, the eigenmodes $\Phi_{0,a}$ satisfying

$$K_\mathrm{s}\Phi_{0,a} = \omega_a^2(M_\mathrm{s} + M_A)\Phi_{0,a},\ \lambda_0^2 = -\omega_a^2,\ \Phi_{0,a}^\intercal(M_\mathrm{s} + M_A)\Phi_{0,a} = 1. \tag{4.43}$$

the sensitivities become for the DVF

$$\frac{\partial\lambda}{\partial\gamma_v}\Big|_{\gamma_v=0} = -\frac{\Phi_{0,a}^\intercal(H_v^\intercal M_* H_v)\Phi_{0,a}}{2} = -\frac{1}{2}\frac{\|H_v\Phi_{0,a}\|^2_{M_*}}{\|\Phi_{0,a}\|^2_{M_s+M_A}}.$$

Then, for the SDF we comparatively obtain

$$\begin{aligned}\frac{\partial\lambda}{\partial\gamma_d}\Big|_{\gamma_d=0} &= -\frac{\Phi_{0,a}^\intercal\big((M_\mathrm{s} + M_A)L_{s,*}^\varepsilon H_d\big)\Phi_{0,a}}{2} = \frac{\Phi_{0,a}^\intercal\big(K_\mathrm{s}L_{s,*}^\varepsilon H_d\big)\Phi_{0,a}}{2\omega_a^2} \\ &= -\frac{\Phi_{0,a}^\intercal H_d^\intercal(L_{s,*}^\varepsilon)^\intercal K_\mathrm{s}L_{s,*}^\varepsilon H_d\Phi_{0,a}}{2\omega_a^2} = -\frac{1}{2}\frac{\|L_{s,*}^\varepsilon(H_d\Phi_{0,a})\|^2_{K_s}}{\|\Phi_{0,a}\|^2_{K_s}}\end{aligned}$$

for the SDF. Note that, by construction of the estimator, the DVF does not include the added-mass matrix in the expression of the sensitivity, while the SDF does. This is the reason why the SDF can outperform the DVF in FSI problems.

To emphasize this point, let us consider a case with complete observations. The sensitivities of the DVF applied to the simplified FSI problem become

$$\frac{\partial\lambda}{\partial\gamma_v}\Big|_{\gamma_v=0} = -\frac{\Phi_{0,a}^\intercal M_\mathrm{s}\Phi_{0,a}}{2} = -\frac{1}{2}\left(1 - \frac{\|\Phi_{0,a}\|^2_{M_A}}{\|\Phi_{0,a}\|^2_{M_s+M_A}}\right), \tag{4.44}$$

to be compared with (4.30) in the pure elastodynamics case. For the problems of interest, for some modes $\Phi_{0,a}^\intercal M_A\Phi_{0,a}$ is close to 1 (see Table 4.1). Thus, the sensitivity is close to zero, which explains the poor behavior of the DVF in the FSI test case presented in Example 1 (Section 4.1.3.1). On the contrary, for the SDF applied to the simplified FSI problem, the sensitity remains:

$$\frac{\partial\lambda}{\partial\gamma_d}\Big|_{\gamma_d=0} = -\frac{1}{2}, \tag{4.45}$$

as in the pure elastodynamics case (4.36).

4.2.3.2 Spectral numerical experiments

The difference of performances can be also understood in Figure 4.11, where the poles of the DVF and the SDF are displayed for different values of gains. As shown in the sensitivity analysis, the SDF is capable to uniformly stabilize the poles. By contrast, the performance of the DVF depends on the added-mass contribution $\Phi_{0,a}^\intercal M_A\Phi_{0,a}$, whose values are shown in Table 4.1. In fact, the response in Example 1 (see Figure 4.3-right) is dominated by the first frequency ($\Im(\lambda_0) = 98$), which confirms the hypothesis of the impact of the added-mass in the performance of the

DVF in this test case.

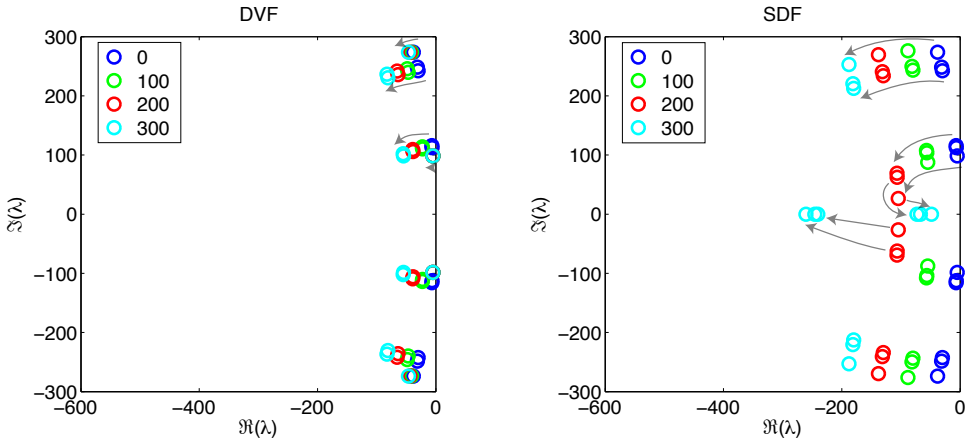

Figure 4.11: Poles of the DVF (left) and the SDF (right) estimators for the elastodynamics/pressure system, with full observation and for different values of the gain.

$\Phi_{0,a}^\intercal M_A \Phi_{0,a}$	0.99	0.61	0.61	0.59	0.58	0.93
frequency ω_a	98	112	116	244	250	276

Table 4.1: Values of coefficient $\Phi_{0,a}^\intercal M_A \Phi_{0,a}$ for the example of Figure 4.11.

4.2.3.3 The DVFam filter improvement for solid velocity measurements

To improve the performance of the DVF in FSI problems, we propose to modify the scalar product used to define the adjoint $\mathcal{H}'$ in (4.10). The DVF designed for elastodynamics problem was based on the standard L^2 scalar product. For FSI problems, we advocate to include the added-mass operator defining a new filter, that will be called DVFam. Whereas the matrix of the DVF was defined by $H_v^\intercal M_* H_v$, the matrix of the DVFam filter is given by:

$$H_v^\intercal (M_* + H_v M_A H_v^\intercal) H_v. \tag{4.46}$$

Repeating *mutatis mutandis* the sensitivity analysis, and assuming complete observations, we can check that

$$\left.\frac{\partial \lambda}{\partial \gamma_v}\right|_{\gamma_v=0} = -\frac{1}{2}, \tag{4.47}$$

with the DVFam. This is a clear improvement compared to (4.44). The spectral analysis reported on Figure 4.12 confirms this behavior.

In practice, to avoid the direct calculation of the added-mass matrix, one can

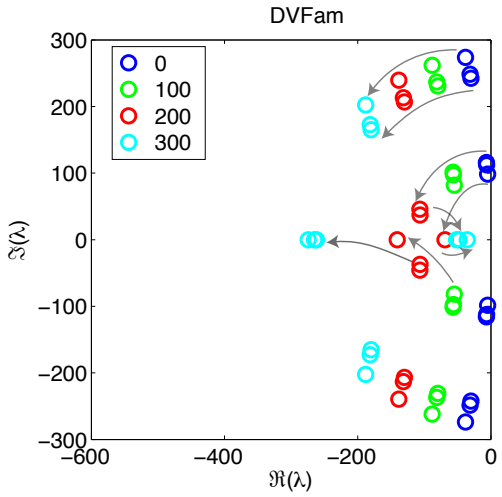

Figure 4.12: Performance of the DVFam filter. Observe the improvement with the respect to the DVF in Figure 4.11, left.

extend the filtered structural system as follows:

$$\begin{bmatrix} K_{\mathrm{s}} & 0 & 0 \\ 0 & M_{\mathrm{s}} & 0 \\ 0 & 0 & 0 \end{bmatrix} \begin{bmatrix} \dot{\widehat{Y}}_{\mathrm{s}} \\ \dot{\widehat{U}}_{\mathrm{s}} \\ \dot{\Lambda} \end{bmatrix}$$
$$= \begin{bmatrix} 0 & K_{\mathrm{s}} & 0 \\ -K_{\mathrm{s}} & -C_{\mathrm{s}} - \gamma_v H_v^{\intercal} M_* H_v & \gamma_v \rho_{\mathrm{f}} H_v^{\intercal} H_v G \\ 0 & -G^{\intercal} H_v^{\intercal} H_v & -K_p \end{bmatrix} \begin{bmatrix} \widehat{Y}_{\mathrm{s}} \\ \widehat{U}_{\mathrm{s}} \\ \Lambda \end{bmatrix} + \begin{bmatrix} 0 \\ \gamma_v H_v^{\intercal} M_* Z + F \\ G^{\intercal} H_v^{\intercal} Z \end{bmatrix}, \quad (4.48)$$

where F denotes the forces coming from the fluid. A less expensive solution would be to use an approximation of the added-mass operator, but this option will not be considered here.

To test this new filter in a nonlinear case with partial observations, we consider again Example 1. The results are presented in Figure 4.13. We observe that the performance of the DVFam filter is similar to the SDF, and much better than the DVF. Note that, for this test case, the added-mass term in the definition of the DVFam filter was not updated to account for the fluid domain deformation.

4.2.4 Elastodynamics-pressure coupling with lumped-parameter model

In hemodynamics, the Windkessel model plays an important role to define the outflow boundary conditions. To better understand its influence on the behavior of the filters, we consider the coupled fluid-structure problem (4.23)-(4.37)-(4.38)

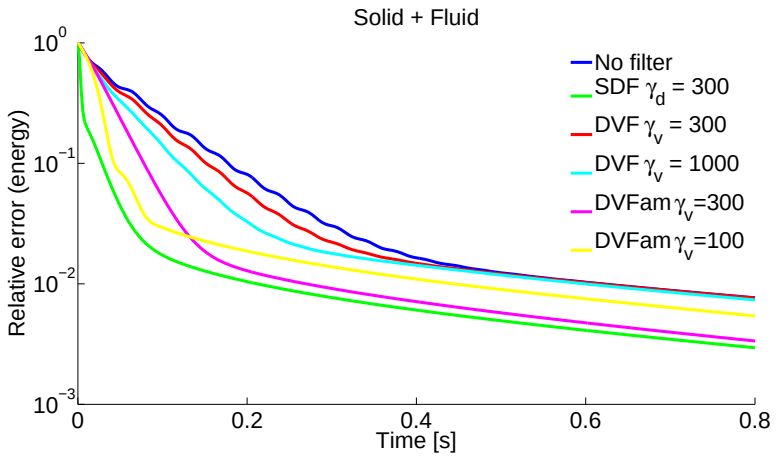

Figure 4.13: Comparison between DVFam, DVF and SDF in Example 1.

in which $p = P$ on Γ^{out}, where P is the Windkessel proximal pressure. We couple then this system with the Windkessel distal pressure model π from equations (4.1b) where the outlet flux Q can be obtained here from the structure displacement

$$Q = -\int_{\Sigma_0} \boldsymbol{u}_{\text{s}} \cdot \boldsymbol{n}_{\text{f}}\, d\Gamma,$$

since there is no inflow on Γ^{in} (recall $(4.37)_2$). After spatial discretization, there exists an operator D such that

$$Q = -D^{\intercal} U_{\text{s}}$$

and we verify that the boundary term G defined in (4.40) verifies $D = -G(1 \ldots 1)^{\intercal}$. In the principle of virtual work, the additional virtual power associated with the new pressure condition $p = P$ on Γ^{out} is then given by

$$\begin{aligned} \forall \boldsymbol{v}_s \in \mathcal{V}_s, \quad \int_{\Sigma_0} P\boldsymbol{v}_{\text{s}} \cdot \boldsymbol{n}_{\text{f}}\, d\Gamma &= \int_{\Sigma_0} (\pi + R_p Q)\boldsymbol{v}_{\text{s}} \cdot \boldsymbol{n}_{\text{f}}\, d\Gamma \\ &= \int_{\Sigma_0} \pi \boldsymbol{v}_{\text{s}} \cdot \boldsymbol{n}_{\text{f}}\, d\Gamma + R_p Q \int_{\Sigma_0} \boldsymbol{v}_{\text{s}} \cdot \boldsymbol{n}_{\text{f}}\, d\Gamma \end{aligned}$$

which discretizes into

$$\forall v_s \in \mathcal{V}_{h,s}, \quad \int_{\Sigma_0} P\boldsymbol{v}_{\text{s}} \cdot \boldsymbol{n}_{\text{f}}\, d\Gamma = V_s^{\intercal}\Big(-R_p D \cdot D^T U_s + D\pi\Big)$$

leading to the spatial discretization

$$\begin{bmatrix} K_\mathrm{s} & 0 & 0 \\ 0 & M_\mathrm{s}+M_A & 0 \\ 0 & 0 & C \end{bmatrix} \begin{bmatrix} \dot{Y}_\mathrm{s} \\ \dot{U}_\mathrm{s} \\ \dot{\pi} \end{bmatrix} = \begin{bmatrix} 0 & K_\mathrm{s} & 0 \\ -K_\mathrm{s} & -C_\mathrm{s}-R_pD\cdot D^\intercal & D \\ 0 & -D^\intercal & -\frac{1}{R_d} \end{bmatrix} \begin{bmatrix} Y_\mathrm{s} \\ U_\mathrm{s} \\ \pi \end{bmatrix} . \tag{4.49}$$

Note that the system (4.49) is clearly dissipative and the energy dissipation associated with the Windkessel is directly $\frac{\pi^2}{R_d} + R_pQ^2$ as in (4.2).

4.2.4.1 Spectral sensitivity analysis

The DVF case. The solid-pressure-windkessel modal system with he DVF reads

$$\begin{cases} K_\mathrm{s}\Phi_v = \lambda K_\mathrm{s}\Phi_d \\ -K_\mathrm{s}\Phi_d - (\gamma_v(H_v^\intercal M_* H_v) + R_pDD^\intercal)\Phi_v + D\Phi_\pi = \lambda(M_\mathrm{s}+M_A)\Phi_v \\ -D^\intercal\Phi_v - \frac{1}{R_d}\Phi_\pi = \lambda C\Phi_\pi \end{cases} \tag{4.50}$$

assuming $\eta_\mathrm{s} = 0$ for the sake of clearness. Rewriting it only in terms of Φ_d, it leads to the following cubic eigenvalue problem

$$\{(1+\lambda\tau)K_\mathrm{s} + (\lambda(R_d+R_p)+R_p\tau\lambda^2)DD^\intercal + (\lambda^2+\lambda^3\tau)(M_\mathrm{s}+M_A)\dots \\ +\gamma_v(\lambda+\lambda^2\tau)(H_v^\intercal M_* H_v)\}\Phi_d = 0, \tag{4.51}$$

with $\tau \overset{\text{def}}{=} R_dC$. As done previously, we can compute the sensitivity of λ with respect to γ_v by implicit derivation of Equation (4.51), then pre-multiplying by $\Phi_{0,w}^\mathsf{H}$ (note that the modes may be now complex) and evaluating at $\gamma_v = 0$ obtaining

$$\left.\frac{\partial\lambda}{\partial\gamma_v}\right|_{\gamma_v=0} = \frac{-(\lambda_0^2\tau+\lambda_0)\|\Phi_{0,w}\|_{M_*}^2}{3\lambda_0^2\tau + 2\lambda_0 + \tau\mathcal{E}_{k,0} + (R_d+R_p+2\lambda_0\tau R_p)|D^\intercal\Phi_{0,w}|^2}. \tag{4.52}$$

Here, $(\lambda_0, \Phi_{0,w})$ denotes the solution to the cubic eigenvalue problem (4.51) with $\gamma_v = 0$, $\mathcal{E}_{k,0} \overset{\text{def}}{=} \Phi_{0,w}^\mathsf{H} K_\mathrm{s}\Phi_{0,w}$ and the normalization is chosen as $\Phi_{0,w}^\mathsf{H}(M_\mathrm{s}+M_A)\Phi_{0,w} = 1$. Note that in the absence of Windkessel's model, namely $R_p = R_d = C = 0$, we recover the sensitivity of the precedent section.

The SDF case. The eigenvalue problem for the case with SDF reads

$$\begin{cases} K_\mathrm{s}\Phi_v = \lambda K_\mathrm{s}\Phi_d + \gamma_d K_\mathrm{s} L_{s,*}^\varepsilon H_d\Phi_d \\ -K_\mathrm{s}\Phi_d - R_pDD^\intercal\Phi_v + D\Phi_\pi = \lambda(M_\mathrm{s}+M_A)\Phi_v \\ -D^\intercal\Phi_v - \frac{1}{R_d}\Phi_\pi = \lambda C\Phi_\pi \end{cases} \tag{4.53}$$

which rewritten only in terms of Φ_d leads to the following cubic eigenvalue problem

$$\{(1+\lambda\tau)K_{\mathrm{s}} + (\lambda(R_d+R_p)+R_p\tau\lambda^2)DD^{\intercal} + (\lambda^2+\lambda^3\tau)(M_{\mathrm{s}}+M_A) + \dots \\ \gamma_d((R_d+R_p+\lambda\tau R_p)DD^T + (\lambda+\lambda^2\tau)(M_{\mathrm{s}}+M_A))L^{\varepsilon}_{s,*}H_d\}\Phi_d = 0. \quad (4.54)$$

Hence, the sensitivity of the poles with respect to filter gain results

$$\left.\frac{\partial\lambda}{\partial\gamma_d}\right|_{\gamma_d=0} = -\frac{\Phi^{\mathsf{H}}_{0,w}\{(R_d+(1+\lambda_0\tau)R_p)DD^{\intercal}+(\lambda_0^2\tau+\lambda_0)(M_{\mathrm{s}}+M_A)\}L^{\varepsilon}_{s,*}H_d\Phi_{0,w}}{3\lambda_0^2\tau+2\lambda_0+\tau\mathcal{E}_k+(R_d+R_p+2\lambda_0\tau R_p)|D^{\intercal}\Phi_{0,w}|^2}. \quad (4.55)$$

Note that using (4.54) for $\gamma_d = 0$ and the relation inferred in (4.35) we can rewrite (4.55) as

$$\left.\frac{\partial\lambda}{\partial\gamma_d}\right|_{\gamma_d=0} = \frac{(1/\lambda_0+\tau)\|L^{\varepsilon}_{s,*}(H_d\Phi_{0,w})\|^2_{K_s}}{3\lambda_0^2\tau+2\lambda_0+\tau\mathcal{E}_k+(R_d+R_p+2\lambda_0\tau R_p)|D^{\intercal}\Phi_{0,w}|^2}. \quad (4.56)$$

4.2.4.2 Spectral numerical experiments

Figure 4.14 shows the spectrum locus for the discrete DVFam and SDF estimators for values of R_{p}, R_{d} and C taken as in Example 2 and considering complete observations. We observe that the DVFam has a negligible effect on first real pole (called "Windkessel pole" in the figure), unlike the SDF which appears to be quite effective, see Figure 4.15.

In order to further compare the impact of both DVFam and SDF on the Windkessel pole, it is useful to write Formulas (4.52) and (4.56) for the case of complete observations. Moreover, it is reasonable to assume that the solid mode $\Phi_{0,w}$ associated with the Windkessel pole has a similar shape as the first mode of the solid-added mass system $\Phi_{0,a}$. Since both modes are normalized to the total mass matrix M_s+M_A, the numerators for the sensitivities become in this situation $-(\tau+1/\lambda_0)\lambda_0^2$ for the DVFam and $(\tau+1/\lambda_0)\omega_a^2$ for the SDF. This evidences first, the different sign of both sensitivities, and second, the different amplitude since $\lambda_0^2 = O(0.5^2)$ and $\omega_a^2 = O(100^2)$.

Concerning the sign of the sensitivities for the real poles, generally the denominators in (4.52) and (4.56) are positive for values of the physical parameters used in hemodynamics. Finally, it can be verified that first real pole λ_0 satisfies $\lambda_0 \approx -1/(R_d(C+C_{3D}))$, with C_{3D} the additional capacitance introduced by the three-dimensional solid. Thus, it usually holds that $\tau + 1/\lambda_0 \approx -R_dC_{3D} < 0$.

Remark 12 (Windkessel's observer)
One way to further stabilize the pole resulting from the Windkessel coupling is to make use of additional measurements on P or π. Hence, we can formulate the observers

$$\tau\dot{\hat{\pi}} + \hat{\pi} = R_{\mathrm{d}}\hat{Q} + \gamma_\pi(z_\pi - \hat{\pi}), \quad (4.57)$$

and

$$\tau\dot{\hat{P}} + \hat{P} = (R_{\mathrm{d}}+R_{\mathrm{p}})\hat{Q} + \tau R_{\mathrm{p}}\dot{\hat{Q}} + \gamma_p(z_P - \hat{P}), \quad (4.58)$$

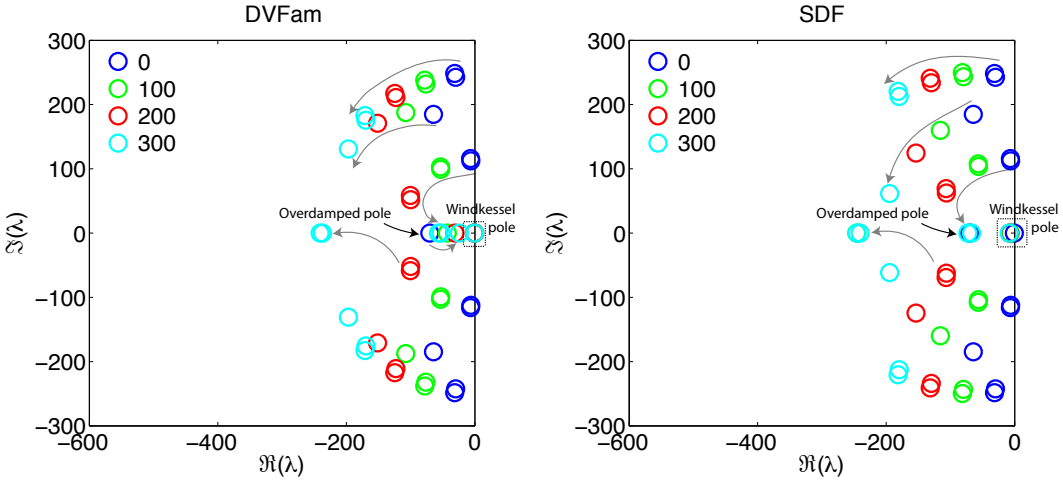

Figure 4.14: Poles of the DVFam (left) and the SDF (right) estimators (elastodynamics-pressure coupling with lumped-parameter model) with full observation and for different values of the gain. The pole marked as "overdamped" appears due to the damping introduced by the Windkessel's resistances.

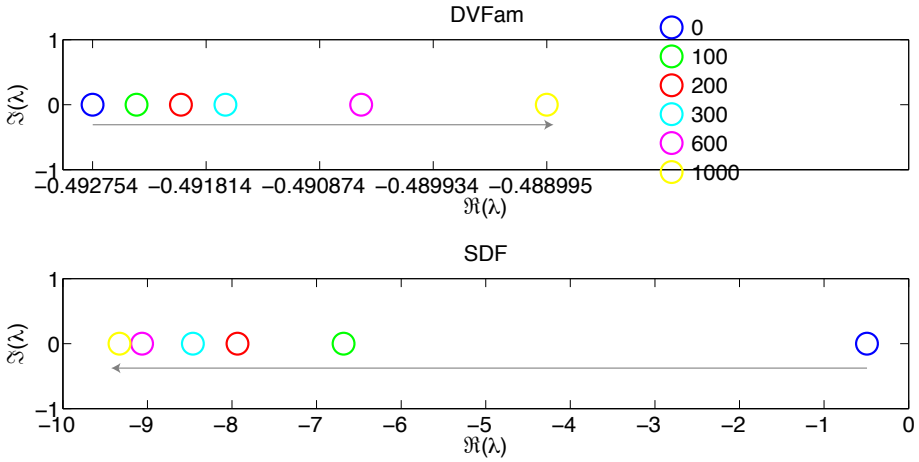

Figure 4.15: Zoom into the Windkessel's pole to show its behavior with respect both filters' gain.

with z_π and z_P the respective measurements.

4.2.5 Elastodynamics-Stokes coupling

In order to better understand the behavior of Luenberger filters in FSI, we isolated so far two physical phenomena: the added-mass effect and the dissipation coming from boundary conditions. In this section, we introduce a simplified model which includes a new physical property, namely the fluid viscosity.

We consider a linear FSI problem consisting of the Stokes equations, set in a fixed domain, with free outflow boundary conditions:

$$\left\{\begin{aligned} \rho_{\mathrm{f}}\partial_t \boldsymbol{u}_{\mathrm{f}} - \boldsymbol{\nabla}\cdot\boldsymbol{\sigma}_{\mathrm{f}}(\boldsymbol{u}_{\mathrm{f}},p) &= \mathbf{0}, \quad \text{in} \quad \Omega_0^{\mathrm{f}},\\ \boldsymbol{\nabla}\cdot\boldsymbol{u}_{\mathrm{f}} &= 0, \quad \text{in} \quad \Omega_0^{\mathrm{f}},\\ \boldsymbol{u}_{\mathrm{f}} &= \boldsymbol{u}_{\mathrm{in}}, \quad \text{on} \quad \Gamma^{\mathrm{in}},\\ \boldsymbol{\sigma}_{\mathrm{f}}(\boldsymbol{u}_{\mathrm{f}},p)\cdot\boldsymbol{n}_{\mathrm{f}} &= 0 \quad \text{on} \quad \Gamma^{\mathrm{out}}, \end{aligned}\right. \tag{4.59}$$

coupled to the solid equations (4.1c) by the usual transmission conditions.

Continuous piece-wise affine finite elements are used for the discretization of this coupled system. This yields the following discrete dynamical system

$$\begin{bmatrix} M_{\mathrm{s}} & 0 & 0 & 0 & 0\\ 0 & M_{\mathrm{s,I}} & M_{\mathrm{s,I\Sigma}} & 0 & 0\\ 0 & M_{\mathrm{s,I\Sigma}}^{\intercal} & M_{\mathrm{s},\Sigma}+M_{\mathrm{f},\Sigma} & M_{\mathrm{f,I\Sigma}}^{\intercal} & 0\\ 0 & 0 & M_{\mathrm{f,I\Sigma}} & M_{\mathrm{f,I}} & 0\\ 0 & 0 & 0 & 0 & 0 \end{bmatrix} \begin{bmatrix} \dot{Y}_{\mathrm{s}}\\ \dot{U}_{\mathrm{s,I}}\\ \dot{U}_{\Sigma}\\ \dot{U}_{\mathrm{f,I}}\\ \dot{P} \end{bmatrix}$$
$$= -\begin{bmatrix} 0 & -M_{\mathrm{s}} & 0 & 0 & 0\\ K_{\mathrm{s,I}} & C_{\mathrm{s,I}} & C_{\mathrm{s,I\Sigma}} & 0 & 0\\ K_{\mathrm{s},\Sigma} & C_{\mathrm{s,I\Sigma}}^{\intercal} & C_{\mathrm{s},\Sigma}+K_{\mathrm{f},\Sigma} & K_{\mathrm{f,I\Sigma}}^{\intercal} & B_{\mathrm{f},\Sigma}^{\intercal}\\ 0 & 0 & K_{\mathrm{f,I\Sigma}} & K_{\mathrm{f,I}} & B_{\mathrm{f,I}}^{\intercal}\\ 0 & 0 & -B_{\mathrm{f},\Sigma} & -B_{\mathrm{f,I}} & K_p^{\varepsilon} \end{bmatrix} \begin{bmatrix} Y_{\mathrm{s}}\\ U_{\mathrm{s,I}}\\ U_{\Sigma}\\ U_{\mathrm{f,I}}\\ P \end{bmatrix}. \tag{4.60}$$

In this expression, the column arrays $U_{\mathrm{s}} \overset{\text{def}}{=} [U_{\mathrm{s,I}}, U_{\Sigma}]^{\intercal}$ and $U_{\mathrm{f}} \overset{\text{def}}{=} [U_{\Sigma}, U_{\mathrm{f,I}}]^{\intercal}$ represent the solid and fluid velocity degrees of freedom, respectively. The fluid pressure degrees of freedom are denoted by P. The fluid (K_{f}, M_{f} and B_{f}) and solid (K_{s}, C_{s} and M_{s}) matrices are defined by blocks, where the subscripts $_{,\mathrm{I}}$ and $_{,\Sigma}$ indicate the internal and interface entries. In particular, we have

$$\forall \boldsymbol{u}_{\mathrm{f}}, \boldsymbol{v}_{\mathrm{f}} \in \mathcal{V}_{f,h}, \quad V_{\mathrm{f}}^{\intercal} K_{\mathrm{f}} U_{\mathrm{f}} = \int_{\Omega_0^{\mathrm{f}}} 2\mu\boldsymbol{\varepsilon}(\boldsymbol{u}_{\mathrm{f}}) : \boldsymbol{\varepsilon}(\boldsymbol{v}_{\mathrm{f}})\, d\Omega,$$
$$\forall \boldsymbol{u}_{\mathrm{f}}, \boldsymbol{v}_{\mathrm{f}} \in \mathcal{V}_{f,h}, \quad V_{\mathrm{f}}^{\intercal} M_{\mathrm{f}} U_{\mathrm{f}} = \int_{\Omega_0^{\mathrm{f}}} \rho_{\mathrm{f}}\boldsymbol{u}_{\mathrm{f}}\cdot\boldsymbol{v}_{\mathrm{f}}\, d\Omega,$$
$$\forall \boldsymbol{v}_{\mathrm{f}} \in \mathcal{V}_{f,h},\ p \in \mathcal{V}_{p,h} \quad V_{\mathrm{f}}^{\intercal} B_{\mathrm{f}}^{\intercal} P = -\int_{\Omega_0^{\mathrm{f}}} p\boldsymbol{\nabla}\cdot\boldsymbol{v}_{\mathrm{f}}\, d\Omega,$$

The term K_p^ε corresponds to the pressure stabilization operator, which here is given by

$$\forall p, q \in \mathcal{V}_{p,h} \quad Q^\intercal K_p^\varepsilon P = \varepsilon_p \int_{\Omega_0^\mathrm{f}} \frac{h^2}{\mu} \boldsymbol{\nabla} p \cdot \boldsymbol{\nabla} q \, d\Omega,$$

with $\varepsilon_p > 0$ the stabilization parameter (see, e.g., [BP84]).

The construction of the observers is performed, as before for the simplified fluid models, by adding the corresponding feedback terms for the DVF and SDF in the structure equations block (i.e., rows 1-3 of (4.60)).

Spectral analysis. For the isolated Stokes problem (i.e., with homogeneous Dirichlet data on Σ),

$$\begin{bmatrix} M_{\mathrm{f,I}} & 0 \\ 0 & 0 \end{bmatrix} \begin{bmatrix} \dot{U}_{\mathrm{f,I}} \\ \dot{P} \end{bmatrix} = - \begin{bmatrix} K_{\mathrm{f,I}} & B_{\mathrm{f,I}}^\intercal \\ -B_{\mathrm{f,I}} & K_p^\varepsilon \end{bmatrix} \begin{bmatrix} U_{\mathrm{f,I}} \\ P \end{bmatrix},$$

all the poles are of course real negative. For the FSI system (4.60), some poles are complex, as in all the previous examples, and some are real negative, because of the dissipation in the fluid.

We studied the behavior of the first 100 poles with smallest modulus. Note that, with the physical parameters considered in this paper, all these poles are real (the complex poles in the FSI case have indeed a very large imaginary part). We observe in Figure 4.16 (left) that these poles are almost the same for the isolated Stokes and the FSI systems (4.60). To study the effect of the filters on the poles, we considered for the first two FSI poles the perturbation $\lambda_\gamma - \lambda_0$ for a gain $\gamma = 200$. These results are reported in Figure 4.16 (right). We observe that the poles are practically insensitive to γ. In other words, the poles coming from the viscosity in the fluid are almost unaffected by the DVF and SDF filters.

This explains the behavior observed in Example 1 (Figures 4.3 and 4.4): the error curves in the fluid have a similar decay rate with and without the filter in the end of the cardiac cycle. The decay rate corresponds approximately to these pure real poles that are almost not perturbed by the solid filters. A similar comment can be done for Example 2 (Figures 4.7 and 4.8): at the end of the cardiac cycle, the decay of the total error is controlled by the poles of the Stokes problem and is almost unaffected by the filters. Hence, the effectiveness of the SDF in the two examples is explained by the fact that the filter operates on a system with small state error in the fluid itself – due to the choice of initial conditions – while the SDF is directly effective on the other constituents in the system.

These observations show that it would be desirable to complement solid measurements with blood flow measurements. In this respect, Ultrasound (US) is still the mostly used imaging modality to inspect blood flows, but MRI acquisition sequences developed over the last two decades offer better image quality. Phase Contrast (PC) MRI can provide the flow speed in one direction over a few slices along the vessel. By acquiring the data in multiple directions, this technique provides 3D blood flow

data PC cine MRI generates "4D" blood flow data, *i.e.* 3D blood flow throughout the cardiac cycle (see more details in Chapter 7). In some circumstances, pressure can also be acquired directly by catheters. Including these data in an observer would certainly improve the results obtained for FSI systems.

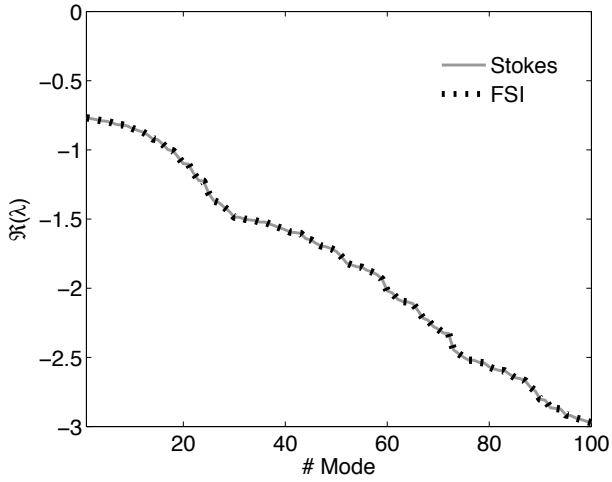

λ_0	SDF	DVF
-0.76	$4.4 \cdot 10^{-5}$	$-5.3 \cdot 10^{-10}$
-0.77	$4.1 \cdot 10^{-5}$	$-4.6 \cdot 10^{-10}$

Figure 4.16: Real poles of the FSI system compared to the Stokes poles (left), and effect of the DVF and SDF (right) represented by the values of $\lambda_\gamma - \lambda_0$, for $\gamma_d = \gamma_v = \gamma = 200$.

4.3 Discussion

4.3.1 Choice of the feedback gain in FSI problems

In the previous section, we investigated Luenberger observers in FSI problems. The aim was not only to understand the difference of performance, but also to find a systematic method for choosing the "optimal" feedback gain, i.e. the coefficient γ in (4.11) which corresponds to the fastest stabilization.

As already mentioned in Section 4.2.5, if we search for the eigenvalues of smallest modulus in the case of a Stokes fluid, we will not find the non-real poles since the modulus of the complex poles is much larger than the modulus of the real ones (around 100 times larger with the physiological parameters of blood flows). Since we are interested in the effect of the filters on the stability of the system, it would be natural to search the eigenvalues with the largest real part. For this purpose, we could apply for example the algorithm used in [FLT03] based on special Cayley transforms. However, we observed that this method may fail when the imaginary part is much larger than the real part. Moreover, it may be difficult to follow the trajectories of the complex poles when increasing the gain.

In view of these difficulties, we suggest in practice to calibrate the feedback gain

by considering the simplified FSI system with added mass-effect (4.39). For example, for the SDF, a first guess can be obtained with (4.42), assuming full observations and no viscosity in the solid. A simple computation gives $\lambda^2+\gamma_d\lambda+\omega_a^2=0$. Hence, the optimal value of γ_d (i.e. which makes $\Im(\lambda)=0$) is given by $\gamma_d=2\,\omega_a^{(1)}$, where $\omega_a^{(1)}$ is the first natural frequency of problem (4.43).

4.3.2 Some inefficient alternative approaches

In this section, we briefly comment on two other approaches that seem natural but lead to very inefficient filters, which further justifies the analysis given in the previous section. In other words, even if the complete proof of the stabilization efficiency of the SDF for FSI is far beyond the scope of this article, the eigenvalue sensitivities allow us to eliminate some inefficient alternative approaches.

SDF by coupling with $U_\mathrm{f}=\dot{Y}_\mathrm{s}$ on Σ. We remind that the SDF modifies the usual relationship between the velocity and the displacement in the solid. For the FSI problem, we advocated to transmit the solid velocity to the fluid ($U_\mathrm{f}=U_\mathrm{s}$). It is natural to ask what whould happen if we were to instead enforce $U_\mathrm{f}=\dot{Y}_\mathrm{s}$. This subtle difference has dramatic effects because the added-mass does not appear in the dissipative term anymore. Indeed, the quadratic eigenvalue problem becomes

$$\left(\lambda^2(M_\mathrm{s}+M_A)+\lambda(C_\mathrm{s}+\gamma_d M_\mathrm{s}K_\varepsilon^{-1}H_d^\intercal M_* H_d)+K_\mathrm{s}+\gamma_d C_\mathrm{s}K_\varepsilon^{-1}H_d^\intercal M_* H_d\right)\Phi_d=0\ . \tag{4.61}$$

Then, we can check the lower performance of this SDF, that will be called SDFd, in both spectral and nonlinear transient analysis shown in Figure 4.17 (Example 1, and Equations (4.38) for the spectral analysis) and Figure 4.18 (Example 2, and Equations (4.49) for the spectral analysis). Note that the SDFd is also inefficient to stabilize the Windkessel pole.

Force displacement feedback (FDF). Instead of using the SDF which modifies the relationship between the velocity and the displacement, it may be tempting to directly apply a collocated displacement feedback in the momentum equation, i.e.,

$$(M_\mathrm{s}+M_A)\ddot{\widehat{Y}}_\mathrm{s}+C_\mathrm{s}\dot{\widehat{Y}}_\mathrm{s}+K_\mathrm{s}\widehat{Y}_\mathrm{s}=\gamma_d H_d^\intercal M_*(Z-H_d\widehat{Y}_\mathrm{s}).$$

This approach is related to the so-called *image force methods*, see e.g. [BSDA08]. The associated quadratic eigenvalue problem has the form

$$\left(\lambda^2(M_\mathrm{s}+M_A)+\lambda C_\mathrm{s}+K_\mathrm{s}+\gamma_d H_d^\intercal M_* H_d\right)\Phi_d=0\ . \tag{4.62}$$

This filter, which acts as an added-stiffness, is known to be efficient only for systems with important natural dissipation. Figure 4.19, left, shows that the FDF behaves poorly in the linear case (4.49). In Figure 4.19, right, this weak performance is confirmed in the nonlinear transient case (Example 2), in spite of the additional dissipation due to the fluid viscosity.

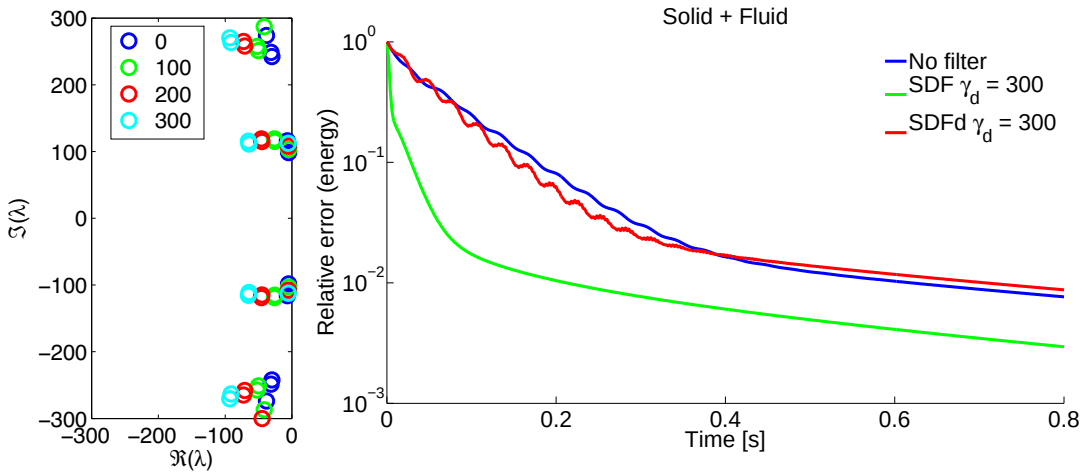

Figure 4.17: Linear spectral (left) and nonlinear transient (right) analysis for Example 1 with the SDFd.

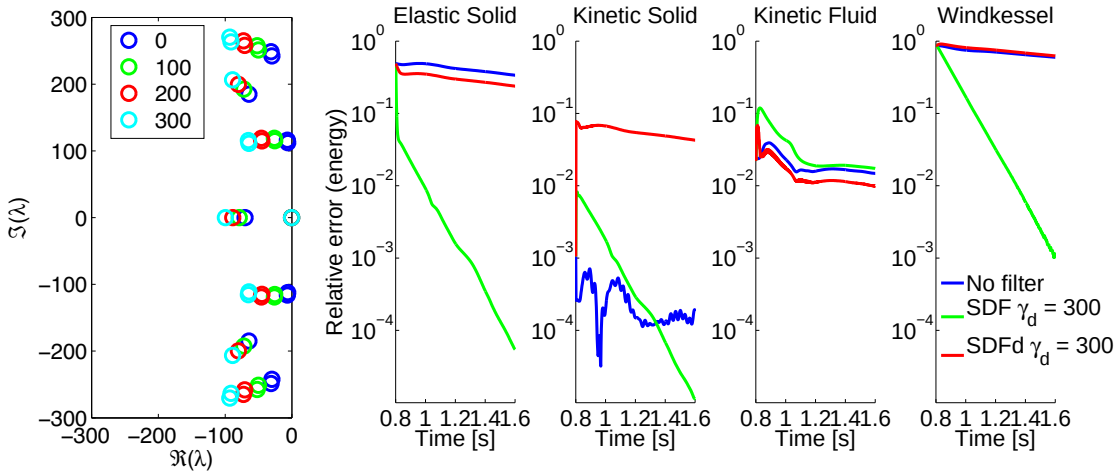

Figure 4.18: Linear spectral (left) and nonlinear transient (right) analysis for Example 2 with the SDFd. The energy components are shown split for sake of clarity.

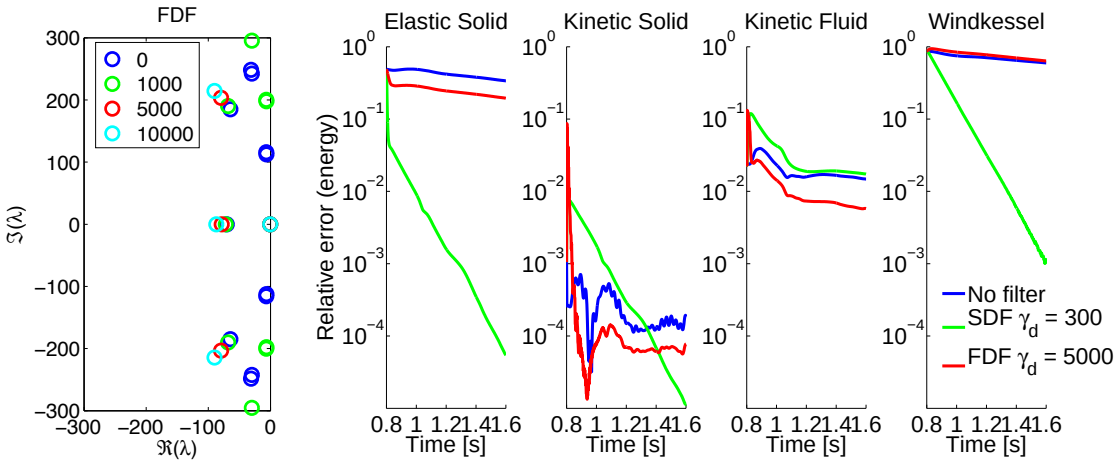

Figure 4.19: Effect of FDF on the FSI+Windkessel system: spectral analysis with a potential fluid (left) and nonlinear transient analysis (right). The energy components are shown split for sake of clarity.

4.4 Conclusions

We analyzed various sequential procedures to reduce the uncertainty in the initial condition of systems involving a viscous incompressible fluid and an elastic structure, assuming that measurements are available only for the solid velocities or displacements.

We recalled two strategies in elastodynamics, and we analyzed them for FSI, with a special emphasis on hemodynamics. We found that the fluid can strongly impact the filters performances, mainly due to the added-mass effect, but also to dissipative boundary conditions. In the case of a displacement feedback where the kinematic condition in the solid between displacement and velocity is perturbed, the choice of the coupling variable is crucial to keep the performance observed in solid mechanics. In the case of velocity measurements, we proposed to include the added-mass in the scalar product used for the observation. This allowed to keep in FSI the good performance observed in solid mechanics. When taking into account the coupling with a Windkessel model, only the SDF filter using displacement measurements proved effective, due to the quasi-static nature of the corresponding pole. Finally, our analysis showed that a filter applied only in the solid has almost no impact on the poles corresponding to the fluid viscosity. In order to circumvent this difficulty we need to consider additional observations in the fluid.

Part III

Application to real physical problems

On ne voit bien qu'avec le coeur. l'essentiel est invisible pour les yeux.
Antoine de Saint-Exupéry, *Le Petit Prince*, 1943.

Chapter 5

In vitro validation of the parameter estimation methodology

In this chapter we test the parameter estimation method on data coming from a silicon aortic phantom. We first present the experimental setting, as well as the acquired data and its processing and segmentation. Then, we describe the setup of fluid-structure model from the acquired data and we estimate the constitutive parameters for linear and non-linear solids. The results are confronted to non-destructive mechanical tests.

This work has been performed in collaboration with Marcel Rutten (phantom construction at Technical University of Eindhoven), Nicholas Gaddum (experimental runs and data acquisition at King's College London), David Barber and Rod Hose (data processing and segmentation at University of Sheffield), and Jean-Frédéric Gerbeau (INRIA).

Contents

5.1 Experimental setting

The experimental system is described in Figure 5.1, and consists of a MR-compatible emulator of the cardiovascular system. The fluid pump (left ventricle) corresponds to a linear servo actuator (ETB-32, Parker Hannifin) and piston assembly, located outside the 5 Gauss line[1] coupled to the ventricle piston via a $2\,m$ rigid boom. The piston ejects water through a tri-leaflet polyurethane valve, (Hemolab, Eindhoven, The Netherlands), and into a $450\,mm$ length and $18.5\,mm$ diameter silicone tube, (TU Eindhoven, The Netherlands). Afterload is maintained by a 3-element Windkessel at the distal end of the tube, after which the working fluid returns to the pump through a venous reservoir and an additional valve. Closed-loop feedback control of the ventricular action was maintained via a multifunction I/O board and a servo controller using LabVIEW software, (PCI-MIO16-E4

[1] It corresponds to the the perimeter around the scanner within which the magnetic field is higher than 5 gauss or $5 \cdot 10^{-4}\,T$.

and PC-servo-4A, National Instruments, Austin, TX, USA). The rig was run at 60 beats-per-minute.

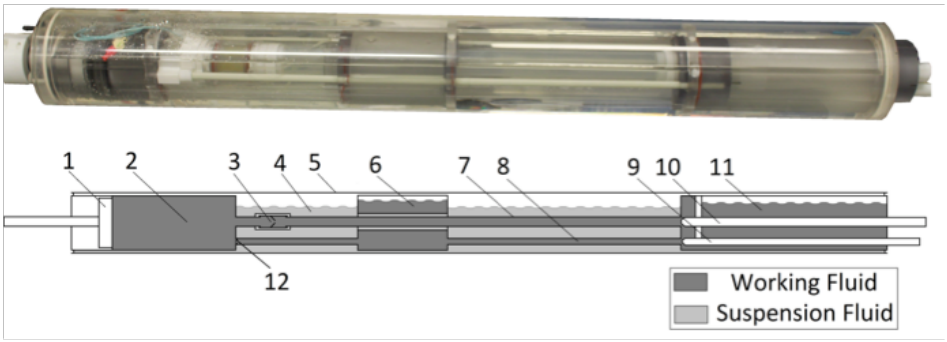

Figure 5.1: MRI compatible mock ventricle and aorta pulsatile phantom, where; 1, reciprocating ventricle piston; 2, ventricle and working fluid; 3, arterial valve; 4, suspension fluid; 5, outer cylindrical case; 6, venous compliance chamber; 7, silicone aorta; 8, venous channel; 9, venous resistance screw; 10, arterial resistance screw and arterial catheter access; 11, arterial compliance chamber; 12, venous valve.

5.2 Measured data

Pressure. Pressure measurements were taken at 13 locations between the venous and arterial compliance chambers with a measurement spacing of $20\,mm$. Raw pressure measurements were taken using a pressure wire, (Certus, St. Jude Medical Systems, Uppsala, Sweden), via an analogue to digital acquisition card, (USB 6211 National Instruments, Austin, TX, USA), at a temporal resolution of $1000\,Hz$ upon a separate PC. The servo motor voltage trigger wave was recorded concurrently with the pressure waveform so as to permit gating of the pressure data at each of the 13 locations for constructing the cycle of $1\,s$. The raw signals were recorded and processed using in-house MATLAB-code, (The MathWorks, Natick, MA, USA), which are shown for the first and last slices later as the model's boundary conditions. Following pressure measurement, the flow phantom was lifted into the scanner for geometry and velocity data acquisition.

Geometry. MR-acquisitions were performed on a 3T scanner, (Philips Achieva, Philips Healthcare, Best, The Netherlands). A 32-element radio-frecquency (RF) coil was used for signal reception. Initial surveys were used to plan the scan orientation. Geometry imaging was captured in a balanced turbo field echo (B-TFE) cine scan with a temporal resolution of 100 data points per cycle ($10\,ms$). Thirteen slices were planned at the $20\,mm$ centres where pressure measurements were taken with an excitation slice thickness of $8\,mm$, and a pixel size of $1.8 \times 2.5\,mm$. The leading edges of the venous and arterial compliance chambers were used for slice

location. A flip angle of 60^o was used with TE/TR = $2.25/4.50\,s$. Segmentation was then carried out on these images using *Shirt* [BOFH07], whose results are shown in Figure 5.2.

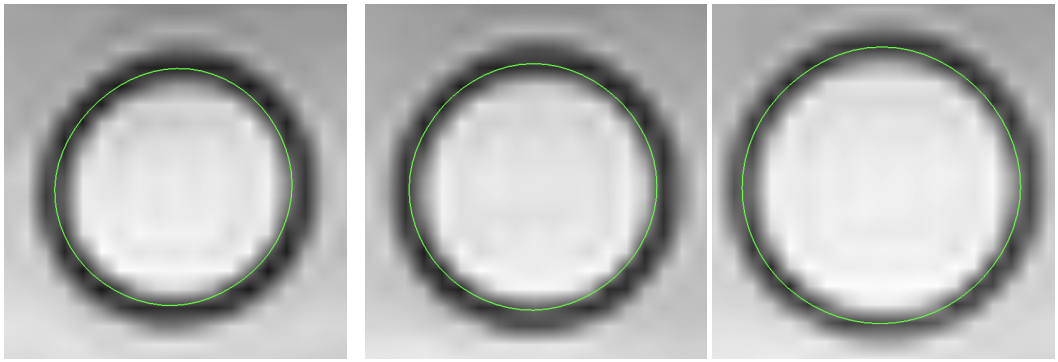

(a) $5mmHg$ (b) $47\,mmHg$ (c) $115\,mmHg$

Figure 5.2: Magnitude image and segmentation result (in green) at the middle of the tube at three acquisition instants with the gated (approximate) pressures.

Velocity. For velocity imaging, 2D phase contrast scan was performed. Velocity encoding was performed in the feet-head direction, with a velocity sensitivity of $80\,cm/s$, a voxel size of $1.8 \times 2.5 \times 8.0\,mm^3$, 2 signal averages (NSA), TE/TR = $2.43/4.17\,ms$ and a flip angle of 10^o. Again, 13 slices were used at the same locations as those used in the geometry acquisition. The scan was retrospectively gated to acquire 100 phases within one averaged cardiac cycle over two and three minutes (depending on heart rate).

Mechanical test. Once the acquisition of the MR data was concluded, a non-destructive mechanical test was performed. The experiment consisted in placing the silicon tube vertically, filling it completely with water, and then imposing an additional controlled water volume V_i while measuring the pressure P_i at the bottom, with $i = 1, \ldots, 27$. The results are plot in Figure 5.3. The raw measurements were filtered by fitting a polynomial of degree 4 to the data in order to get a monotone compliance curve.

5.3 Forward FSI model setting

The FSI model was constructed from the data set as follows. Note that all units are expressed in the CGS system unless indicated explicitly.

The geometry used for the mesh construction (and also initial condition) was chosen as the segmented surfaces at the lowest pressure, namely the configuration shown in Figure 5.2-a. The surface was then remeshed using *3-matic* (Materialise,

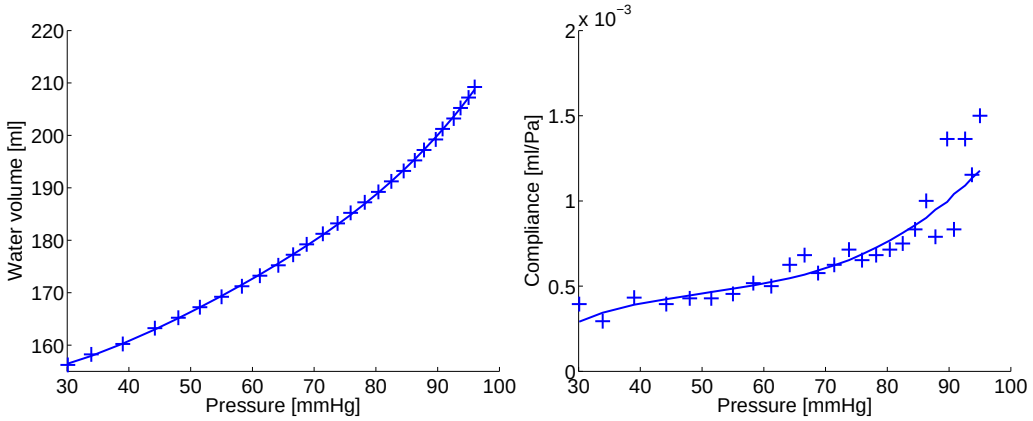

Figure 5.3: Left: pressure P_i and volume V_i, $i = 1, \ldots, 27$, acquired from the mechanical test. Right: derived compliance $C_i = (V_{i+1} - V_i)/(P_{i+1} - P_i)$ versus the pressure P_i, $i = 1, \ldots, 26$. The raw data is plot with + and the filtered data with continues lines.

Leuven, Belgium), and the volume was closed with additional surfaces at the outlet and the inlet. Then, using *Gmsh* [GR09], the surface was extruded outwards the cylinder in two tetrahedral layers with total thickness of $e = 0.1$. Finally both solid's and fluid's volume meshes were constructed with 135840 and 255023 tetrahedra, respectively. The meshes are shown in Figure 5.4.

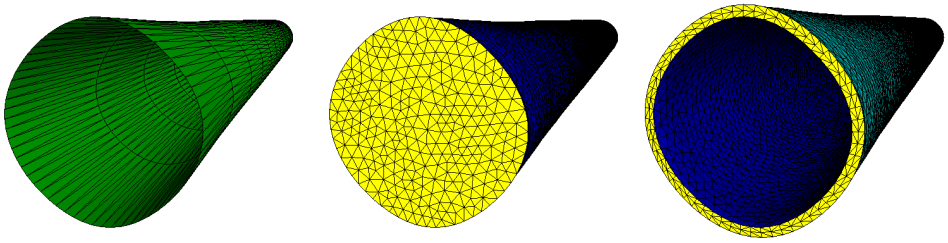

(a) Segmented surface (b) Fluid mesh (c) Solid mesh

Figure 5.4: Meshes at the first time frame.

The boundary conditions for the fluid were directly taken from the pressure measurements at inlet and outlet. For the solid, both inlet and outlet were fixed only in the Z-direction, and left-free in the XY-plane. Moreover, in order to represent the fact that the tube is also immersed in a fluid a small surface viscosity of $c_\Gamma = 10^4$ was added, see Equation (1.6c).

For the initial condition, one cycle of pure Navier-Stokes Equations was run (i.e., with imposing zero velocity at the fluid-structure interface), and the final velocity field was used as initial condition for the FSI simulation, whereas the structure is

taken at rest. As in the previous chapters, the loads received by the solid are corrected by the initial one. The FSI-model was solved through Algorithm 5, Chapter 3. The time step is taken as $\tau = 0.002\,s$.

A fluid viscosity of $\mu = 0.035$ and a density of 1 were assumed. Two types of solid models are analyzed. First, a linear model with density $\rho_s = 1.2$, Poisson's ratio $\nu = 0.45$ and no viscosity ($\eta_s = 0$) is considered. Here, we aim to estimate the incremental Young's modulus $E = 2^{\theta}\,MPa$. We will also consider a second solid model consisting of an quasi-incompressible Mooney-Rivlin hyperelastic model with parameters $c_1 = 1.5 \cdot 10^6 \cdot 2^{\theta}$, $c_2 = 5 \cdot 10^4$, $\kappa = 10^8$, and we estimate θ. Figure 5.5 presents an example for a simulation with the nonlinear solid model.

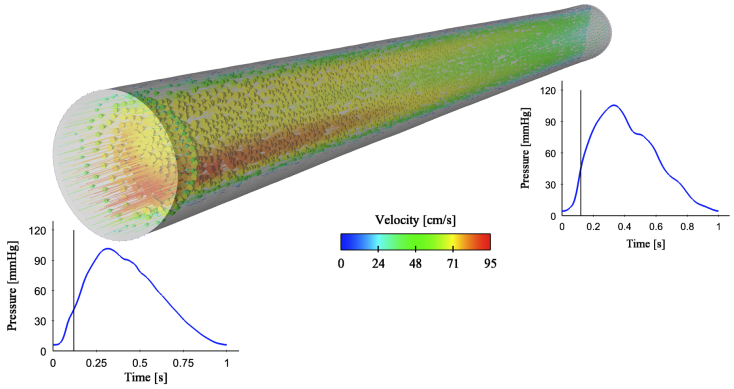

Figure 5.5: Snapshot of the FSI simulation of the phantom with the nonlinear solid model with $c_1 = 1.5 \cdot 10^6$.

5.4 Estimation results

Nonlinear observation operator. In Part II the measurements used for both state and parameter estimation algorithms were assumed to be the Lagrangian displacements at each node of the fluid-structure interface. Nevertheless, segmentation procedures of the medical images usually produce a set of surfaces, which in our case correspond to the fluid-structure interface at each acquisition time. Hence, classical data assimilation representation of the observation (see, e.g., (3.14) or (4.4)) does not hold anymore since it is usually not possible to determine the Lagrangian position of a particular material point.

In such cases, we are only able to quantify an observation error by computing the (signed) distance field between these surfaces and the deformed fluid-structure interface of the model, see Figure 5.6. As proposed in [MCLT09], we call this error measurement for each node i on the fluid-structure interface $\mathrm{D}_i(Y_k^d, S_k)$, with S_k the acquired surface and Y_k^d the Lagrangian displacement field of the solid at the acquisition time k. We can also assume that the observation error is available at

any time t through interpolation, i.e.,

$$W_i^d(Y^d,t) = \alpha_k(t)\mathrm{D}_i(Y^d,S_k) + (1-\alpha_k(t))\mathrm{D}_i(Y^d,S_{k+1}) \ , \ i=1,\ldots,m, \tag{5.1}$$

with m the number of nodes on the discrete interface $\Sigma(t)$. Note that other type of time interpolations may also be used if stonger requirements on the data regularity have to be imposed. However, linear interpolation of the measurements have been found to be enough in the applications in this thesis, while in Chapter 6 a stronger regularity is required when imposing the data directly in Dirichlet boundaries.

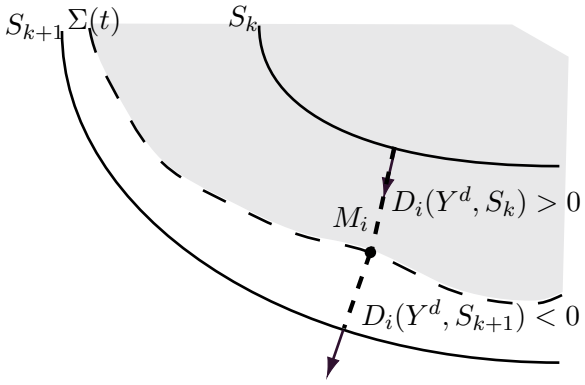

Figure 5.6: Distance from point M_i of the fluid-structure interface to two successive extracted surfaces from the images (adapted from [MCLT09]).

Estimation of the solid constitutive parameter. Using exactly the same algorithm as in Chapter 3, but with the innovation defined by

$$\Gamma_n = [W_i^d(Y^d,t_n)]_{1\leq i\leq m} \ , \tag{5.2}$$

we perform the estimation for the linear and nonlinear solid models on their respective parameter θ using the segmented surfaces. For both cases, we consider two initial guesses for $\widehat{\theta}_0$, 0 and -1, with a unitary initial parameter covariance and several values of the feedback for the Kalman gain γ (see Equation 3.46). The results are shown in Figure 5.7. Note that the final estimated value in both cases does not depend on the initial guess nor on the filter gain.

In Figure 5.8-left we show a cut for the fluid-structure interface for the segmentation and simulations with linear and nonlinear solid models with their respective optimal parameters at the peak pressure instant. We can appreciate that the nonlinear solid model seems to give a better result when comparing with the segmented surface. This observation can be quantified by computing the accumulated measurement error

$$\mathcal{I}_n \stackrel{\text{def}}{=} \sum_{k=1}^{n} \tau \|\Gamma_k\|^2_{L^2(\Sigma(0))} \ , \ n=1,\ldots,N_T. \tag{5.3}$$

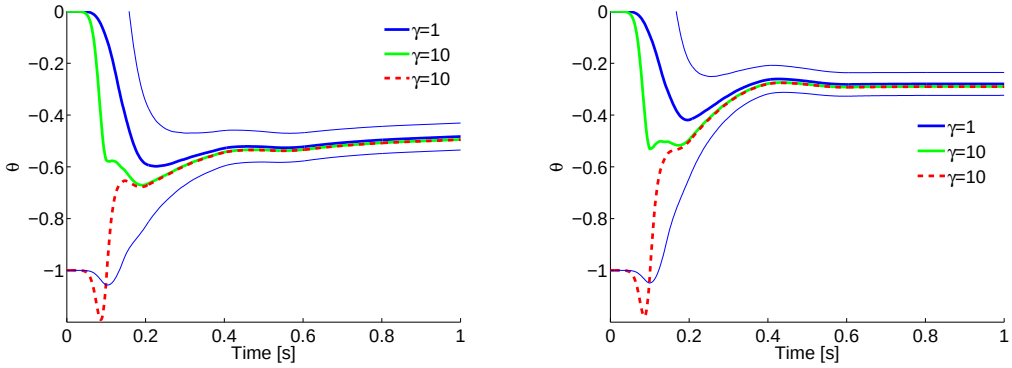

(a) Linear solid (b) Nonlinear solid

Figure 5.7: Estimation results for the parameter θ of both linear and nonlinear solid models. The thick lines represent the mean values, and the thin blue lines the confidence interval for the case of $\gamma = 1$.

taking the final estimated value $\hat{\theta}_{N_T}$ for solving the model dynamics and computing Γ_k. Assuming that the gain γ was taken large enough, $\mathcal{I}_{N_T}$ corresponds to the quantity that we aim to minimize with the data assimilation algorithm.

In Figure 5.8-right we show the curves for $\mathcal{I}_n$ for both solid models before and after the estimation. We can appreciate that in all cases, the data assimilation algorithm is performs well by finding a parameter which reduces the discrepancy between model and measurements. The higher capacity of the nonlinear structure for representing this physical system is also confirmed in the figure: the discrepancy with respect to the dynamic segmentation is smaller for the nonlinear than for the linear solid model. We present some snapshots for the segmentation and nonlinear solid model with optimized parameter in Figure 5.9.

Note that, in Figure 5.7, the estimated value using the linear solid model does not stabilize to a constant value at the end of the cycle, contrary to what happens in the nonlinear case. An explanation to this can be found in Figure 5.8-left, where we show a cut of the fluid-structure interfaces and segmented surface at the peak pressure for the optimal parameters. Notice that the linear solid deforms in a unphysical way (taking as reference the segmented surface). The reason is that, since the original geometry is not perfectly cylindrical, the fluid loads' directions change with the domain deformation (due to the ALE), but for the linear solid they are still applied at the original position. Hence, the loads received by the linear solid are not aligned with the displacement field, in contrast to the simulation with the nonlinear model, see Figure 5.10.

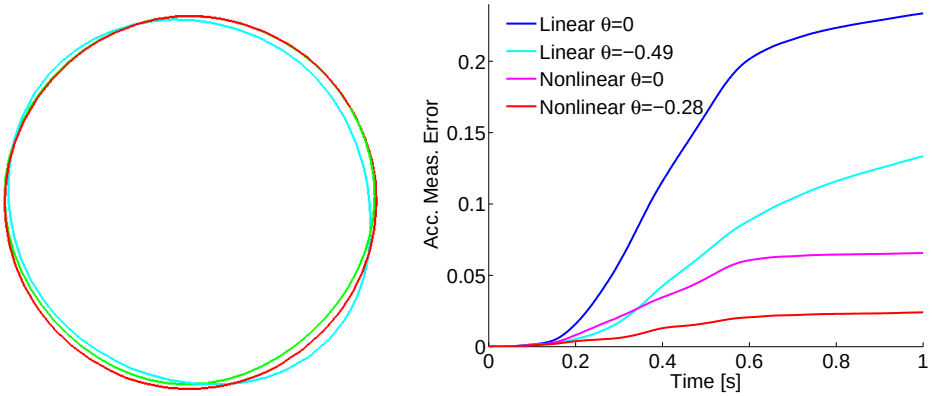

Figure 5.8: Comparison of the segmentation of the real data and the models with initial and optimized parameters. Left: cut at the tube's midpoint of the segmented surface (green), models with linear (cyan) and nonlinear (red) solids with optimized parameters at peak pressure ($t = 0.37\,s$). Right: accumulated measurement errors (Equation (5.3)) before and after the estimation.

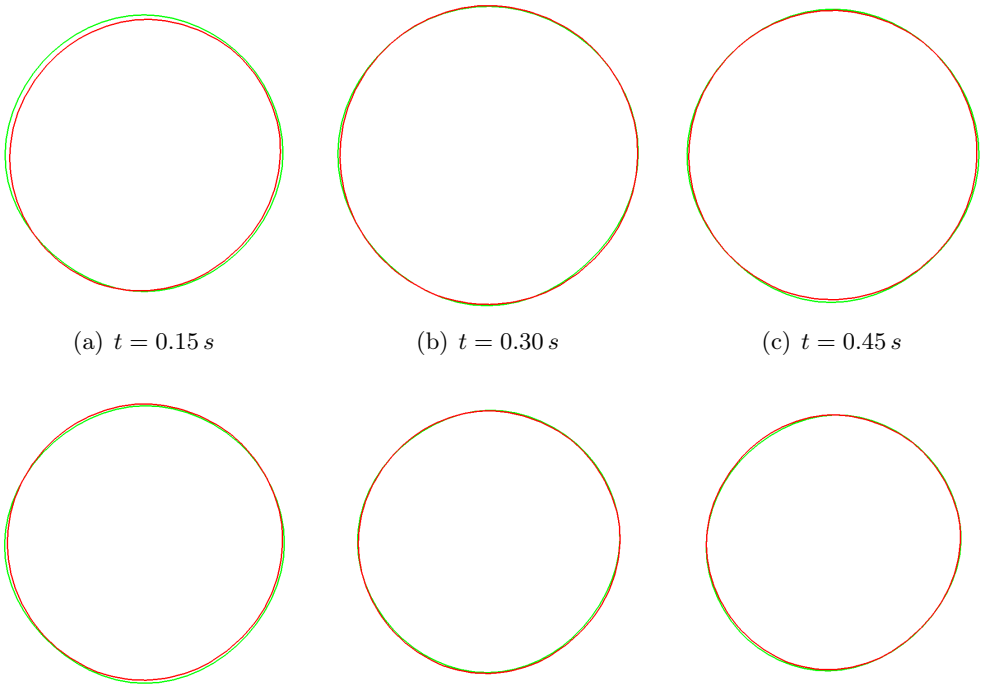

(a) $t = 0.15\,s$ (b) $t = 0.30\,s$ (c) $t = 0.45\,s$

(d) $t = 0.60\,s$ (e) $t = 0.75\,s$ (f) $t = 0.90\,s$

Figure 5.9: Some snapshots for a cut at the tube's midpoint for the segmented (green) and optimized nonlinear model (red).

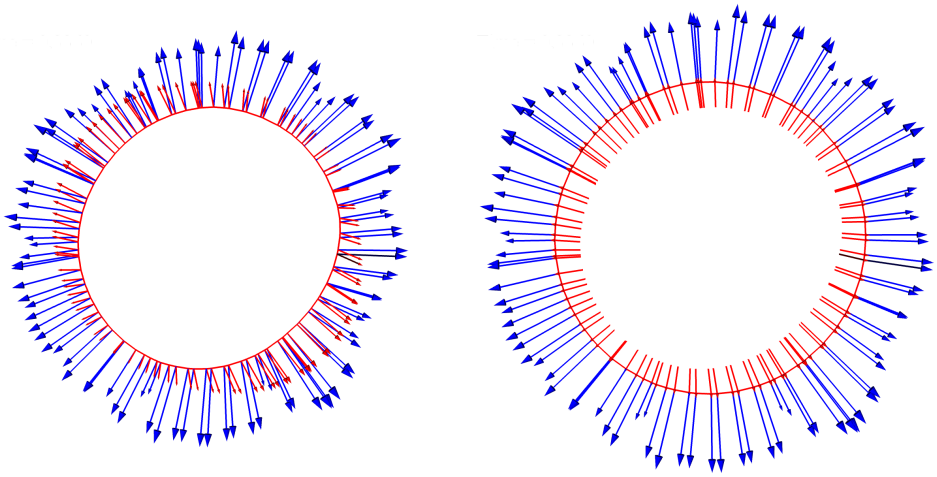

(a) Linear solid (b) Nonlinear solid

Figure 5.10: Comparison of the fluid loads and displacement field for the FSI simulations for linear and nonlinear solids at the tube's midpoint at peak pressure. The displacement field is represented in red and the fluid forces in blue. For the linear solid both fields are plotted at the original position, while in the nonlinear solid the fluid loads are represented at the deformed configuration.

5.5 Comparison with the experimental data

Our results show that the estimation procedure effectively selects the solid constitutive parameters in order to reduce the measurement error. As it will be explained later, we now setup a second FSI simulation which will allow to compare the estimated Young's modulus with the one derived from the mechanical test on the same silicon tube (see Figure 5.3).

Analytic computation of the Young's modulus. From pressure-volume data, a Young's modulus can be computed at every configuration represented, for instance, by a radius r assuming an infinitely long pressure vessel. In this case, the stress field is given by

$$\sigma_\theta = \frac{\delta p\, r}{e} \ , \ \sigma_z = \frac{\delta p\, r}{2\, e}, \tag{5.4}$$

for the tangential σ_θ and longitudinal σ_z stresses. Note that the stress in the radial direction σ_r varies from p to 0 when moving outwards through the vessel's wall, hence we can neglect it with respect to σ_θ and σ_z when h is small. The tangential strain is

$$\varepsilon_\theta = \frac{\delta r}{r} \ , \tag{5.5}$$

and can be related to the stresses through the classical equation of Hook's law

$$\varepsilon_\theta = \frac{\sigma_\theta - \nu(\sigma_r + \sigma_z)}{E} \,, \tag{5.6}$$

obtaining the following expression for the Young's modulus

$$E = \frac{\delta p}{\delta r} \frac{r^2 \,(1 - \nu/2)}{e}. \tag{5.7}$$

Using relations $V = \pi r^2 L$ and $\delta V = 2\pi r L \delta r$ we finally obtain

$$E = \frac{\pi L}{C\, e} \left(\frac{V}{\pi L} \right)^{3/2} (2 - \nu) \tag{5.8}$$

with L the original length of the cylinder and $C = \delta V / \delta p$ the compliance.

Estimation results. In order to validate the estimation using the FSI model and the data assimilation procedure, we have to start the simulation from a configuration such that the linear solid assumption holds. For that purpose, we construct the FSI model from the pressure and segmented geometry at $t = 0.126\, s$, which corresponds to pressures at the inlet and outlet of 44 and $50\, mmHg$, respectively. As in the previous section, the fluid was initialized from a Navier-Stokes simulation, the fluid loads were corrected by the initial one and the solid started at rest. Note that we show the results only until $t = 0.6\, s$, since after that the solid is under compression and buckles.

Figure 5.11 presents the estimation result and the comparison with the Young's modulus computed with Formula (5.8) using the same parameters as in the FSI simulation, namely $e = 0.1$ and $\nu = 0.45$. The length of the vessel is taken as $L = 40$ since the whole tube was tested in the experiment. In Figure 5.11-left is plotted the curve of Young's modulus in terms of the measured pressure (in blue), whereas the two vertical green lines correspond to both starting inlet's and outlet's pressures. The intersection of them with the Young's modulus curve gives a range of 0.68 to $0.65\, MPa$ (horizontal black lines in both figures). Figure 5.11-right shows the result for the estimation algorithm converging to $0.64\, MPa$, which is in very good agreement with the range obtained from the mechanical test. Moreover, in the same figure we can observe that the estimation converges well, which confirms that the linear solid model is more appropriate in that case since the fluid loads are reasonably small.

5.6 Conclusions

In this chapter we performed an in vitro validation of the parameter estimation algorithm presented in Chapter 3. We considered a real physical system consisting of a silicon rubber tube emulating the aorta, connected with a mechanical model of the main components of the cardiovascular system. We constructed a FSI computational

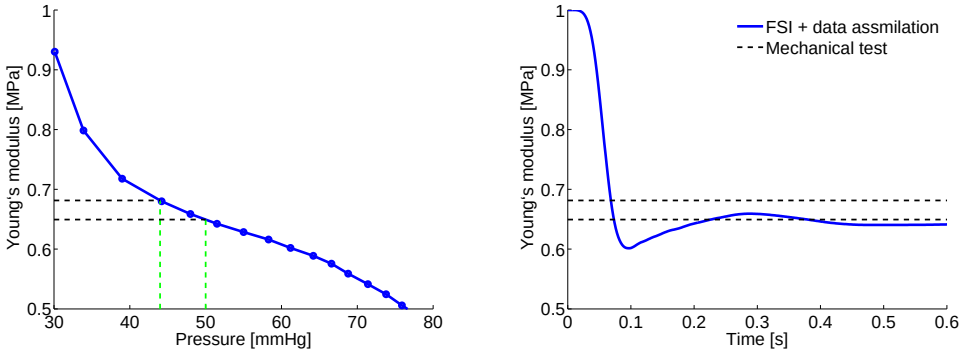

Figure 5.11: Comparison between the FSI-based Young's modulus estimation and the value obtained from the mechanical test. Left: Young's modulus vs. pressure (blue) derived from the experimental data. In green are plotted the initial pressure range, and in black the range derived for the Young's modulus. Right: estimated Young's modulus from the data assimilation procedure for $\gamma = 1$.

model of the cylinder based on the data segmented from dynamic MR-images and we used pressure measurements for the fluid boundary conditions. We estimated the Young's modulus for a linear solid and one of the Mooney-Rivlin constitutive parameters for a nonlinear solid. In all cases, the estimated parameters reduced the discrepancy between model and measurements. Moreover, we verified one of the estimated parameters from data coming from an independent non-destructive mechanical test.

Chapter 6

Towards the biophysical personalization of an aortic FSI model

This chapter is devoted to the FSI simulation of an aorta with repaired coarctation using the patient clinical data. We first detail the available measurements and its processing and then proceed with the description of the setup of the FSI model. We then estimate the stiffness distribution from space-time resampled synthetic surfaces. We conclude by presenting preliminary estimation results from the original MR-segmented surfaces.

This work has been performed in collaboration with Israel Valverde (clinical data acquisition, King's College London), David Barber, Rod Hose and Cristina Staicu (data processing/segmentation at University of Sheffield), and Jean-Frédéric Gerbeau (INRIA).

Contents

6.1 Clinical data

The available clinical data corresponds to a 19 year old male subject with a mild (repaired) coarctation of the descending aorta. Figure 6.1 summarizes the processed data, which will be described in detail in the following paragraphs.

3D static geometry (3D-Gd). A static MR-image (see Figure 6.2) was acquired at the end of the diastole using a gadolinium contrast agent in order to increase the resolution of the aortic lumen. The voxel size is $1.36 \times 1.36 \times 1.8\,mm$. The lumen's outer surface was then segmented with a registration based segment growing algorithm [BSV+12].

2D static *Black-Blood* geometry (2D-BB). It corresponds to a two-dimensional static scan with high resolution ($0.625 \times 0.625\,mm$ of pixel size), which allows to distinguish the lumen (black) to the tissues (white), see Figure 6.3. Hence,

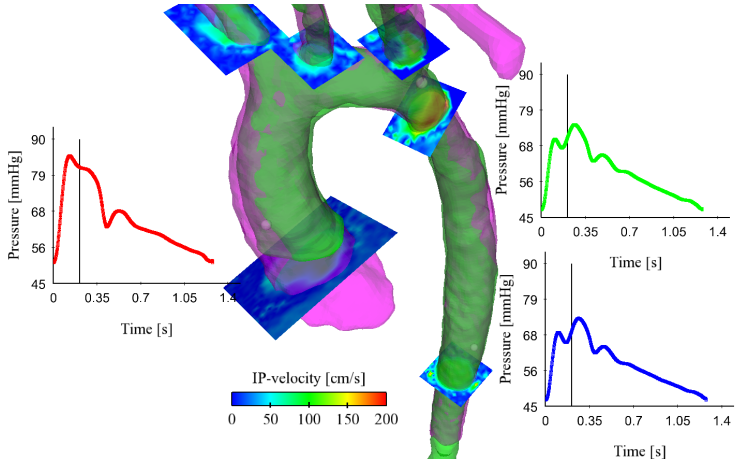

Figure 6.1: Measurements available for the study case 10 of the *euHeart* database. Static segmentation (pink geometry); dynamic segmentation (green geometry); invasive pressure measurements at three locations: ascending (red), descending (green) and abdominal (blue) aorta; and In-Plane velocity measurements.

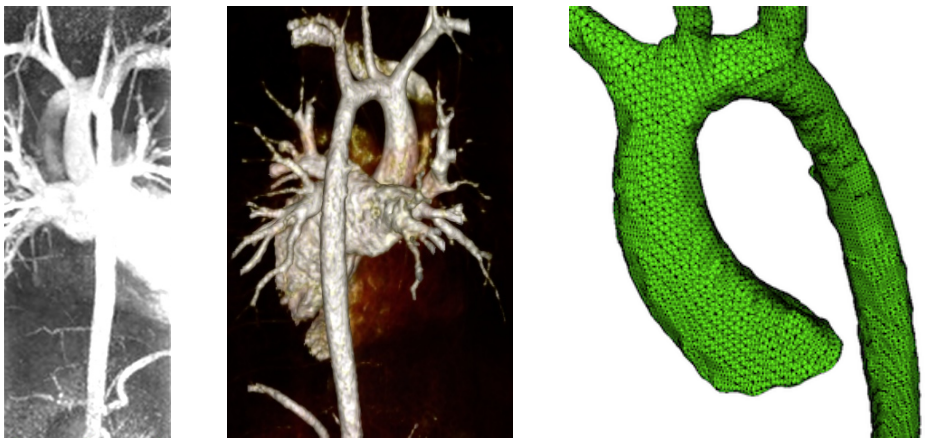

Figure 6.2: Different representations of the static geometry acquisition (3D-Gd) of the subject's aorta. Left: picture in perspective of the MR-image. Center: volume rendering using Osirix [RSR04]. Right: raw segmented surface mesh.

it can serve for instance for the identification of the thickness of the aortic wall. Moreover, it also helps to distinguish the pulmonary trunk and the superior vena cava that are in contact with the ascending aorta. As we will see later, this impacts the aorta's dynamics and these veins should be included in the FSI-model for a proper estimation of the aortic wall properties, at least in a simplified manner.

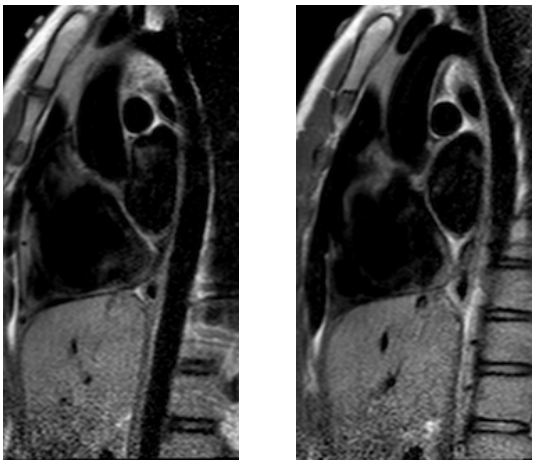

Figure 6.3: Two slices acquired with the 2D-BB protocol.

3D dynamic geometry (4D-SSFP). 25 three-dimensional MR-images along the cardiac cycle of $1.324\,s$ were acquired with a spatial resolution (voxel size) of $1.29 \times 1.29 \times 2.4\,mm$. Consequently, the 25 surfaces were segmented using an image registration algorithm implemented in *Shirt* [BOFH07] with the template mesh obtained from the 3D-Gd (Figure 6.2-right). All time frames are shown in Figure 6.4 for one representative slice together with the MR-image. Note that there are important variations of the image resolution in the lumen due to the big variations of the blood velocity, making an automatic segmentation of the these images an extremely difficult task. Particularly in the descending and abdominal aortas, where the turbulent flow do not really allow to correctly distinguish the boundaries of the aortic lumen. Hence, the registration algorithm tries to follow these changes in contrast, obtaining a segmentation with a low signal-to-noise ratio (SNR). We will see later, that the nonlinear Kalman filter produces reasonable results with this type of data.

In-plane dynamic velocity (IP-Vel). Four fixed-in-space slices of in-plane velocity phase contrast MR-images (i.e., the velocity component perpendicular to the plane) were acquired, as summarized in Figure 6.1 and detailed in Figure 6.5: (a) one cutting the ascending aorta, (b) one cutting the three supra aortic branches (separated into three for the sake of clearness), (c) one cutting the descending aorta, and (d) one cutting the abdominal aorta.

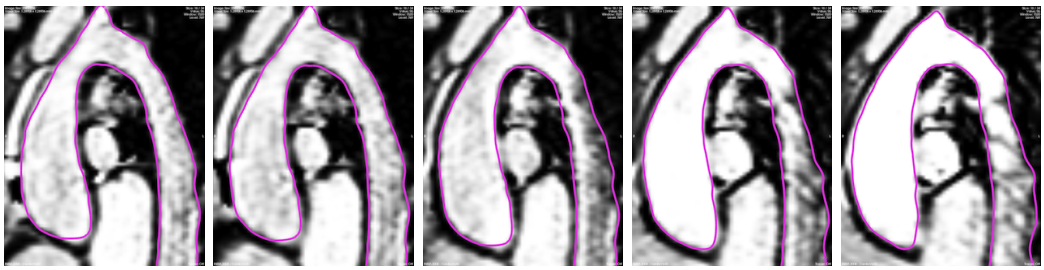

(a) $t = 0\,s$ (b) $t = 0.055\,s$ (c) $t = 0.110\,s$ (d) $t = 0.165\,s$ (e) $t = 0.221\,s$

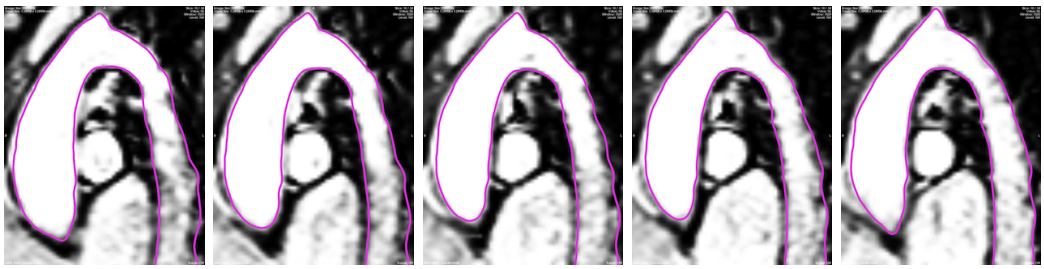

(f) $t = 0.276\,s$ (g) $t = 0.331\,s$ (h) $t = 0.386\,s$ (i) $t = 0.441\,s$ (j) $t = 0.496\,s$

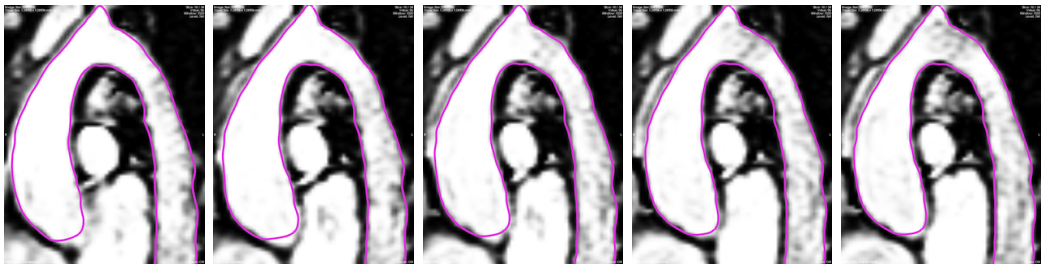

(k) $t = 0.552\,s$ (l) $t = 0.607\,s$ (m) $t = 0.662\,s$ (n) $t = 0.717\,s$ (o) $t = 0.772\,s$

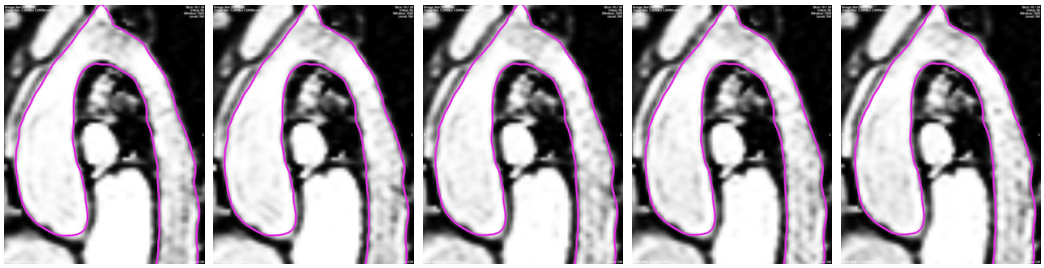

(p) $t = 0.827\,s$ (q) $t = 0.883\,s$ (r) $t = 0.938\,s$ (s) $t = 0.993\,s$ (t) $t = 1.048\,s$

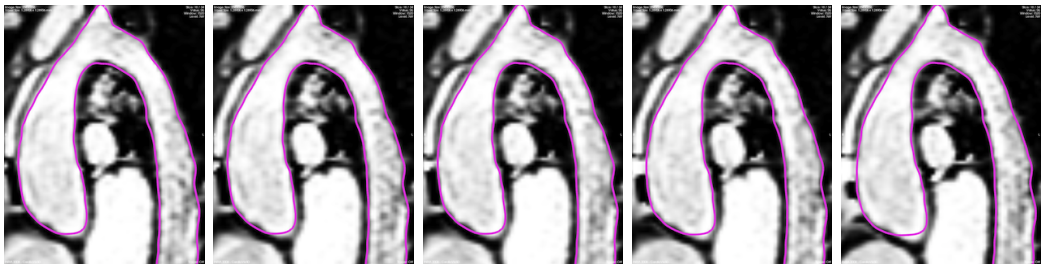

(u) $t = 1.103\,s$ (v) $t = 1.158\,s$ (w) $t = 1.213\,s$ (x) $t = 1.269\,s$ (y) $t = 1.324\,s$

Figure 6.4: The 25 MR time frames and the segmented surfaces (in magenta) for a representative slice of the 4D-SSFP sequence. Notice the changes of contrast of the images due to the changes in blood velocity, see for example: from (c) to (d) the ascending aorta, and from (c) to (j) the flow vortices at the descending and abdominal aorta producing artificial oscillations in the segmented surfaces.

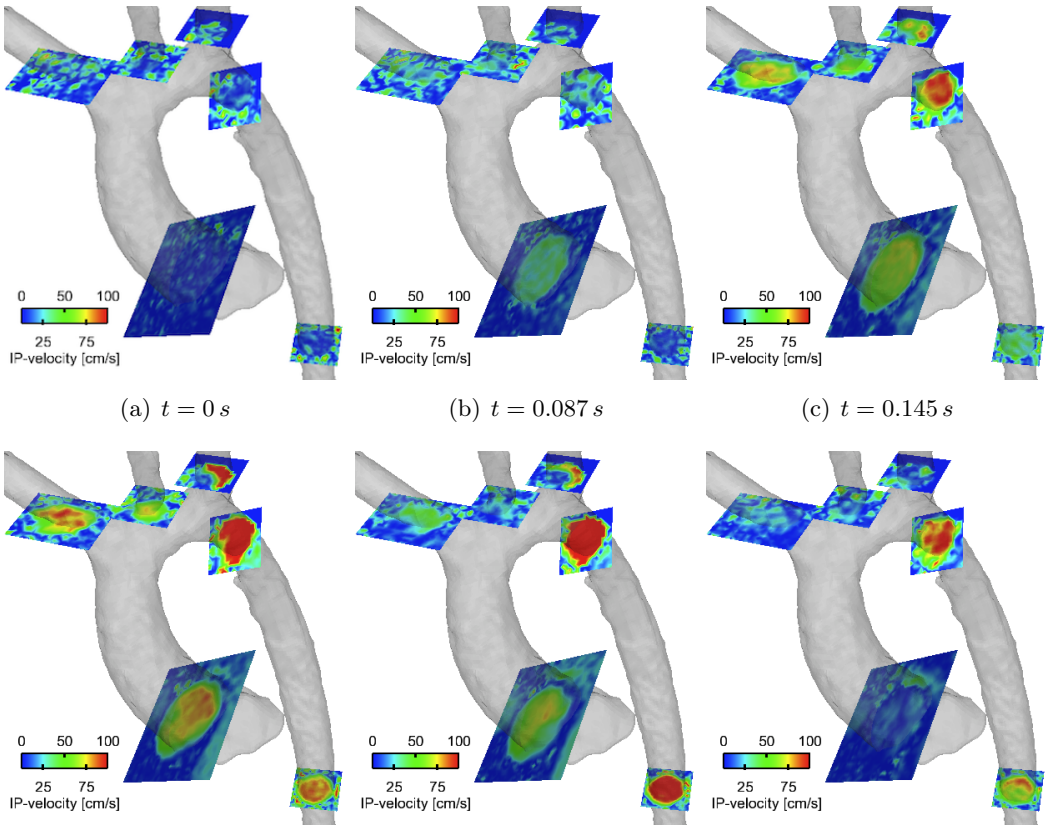

(a) $t = 0\,s$ (b) $t = 0.087\,s$ (c) $t = 0.145\,s$

(d) $t = 0.190\,s$ (e) $t = 0.274\,s$ (f) $t = 0.401\,s$

Figure 6.5: Snapshots of the in-plane velocity measurements.

Additionally, flow curves were computed after the MR-acquisition from the in-plane velocity data by selecting a region-of-interest (ROI), see Figure 6.6. Even though these curves provide a valuable information for setting up the simulation (see below in this chapter), they should be interpreted carefully. First, they represent a fixed plane in space for all times, whereas the fluid domain is moving due to the arterial wall displacements. Second, the slices are not always perpendicular to the flow, specially at the ascending aorta and at the supra-aortic branches, where only one slice was used for the three arteries simultaneously. Third and finally, as mentioned above the ROIs are fixed for all time frames so that the deformation of the solid is not taken into account. This can lead to important errors in the calculation of the flux, specially for the places where deformation is important like in the ascending aorta.

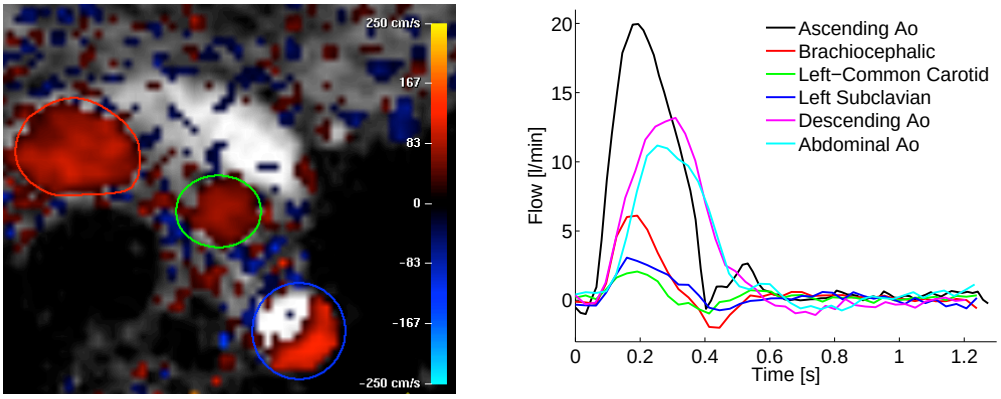

Figure 6.6: Computation of flow curves from the in-plane phase contrast images. Left: ROI for the supra-aortic branches. Right: extracted flow curves.

Pressure measurements. A MRI-gated catheter study was performed in order to assess more precisely the severity of the coarctation. Hence, invasive pressures were measured at the ascending, descending, and abdominal aorta as shown in Figure 6.7.

6.2 Forward FSI simulations

In this section we describe the FSI simulations, without any estimation procedure. We present in detail how the computational models for both fluid and solid were setup from the clinical data (for geometry and boundary conditions). We also show some results of the simulations and we compare them with the measurements.

Note that all units are expressed in the CGS system unless indicated explicitly.

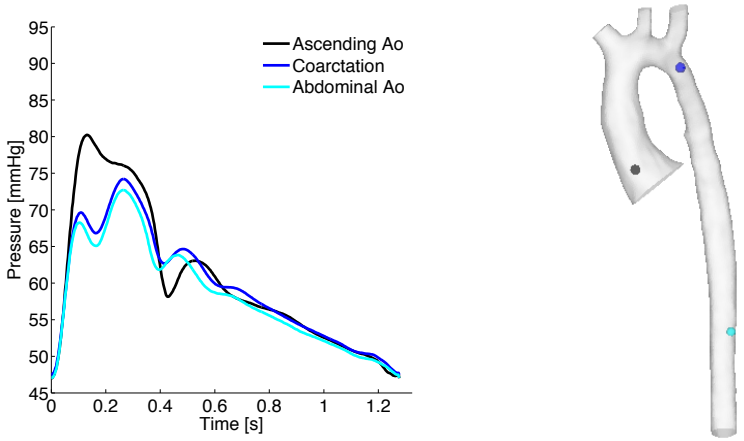

Figure 6.7: Pressures measurements at three locations in the aorta (left) and their respective locations (right).

6.2.1 Model setup

Geometry. The geometry used for building the model's mesh was chosen at the first segmented frame of the 4D SSFP sequence (Figure 6.8-left). The surface was then remeshed and smoothed using *3-matic* (Materialise, Leuven, Belgium), and the volume was cut and closed with artificial plane surfaces at the inlet and four outlets (Figure 6.8-center). Then, using *Gmsh* [GR09], the surface was extruded outwards the cylinder in two layers of tetrahedra in order to obtain a uniform wall thickness of $e = 0.2$ (Figure 6.8-right) estimated from the 2D-BB sequence. Finally, both solid and fluid volume meshes were generated with 103406 and 138648 tetrahedra, respectively. Note that the solid mesh was divided into 5 regions colored differently in Figure 6.8-right in order to assign different mechanical properties to the arterial wall.

Constitutive parameters. A fluid viscosity of $\mu = 0.035$ and a density of 1 were assumed. For the solid, a density of $\rho_s = 1.2$ was taken in the whole domain. The solid volume was divided into 5 regions (see Figure 6.8-left) where a Mooney-Rivlin constitutive with parameters $c_1^j = 3 \cdot 10^5 \cdot 2^{\theta^j}$, $c_2^j = 10^4$ and $\kappa^j = 10^8$ (see definition in Equation (1.1)), for each region $j = 1, \ldots, 5$. The parameters $\theta^1, \ldots, \theta^5$ will be chosen depending on the test-case. Moreover, a solid viscosity parameter of $\eta_s = 10^5$ is considered.

Solid boundary conditions. In the solid, the outlets of the supra-aortic branches were left free (i.e., $k_\Gamma = c_\Gamma = 0$), whereas at the distal outlet a simplified tissue support with parameters $k_\Gamma = 10^5$ and $c_\Gamma = 10^4$ was included (see definition in Equation $(1.6c)_4$). Moreover, in order to represent the fact that the tube is also immersed in a viscous medium, a surface viscosity of $c_\Gamma = 10^4$ was added on the

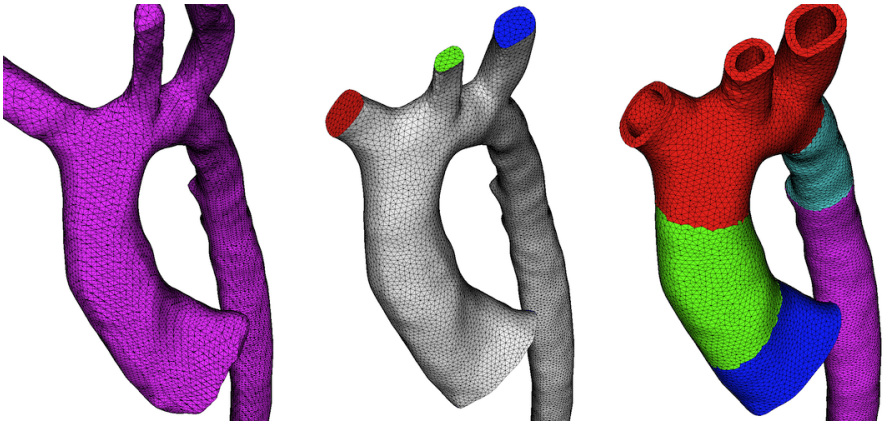

Figure 6.8: Meshes at the first time frame. Left: Segmented surface. Center: Fluid mesh. Right: Solid mesh.

external surface of the aortic wall, as done for the phantom in Chapter 5.

On the images (see Figure 6.4) it can be clearly seen that close to the inlet the ascending aorta is deforming considerably in part due to the motion of the heart. Hence, inspired by [MXA+11], we extract a displacement field from the segmented surfaces and impose it at the model's inlet by performing the following steps:

1. For each node of the solid's inlet at the first frame, the closest node of the first segmented surface was identified.

2. For each of the identified nodes, a dynamic displacement was computed by subtracting to the coordinates of the node for each segmented surface the one of the first frame. This is possible since the dynamic segmentation was performed by an image registration method, thus every surface has the same number of nodes.

3. The extracted displacement field was interpolated with cubic splines to the simulation time step to avoid jumps in the pressure in time, which could occur when using linear interpolation.

4. This interpolated displacement field is then strongly imposed to each node of the solid's inlet.

The deformed solid inlet together with the segmented surfaces for some of the time instants are presented in Figure 6.9. We are aware that the nature of the segmented surfaces is Eulerian, meaning that in practice we are not able to track the material points of the arterial wall from the segmented surfaces. A more proper approach would be to identify (or to tagg) material points like for instance the coronaries as done in [MXA+11]. Unfortunately, from this clinical data set we are not able to recognize such points, but we believe that doing as explained above is more realistic than just fixing the inlet. However, more sophisticated image registartion algorithms could be applied, see for instance [Mod04] for an overview.

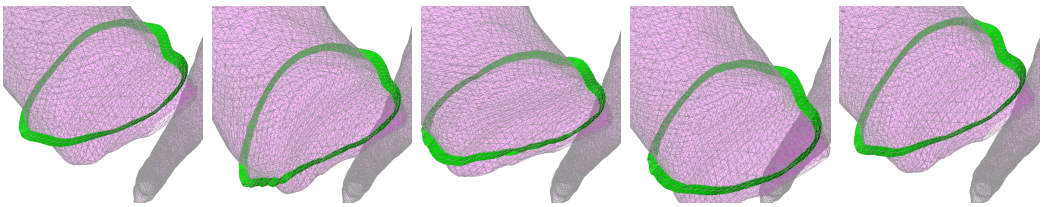

(a) $t = 0\,s$ (b) $t = 0.165\,s$ (c) $t = 0.221\,s$ (d) $t = 0.386\,s$ (e) $t = 0.717\,s$

Figure 6.9: Motion of the solid inlet (green) extracted from the dynamic segmentation (magenta) for some representative time frames.

Fluid boundary conditions. As usual, for the fluid mesh computation (ALE step, see Chapter 3, Equation (3.40)) the displacements of the structure were imposed at the fluid-structure interface, while at the four outlets homogeneous Neumann boundary conditions are applied. For the inlet, we have to proceed more carefully: the superposition of the inlet motion and the deformation of the fluid-structure interface at the ascending aorta make the fluid inlet subject of important deformations towards the interior of the domain during systole if homogeneous Neumann boundary conditions are used (see Figure 6.10-left). This can lead to excessively stretched elements in the fluid mesh. To improve the robustness of the computations, we impose Dirichlet boundary conditions obtained from a preliminar two-dimensional harmonic lifting of the displacements at the inlet's intersection with the wall. A comparison between the homogeneous Neumann boundary condition for the ALE and the two-dimensional lifting is shown in Figure 6.10. We remark that this approach can be used for all parts of the boundary where the displacement of the fluid is not a priori known by doing it "online" during the simulation as a preprocessing for the ALE step. However, for this application the supra-aortic branches and distal aorta move approximately rigidly so that the fluid's outlets remain reasonably plane during the simulation.

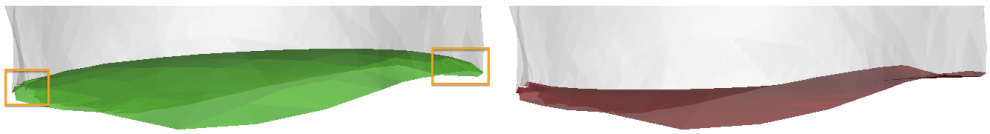

Figure 6.10: Comparison of the deformed fluid's inlet from the FSI simulation with homogenous Neumann conditions for the ALE step (green) and the Dirichlet conditions from 2D-lifting from the contour displacements (red). The arterial wall is represented in grey. Examples of zones where usually elements stretch are indicated by the orange squares.

For the velocity at the inlet, a constant velocity profile in direction to the mean normal vector of the moving inlet was computed at each time step to enforce the

desired flow. The flow corresponds to an interpolation (again, with cubic splines) to the simulation time step of the inflow until $\approx 0.6\,s$ and after this a zero inflow was enforced, see Figure 6.11.

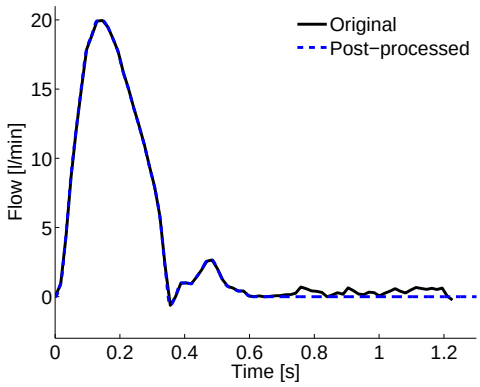

Figure 6.11: Original and processed input flows.

The boundary conditions for the fluid's outlets were chosen as three-elements Windkessel models with constants calibrated manually in order to have a similar flow split for a pressure of around $75\,mmHg$. The values of the constants are the same as in Table 2.1. We point out that the "true" Windkessel model parameters have to be calibrated/estimated considering properties of the upstream three-dimensional domain, specially the elastic characterization of the aortic wall. Moreover, in order to diminish the impact of the backflow instabilities due to the convection, the velocity direction was enforced to be normal to the outlet surface, however other techniques may be used (see [MBH+11] for an overview).

Initial condition. For the initial condition, a zero velocity field in the fluid with a constant pressure $\pi_l(0) = 62650 \approx 47\,mmHg$, $l = 1, \ldots, 4$ was considered (based on the available pressure measurements). The solid was started at rest and the loads from the fluid are corrected by the initial one. This can be viewed as a simple way to account for prestress. For more general approaches we refer to [GFW10].

Numerical algorithm. The physical model described above was solved through Algorithm 5, Chapter 3. The time step was taken as $\tau = 0.002\,s$. A forward simulation takes about 15 hours on a standard, single processor workstation (3.2 Ghz). In general, 2 to 3 FSI iterations are performed at each time step (i.e., the same number of linear pressure and nonlinear solid problems), with about 9 to 19 tangent problems (i.e., the same number of linear pressure problems and linear solid problems) for a relative tolerance of 10^{-3} on the fluid-solid interface displacements residual. This results in a cpu-time of 1'15" to 1'30" per time iteration.

6.2.2 Simulation results and comparison with clinical data

We now present the results for the FSI simulation with parameters $\theta^1 = 0$, $\theta^2 = 0.1155$, $\theta^3 = 0.2224$, $\theta^4 = 0.4150$, $\theta^5 = 0.3219$, namely $c_1 = 3 \cdot 10^5$, $c_2 = 3.25 \cdot 10^5$, $c_3 = 3.5 \cdot 10^5$, $c_4 = 4 \cdot 10^5$, $c_5 = 3.75 \cdot 10^5$. These values were chosen following physiological considerations about the stiffness distribution along the aorta, namely that the Pulse Wave Velocity (proportional to the square root of the arterial stiffness, see Chapter 1, Section 1.1.3) can double from the ascending to the descending aorta [LCVB+06].

Figure 6.12 shows the original and deformed fluid-structure interfaces, while Figure 6.13 presents the velocity and pressure distributions for peak systole at the deformed configuration. Then, Figure 6.14 shows the mean pressures and flows at the inlet and outlets.

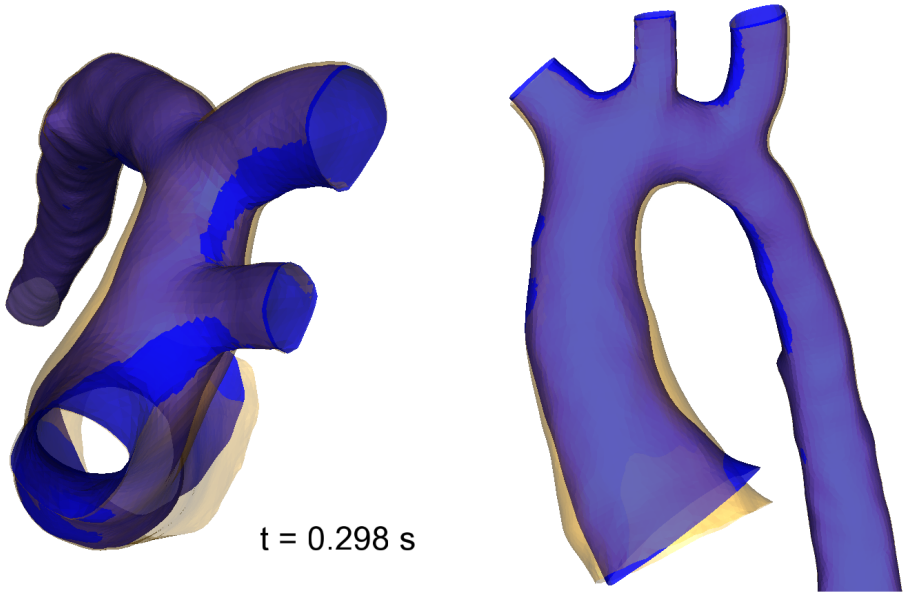

Figure 6.12: Three-dimensional views of the FSI simulation in terms of the position of the fluid-structure interface. Initial (blue) and deformed (orange) geometries.

We perform a first, rather qualitative, comparison with the segmented surfaces in Figure 6.15. It can be clearly seen that in the model the pulmonary trunk and also the superior vena cava are missing. In practice, they locally restrict the deformation of the ascending aorta, which also leads to a larger deformation in the opposite sites to these vessels.

Concerning the fluxes at the inlet and outlets, the interpretation of the simulation results must be done carefully. First, comparing the measured and computed fluxes, presented together in Figure 6.16 for the sake of readability, it can be appreciated that in general the fluxes agree except at the abdominal aorta. In fact, we assume that the measured flow at the abdominal aorta is correct since: (a) the imaged plane

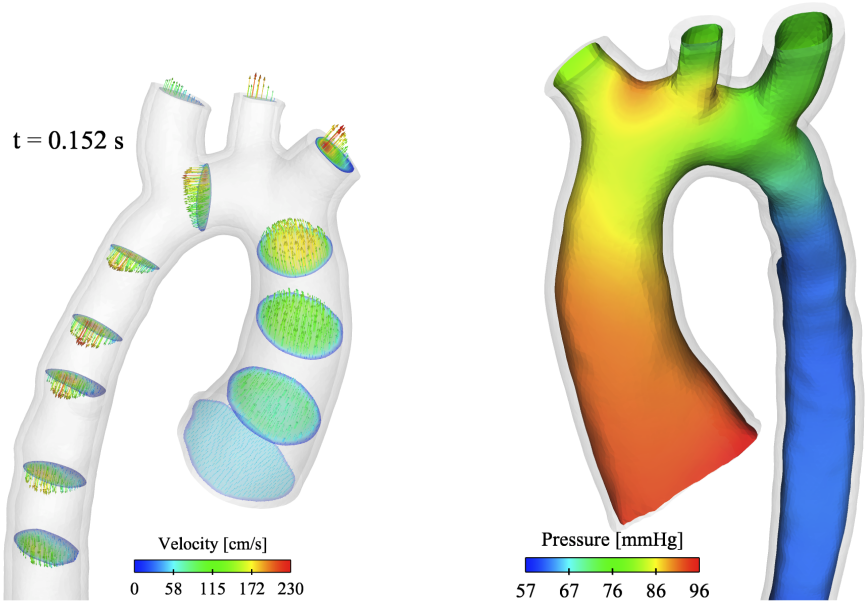

Figure 6.13: Snapshot of the FSI simulation at peak systole with deformed domain. Left: fluid velocity distribution. Right: fluid pressure distribution.

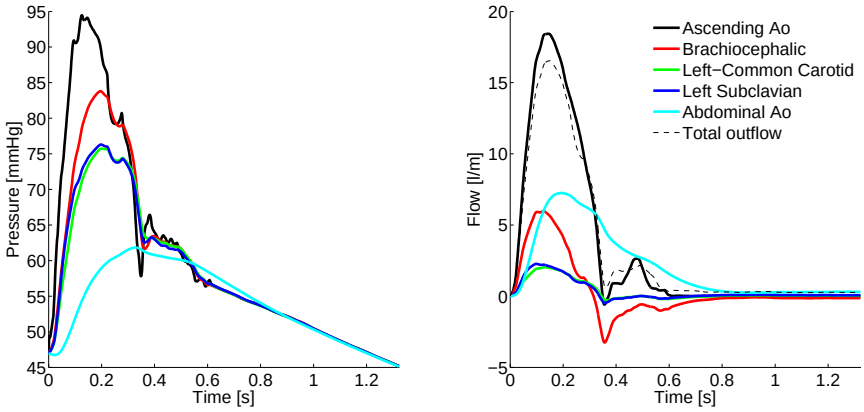

Figure 6.14: Windkessel models' output of the FSI simulation. Left: mean pressures at the boundary surfaces. Right: fluxes. The gap between inflow (ascending aorta) and total outflow is due to the storage of fluid in the aorta resulting from the deformation of the arterial wall.

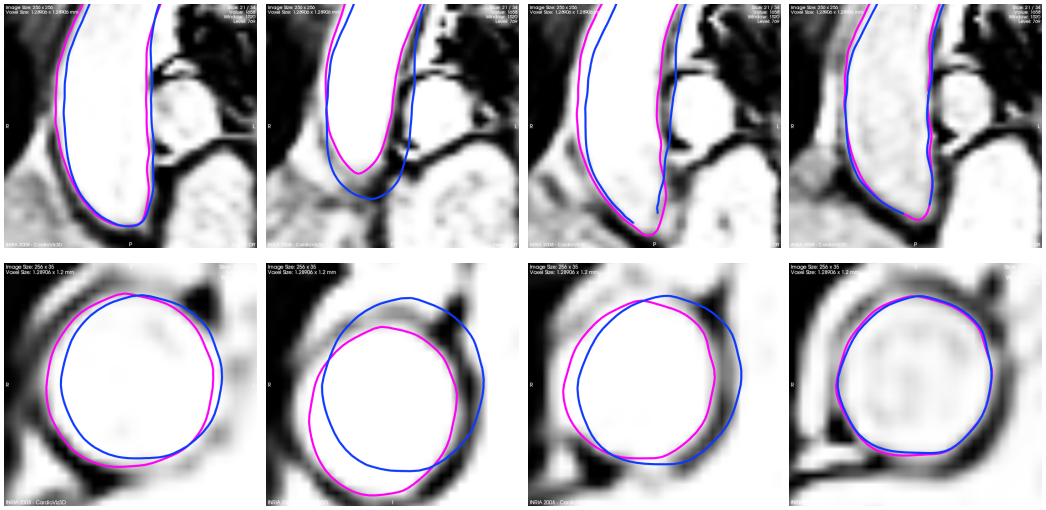

(a) $t = 0.159\,s$ (b) $t = 0.418\,s$ (c) $t = 0.538\,s$ (d) $t = 1\,s$

Figure 6.15: Some snapshots of the fluid-structure interface of the FSI model (blue) and the segmented surfaces (magenta), superposed with the MR-image. Top: foot-head view. Bottom: left-right view.

is perpendicular to the vessel and (b) due to the small solid deformations, fixing the region-of-interest used for the flow computation should reasonably approximate the flow. Hence, this important difference between model and measurements at the abdominal aorta may come from an underestimation of the model's inflow: the flow data was extracted from a plane in a fixed location and therefore does not necessarily represent the flow across the model's moving inlet. This can obviously lead to an underestimation of the distal outflow. As explained above, note also that the flow at the inlet (continuos black curves) is perturbed due to imposed inlet motion in the structure, whose velocity is enforced at the fluid inlet's contour.

For the pressures, a comparison between measurements and model is shown in Figure 6.17. At the abdominal aorta, the ratio between model's and measured pressure pulses is about the same as in the flow curves. Hence, for obtaining pressures closer to the measurements, the right flow at the outlet should be obtained.

At the ascending aorta, the model overestimates the pressure. One factor can be, as discussed above, the significant uncertainty in the inflow curve. Moreover, some mesh convergence studies in the pure Navier-Stokes case (not shown here) put in evidence that mesh refinement should reduce the pressure pulse at the ascending aorta. In contrast, at the coarctation site, the model gives an pressure pulse much closer to the measurements, at least in terms of the pressure pulse.

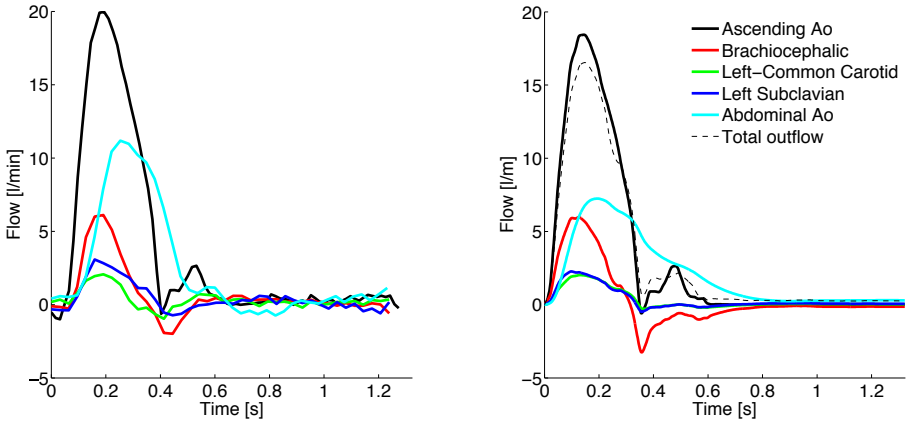

Figure 6.16: Comparison of measured (left) and model's (right) flows.

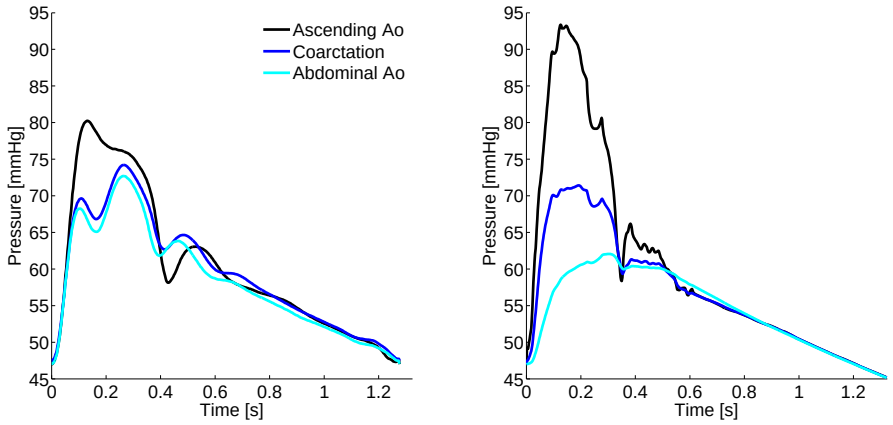

Figure 6.17: Comparison between measured (left) and simulated (right) pressures at three locations in the aorta.

6.3 Estimation results with synthetic data

In this section we present some results for the estimation of the spatial distributed constitutive parameter $c_1^j = 3 \cdot 10^5 \cdot 2^{\theta_j}$ in terms of θ^j for $j = 1, \ldots, 5$. The measurements correspond to the fluid-structure interface's surface with $\theta^1 = 0$, $\theta^2 = 0.1155$, $\theta^3 = 0.2224$, $\theta^4 = 0.4150$, $\theta^5 = 0.3219$ (see Section 6.2.2), which were then resampled to 25 time instants as in the clinical data (i.e. the 4D-SSFP acquisition, see Figure 6.4). The initial guesses for the parameters were chosen as $\hat{\theta}_0^1 = \cdots = \hat{\theta}_0^5 = 0$ and the initial covariance equal to the identity. The gain for the measures (see Chapter 3, Equation (3.46)) is taken as $\gamma = 10^3$ so that the estimated parameters converges with respect to the gain, as exemplified in Chapter 3, Figure (3.3), and also done in Chapter 5 for the aortic phantom.

The results are shown in Figure 6.18. We can see that we satisfactory converge to the reference values for the 5 regions in spite of the important (and realistic) time resampling. However, the confidence interval for the coarctation - and stiffer - region (cyan) is larger than for the rest - more flexible - regions. This behavior is can be also seen with not resampled measurements (results not shown here).

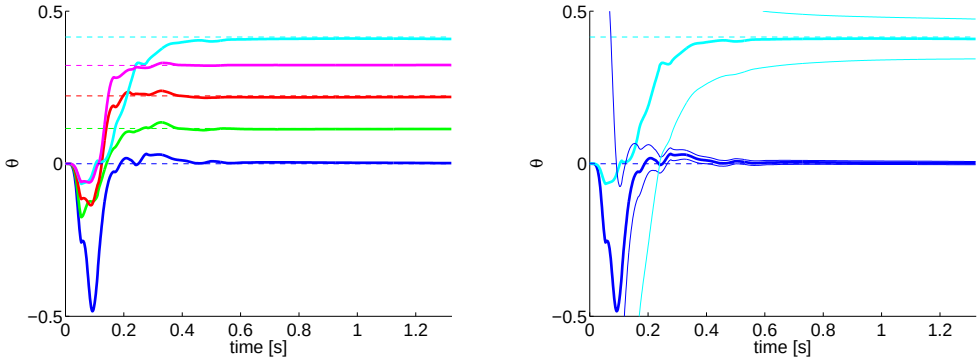

Figure 6.18: Estimation of the constitutive parameters θ^j, $j = 1, \ldots, 5$, using synthetic surfaces resampled to the same times as the segmented surfaces. The results are presented in terms of the mean values (thick lines), the confidence interval (thin lines) and reference values (dashed lines). The colors correspond to the regions distinguished in Figure 6.8-left.

We additionally perturb the measurements by remeshing the 25 synthetic surfaces allowing a geometrical error of around $0.5\,mm$ and a maximal triangle length of $1.5\,mm$, see Figure 6.19. The estimation results with these remeshed surfaces are presented in Figure 6.20. Note that even though the modifications to the synthetic surfaces appear not to be significative, the remeshing has a considerably impact on the estimation's performance in the regions with lower SNR (coarctation and abdominal aorta). In particular, we observe that the estimated parameters at the coarctation (cyan) and abdominal aorta (magenta) do not converge to the reference values, see Figure 6.20-left. Unfortunately, the standard deviation indicator (thin

curves in both Figures) does not help to discriminate the confidence of the estimated parameters as shown in Chapter 3, Figure 3.4.

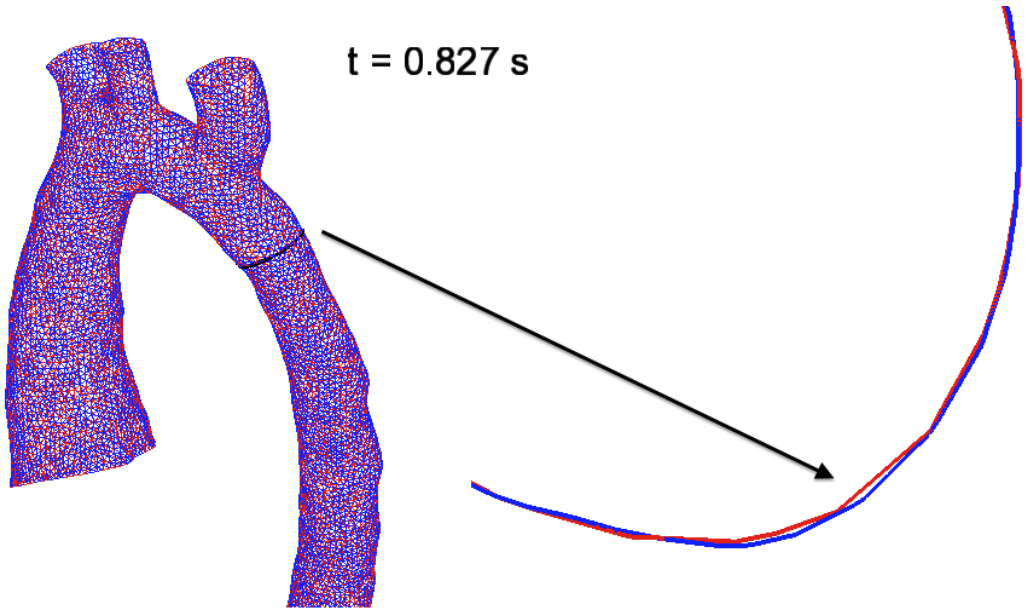

Figure 6.19: Example of an original (blue) and remeshed (red) synthetic fluid-structure interfaces. Left: three-dimensional view. Right: zoom at the coarctation level.

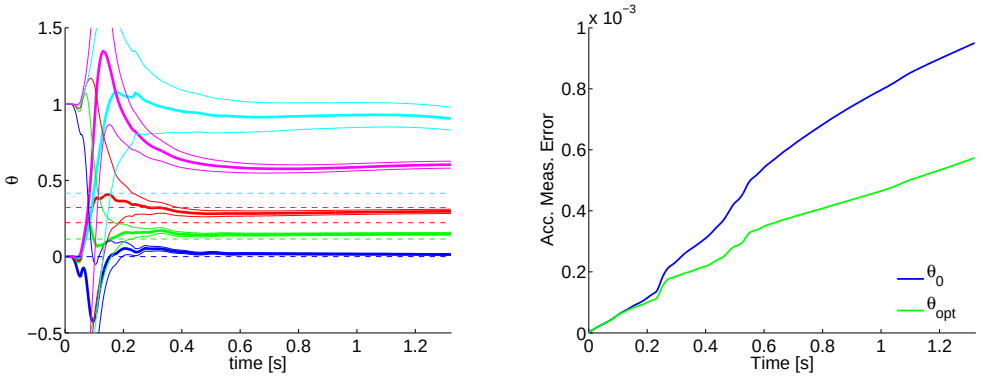

Figure 6.20: Estimation results for the constitutive parameters θ^j, $j = 1, \ldots, 5$, using synthetic surfaces resampled and remeshed synthetic surfaces. Left: mean values (thick lines), confidence intervals (thin lines) and reference values (dashed lines). Right: Accumulated measurement error (space-time L^2-norm, see Equations (5.2)-(5.3)) for the model with initial guess $\theta^1 = \cdots = \theta^5 = 0$ (blue) and the final estimated values $\theta^1 = 0.013$, $\theta^2 = 0.149$, $\theta^3 = 0.296$, $\theta^4 = 0.904$, $\theta^5 = 0.602$ (green).

6.4 Preliminary results with clinical data

In this section we present the very first results for the estimation of the stiffness parameters in the aorta using the segmented dynamic surfaces. As shown in Figure 6.21, the segmented surfaces were remeshed in order to decrease the number of triangles and hence the cost of the computation of the distances between the model's and segmented surfaces.

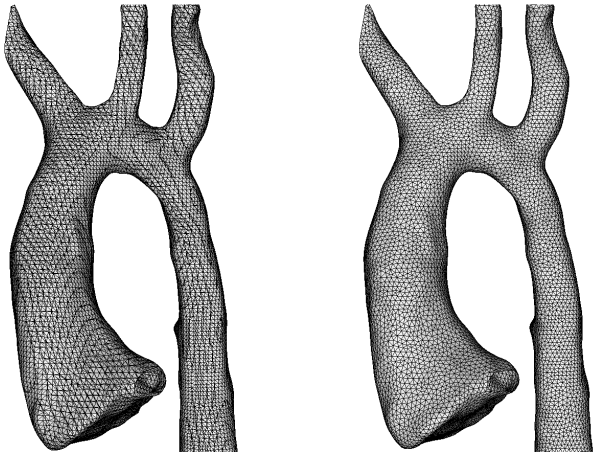

Figure 6.21: Segmented first frame. Left: original. Right: remeshed.

The estimation results are presented in Figure 6.22. In spite of the several model imperfections mentioned in the previous sections, we can see that we are able to obtain some meaningful results, with no additional effort with respect to the testcases using synthetic measurements.

For the first two regions of the ascending aorta (blue and green curves) the data assimilation algorithm recognizes that they should be stiffer, which somehow confirms that the model does not include the surrounding vessels in this portion of the artery. For the coarctation region, the estimation is not able to converge (cyan curve), probably due to extremely low SNR resulting, as explained before, from the poor image resolution due to the high blood velocity in this zone, see Figure 6.4.

We present some time frames of the MR-images, segmentation and models with the initial and calibrated parameters in Figure 6.23. Note that the model with calibrated parameters follows the segmented surfaces closer.

6.5 Conclusions

In this chapter we presented preliminary results of the estimation of the mechanical properties of an aorta with repaired coarctation. We started summarizing the clinical data available, and then we described how the FSI model is constructed from this data. We noted that the model's output is reasonably close to some of the measured data. However, we remarked that the current model has some limitations, for

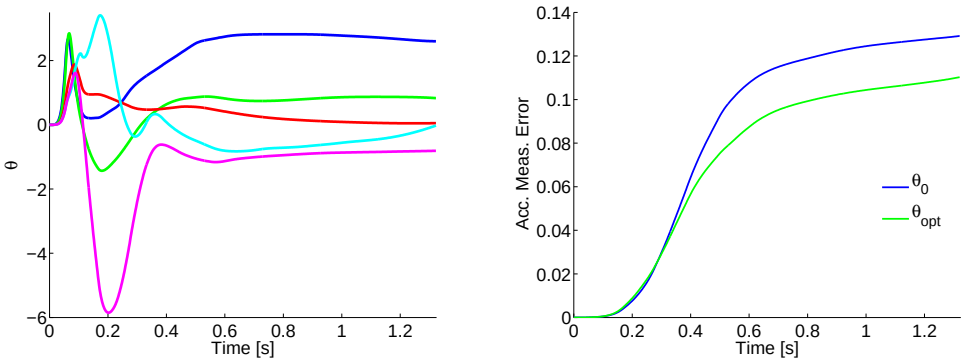

Figure 6.22: Estimation results for the constitutive parameters θ^j, $j = 1, \ldots, 5$, using the segmented surfaces. Left: mean estimated values. Right: Accumulated measurement error (space-time L^2-norm, see Equations (5.2)-(5.3)) for the model with initial guess $\theta^1 = \cdots = \theta^5 = 0$ (blue) and the final estimated values $\theta^1 = 2.60$, $\theta^2 = 0.83$, $\theta^3 = 0.05$, $\theta^4 = -0.02$, $\theta^5 = -0.81$ (green).

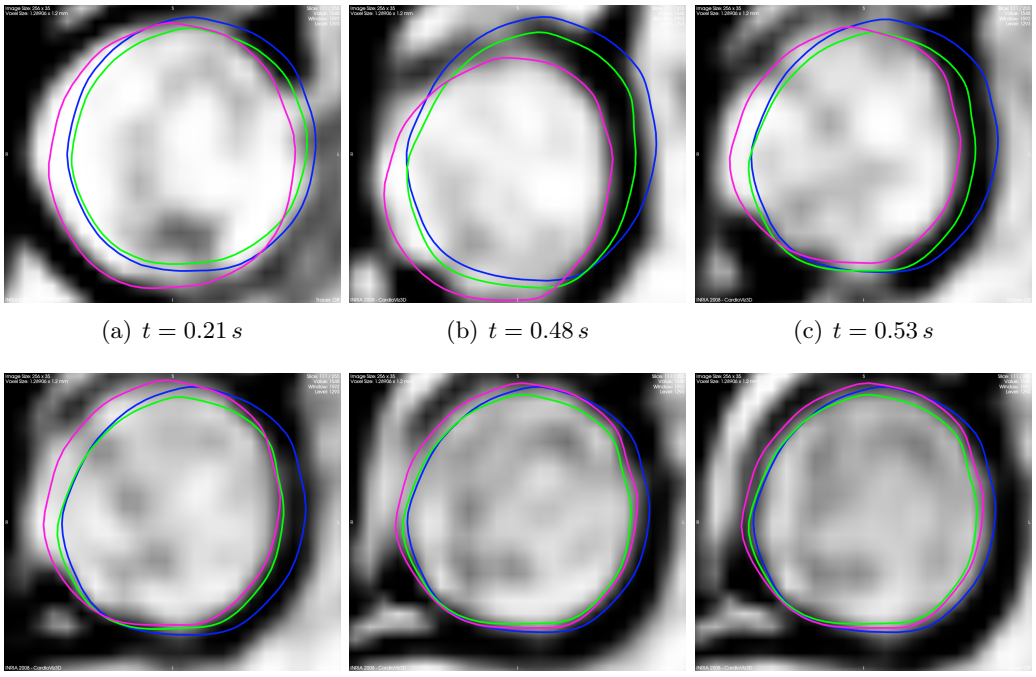

(a) $t = 0.21\,s$ (b) $t = 0.48\,s$ (c) $t = 0.53\,s$

(d) $t = 0.58\,s$ (e) $t = 0.64\,s$ (f) $t = 0.69\,s$

Figure 6.23: Comparison for some time instants between image, segmented surface (magenta), and FSI-model with initial (blue) and optimal (green) parameters. The view corresponds to a foot-head cut of the ascending aorta at the level of the pulmonary trunk.

example the absence of models for the some external organs. Moreover, there exists important measurements uncertainties, for example the underestimated inflow and the poor SNR for the segmented surfaces at the descending and abdominal aorta. Then, we presented some results of the estimation of the constitutive parameters distribution with perturbed synthetic data. Finally, we showed the first estimation result with real data, namely with the segmented surfaces from the 4D-SSFP sequence, obtaining meaningful results for the estimated parameter values.

Conclusions and Perspectives

Damit das Mögliche entsteht,
muss immer wieder das Unmögliche versucht werden.
Hermann Hesse, 1960.

Chapter 7

Conclusions and perspectives

In this last chapter we give a general overview the work and the contributions of this thesis and give some perspectives for future research.

Contents

7.1 Work summary

7.1.1 Coupling of 3D-FSI and 0D models

In Chapter 2 we presented and analyzed some numerical schemes for solving the three-dimensional (3D) FSI systems coupled with Windkessel's (0D) models for the outflow boundaries. The work was motivated by instabilities present in physiological numerical simulations.

Focusing firstly on the Navier-Stokes Equations (i.e., without interaction with a structure), we analyzed two possible coupling schemes between the 3D and the 0D models, when the 3D fluid is solved through a projection method. Hence, since the velocity and pressure are solved explicitly, the natural way to compute the 0D pressures consists in using the flows from the velocity of the previous viscous step. We showed theoretically and numerically, that this choice may lead to numerical instabilities when dealing with multiple-outlet geometries.

Hence, we proposed a semi-implicit formulation that solves the Windkessel's model and the 3D pressure field implicitly, fixing the instability sources of the explicit approach. We also presented an implementation of this scheme which is minimally intrusive, in the sense that we can keep the standard pattern of the finite element system. For the realistic testcases shown here, the numerical resolution of this formulation involves a negligible additional computational cost for the pressure-0D projection step with respect to the explicit scheme.

We also extended the formulation and the analysis of the fluid-structure interaction semi-implicit scheme reported in [FGG07] to the lumped modeling of the downstream boundaries. Our analysis showed that in this case the explicit 3D-0D coupling introduces an artificial uncontrolled power which might lead to numerical instabilities, even for single-outlet geometries. In contrast, for the 3D-0D semi-implicit scheme stability is guaranteed under the same condition derived in [FGG07] with a traction-free boundary condition on the outlet.

7.1.2 Data assimilation in FSI

In Chapter 3 we applied the reduced-order nonlinear Kalman filter for the estimation of uncertain parameters in fluid-structure models. We gave a comprehensive derivation of the algorithm, starting from linear least squares and reviewing the key aspects of the *unscented transforms* for propagating the statistics (mean and covariance) of vectors by nonlinear functions. We pointed out some algorithmic aspects needed for the success of the estimation in the FSI framework, and we concluded with several numerical examples in realistic configurations with noisy synthetic data. The results are very promising in terms of precision of the estimation, computational cost and complexity. It should be noted that these results are the first reported for data assimilation in 3D-FSI.

In Chapter 4 we dealt with the estimation of the trajectory of a fluid-structure system assuming only an uncertainty in the initial condition. For that purpose, we proposed a formulation of a *Luenberger observer* for FSI problems. Observers consist basically in adding a well chosen feedback term - proportional to the discrepancy between measurements and model - to the original dynamical system. In particular, we analyze and extended the feedbacks used for solid mechanics based on partially measured velocities or displacements in FSI. We illustrated first their performance in a general non-linear FSI setting. We then carried out more detailed analysis using simplified, but representative FSI models, mainly based in linear spectral analysis. This allowed us to understand the different behaviors and to propose improvements of the filters when their performance was not satisfactory.

7.1.3 Application to real systems

The last part of this thesis was devoted to the application of the FSI-models and the nonlinear Kalman filter using measured data coming from real physical systems.

Chapter 5 successfully validated, in a simple but real configuration, the estimation of the solid stiffness from dynamic MR-images and pressure data by considering a linear elastic and a nonlinear hyperelastic (Mooney-Rivlin) solid models. For a large pressure range ($\delta p \approx 110\, mmHg$), the optimized nonlinear solid gave a smaller discrepancy with the real measures than the optimized linear one. Moreover, in the linear case and for a lower pressure range ($\delta p \approx 55\, mmHg$) the estimated Young's modulus satisfactory matched the value computed independently using data coming from a non-destructive mechanical test.

Chapter 6 was devoted to the the fluid-structure simulation of a patient-specific aorta and the estimation of the stiffness distribution from clinical data. In this context, we summarized the available clinical data consisting mainly of: static and dynamic magnitude MR-images for the assessment of the aorta's geometry, phase MR-images for measuring the velocity field perpendicular to some image slices, and catheter pressure measurements. Then, we described in detail how this data was used for the set up of the forward FSI-model. Here, a technical difficulty was to deal with the motion "imposed" by the heart at the ascending aorta. We compared the simulation results (for wall displacements, flows and pressures) with the clinical data. This put in evidence the strengths and weaknesses of the model and gave insights for future developments, particularly for the proper inclusions of the external organs as solid boundary conditions like the pulmonary trunk and the superior vena cava.

Then, we estimate one of the nonlinear constitutive parameters in five different regions of the aorta from noisy synthetic data. Finally, we presented preliminary results for the estimation of the same parameters from the segmented surfaces coming from the real medical images. The result showed that despite the model and data imperfections, the estimation procedure was able to give meaningful results.

7.2 Perspectives

In this thesis we have only dealt with the assimilation of solid measurements for FSI problems. However, for the design of Luenberger observers (Chapter 4), we showed that the real poles of the FSI-spectrum are almost indistinguishable from the pure fluid case, see Figure 4.16. Since the solid feedbacks do not affect this part of the spectrum, we proposed to include a feedback based on fluid measurements to improve the stabilization of the viscous poles of the fluid part.

7.2.1 Assimilation of measurements of the fluid velocity

As shown in Chapter 6 for the aorta's simulation, modern acquisition techniques also allow to measure valuable hemodynamical quantities, e.g., the in-plane velocity data and the invasive pressures shown in Chapter 6. However, a time sequence of the 3D velocity components in a spatial box, called *4D-Flow* (see, e.g., [UBS+09]), offers promising perspectives for data assimilation in hemodynamics. An example of 4D-Flow data for the patient studied in Chapter 6 is shown in Figure 7.1.

In particular, this type of data could be used to estimate the pressure field proximal to the heart, together with distal (and minimally invasive) pressure measurements. As mentioned in the introduction, the pressure afterload of the heart is one of the most relevant indicators of severity in cardiovascular diseases.

The task of estimating the pressure distribution can be seen as a state estimation

problem, for which we could intend to design the following observer

$$\begin{cases} \rho_{\mathrm{f}} \dfrac{\partial \widehat{\boldsymbol{u}}_{\mathrm{f}}}{\partial t} + \rho_{\mathrm{f}} \widehat{\boldsymbol{u}}_{\mathrm{f}} \cdot \boldsymbol{\nabla} \widehat{\boldsymbol{u}}_{\mathrm{f}} - \boldsymbol{\nabla} \cdot \boldsymbol{\sigma}_{\mathrm{f}}(\widehat{\boldsymbol{u}}_{\mathrm{f}}, \widehat{p}) = \gamma_u \mathbb{1}_{\omega}(\boldsymbol{z}_u - \hat{\boldsymbol{u}}_{\mathrm{f}}|_{\omega}), & \text{in} \quad \Omega^{\mathrm{f}}, \\ \boldsymbol{\nabla} \cdot \widehat{\boldsymbol{u}}_{\mathrm{f}} = 0, & \text{in} \quad \Omega^{\mathrm{f}}, \\ \boldsymbol{\sigma}_{\mathrm{f}}(\widehat{\boldsymbol{u}}_{\mathrm{f}}, \widehat{p}) \cdot \boldsymbol{n}_{\mathrm{f}} = \widetilde{\gamma}_u \mathbb{1}_{\widetilde{\omega}}(\widetilde{\boldsymbol{z}}_u - \widehat{\boldsymbol{u}}_{\mathrm{f}}|_{\widetilde{\omega}}), & \text{on} \quad \partial\Omega^{\mathrm{f}} \backslash \Gamma^{\mathrm{out}}, \\ \boldsymbol{\sigma}_{\mathrm{f}}(\widehat{\boldsymbol{u}}_{\mathrm{f}}, \widehat{p}) \cdot \boldsymbol{n}_{\mathrm{f}} = -\widehat{P}\, \boldsymbol{n}_{\mathrm{f}}, & \text{on} \quad \Gamma^{\mathrm{out}}. \end{cases} \tag{7.1}$$

where the term $\gamma_u \mathbb{1}_{\omega}(\boldsymbol{z}_u - \hat{\boldsymbol{u}}_{\mathrm{f}}|_{\omega})$ corresponds to the feedback based on the fluid velocity measurements $\boldsymbol{z}_u$ in the domain $\omega \subseteq \Omega^{\mathrm{f}}$. In the case of the 4D-flow, the measurements can be assumed in all the domain Ω^{f}. Thus, after spatial discretization of Problem (7.1), the operator $\mathbb{1}_{\omega}$ can be interpreted as an interpolator from the measurement to the computational domain. Similarly, we impose weakly the Dirichlet boundary conditions for $\hat{\boldsymbol{u}}_{\mathrm{f}}$ using the measurements $\widetilde{\boldsymbol{z}}_u$ in the domain $\widetilde{\omega} \supseteq \partial\Omega^{\mathrm{f}} \backslash \Gamma^{\mathrm{out}}$, see Equation $(7.1)_3$, coming from the same data set as $\boldsymbol{z}_u$ or from another imaging modality with higher resolution. The boundary conditions $\widehat{P}(t)$ can come directly from pressure measurements, from 0D models and/or observers for the Windkessel's model, see Equation (4.58).

This feedback design simply corresponds to the analog of the DVF for fluid velocity measurements, and a similar one has been already used in parabolic systems for applications in oceanography, see for example [AB08]. It can be easily shown, for instance by a linear spectral analysis, that such a feedback stabilizes the poles of the error equation derived from the (linearized) state estimator (7.1). If velocity measurements are available in all the domain, augmenting the gain γ_u will always improve the stabilization to zero of the error in the initial condition. Hence, the only constraint in the choice of γ_u would be to avoid to penalize the noise excessively, namely forcing the estimator $\widehat{\boldsymbol{u}}_{\mathrm{f}}$ being equal to the measurements $\boldsymbol{z}_u$.

However, in the case that only velocity measurements are available in few slices (as the IP-velocity data presented in Chapter 6), it can be shown that the poles of the error dynamics will converge (with respect to γ_u) to a problem with homogeneous Dirichlet conditions on this slices. In fact, the values of these poles are typically controlled by $1/r^2$, with r the shortest dimension of the vessel (usually the radius, which explains the notation). Hence, if these slices are placed perpendicularly along the vessel, the distance between these slices should be much smaller than r for an effective stabilization of the error, which is somehow similar to acquiring 4D-flow data. Note, however, that this does not mean than another, more efficient, observer can be designed for these type of problems and data. In particular, some numerical tests (not shown here) suggest that a feedback based on a reduced order Kalman filter (built for example from a *Proper-Orthogonal Decomposition* (POD) basis, see e.g. [KV03]) would be a valid alternative.

We remark that other approaches have been studied for assimilating flow data. In particular, in [DPV11] a simplified variational approach was used, where the discrepancy between model and measurements is minimized independently at each time step. Moreover, in [HMM+10, Dwi10] it was proposed to apply Least Squares Finite

Element methods for stationary flows consisting in writing the partial differential equations as an (energy) minimization problem and then to penalize the discrepancy between model and measurements. In [IH08, FHSY08], a feedback-based approach was already applied to the assimilation of Ultrasound data in an aorta.

7.2.2 Assimilation of pressure measurements

As the fluid velocity data, the available pressure measurements (see for example Chapter 6) have been only used for the sake of comparison and manual calibration of the Windkessel's model, but they have not been used in the data assimilation framework. In fact, they could directly enter in the nonlinear Kalman filtering procedure (see Chapter 3, Section 3.2.4) by including in the innovation a term $Z_p^{n+1} - p^{n+1}$, with Z_p^{n+1} the pressure measurement at time t_{n+1}.

For the design of an observer based on the pressures, as mentioned above, it is easy to construct an estimator in the case of pressure measurements at the outlets as shown in Chapter 4, Equation (4.58). However, in the case where measurements at the interior of the domain are available, which we denote by z_p in the domain $\Pi \subseteq \Omega^{\mathrm{f}}$, a feedback term for the Navier-Stokes equations can be proposed as

$$\begin{cases} \rho_{\mathrm{f}} \dfrac{\partial \widehat{\boldsymbol{u}}_{\mathrm{f}}}{\partial t} + \rho_{\mathrm{f}} \widehat{\boldsymbol{u}}_{\mathrm{f}} \cdot \boldsymbol{\nabla} \widehat{\boldsymbol{u}}_{\mathrm{f}} - \boldsymbol{\nabla} \cdot \boldsymbol{\sigma}_{\mathrm{f}}(\widehat{\boldsymbol{u}}_{\mathrm{f}}, \widehat{p}) = \boldsymbol{0}, & \text{in} \quad \Omega^{\mathrm{f}}, \\ \boldsymbol{\nabla} \cdot \widehat{\boldsymbol{u}}_{\mathrm{f}} - \gamma_p \mathbb{1}_{\Pi}(z_p - \hat{p}|_{\Pi}) = 0, & \text{in} \quad \Omega^{\mathrm{f}}, \\ \widehat{\boldsymbol{u}}_{\mathrm{f}} = \boldsymbol{u}_{\mathrm{in}}, & \text{on} \quad \Gamma^{\mathrm{in}}, \\ \widehat{\boldsymbol{u}}_{\mathrm{f}} = \boldsymbol{u}_{\Sigma}, & \text{on} \quad \Sigma, \\ \boldsymbol{\sigma}_{\mathrm{f}}(\widehat{\boldsymbol{u}}_{\mathrm{f}}, \widehat{p}) \cdot \boldsymbol{n}_{\mathrm{f}} = -\widehat{P}\, \boldsymbol{n}_{\mathrm{f}}, & \text{on} \quad \Gamma^{\mathrm{out}}. \end{cases} \tag{7.2}$$

which we naturally call *Artificial Compressibility Feedback* (ACF) with the gain given by γ_p. Note that since anyway Dirichlet data is required this observer could be combined with System (7.1) when velocity and pressure measurements are simultaneously available.

It is interesting to analyze the efficacy of such a filter in FSI systems. In the case of considering (7.2) coupling with a linear elastic solid (i.e., $\boldsymbol{u}_{\Sigma} = \boldsymbol{u}_{\mathrm{s}}|_{\Sigma_0}$), and assuming an irrotational fluid as in Chapter 4, we can write the following linear system for the error

$$\begin{bmatrix} K_{\mathrm{s}} & 0 & 0 \\ 0 & M_{\mathrm{s}} & 0 \\ 0 & -\rho_{\mathrm{f}} G^{\intercal} & -\gamma_p H_p^{\intercal} M_{\Pi} H_p \end{bmatrix} \begin{bmatrix} \Phi_d \\ \Phi_v \\ \Phi_p \end{bmatrix} \lambda = \begin{bmatrix} 0 & K_{\mathrm{s}} & 0 \\ -K_{\mathrm{s}} & 0 & G \\ 0 & 0 & K_p \end{bmatrix} \begin{bmatrix} \Phi_d \\ \Phi_v \\ \Phi_p \end{bmatrix}, \tag{7.3}$$

with M_{Π} the $L^2(\Pi)$ mass matrix, H_p the discrete observation operator for the pressure, and the rest of the terms defined in Chapter 4. Rewritting it as a cubic eigenvalue problem in Φ_d and computing the sensitivity of λ with respect to γ_p at $\gamma_p = 0$ results

$$\frac{\partial \lambda}{\partial \gamma_p}\Big|_{\gamma_p = 0} = -\frac{1}{2\omega_a^2 \rho_{\mathrm{f}}} \|\Phi_{0,p}\|^2_{L^2(\Pi)}$$

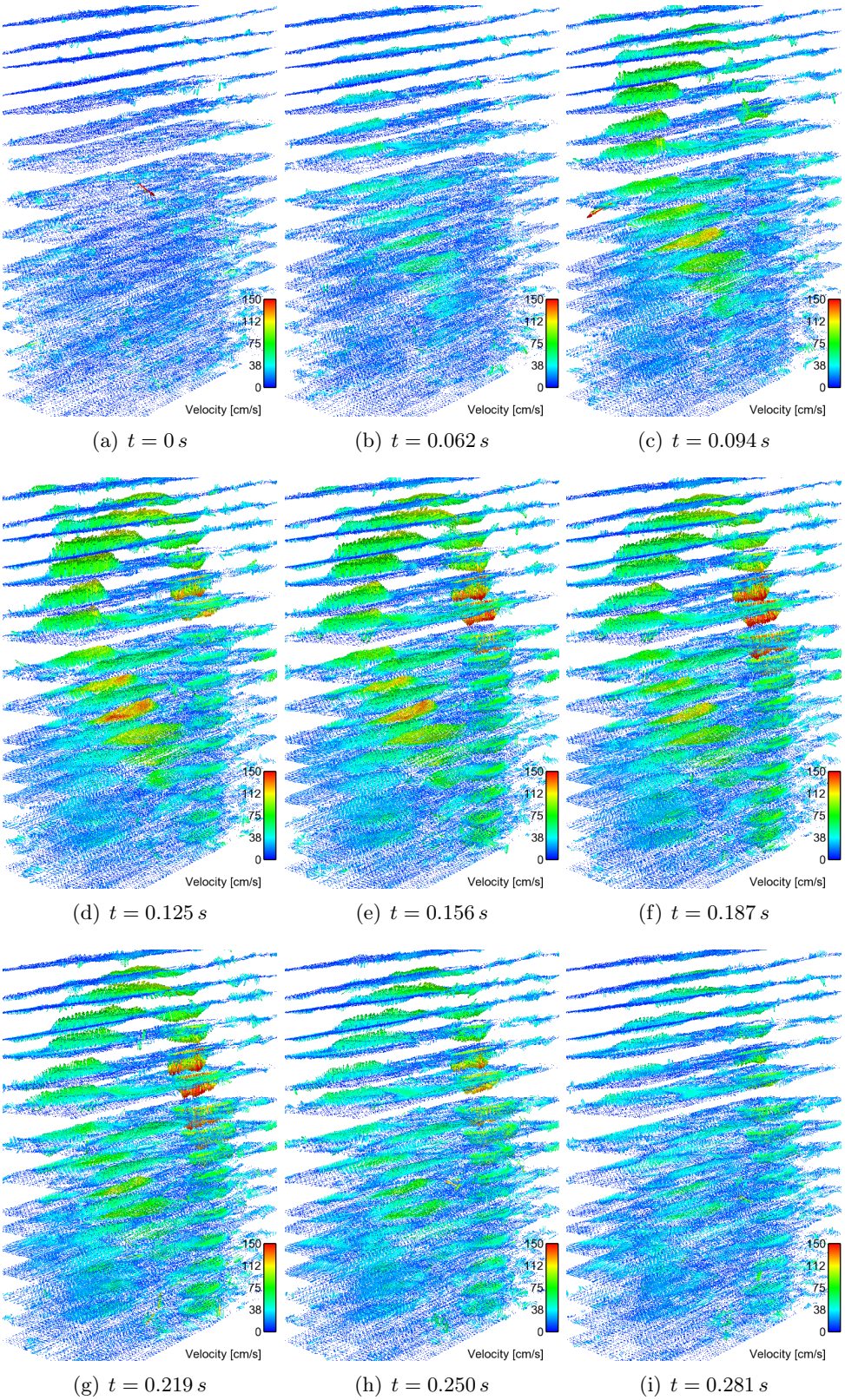

(a) $t = 0\,s$ (b) $t = 0.062\,s$ (c) $t = 0.094\,s$

(d) $t = 0.125\,s$ (e) $t = 0.156\,s$ (f) $t = 0.187\,s$

(g) $t = 0.219\,s$ (h) $t = 0.250\,s$ (i) $t = 0.281\,s$

Figure 7.1: Snapshots of the 3D velocity field on several cutting planes of the 4D-flow data in study case 10 of the euheart database. The MR-image data was courtesy of Israel Valverde (King's College of London).

with $\Phi_{0,p}$ the mode for the pressure with $\gamma_p = 0$. This analysis is confirmed numerically in Figure 7.2, where it is shown that the efficiency of the ACF varies depending on the pole, similarly to what happens with the DVF. Of course, these preliminary results should be pursued considering incomplete observations and including Windkessel's models, as well as studying the impact on a (Navier-) Stokes system.

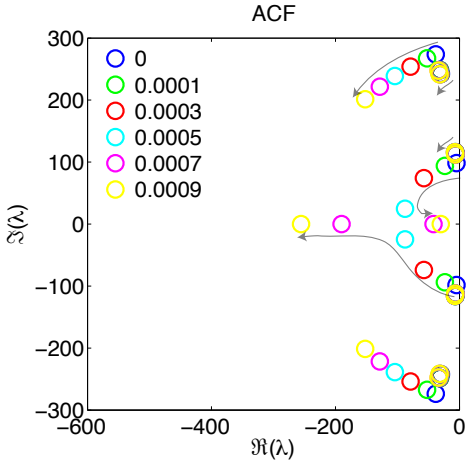

Figure 7.2: Poles of the ACF with respect to the gain γ_p for full pressure observations and $\eta_s = 10^{-3}$. The grey arrows sketch the trajectory of the poles when increasing feedback gain.

7.2.3 Application to real systems

Current work is being carried out in order to deal with more complex in vitro physical configurations, which offer interesting perspectives for clinical practice (e.g., the detection of artherosclerotic plaques and their implications in the surrounding hemodynamic environment). Hence, in order to asses the capacity to detect variable stiffness along the vessel from real measurements (see Chapters 3 and 6 for synthetic measurements), data was acquired fixing an elastic strap in a portion of the same silicon tube at the proximal end, see Figure 7.3. The aim is to test if the algorithm is capable to localize the stiffer region (compared with the value for the silicon already estimated).

Next steps would be to validate the algorithms for more realistic in vitro configurations, e.g., in geometries based on patient specific aortas. These tests could serve for determining the needs for the data acquisition and modeling assumptions, as well as the required numerical precision for reliable simulation results. In this context, several and precise measurements of the wall motion and hemodynamical quantities could be obtained, since there would not be any time or ethics constraints like in real patients. Based on these in vitro tests, data acquisitions protocols may be tested in order to carry out meaningful trials with patient's. Moreover, using state-of-the art

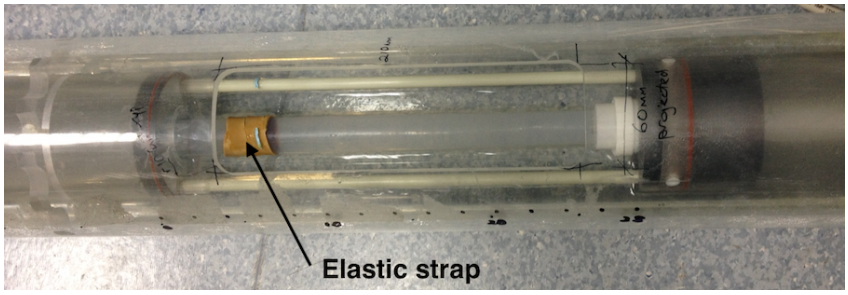

Figure 7.3: Experimental setup for the data acquisition with an artificial stiffening (courtesy of Nicholas Gaddum, King's College of London).

numerical methods for fluid, structure and coupled FSI problems and expecting an increase of computational power, studies in large number of patients could be performed. This would allow to investigate and propose new diagnosis and treatment methodologies based on these sophisticated mathematical and computational tools.

Bibliography

[AB08] D. Auroux and J. Blum. A nudging-based data assimilation method for oceanographic problems: the back and forth nudging (bfn) algorithm. *Nonlin. Proc. Geophys.*, 15:305–319, 2008.

[ABD10] S. Avril, P. Badel, and A. Duprey. Anisotropic and hyperelastic identification of in vitro human arteries from full-field optical measurements. *J Biomech*, 43(15):2978–85, 2010.

[ACF09] M. Astorino, F. Chouly, and M. A. Fernández. Robin based semi-implicit coupling in fluid-structure interaction: Stability analysis and numerics. *SIAM J. Sci. Comp.*, 31(6):4041–4065, 2009.

[amh07] *The American Heritage Medical Dictionary*. Houghton Mifflin Company, 2007.

[ASK+11] H. Astrand, J. Stalhand, J. Karlsson, M. Karlsson, B. Sonesson, and T. Länne. In vivo estimation of the contribution of elastin and collagen to the mechanical properties in the human abdominal aorta: effect of age and sex. *Journal of Applied Physiology*, 110(1):176–187, 2011.

[BALS12] P. Badel, S. Avril, S. Lessner, and M. Sutton. Mechanical identification of layer-specific properties of mouse carotid arteries using 3d-dic and a hyperelastic anisotropic constitutive model. *Computer Methods in Biomechanics and Biomedical Engineering*, 15(1):37–48, 2012.

[BBC+07] S. Balocco, O. Basset, G. Courbebaisse, E. Boni, P. Tortoli, and C. Cachard. Noninvasive Young's modulus evaluation of tissues surrounding pulsatile vessels using ultrasound doppler measurement. *Ultrasonics, Ferroelectrics and Frequency Control, IEEE Transactions on*, 54(6):1265–1271, 2007.

[BBC+10] S. Balocco, O. Basset, G. Courbebaisse, E. Boni, A.F. Frangi, P. Tortoli, and C. Cachard. Estimation of the viscoelastic properties of vessel walls using a computational model and Doppler ultrasound. *Physics in Medicine and Biology*, 55(12):3557, 2010.

[Bel57] R.E. Bellman. *Dynamic programming*. Princeton University Press, 1957.

[BGH+09] Y. Bazilevs, JR Gohean, TJR Hughes, RD Moser, and Y. Zhang. Patient-specific isogeometric fluid-structure interaction analysis of thoracic aortic blood flow due to implantation of the jarvik 2000 left ventricular assist device. *Computer Methods in Applied Mechanics and Engineering*, 198(45-46):3534–3550, 2009.

[BK89] H. T. Banks and K. Kunisch. *Estimation techniques for distributed parameter systems*, volume 1 of *Systems & Control: Foundations & Applications*. Birkhäuser Boston Inc., Boston, MA, 1989.

[BOFH07] D.C. Barber, E. Oubel, A.F. Frangi, and D.R. Hose. Efficient computational fluid dynamics mesh generation by image registration. *Medical Image Analysis*, 11(6):648 – 662, 2007.

[BP84] F. Brezzi and J. Pitkäranta. On the stabilization of finite element approximations of the Stokes equations. In *Efficient solutions of elliptic systems (Kiel, 1984)*, volume 10 of *Notes Numer. Fluid Mech.*, pages 11–19. Vieweg, 1984.

[BQQ08] S. Badia, A. Quaini, and A. Quarteroni. Splitting methods based on algebraic factorization for fluid-structure interaction. *SIAM J. Sci. Comput.*, 30(4):1778–1805, 2008.

[BSDA08] F. Billet, M. Sermesant, H. Delingette, and N. Ayache. Cardiac motion recovery by coupling an electromechanical model and cine-MRI data: First steps. In K. Miller and P.M.F. Nielsen, editors, *Proc. of the Workshop on Computational Biomechanics for Medicine III. (Workshop MICCAI-2008)*, September 2008.

[BSV+12] D.C. Barber, C. Staicu, I. Valverde, P. Beerbaum, and D.R. Hose. Registration based segment growing for vascular segmentation. *Submitted to IEEE Transactions on Medical Imaging*, 2012.

[CCdBM11] D. Chapelle, N. Cîndea, M. de Buhan, and P. Moireau. Exponential convergence of an observer based on partial field measurements for the wave equation. Research Report 7728, INRIA, 2011. Submitted to CRAS Series I, http://hal.inria.fr/inria-00619504/fr.

[CCM] D. Chapelle, N. Cîndea, and P. Moireau. Improving convergence in numerical analysis using observers - the wave-like equation case. Submitted to M3AS.

[CGN05] P. Causin, J-F. Gerbeau, and F. Nobile. Added-mass effect in the design of partitioned algorithms for fluid-structure problems. *Comput. Methods Appl. Mech. Engrg.*, 194(42–44):4506–4527, 2005.

[Cha09] G. Chavent. *Nonlinear least squares for inverse problems*. Scientific Computation. Springer, New York, 2009. Theoretical foundations and step-by-step guide for applications.

[Cho68] A. J. Chorin. Numerical solution of the Navier-Stokes equations. *Math. Comp.*, 22:745–762, 1968.

[CLRAM11] J. Cavalcante, J. Lima, A. Redheuil, and M. Al-Mallah. Aortic stiffness: current understanding and future directions. *Journal of the American College of Cardiology*, 57(14):1511–1522, 2011.

[CML+11] R. Chabiniok, P. Moireau, P.-F. Lesault, A. Rahmouni, J.-F. Deux, and D. Chapelle. Estimation of tissue contractility from cardiac cine-mri using a biomechanical heart model. *Biomechanics and Modeling in Mechanobiology*, pages 1–22, 2011. 10.1007/s10237-011-0337-8.

[CMLT09] D. Chapelle, P. Moireau, and P. Le Tallec. Robust filtering for joint state-parameter estimation in distributed mechanical systems. *DCDS–A*, 23(1/2):65–84, January/February 2009. A special issue Dedicated to Ta-Tsien Li on the Occasion of his 70th Birthday.

[Cor07] J.M. Coron. *Control and nonlinearity*. Mathematical surveys and monographs. American Mathematical Society, 2007.

[CZ95] R.F. Curtain and H.J. Zwart. *An introduction to infinite-dimensional linear systems theory*. Texts in applied mathematics. Springer-Verlag, 1995.

[dKHvdS11] Chris L. de Korte, Hendrik H. G. Hansen, and Anton F. W. van der Steen. Vascular ultrasound for atherosclerosis imaging. *Interface Focus*, 1(4):565–575, 2011.

[DMP+11] M. D'Elia, L. Mirabella, T. Passerini, M. Perego, M. Piccinelli, C. Vergara, and A. Veneziani. Applications of variational data assimilation in computational hemodynamics. Technical Report TR-2011-002, Emory University, 2011.

[Doy12] M.M. Doyley. Model-based elastography: a survey of approaches to the inverse elasticity problem. *Physics in Medicine and Biology*, 57(3):R35, 2012.

[DPV11] M. D´Elia, M. Perego, and A. Veneziani. A variational data assimilation procedure for the incompressible navier-stokes equations in hemodynamics. *Journal of Scientific Computing*, pages 1–20, 2011.

[Dwi10] R.P. Dwight. Bayesian inference for data assimilation using least-squares finite element methods. In *IOP Conference Series: Materials Science and Engineering*, volume 10, page 012224. IOP Publishing, 2010.

[EG04] A. Ern and J.-L. Guermond. *Theory and practice of finite elements*, volume 159 of *Applied Mathematical Sciences*. Springer-Verlag, New York, 2004.

[ESP+05] P. Ewert, S. Schubert, B. Peters, H. Abdul-Khaliq, N. Nagdyman, and P.E. Lange. The CP stent short, long, covered for the treatment of aortic coarctation, stenosis of pulmonary arteries and caval veins, and Fontan anastomosis in children and adults: an evaluation of 60 stents in 53 patients. *Heart*, 91(7):948–953, 2005.

[Eve09] G. Evensen. *Data assimilation: the ensemble Kalman filter*. Springer Verlag, 2009.

[Fer11] M.-A. Fernández. Coupling schemes for incompressible fluid-structure interaction: implicit, semi-implicit and explicit. *SeMA J.*, (55):59–108, 2011.

[FFP79] Y.C. Fung, K. Fronek, and P. Patitucci. Pseudoelasticity of arteries and the choice of its mathematical expression. *American Journal of Physiology*, 237(5):H620–31, 1979.

[FG09] M.A. Fernández and J-F. Gerbeau. *Fluid structure interaction problems in haemodynamics*, chapter 9. Springer Verlag, 2009. in *Cardiovascular Mathematics. Modeling and simulation of the circulatory system*, L. Formaggia, A. Quarteroni, A. Veneziani editors.

[FGG06] M.A. Fernández, J-F. Gerbeau, and C. Grandmont. A projection algorithm for fluid-structure interaction problems with strong added-mass effect. *C. R. Math. Acad. Sci. Paris*, 342(4):279–284, 2006.

[FGG07] M.A. Fernández, J.F. Gerbeau, and C. Grandmont. A projection semi-implicit scheme for the coupling of an elastic structure with an incompressible fluid. *Int. J. Num. Meth. Engrg.*, 69(4):794–821, 2007.

[FHSY08] K. Funamoto, T. Hayase, Y. Saijo, and T. Yambe. Numerical experiment for ultrasonic-measurement-integrated simulation of three-dimensional unsteady blood flow. *Annals of biomedical engineering*, 36(8):1383–1397, 2008.

[Fle97] Wendell H. Fleming. Deterministic nonlinear filtering. *Annali della Scuola Normale Superiore di Pisa - Classe di Scienze*, 25:435–454, 1997.

[FLT03] M.A. Fernández and P. Le Tallec. Linear fluid-structure stability analysis with transpiration. part ii: numerical analysis and applications. *Comput. Methods Appl. Mech. Engrg.*, 192(43):4837–4873, 2003.

[FMN07] L. Formaggia, A. Moura, and F. Nobile. On the stability of the coupling of 3d and 1d fluid-structure interaction models for blood flow simulations. *ESAIM-Mathematical Modelling and Numerical Analysis*, 41(4):743–770, 2007.

[FQV09] L. Formaggia, A. Quarteroni, and A. Veneziani, editors. *Cardiovascular Mathematics. Modeling and simulation of the circulatory system*, volume 1 of *Modeling, Simulation and Applications*. Springer, 2009.

[FVH11] J. Ferruzzi, D.A. Vorp, and J.D. Humphrey. On constitutive descriptors of the biaxial mechanical behaviour of human abdominal aorta and aneurysms. *Journal of the Royal Society Interface*, 8(56):435–50, 2011.

[GFW10] M. W. Gee, Ch. Förster, and W. A. Wall. A computational strategy for prestressing patient-specific biomechanical problems under finite deformation. *International Journal for Numerical Methods in Biomedical Engineering*, 26(1):52–72, 2010.

[GJDB08] A.M. Gaca, J.J. Jaggers, L.T. Dudley, and G.S. Bisset. Repair of Congenital Heart Disease: A Primer–Part 2. *Radiology*, 248(1):44–60, 2008.

[GMS06] J. L Guermond, P. Minev, and J. Shen. An overview of projection methods for incompressible flows. *Comp. Meth. Appl. Mech. Engrg.*, 195(44–47):6011–6045, 2006.

[GQ98] J.-L. Guermond and L. Quartapelle. On stability and convergence of projection methods based on pressure Poisson equation. *Internat. J. Numer. Methods Fluids*, 26(9):1039–1053, 1998.

[GR09] Christophe Geuzaine and Jean-Francois Remacle. Gmsh: A 3-d finite element mesh generator with built-in pre- and post-processing facilities. *International Journal for Numerical Methods in Engineering*, 79(11):1309–1331, 2009.

[GV03] J-F. Gerbeau and M. Vidrascu. A quasi-Newton algorithm based on a reduced model for fluid-structure interactions problems in blood flows. *Math. Model. Num. Anal.*, 37(4):631–648, 2003.

[GVD09] M. Grobbelaar-Van Dalsen. A new approach to the stabilization of a fluid-structure interaction model. *Appl. Anal.*, 88(7):1053–1065, 2009.

[HGO00] G. Holzapfel, T. Gasser, and R. Ogden. A new constitutive framework for arterial wall mechanics and a comparative study of material models. *Journal of Elasticity*, 61(1):1–48, 2000.

[HMM+10] J.J. Heys, T.A. Manteuffel, S.F. McCormick, M. Milano, J. Westerdale, and M. Belohlavek. Weighted least-squares finite elements based on particle imaging velocimetry data. *Journal of Computational Physics*, 229(1):107–118, 2010.

[HO09] G.A. Holzapfel and R.W. Ogden. On planar biaxial tests for anisotropic nonlinearly elastic solids: a continuum mechanical framework. *Mathematics and Mechanics of Solids*, 14:474–489, 2009.

[HO10] G.A. Holzapfel and R.W. Ogden. Constitutive modelling of arteries. *Proceedings of the Royal Society A: Mathematical, Physical and Engineering Science*, 2010.

[Hol06] G.A. Holzapfel. Determination of material models for arterial walls from uniaxial extension tests and histological structure. *Journal of Theoretical Biology*, 238(2):290–302, 2006.

[HPB02] I. Hoteit, D.-T. Pham, and J. Blum. A simplified reduced order Kalman filtering and application to altimetric data assimilation in Tropical Pacific. *Journal of Marine Systems*, 36(1–2):101–127, 2002.

[Hum02] J.D. Humphrey. *Cardiovascular solid mechanics: cells, tissues, and organs*. Springer, 2002.

[Hut71] G. Hutchins. Coarctation of the Aorta Explained as a Branch-Point of the Ductus Arteriosus. *American Journal of Pathology*, 63(2):203–214, 1971.

[HZCM07] L. Horný, R. Zitný, H. Chlup, and H. Macková. Identification of the material parameters of an aortic wall. *Bulletin of Applied Mechanics*, 2(8), 2007.

[IH08] K. Imagawa and T. Hayase. Eigenvalue analysis for error dynamics of measurement integrated simulation to reproduce real flows. *Bulletin of the American Physical Society*, 53, 2008.

[JUDW95] S. Julier, J. Uhlmann, and H.F. Durrant-Whyte. A new approach for filtering nonlinear systems. In *American Control Conference*, pages 1628–1632, 1995.

[JUDW00] S. Julier, J. Uhlmann, and H.F. Durrant-Whyte. A new method for the nonlinear transformation of means and covariances in filters and estimators. *Automatic Control, IEEE Transactions on*, 45(3):477–482, 2000.

[Jul03] S. Julier. The spherical simplex unscented transformation. In *Proc. of the American Control Conference*, pages 2430–4234, 2003.

[KB61] R. Kalman and R. Bucy. New results in linear filtering and prediction theory. *Trans. ASME J. Basic. Eng*, 83:95–108, 1961.

[Kla11] R. Klabunde. *Cardiovascular Physiology Concepts*. http://www.cvphysiology.com, 2011.

[KS06] T. Korakianitis and Y. Shi. A concentrated parameter model for the human cardiovascular system including heart valve dynamics and atrioventricular interaction. *Medical Engineering & Physics*, 28:613–628, 2006.

[KV03] K. Kunisch and S. Volkwein. Galerkin proper orthogonal decomposition methods for a general equation in fluid dynamics. *SIAM Journal on Numerical Analysis*, 40(2):pp. 492–515, 2003.

[Lag99] P.-Y. Lagrée. An inverse technique to deduce the elasticity of a large artery. *Eur. Phys. J. AP*, 9:153–163, 1999.

[LAVC+11] J.F. Ladisa, F.C. Alberto, I.E. Vignon-Clementel, K.H. Jin, N. Xiao, L.M. Ellwein, F.P. Chan, J.A. Feinstein, C.A. Taylor, et al. Computational simulations for aortic coarctation: representative results from a sampling of patients. *Journal of biomechanical engineering*, 133(9):091008, 2011.

[LBMV09] M.R. Labrosse, C.J. Beller, T. Mesana, and J.P. Veinot. Mechanical behavior of human aortas: Experiments, material constants and 3-d finite element modeling including residual stress. *J Biomech*, 42(8):996–1004, 2009.

[LCVB+06] S. Laurent, J. Cockcroft, L. Van Bortel, P. Boutouyrie, C. Giannattasio, D. Hayoz, B. Pannier, C. Vlachopoulos, I. Wilkinson, and H. Struijker-Boudier. Expert consensus document on arterial stiffness: methodological issues and clinical applications. *European Heart Journal*, 27(21):2588–2605, 2006.

[LT94] P. Le Tallec. Numerical methods for nonlinear three-dimensional elasticity. In *Handbook of numerical analysis, Vol. III*, pages 465–622. North-Holland, 1994.

[LT03] I. Lasiecka and R. Triggiani. $L_2(\Sigma)$-regularity of the boundary to boundary operator B^*L for hyperbolic and Petrowski PDEs. *Abstr. Appl. Anal.*, (19):1061–1139, 2003.

[Lue71] D. G. Luenberger. An introduction to observers. *IEEE Transactions on Automatic Control*, 16:596–602, 1971.

[Mad09] Y. Maday. Analysis of coupled models for fluid-structure interaction of internal flows. In *Cardiovascular mathematics*, volume 1 of *MS&A. Model. Simul. Appl.*, pages 279–306. Springer, 2009.

[MBDQ11] A. Cristiano I. Malossi, Pablo J. Blanco, Simone Deparis, and Alfio Quarteroni. Algorithms for the partitioned solution of weakly coupled fluid models for cardiovascular flows. *International Journal for Numerical Methods in Biomedical Engineering*, 27(12):2035–2057, 2011.

[MBH+11] M. Moghadam, Y. Bazilevs, T.-Y. Hsia, I. Vignon-Clementel, A. Marsden, and Mocha Modeling Of Congenital Hearts Alliance Investigators. A comparison of outlet boundary treatments for prevention of backflow divergence with relevance to blood flow simulations. *Computational Mechanics*, 48(3):277–291, 2011.

[MBL+08] I. Masson, P. Boutouyrie, S. Laurent, J.D. Humphrey, and M. Zidi. Characterization of arterial wall mechanical behavior and stresses from human clinical data. *Journal of Biomechanics*, 2008.

[MBX+12] P. Moireau, C. Bertoglio, N. Xiao, C.A. Figueroa, C.A. Taylor, D. Chapelle, and J.-F. Gerbeau. Sequential identification of boundary support parameters in a fluid-structure vascular model using patient image data. *Biomechanics and Modeling in Mechanobiology*, pages 1–22, 2012.

[MC11a] P. Moireau and D. Chapelle. Erratum of article "reduced-order Unscented Kalman Filtering with application to parameter identification in large-dimensional systems". *COCV*, 17:406–409, 2011. doi:10.1051/cocv/2011001.

[MC11b] P. Moireau and D. Chapelle. Reduced-order Unscented Kalman Filtering with application to parameter identification in large-dimensional systems. *COCV*, 17:380–405, 2011. doi:10.1051/cocv/2010006.

[MCDG05] V. Martin, F. Clément, A. Decoene, and J-F. Gerbeau. Parameter identification for a one-dimensional blood flow model. *ESAIM-Proceedings*, 14:174–200, 2005.

[MCLT08] P. Moireau, D. Chapelle, and P. Le Tallec. Joint state and parameter estimation for distributed mechanical systems. *Computer Methods in Applied Mechanics and Engineering*, 197:659–677, 2008.

[MCLT09] P. Moireau, D. Chapelle, and P. Le Tallec. Filtering for distributed mechanical systems using position measurements: Perspective in medical imaging. *Inverse Problems*, 25(3):035010–035035, March 2009.

[MGE10] Yogesh K. Mariappan, Kevin J. Glaser, and Richard L. Ehman. Magnetic resonance elastography: A review. *Clinical Anatomy*, 23(5):497–511, 2010.

[Mod04] J. Modersitzki. *Numerical Methods for Image Registration*. Oxford university press, 2004.

[Moi08] P. Moireau. *Filtering based data assimilation for second order hyperbolic PDE. Applications in cardiac mechanics*. PhD thesis, Ecole Polytechnique, 2008.

[MVCFM12] M.E. Moghadam, I.E. Vignon-Clementel, R. Figliola, and A.L. Marsden. A modular numerical method for implicit 0d/3d coupling in cardiovascular finite element simulations. *Journal of Computational Physics*, 2012.

[MXA+11] P. Moireau, N. Xiao, M. Astorino, C.A. Figueroa, D. Chapelle, C.A. Taylor, and J-F. Gerbeau. External tissue support and fluid-structure simulation in blood flows. *Biomechanics and Modeling in Mechanobiology*, 2011. doi: 10.1007/s10237-011-0289-z.

[NOH05] W.W. Nichols, M.F. O'Rourke, and C. Hartley. *McDonald's blood flow in arteries: theoretical, experimental and clinical principles*, volume 340809418. Hodder Arnold London, 2005.

[PMLL09] K. Poprawski, M. Michalski, M. Lawniczak, and K. Lacka. Cardiovascular abnormalities in patients with turner syndrome according to karyotype: own experience and literature review. *Pol Arch Med Wewn*, 119(7-8):453–60, 2009.

[Pou07] Nicole Poussineau. *Réduction variationnelle d'un couplage fluide-structure. Application à l'hémodynamique.* PhD thesis, Université Pierre et Marie Curie, Paris 6, 2007.

[Pre02] A. Preumont. *Vibration Control of Active Structures, An Introduction.* Kluwer Academic Publishers, 2nd edition, February 2002.

[Pro09] N. Proudfoot. The acute effects of moderate intensity exercise on vascular stiffness in children with repaired coarctation of the aorta. Master's thesis, McMaster University, 2009.

[PVG98] D.-T. Pham, J. Verron, and L. Gourdeau. Filtres de Kalman singuliers évolutifs pour l'assimilation de données en océanographie. *Comptes Rendus de l'Académie des Sciences - Series IIA*, 326(4):255–260, 1998.

[PVV11] M. Perego, A. Veneziani, and C. Vergara. A variational approach for estimating the compliance of the cardiovascular tissue: An inverse fluid-structure interaction problem. *SIAM J. Sc. Comp.*, 33(3):1181–1211, 2011.

[QQ07] A. Quaini and A. Quarteroni. A semi-implicit approach for fluid-structure interaction based on an algebraic fractional step method. *Math. Models Methods Appl. Sci.*, 17(6):957–983, 2007.

[Ray10] Jean-Pierre Raymond. Feedback stabilization of a fluid-structure model. *SIAM J. Control Optim.*, 48(8):5398–5443, 2010.

[RSR04] A. Rosset, L. Spadola, and O. Ratib. Osirix: An open-source software for navigating in multidimensional dicom images. *Journal of Digital Imaging*, 17:205–216, 2004. 10.1007/s10278-004-1014-6.

[SH12] G. Sommer and G.A. Holzapfel. 3d constitutive modeling of the biaxial mechanical response of intact and layer-dissected human carotid arteries. *J Mech Behav Biomed Mater*, 5(1):116–28, 2012.

[Sim06] D. Simon. *Optimal state estimation: Kalman, H infinity, and nonlinear approaches*. Wiley-Interscience, 2006.

[Sim09] D. Simon. Kalman filtering with state constraints: A survey of linear and nonlinear algorithms. IET Control Theory & Applications, accepted for publication, 2009.

[SLH11] Y. Shi, P. Lawford, and R. Hose. Review of zero-d and 1-d models of blood flow in the cardiovascular system. *Biomed Eng Online*, 10:33, 2011.

[SLVH94] B. Sonesson, T. Länne, E. Vernersson, and F. Hansen. Sex difference in the mechanical properties of the abdominal aorta in human beings. *Journal of Vascular Surgery*, 20(6):959–69, 1994.

[SS11] R. Syamasundar and P. Seib. *Medscape Reference. Coarctation of the Aorta*. http://emedicine.medscape.com/article/895502-overview, 2011.

[Sta09] J. Stalhand. Determination of human arterial wall parameters from clinical data. *Biomechanics and Modeling in Mechanobiology*, 8(2):141–148, 2009.

[SZP+11] A.J. Schriefl, G. Zeindlinger, D.M. Pierce, P. Regitnig, and G.A. Holzapfel. Determination of the layer-specific distributed collagen fibre orientations in human thoracic and abdominal aortas and common iliac arteries. *Journal of the Royal Society Interface*, 2011.

[Tal11] Talk Talk Encyclopaedia. *Circulatory system*. http://www.talktalk.co.uk/reference/encyclopaedia/hutchinson/m0006777.html, 2011.

[Tem69] R. Temam. Sur l'approximation de la solution des equations de Navier-Stokes par la méthode des pas fractionaires I. *Arch. Rational Mech. Anal.*, 32:135–153, 1969.

[The10] The Reference Values for Arterial Stiffness' Collaboration. Determinants of pulse wave velocity in healthy people and in the presence of cardiovascular risk factors: establishing normal and reference values. *European Heart Journal*, 31:2338–2350, 2010.

[UBS+09] S. Uribe, P. Beerbaum, T. Sørensen, A. Rasmusson, R. Razavi, and T. Schaeffter. Four-dimensional (4d) flow of the whole heart and great vessels using real-time respiratory self-gating. *Magnetic Resonance in Medicine*, 62(4):984–992, 2009.

[Val12] I. Valverde. *Evaluation of Magnetic Resonance Imaging for Image-Based Computational Fluid Dynamic Modelling in Aaortic Coarctation*. PhD thesis, King's College of London, 2012.

[VDK+05] Thomas Völkl, Karin Degenhardt, Andreas Koch, Diemud Simm, Helmuth Dörr, and Helmut Singer. Cardiovascular anomalies in children and young adults with ullrich-turner syndrome the erlangen experience. *Clinical Cardiology*, 28(2):88–92, 2005.

[Vir08] J. Virues. *Mechanical Properties of Arterial Wall*. PhD thesis, The University of British Columbia, 2008.

[Wik11] Wikipedia Encyclopedia. *Circulatory system*. http://en.wikipedia.org/wiki/Circulatory_system, 2011.

[WRL+06] D.A. Woodrum, A.J. Romano, A. Lerman, U.H. Pandya, D. Brosh, P.J. Rossman, L.O. Lerman, and R.L. Ehman. Vascular wall elasticity measurement by magnetic resonance imaging. *Magnetic Resonance in Medicine*, 56(3):593–600, 2006.

[WSC+12] D.C. Wendell, M.M. Samyn, J.R. Cava, L.M. Ellwein, M.M. Krolikowski, K.L. Gandy, A.N. Pelech, S.C. Shadden, and J.F. LaDisa. Including aortic valve morphology in computational fluid dynamics simulations: Initial findings and application to aortic coarctation. *Medical Engineering & Physics*, 2012.

[WWB+08] C.A. Warnes, R.G. Williams, T.M. Bashore, J.S. Child, H.M. Connolly, J.A. Dearani, P. del Nido, J.W. Fasules, T.P. Graham, Z.M. Hijazi, S.A. Hunt, M.E. King, M.J. Landzberg, P.D. Miner, M.J. Radford, E.P. Walsh, and G.D. Webb. ACC/AHA 2008 Guidelines for the Management of Adults with Congenital Heart Disease: a report of the American College of Cardiology/American Heart Association Task Force on Practice Guidelines (writing committee to develop guidelines on the management of adults with congenital heart disease). *Circulation*, 118(1):714–833, 2008.

[XCY+12] L. Xu, J. Chen, M. Yin, K.J. Glaser, Q. Chen, D.A. Woodrum, and R.L. Ehman. Assessment of stiffness changes in the ex vivo porcine aortic wall using magnetic resonance elastography. *Magnetic Resonance Imaging*, 30:122–127, 2012.

[ZDRVB10] S. Zeinali-Davarani, L.G. Raguin, D.A. Vorp, and S. Baek. Identification of in vivo material and geometric parameters of a human aorta: toward patient-specific modeling of abdominal aortic aneurysm. *Biomechanics and Modeling in Mechanobiology*, 10(5):689–99, 2010.

[ZZ07] X. Zhang and E. Zuazua. Long-time behavior of a coupled heat-wave system arising in fluid-structure interaction. *Arch. Ration. Mech. Anal.*, 184(1):49–120, 2007.